



CERN-THESIS-2005-106

STRANGE PARTICLE AND
ANTIPARTICLE PRODUCTION IN
PROTON-BERYLLIUM INTERACTIONS
AT 40 GeV/ c AT THE CERN NA57
EXPERIMENT

Stephen Andrew Bull

*Thesis submitted for the degree of
Doctor of Philosophy*



Particle Physics Group,
School of Physics and Astronomy,
University of Birmingham.

May, 2005.

Abstract

Results are presented on the production of singly strange Λ and $\bar{\Lambda}$ hyperons and K_S^0 mesons in p–Be collisions at 40 GeV/c beam momentum. The data were obtained by the NA57 experiment at the CERN SPS in the 1999 data taking period. A comprehensive study of yields and transverse mass spectra for each of the three particle species is given. The results are compared to Pb–Pb data at 40 A GeV/c. In particular, the yields per wounded nucleon are seen to increase for all three particle species when going from p–Be to Pb–Pb collisions. This is a proposed signature that marks the transition of hadronic matter into a new phase of matter known as a *Quark-Gluon Plasma* (QGP).

An overview of QGP physics, its signatures and experimental results together with its importance to the understanding of QCD is given. The NA57 experimental apparatus is described in detail and the analysis procedures and techniques along with the results detailed. A study of the systematics is made. The results are compared to WA97/NA57 results at the top SPS energy and to results from other SPS and RHIC experiments. A brief insight into future experiments that will study the QGP is given.

Author's Contribution

All work presented in this thesis relating to the Λ , $\bar{\Lambda}$ and K_S^0 particle species from the NA57 p–Be 40 GeV/c data set collected by the collaboration in 1999 is my own. However, due to the collaborative nature of experimental High Energy Physics the analysis makes use of well established software, available to all within the collaboration. I have developed this software in order to analyse the 1999 data sets, for which I have been responsible.

More specifically, I have extracted Λ , $\bar{\Lambda}$ and K_S^0 candidates from the raw data, by optimising the selection criteria needed to reconstruct these candidates. The code for some of these selections needed adding to the existing code. Principally, I wrote a routine to calculate the primary vertex of the V^0 within the thick Be target and confirmed the position of the proton beam in the database using a ‘direct V^0 ’ analysis. I estimated the combinatorial background beneath the $\bar{\Lambda}$ and K_S^0 signals.

I set up and thoroughly tested the ‘weighting chain’ specific to the 1999 data set. I optimised the GEANT software to include details of the NA57 apparatus specific to the set up required for the p–Be data run. I verified the proton beam profile obtained by the CERN beam physicists. I have calculated weights to take into account acceptance and reconstruction efficiency for a sample of Λ , $\bar{\Lambda}$ and K_S^0 experimental data. I have calculated fully corrected transverse mass distributions and extrapolated yields for all three particle species, which I have checked for stability. I have undertaken a detailed study of systematic effects on these results and

have been one of the two principal contributors in a detailed comparison between these 1999 results and those obtained for a second p–Be data set at the same energy collected in 2001. The 2001 data were analysed in Košice.

I have compared the 1999 results to Pb–Pb results at the same energy, to WA97/NA57 results at the top SPS energy and to the results of a variety of other experiments.

Acknowledgements

Over the past $4\frac{2}{3}$ years I have been privileged to be part of the Particle Physics Group at the University of Birmingham studying for my Ph.D. During this time I have received a lot of help and support from colleagues, friends and family and I should like to take this opportunity to say thank you for these invaluable contributions.

To begin, I would like to thank all those responsible within the School of Physics and Astronomy for giving me the opportunity to study for a Ph.D in Particle Physics. I would like to thank the Particle Physics and Astronomy Research Council (PPARC) for financially supporting this work.

I would like to thank all members of the Birmingham NA57 Group for their friendship, support, expertise in the subject and lively discussions (not always about Physics!). More specifically, I would like to thank Dr. David Evans who has been an excellent supervisor and has provided help and advice on all aspects of the work. I would like to thank Dr. Roman Lietava and Dr. Orlando Villalobos Baillie for their expert knowledge and help with all aspects of the analysis as well as to fellow student (now Dr.) Rory Clarke who has helped me in many ways over the duration of my Ph.D. I would like to thank Dr. Gron Jones, Professor John Kinson, Dr. Paul Norman and Dr. Frank Votruba for their experience and encouragement. My thanks to current students Mr. Paul Bacon and Mr. Richard Platt and I wish them all the best with the remainder of their studies. I would like to thank all NA57 collaborators outside of Birmingham who I have worked with, particularly spokesperson Dr. Fed-

erico Antinori, Dr. Ivan Králik, Dr. Adam Jacholkowski and Mr. Marek Bombara. Thank you to Dr. David Evans, Dr. Orlando Villalobos Baillie, Dr. Roman Lietava and Dr. Federico Antinori for proof reading all or part of this thesis and for making many useful comments and suggestions. My thanks to Dr. Lawrence Lowe who has consistently provided solutions to my many computing queries.

Thank you to all members of the Birmingham Particle Physics Group, it has been a very friendly and supportive atmosphere in which to work. My thanks to fellow postgraduate students, (mainly within, but also outside of Particle Physics) whom I have known whilst at Birmingham, for their friendship, support, conversation and for making day-to-day life enjoyable. I would like to thank my undergraduate Particle Physics lecturers and, in particular, final year undergraduate project supervisor Dr. John Wilson for getting me interested in the fascinating subject of Particle Physics.

Since January 2001 I have not enjoyed the best of health and I would like to thank all in the medical profession who have provided support and encouragement during my recovery. In particular, I would like to thank Dr. David Cripps, Mr. Marcus Webb, Mrs. Sue Gordon Saner and all at Action Heart. I would like to thank all those who have gone out of their way to help me over this time. I am indebted to those at the University who have helped me continue with this degree. I would like to thank Dr. David Evans, Professor Peter Watkins, the current head of Particle Physics, as well as his predecessor, Professor John Dowell, for all their efforts in accommodating my situation. I would particularly like to thank Professor John Kinson, Dr. Andrew Critchley and the now Drs. David Acreman, Paul Bell, Rory Clarke, Hazel Craven and Michael Taylor who have helped me on a regular basis with transport to and from the University. I would like to thank all those who have presented work on my behalf when I was unable to visit CERN and, more recently, all those who have helped me whilst at CERN. In particular, I would like to thank Mr. Paul Bacon and Dr. Rory Clarke who have made these more recent

visits possible.

Finally, and physics aside, a big thank you to all my friends, both at Birmingham and elsewhere, who have stuck by, supported and not given in on me. I would like to thank my entire family (including my late grandparents who would have loved to have seen me complete this thesis) for their love and support throughout and particularly Mum, Dad and my brother David for being the best.

Stephen Bull, May 2005.

Contents

1	The Quark-Gluon Plasma	1
1.1	Introduction	1
1.2	Quantum Chromodynamics (QCD)	2
1.2.1	The Strong Potential	3
1.2.2	Asymptotic Freedom	4
1.2.3	The QCD Vacuum	7
1.2.4	Achieving Asymptotic Freedom	8
1.3	The Phase Diagram	9
1.4	Heavy Ion Physics	11
1.5	Heavy Ion Terminology	13
1.5.1	Collision Centrality	13
1.5.2	Transverse and Longitudinal Momentum	13
1.5.3	Rapidity	15
1.6	Strangeness Enhancement	16

1.7	Other Signatures of a QGP	21
1.7.1	J/ψ Suppression	21
1.7.2	Dilepton Pairs	22
1.7.3	Direct Photons	24
1.7.4	High p_T Suppression and Jet Quenching	26
1.8	An Overview of High Energy Heavy Ion Physics Experiments	30
2	The NA57 Experiment	33
2.1	The WA97 Experiment	33
2.2	Motivation for the NA57 Experiment	34
2.3	The CERN SPS	34
2.4	The NA57 Experiment	36
2.4.1	Beam	36
2.4.2	Target	38
2.4.3	Telescope	38
2.4.4	Trigger	41
2.5	The NA57 Experiment for Pb–Pb Interactions	44
2.5.1	Beam	44
2.5.2	Target	44
2.5.3	Telescope	44

2.5.4	Trigger	46
2.5.5	Multiplicity Detectors	47
2.6	The Data Sets	47
3	Λ and $\bar{\Lambda}$ Reconstruction in p–Be Collisions	49
3.1	Introduction	49
3.2	Data Acquisition	50
3.3	Sailor and Cowboy Decays	50
3.4	Reconstruction of a V^0 Candidate	51
3.5	The Primary Vertex	52
3.6	Verifying the Database using a “Direct V^0 ” Analysis	55
3.7	Separating V^0 Candidates into Λ , $\bar{\Lambda}$ and K_S^0 Candidates	59
3.7.1	The Armenteros-Podolanski Plot	59
3.7.2	The K_S^0 Mass Selection	61
3.8	Further Selection Criteria	63
3.8.1	The x Decay Vertex	63
3.8.2	The B_y Parameter of the V^0	65
3.8.3	The B_y Parameter of the Charged Tracks	67
3.8.4	The V^0 Internal Decay Angle	67
3.9	Summary of Λ and $\bar{\Lambda}$ Selection Criteria	70

3.10	Gold-Plated Λ and $\bar{\Lambda}$ Samples	72
3.11	Estimation of the Combinatorial Background Beneath the $\bar{\Lambda}$ Signal	75
3.11.1	Comparing the Clean Λ and $\bar{\Lambda}$ Signals	75
3.11.2	Fitting a Combinatorial Background to the $\bar{\Lambda}$ Signal	76
4	Analysis of the Selected Λ and $\bar{\Lambda}$ Data	81
4.1	Introduction	81
4.2	The Weighting Chain	82
4.2.1	Monte-Carlo Simulation	82
4.2.2	Background Mixing	83
4.2.3	Track Reconstruction	84
4.2.4	V^0 Reconstruction	84
4.2.5	Weight Calculation	84
4.3	The Weighted Λ and $\bar{\Lambda}$ Samples from the 1999 p-Be Data Set	85
4.4	The Region of Good Acceptance	88
4.5	Transverse Mass Spectra	90
4.6	Particle Yields	93
4.7	Stability of Results	96
4.8	Combinatorial Background Corrections for the $\bar{\Lambda}$ Inverse Slope and Yield	98
4.8.1	$\bar{\Lambda}$ Inverse Slope	99

4.8.2	$\bar{\Lambda}$ Yield	101
4.9	Errors	101
5	Reconstruction and Correction of K_S^0 Candidates in p–Be Collisions	103
5.1	Introduction	103
5.2	K_S^0 Selection Criteria	104
5.2.1	The Armenteros-Podolanski Plot	105
5.2.2	The x Decay Vertex	105
5.2.3	The B_y Parameter of the V^0	107
5.2.4	The B_y Parameter of the Charged Tracks	107
5.2.5	The z Separation Parameter	109
5.3	Summary of K_S^0 Selection Criteria	112
5.4	Combinatorial Background Beneath the K_S^0 Mass Signal	114
5.5	The Weighted K_S^0 Sample	116
5.6	The Region of Good Acceptance	116
5.7	K_S^0 Transverse Mass Spectra	119
5.8	K_S^0 Yield	122
5.9	Stability of Results	122
6	Study of Systematics	126

6.1	Introduction	126
6.2	The Number of p–Be Interactions	126
6.3	Rapidity Distributions	129
6.4	Results from the 2001 p–Be Data	132
6.5	The Data Analysis Programs and Selection Criteria	134
6.5.1	Monte-Carlo Simulation	135
6.5.2	Background Mixing	137
6.5.3	Track reconstruction	137
6.5.4	V^0 Reconstruction and Selection Criteria	139
6.5.5	Weight Calculation	141
6.5.6	The 2001 Analysis Programs using the 1999 Data	141
6.5.7	The 1999 Analysis Programs using the 2001 Data	142
6.5.8	Summary of Checks on the Analysis Programs	143
6.6	Properties of the Proton Beam	144
6.6.1	Beam Spread	144
6.6.2	Beam Position	145
6.7	Estimation of Overall Systematic Errors	147
6.8	Conclusions	147
7	Physics Interpretation of Results, Outlook and Conclusions	150

7.1	Introduction	150
7.2	Strangeness Enhancement at 40 A GeV/c	151
7.3	Inverse Slopes at 40 A GeV/c	154
7.4	Comparison with Other Experiments	156
7.5	Energy Dependence	160
7.5.1	Strangeness Enhancement and Particle Yields	160
7.5.2	Inverse Slopes	167
7.6	Summary	168
7.7	The Future for Heavy Ion Physics	168
7.8	Conclusion	172
A	Energy Available for New Particle Production in Fixed Target and Colliding Beam Experiments	174
B	The Primary Vertex	177
C	The Armenteros-Podolanski Plot	179
C.1	Features of the Armenteros-Podolanski Plot	179
C.2	Expressing p^* in Terms of Mass	183
C.3	Numerical Values of a , $\bar{\alpha}$ and p^*	184
D	The Equation of the Curved Edges of the Acceptance Window	185

List of Figures

1.1	Debye Screening of electric charge and antiscreening of colour charge.	5
1.2	Phase diagram of matter in the temperature–baryon chemical potential plane.	9
1.3	Pictorial representation of the creation of a Quark-Gluon Plasma by a Pb-Pb collision in the laboratory.	12
1.4	Pictorial representation of a central and a peripheral collision.	14
1.5	Methods of producing strange quark-antiquark pairs via thermal gluon fusion and via lighter quark-antiquark annihilation.	17
1.6	Production of strange particles and antiparticles as a signature of a QGP.	18
1.7	Yield per participant of strange and multistrange particles in Pb–Pb, relative to p–A, collisions at 158 A GeV/c as a function of number of participants.	20
1.8	Yield of J/ψ particles in S–U and Pb–Pb collisions at 158 GeV/c, normalised to p–A collisions as a function of number of participants.	23
1.9	Mass spectra of e^+e^- pairs in Pb–Au collisions at 158 A GeV/c compared to the sum of the expected contributions from hadron decays.	25

1.10	The $(N_\gamma)_{Meas}/(N_\gamma)_{Bkgd}$ ratio as a function of transverse momentum for peripheral and central Pb–Pb collisions at 158 A GeV/c.	27
1.11	Angular correlations between pairs of high p_T charged particles, referenced to a selected particle, for p–p, d–Au and Au–Au collisions at $\sqrt{s_{NN}} = 200$ GeV.	29
2.1	The 9 km circumference CERN SPS	35
2.2	The NA57 experiment for p–Be collisions at 40 GeV/c.	37
2.3	Silicon pixels connected to their corresponding readout cells.	39
2.4	An Omega2 silicon pixel plane made up of two half planes.	40
2.5	The NA57 experiment for Pb–Pb collisions at both 40 and 158 A GeV/c.	45
3.1	Cowboy and sailor topologies.	51
3.2	The primary vertex as determined in the $x - y$ and $x - z$ planes.	53
3.3	$xtarg$ calculated in the $x - z$ plane.	54
3.4	Charged tracks detected by the telescope, produced from the decay of a real V^0 and the decay of a “direct V^0 ”.	56
3.5	y_0 and z_0 defined by the direct V^0 method.	57
3.6	$xtarg$ defined by the direct V^0 method.	58
3.7	The Armenteros-Podolanski Plot for the 1999 p–Be data.	60
3.8	Various $\bar{\Lambda}$ effective mass plots which illustrate the choice of the K_S^0 effective mass selections.	62

3.9	A schematic diagram of a V^0 decay, illustrating the definition of the x decay vertex of the V^0	63
3.10	Various $\bar{\Lambda}$ effective mass plots which illustrate the choice of the x decay vertex selections.	64
3.11	A schematic diagram of a V^0 decay, illustrating the definition of the B_y parameter of the V^0	65
3.12	Various $\bar{\Lambda}$ effective mass plots which illustrate the choice of the B_y parameter of the V^0 selections.	66
3.13	A schematic diagram of a V^0 decay, illustrating the definition of the B_y parameter of the charged tracks.	68
3.14	$\bar{p}\pi^+$ mass versus the B_y parameter of both of the charged decay tracks.	68
3.15	A schematic diagram illustrating the definition of the ϕ angle.	69
3.16	The decay geometry with the ϕ angle at $\phi = 0^\circ$ and $\phi = 90^\circ$	70
3.17	Various $\bar{\Lambda}$ effective mass plots which illustrate the choice of the internal decay angle selections.	71
3.18	Λ and $\bar{\Lambda}$ mass signals with selection criteria applied.	73
3.19	Gold-Plated Λ and $\bar{\Lambda}$ mass signals.	74
3.20	$\bar{\Lambda}$ mass signal showing the estimated combinatorial background with the fitted 4th degree polynomial superimposed.	77
3.21	$\bar{\Lambda}$ mass signal with Gaussian and Granet functions superimposed.	79
4.1	Comparison of simulated to real Λ data on various distributions used in the selection criteria of the real data.	86

4.2	Comparison of simulated to real Λ data on the B_y distribution of the V^0 using differing beam profiles.	87
4.3	p_T versus rapidity for the weighted Λ candidates, with the acceptance window superimposed on top	88
4.4	p_T versus rapidity for the weighted $\bar{\Lambda}$ candidates, with the acceptance window superimposed on top	89
4.5	The rapidity distribution for the Λ particle.	91
4.6	$\ln\left(\frac{1}{m_T} \frac{dN}{dm_T}\right)$ versus m_T for the Λ particle.	92
4.7	$\ln\left(\frac{1}{m_T} \frac{dN}{dm_T}\right)$ versus m_T for the $\bar{\Lambda}$ particle.	92
4.8	Inverse slopes and extrapolated yields for the Λ , calculated separately in six different consecutive time periods.	97
4.9	Inverse slopes and extrapolated yields for the $\bar{\Lambda}$, calculated separately in six different consecutive time periods.	98
4.10	$\ln\left(\frac{1}{m_T} \frac{dN}{dm_T}\right)$ versus m_T for the $\bar{\Lambda}$ particle showing both the background corrected and uncorrected data.	100
5.1	Various K_S^0 effective mass plots which illustrate the choice of the x -decay vertex selections.	106
5.2	Various K_S^0 effective mass plots which illustrate the choice of the B_y parameter of the V^0 selections.	108
5.3	The internal decay angle, ϕ , versus the K_S^0 effective mass	109
5.4	The definition of the $zsep$ parameter of the charged decay tracks. . .	110

5.5	Various K_S^0 effective mass plots which illustrate the choice of the z separation selection.	111
5.6	K_S^0 mass signals with all selection criteria implemented, showing the effect of the inclusion of the K_S^0 mass selection.	113
5.7	K_S^0 mass signal with Gaussian and exponential functions superimposed.	115
5.8	Comparison of simulated to real K_S^0 data on various distributions used in the selection criteria of the real data.	117
5.9	p_T versus rapidity for the weighted K_S^0 candidates, with the acceptance window superimposed on top	118
5.10	The rapidity distribution for the K_S^0 particle.	120
5.11	$\ln\left(\frac{1}{m_T} \frac{dN}{dm_T}\right)$ versus m_T for the K_S^0 particle.	121
5.12	p_T versus rapidity showing three acceptance windows.	124
5.13	Inverse slopes and extrapolated yields for the K_S^0 , calculated separately using three different acceptance windows.	125
6.1	Fraction of the beam which are not protons for run number 7143. . .	128
6.2	The rapidity distribution for the $\bar{\Lambda}$ particle, onto which is fitted a flat and a Gaussian description of the data.	130
6.3	Comparison of Λ weights calculated using the 1999 GEANT program and the weights calculated using the 2001 GEANT program.	136
7.1	Particle yields as a function of the number of wounded nucleons at 40 A GeV/c.	152

7.2	Particle yields per wounded nucleon in Pb–Pb, relative to p–Be, interactions at $40 A$ GeV/ c as a function of the number of wounded nucleons.	153
7.3	Yields of Λ , $\bar{\Lambda}$ and K_S^0 particles as a function of the Fermi variable in p–p and p–Be collisions over differing rapidity intervals.	158
7.4	K^+/π^+ ratio as a function of the centre of mass collision energy for central Pb–Pb and Au–Au collisions and inelastic p–p collisions. . . .	161
7.5	Particle yields per wounded nucleon in Pb–Pb, relative to p–A, interactions at $158 A$ GeV/ c as a function of number of wounded nucleons.	162
7.6	Particle yields per participant in Au–Au, relative to p–p, interactions at $\sqrt{s_{NN}} = 200$ GeV as a function of number of participants.	163
7.7	Predictions by the canonical suppression model of particle yields per participant in central Pb–Pb relative to p–p collisions.	165
7.8	Energy dependence of extrapolated yields in A – A collisions for K_S^0 , Λ , Ξ and Ω as a function of energy.	166
7.9	A schematic diagram showing the ALICE detector.	170
7.10	Effective mass distributions for the K_S^0 , Λ , Ξ^- and Ω^- candidates from central Pb–Pb events from an ALICE Monte-Carlo Simulation. .	171
C.1	The decay of a neutral V^0 into two charged tracks in the laboratory system and the centre of mass system.	180
C.2	The Armenteros-Podolanski plot showing the K_S^0 , $\bar{\Lambda}$ and Λ half ellipses.	182

List of Tables

1.1	Comparison of some of the main characteristics of heavy ion collisions at the SPS, RHIC and LHC facilities.	32
2.1	Summary of data taken by the NA57 experiment	47
3.1	Summary of the centred positions of $xtarg$, y_0 and z_0 , verified by the direct V^0 analysis	58
3.2	Summary of the number of gold-plated Λ and $\bar{\Lambda}$ candidates found. . .	75
3.3	Parameters obtained from the CENTKK program which are used in the fit to describe the $\bar{\Lambda}$ signal.	79
4.1	Summary of the number of Λ and $\bar{\Lambda}$ candidates selected for weighting.	85
4.2	Parameters of the acceptance window used for the weighted Λ and $\bar{\Lambda}$ candidates.	90
4.3	Inverse slopes of the weighted Λ and $\bar{\Lambda}$ candidates within the acceptance window.	93
4.4	Λ and $\bar{\Lambda}$ extrapolated yields.	95

4.5	The six time periods of the Λ data used to determine stability of the inverse slope and yield.	97
4.6	The six time periods of the $\bar{\Lambda}$ data used to determine stability of the inverse slope and yield.	97
4.7	Combinatorial background uncorrected and corrected $\bar{\Lambda}$ inverse slopes.	100
4.8	Combinatorial background uncorrected and corrected $\bar{\Lambda}$ extrapolated yields.	101
5.1	Summary of the number of gold-plated K_S^0 candidates found.	114
5.2	Parameters of the acceptance window used for the weighted K_S^0 candidates.	118
5.3	Fit parameters which define the straight line fitted to the K_S^0 rapidity distribution.	120
5.4	Inverse slope obtained using a maximum likelihood fit for the weighted K_S^0 candidates within the acceptance window.	121
5.5	K_S^0 extrapolated yield	123
5.6	The number of weighted K_S^0 candidates within each of three acceptance windows to determine stability of the inverse slope and yield. .	124
6.1	Proton fraction obtained from each of four special runs taken during 1999 data collection where only the beam trigger was implemented. .	127
6.2	Fit parameters which define the straight line fitted to the Λ rapidity distribution.	129

6.3	Inverse slopes and extrapolated yields assuming different descriptions of the Λ rapidity distribution.	130
6.4	Combinatorial background uncorrected inverse slopes and extrapolated yields assuming different descriptions of the $\bar{\Lambda}$ rapidity distribution.	131
6.5	Inverse slopes and extrapolated yields assuming different descriptions of the K_S^0 rapidity distribution.	131
6.6	Systematic effects on inverse slopes and extrapolated yields assuming different descriptions of rapidity distributions.	132
6.7	Inverse slopes and extrapolated yields for the Λ , $\bar{\Lambda}$ and K_S^0 particle species obtained from the 2001 p-Be data	133
6.8	Inverse slopes and extrapolated yields for the Λ , $\bar{\Lambda}$ and K_S^0 particle species obtained from the 1999 p-Be data	133
6.9	Inverse slopes and extrapolated yields calculated for a sample of Λ candidates using either the 1999 or 2001 GEANT program.	136
6.10	Inverse slopes and extrapolated yields calculated for a sample of Λ candidates using either the 1999 or 2001 MIXRAWMC program.	137
6.11	Tracks found in the telescope and weights calculated for a small sample of Λ candidates using either the 1999 or 2001 ORHION program.	138
6.12	Inverse slopes and extrapolated yields calculated for a sample of Λ candidates using either the 1999 or 2001 ORHION program.	139
6.13	Inverse slopes and extrapolated yields calculated for a sample of Λ candidates using either the 1999 or 2001 ANALYZE program.	141

6.14	Inverse slopes and extrapolated yields calculated for a sample of 1999 Λ data using all of either the 1999 or 2001 analysis programs.	142
6.15	Inverse slopes and extrapolated yields calculated for a sample of 2001 Λ data using all of either the 1999 or 2001 analysis programs.	143
6.16	Inverse slopes and extrapolated yields calculated for a sample of Λ candidates using a variety of beam profiles in GEANT.	145
6.17	Inverse slopes and extrapolated yields calculated for a sample of Λ candidates using a variety of beam positions.	146
6.18	Summary of individual and overall systematic errors obtained for each of the three particle species studied on the inverse slope.	148
6.19	Summary of individual and overall systematic errors obtained for each of the three particle species studied on the extrapolated yield.	148
6.20	Results of inverse slopes and extrapolated yields for the Λ , $\bar{\Lambda}$ and K_S^0 particle species obtained from the 1999 p–Be data	148
7.1	Inverse Slopes for p–Be and the most central 53% of Pb–Pb collisions at 40 A GeV/c.	155
7.2	Inverse slopes for NA57 p–Be and the most central Pb–Pb (NA57 and NA49) and Pb–Au (NA45/CERES) collisions at 40 A GeV/c.	157
7.3	Hyperon extrapolated yields for p–Be interactions at 40 GeV/c and 158 GeV/c.	159
7.4	Inverse Slopes for p–Be and the most central 53% of Pb–Pb collisions at 158 A GeV/c.	167

7.5	Inverse slopes for central Pb–Pb collisions at NA57 at $\sqrt{s_{NN}} = 8.73$ GeV and 17.3 GeV and Au–Au collisions at STAR at $\sqrt{s_{NN}} = 130$ GeV. .	168
C.1	Numerical values in the Armenteros-Podolanski plot	184
F.1	Yields at 40 A GeV/ c in p–Be and in the five Pb–Pb centrality classes.	191
F.2	Yields at 158 A GeV/ c in p–Be, p–Pb and in the five Pb–Pb centrality classes.	192

Chapter 1

The Quark-Gluon Plasma

1.1 Introduction

The bulk of visible matter in the Universe today is found in the nuclei of atoms, confined inside neutrons and protons. It is now well known that neutrons and protons are made up of smaller particles called quarks. A neutron contains two “down” quarks and one “up” quark, while a proton contains two up quarks and one down quark. The quarks inside the proton and neutron are held together by the strong nuclear force, which is transmitted by uncharged particles called gluons.

In all, there are six types (flavours) of quarks, the other four are heavier than the up and down and are known as strange, charm, bottom and top quarks. In addition, corresponding to each quark is an antiquark which has the same mass, but opposite charge. All particles that contain quarks are known as hadrons.

Hadronic matter can be further sub-divided into baryons and mesons. Baryons contain groups of three bound quarks (such as the proton and neutron) or antiquarks (such as the antiproton and antineutron), mesons contain bound quark-antiquark pairs. In both cases the quarks (and antiquarks) are confined by gluons. Under

normal conditions it is not possible to observe ‘free’ quarks, antiquarks and gluons. However, under extreme conditions of temperature or pressure, for example those similar to what is believed to have existed up until 10^{-5} seconds after the Universe began, hadronic matter undergoes a phase transition into a hot dense ‘soup’ of matter known as a Quark-Gluon Plasma (QGP) in which quarks, antiquarks and gluons become deconfined. More formally, a QGP is usually defined as a state of deconfined strongly interacting matter.

Heavy ion experiments attempt to look back in time by recreating these extreme conditions in the form of a very hot, dense fireball. One such experiment is NA57 [1] at the CERN Super Proton Synchrotron (SPS) which fires a beam of ultra-relativistic lead ions at a lead target. The QGP cannot be observed directly and so a signature marking its existence must be sought; in the case of NA57 this is *strangeness enhancement*. To know if strangeness enhancement has occurred the results from the lead-lead interactions have to be compared to a case where the QGP is not expected to form. For the case of NA57 this is done using a proton beam fired at a Beryllium target. It is this reference data set which is the subject of this thesis.

1.2 Quantum Chromodynamics (QCD)

Quantum Chromodynamics (QCD) [2, 3] is the theory that describes strongly interacting matter. Its main features can readily be compared to the well understood theory of electricity and magnetism, known as Quantum Electrodynamics (QED) [2].

In QED the electromagnetic interaction between two charged particles is mediated by photon exchange. In the case of the strong interaction between quarks the mediating boson is called a gluon which is the massless carrier of the strong force analogous to the photon in QED.

In QED, there are two types of charge: positive and negative, In QCD there are six types of strong charge, called “colour”. A quark can carry one of three colours: red, blue and green, with antiquarks carrying one of the three corresponding anticolours. Whilst the exchange photon in QED has a neutral electric charge, the exchange gluon in QCD carries colour, this allows more than one type of gluon to exist. In all there are eight gluons, all carrying a different colour charge, made up of colour-anticolour combinations.

All hadrons have two important properties [4]: firstly they are colour singlets [5], obtained by an equal amount of each colour or by a colour and the same anticolour quark pairing. Secondly they have a mass which is much heavier than the quarks inside it. For example the proton has a mass of 938 MeV; its constituent uud quarks have a total bare mass of 20 MeV [6]. QCD describes how the light quarks and massless gluons bind to form these heavy but colour singlet packages.

1.2.1 The Strong Potential

The strong interaction takes place between constituent quarks which make up the hadrons. The potential between any two quarks [2, 7] can be approximated as:

$$V_s \approx -\frac{\alpha_s}{r} + kr \quad (1.1)$$

where α_s is the magnitude of the coupling between two quarks, known as the strong coupling constant (it will be seen in section 1.2.2 that despite its name, α_s is not ‘constant’). k is the string tension and r is the separation of the quarks.

The first term in (1.1) dominates at small r (or high q^2 ; where q^2 is the 4-momentum transfer squared of the exchange gluon related to r by the uncertainty principle $qr \simeq \hbar$) and arises from single gluon exchange (here $\alpha_s < 1$); it is equivalent to the Coulomb potential V_{em} between two elementary charges [2]:

$$V_{em} = -\frac{\alpha_{em}}{r} \quad (1.2)$$

where α_{em} is the electromagnetic coupling constant.

As r increases (or q^2 decreases) multiple gluon exchange occurs and $\alpha_s \sim 1$ [2]. In this regime the second term in (1.1) dominates and is responsible for confinement at large r . As two quarks are separated QCD dictates colour lines of force between the quarks pull together to form a ‘string’ (or ‘fluxtube’) [7], the stored energy of which is kr . At some point, as r increases, it becomes energetically more favourable to create a quark-antiquark pair (meson) with two short strings, rather than one long one.

1.2.2 Asymptotic Freedom

In quantum field theory, an electron can suddenly emit a virtual photon, or it can emit a virtual photon that subsequently decays into a virtual electron-positron pair (e^+e^-), and so on [3], as shown in figure 1.1a(i). The result of which will mean that the original electron will be surrounded by virtual e^+e^- pairs and, because opposite charges attract, the virtual positrons will be preferentially closer to the electron, thus the negative charge of the electron is effectively screened by the positive charge of the virtual positrons, as shown in figure 1.1a(ii). If the charge on the electron was then measured by moving a test charge towards it and measuring the Coulomb force which the test charge experienced, it would be seen that as the test charge penetrated the cloud of virtual positrons, which screens the electron’s charge, the charge measured would become larger. In quantum field theory the vacuum surrounding the electron has become a polarised media. This effect is known as Debye screening [3]; as a result the “measured charge” depends on the distance at which one is probing the electron, as shown in figure 1.1a(iii).

This idea can be carried forward for the colour charge of a quark and would be the same were it not for the fact that gluons carry colour and thus can interact with one another, as shown in figure 1.1b(i). It turns out that this fact reverses the QED

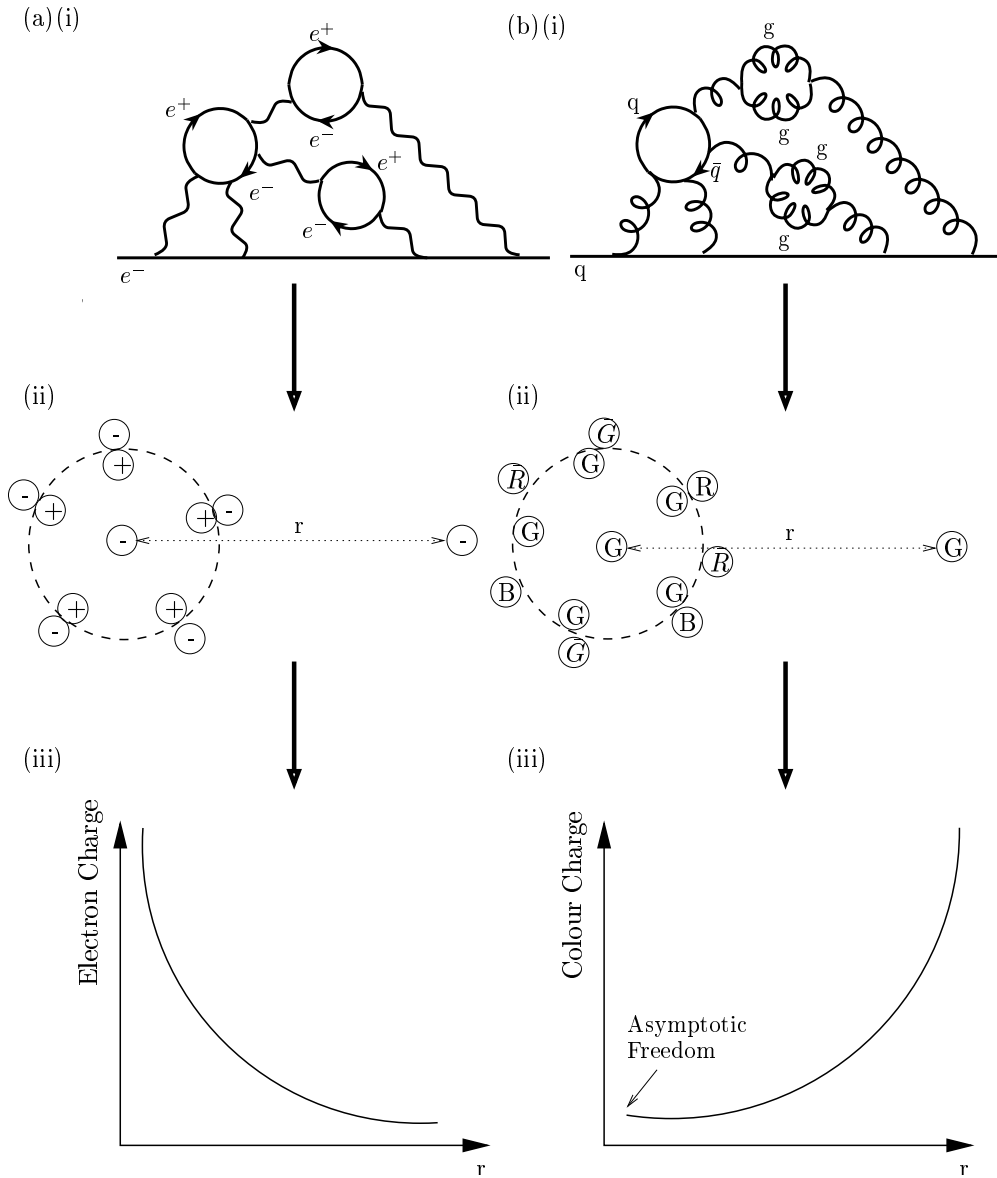


Figure 1.1: (a) Debye Screening of the electric charge: an e^- can emit virtual photons and e^+e^- pairs causing the original e^- to become ‘screened’ by virtual e^+ s, thus moving a test charge towards the e^- will measure a greater electron charge as the distance, r , gets smaller. (b) Antiscreening of colour charge: a q can emit both virtual $q\bar{q}$ and gg pairs causing the original q to become ‘antiscreened’ by particles of the same colour, thus moving a test charge towards the q will measure a lesser colour charge as r gets smaller, allowing asymptotic freedom to occur (based on an original by [3]).

result explained above [3]; a green charge (for example) is preferentially surrounded by virtual green charges, as shown in figure 1.1b(ii). If the test probe experiment is repeated for colour charges it is seen that as the test probe moves closer to the original green quark, the probe penetrates a sphere of predominantly green charge and the amount of green charge measured decreases. The resultant “antiscreening” of the green colour is referred to as “asymptotic freedom” [8, 9]. Asymptotically, as quark energy increases, two green quarks interact through colour fields of reduced strength and approach a state where they behave as essentially free, noninteracting particles, as shown in figure 1.1b(iii). So as the distance between two quarks tends to zero, the strong coupling constant also tends to zero.

It turns out that α_s can be related to r via (1.3) [2, 3, 10]. However the equation is expressed in terms of Q^2 , where $Q^2 = -q^2$, and q^2 is inversely proportional to r (as seen in section 1.2.1):

$$\alpha_s(Q^2) \approx \frac{\alpha_s(Q_0^2)}{1 + \frac{\alpha_s(Q_0^2)}{12\pi}(33 - 2N_f)\ln(\frac{Q^2}{Q_0^2})} \quad (1.3)$$

α_s is expressed in terms of Q_0^2 which is a reference 4-momentum transfer squared, to ensure that (1.3) contains only finite, physically measurable quantities. N_f is the number of quark flavours, (required to be less than sixteen) and the coefficient of $\ln(\frac{Q^2}{Q_0^2})$ comes about as a result of gluons carrying colour (if gluons did not carry colour, or the number of flavours exceeded sixteen, the sign of the coefficient would change and asymptotic freedom could not occur).

From (1.3) it can be seen that for small Q^2 (such that $Q^2 \ll Q_0^2$), $\alpha_s(Q^2)$ is large; as Q^2 gets larger, (smaller r) $\alpha_s(Q^2)$ gets smaller. So for $Q^2 \gg Q_0^2$, $\alpha_s(Q^2)$ becomes very small and *asymptotic freedom* occurs.

1.2.3 The QCD Vacuum

Asymptotic freedom is a consequence of the QCD vacuum [4, 11, 12]. This vacuum, contrary to what the name suggests, is not empty: instead it is filled with virtual quarks, antiquarks and gluons all arranged such as to have the lowest possible energy. In particular the vacuum can be thought of as three condensates (strongly ordered matter at zero temperature): The first of *Higgs Particles* [13] required in order to give the quarks mass. The second is a *gluon condensate* [14] which describes the density of virtual gluon (gg) pairs in the vacuum. The third condensate, the *quark condensate* [11, 14], describes the density of virtual quark-antiquark ($q\bar{q}$) pairs in the QCD vacuum. These latter two condensates are responsible for the hadrons being colour singlets and having a larger mass than that of the constituent quarks. It is these condensates which are of interest to this discussion and are described further here.

The gluon condensate is filled with virtual gg pairs in such a way that overall the condensate is colour neutral. In the quark condensate virtual $q\bar{q}$ pairs must either be $u\bar{u}$, $d\bar{d}$, $u\bar{d}$ or $d\bar{u}$ (as heavier quarks are unstable); thus a vector in 4-d space with axes labelled $u\bar{u}$, $d\bar{d}$, $u\bar{d}$, $d\bar{u}$ can be constructed [11]. In order to achieve the lowest energy, QCD predicts all these vectors must be aligned in the same direction. The fact that these vectors all align in only one direction and are not all orientated in random directions (as one might expect) is known as *chiral symmetry breaking* [11, 15].

Massive Hadrons

As mentioned already in this section hadrons have a greater mass than that of their constituent quarks. For example the proton has a mass nearly 46 times that of $2u$ and $1d$ quarks [6]. If quarks are added to the QCD vacuum they will interact with the $q\bar{q}$ condensate and, as a result, they will behave as if they have a larger mass. Similarly a hadron in the presence of the QCD vacuum will disturb the $q\bar{q}$

condensate. The energy of this disturbance provides the ‘missing mass’ and hence explains why hadrons are much heavier than their constituent quarks [11].

Colourless Hadrons

An important feature of the QCD vacuum is that it is colour neutral and abhors colour [4]. If a single green quark (for example) is added to the vacuum, the vacuum is disturbed (as it is no longer colour neutral) and consequently responds by virtual particles from the quark and gluon condensates surrounding the green quark [11], this requires a large amount of energy. Now, if a colourless combination of quarks and antiquarks are added (i.e. a hadron) the vacuum is disturbed much less (as the vacuum remains colour neutral overall), therefore a lot less energy is required, which strongly favours colourless hadrons.

1.2.4 Achieving Asymptotic Freedom

Asymptotic freedom implies quarks must be very close together for them to behave as ‘free’ particles. There are two ways [11] of achieving this: firstly squeezing nuclei together pushes quarks in protons and neutrons very close together where $\alpha_s \rightarrow 0$. Secondly by increasing the temperature: as the temperature is increased from zero the virtual $q\bar{q}$ pairs in the quark condensate gain kinetic energy and begin to oscillate from their direction of alignment. Eventually above a critical temperature, T_c , the $q\bar{q}$ pairs oscillate so wildly they become orientated in all directions, showing no favoured direction and the vacuum disappears and *chiral symmetry restoration* occurs [11]. As chiral symmetry restoration occurs the hadrons cannot continue to exist as their constituent quarks no longer have the QCD vacuum to interact with. Furthermore, the masses of the constituent quarks reduces to their bare masses. As this happens a phase transition takes place to a plasma of quarks, antiquarks and gluons (originating from the former hadrons and previously virtual particles

of the $q\bar{q}$ and gg condensates), known as a *Quark-Gluon Plasma* in which quarks, antiquarks and gluons can move around as ‘free’ particles.

1.3 The Phase Diagram

The phase transition from hadronic matter to a QGP described in the previous section can be seen clearly on a phase diagram of temperature, T , versus baryon chemical potential, μ , which is a convenient measure of net quark density (i.e. the number of quarks minus the number of antiquarks per unit volume), as seen in figure 1.2 [7, 11]. The vacuum described in section 1.2.3 can be seen in the bottom left, having zero temperature and no net quark density.

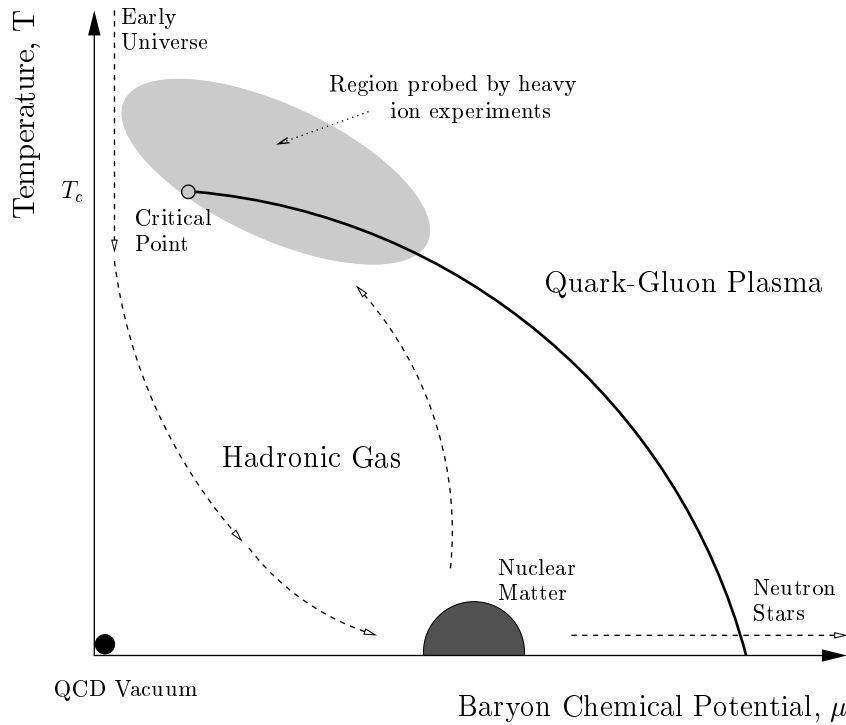


Figure 1.2: Phase diagram of matter in the temperature–baryon chemical potential plane, showing the two distinct phases of hadronic matter and QGP. Three examples of where matter exists (or has existed) in the QGP phase are also shown.

In the low T and low μ region of the phase diagram hadronic matter exists. At higher T and at higher μ one enters the QGP region. The phase transition between hadronic matter and the QGP can be seen clearly on the diagram: at high T and very low μ a ‘critical point’ can be seen on the diagram, in this region it is not certain that there is a distinct phase boundary, instead a gradual change from one phase to the other is expected [11].

To get from the hadronic matter to QGP region, nuclei must be squeezed together or heated up. Squeezing nuclei (without heating) pushes matter to the right of the diagram (as the number of quarks minus the number of antiquarks has stayed the same, but the volume in which they exist has decreased) and into the QGP phase. Heating matter moves it upwards on the diagram as heating matter (described in section 1.2.4) melts the QCD vacuum, this leaves nothing for the hadrons to interact with and thus allows the hadron’s constituent quarks and gluons to move freely around in the resulting QGP phase.

There are three further points of interest on the phase diagram. These are circumstances in which matter exists or has existed in the QGP phase. The first of these is the early Universe: it is believed that until $40\mu s$ after the Universe began quarks, antiquarks and gluons were all deconfined in a QGP [7]. After this time the Universe expanded and cooled and hadronisation took place. The second point of interest is in a neutron star. Neutron stars are $\sim 10^{14}$ times more dense than the sun and they are thought to be the only example in which a QGP could occur in nature by squeezing matter together (although there is no experimental evidence to support this claim at present) [16]. The third point of interest on the phase diagram is the short-lived QGP which can be made in the laboratory by heavy ion collisions, the region on figure 1.2 in which these experiments probe is shown in the grey shaded region. It is this feature on the phase diagram which is of interest and is the subject of the following section.

1.4 Heavy Ion Physics

The aim of ultra-relativistic heavy ion physics is to create a QGP in the laboratory [7, 17]. In the QGP which was believed to exist up until $40 \mu\text{s}$ after the Universe began, the temperature exceeded 10^{12} K: about 150,000 times hotter than the core of the Sun. So in order to recreate a QGP, similar conditions need to be produced in the laboratory. Collisions between elementary particles cannot accomplish this because they cannot pack enough energy into a large enough volume. This means they cannot form a macroscopic fireball in which quarks can roam freely. To overcome this problem it is necessary to collide large atomic nuclei together, thus allowing the nucleons inside to plough into one another, producing many quark-antiquark pairs, raising the energy density locked inside the fireball. Initially, when the colliding nuclei meet, high energy inelastic collisions between individual nucleons occur which liberates many partons. Because of the high density of nuclear material, the released partons undergo further collisions and reorganise themselves in thermal and chemical equilibrium, as happened in the early Universe, by this time the temperature should have exceeded 10^{12} K (~ 200 MeV). The matter then starts to expand and cool and the QGP remains until the temperature drops below the critical temperature ($\sim 1.4 \times 10^{12}$ K) at this time quarks, antiquarks and gluons become confined into hadrons. At around this time the chemical composition of particles becomes fixed, this is known as *chemical freezeout* [18]. The hadronic gas continues to cool, and during this time the hadrons continue to rescatter. Rescattering continues until the expanding matter becomes dilute, and interaction rates become insufficient to maintain thermal equilibrium, so that the fireball falls apart into individual hadrons. This is known as *thermal freezeout* [7, 18]. The hadrons continue unimpeded by further material until they reach the detectors that surround the collision zone.

Figure 1.3 shows a visualisation of the heavy ion collision between two lead nuclei in a “micro bang” leading to a QGP [4]. The incoming nuclei are travelling at 99.95% the speed of light are Lorentz contracted and look more like disks than

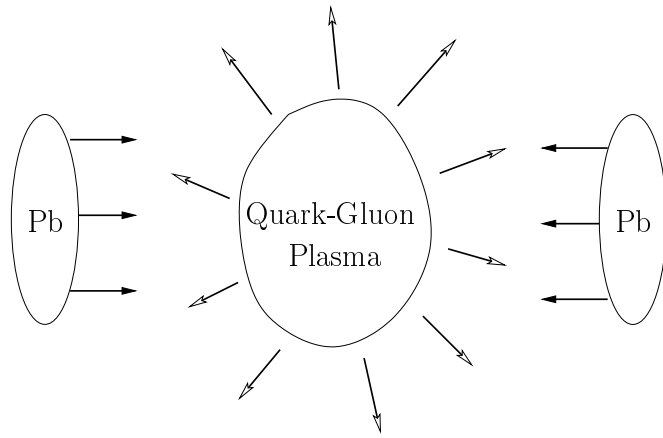


Figure 1.3: Pictorial representation of the creation of a Quark-Gluon Plasma by a Pb-Pb collision in the laboratory, the Pb ions are Lorentz contracted as they are travelling close to the speed of light.

spheres. The new state survives in the laboratory for approximately ten times the time taken for light to travel the diameter of a proton, before exploding: much less than after the Universe began. The principle reason for this difference in time scale is due to the role of gravitation in the early Universe [4]: in the QGP created in the laboratory there is no gravitation to slow the expansion of the fireball and hence the time in the QGP phase is much reduced. Another difference between the QGP which existed just after the Universe began and the QGP created in the laboratory is in the net quark density (i.e. the number of quarks minus that of antiquarks per unit volume). Although an equal density of quarks and antiquarks are produced in both cases there is a net excess of quarks (over antiquarks) in the laboratory QGP due to the initial valence quarks present in the colliding nuclei. As higher energy heavy ion beams become available these two differences between the QGP which existed just after the Universe began and the QGP created in the laboratory reduce. Higher energy beams implies a higher energy density and thus the fireball remains in the QGP phase longer. Further, the higher energy beams allows the initial nuclei to collide and pass through one another, allowing the initial quarks inside the nuclei to be clear of the collision zone by the time hadronisation occurs, thus allowing the

net quark density to tend to zero.

1.5 Heavy Ion Terminology

There are a number of terms which are useful to the discussion of heavy ion physics and will be used throughout this thesis, an outline of the more important ones are given here.

1.5.1 Collision Centrality

The centrality of a collision describes the ‘overlap’ of two incoming ions at the point at which they collide. A *central* collision is one in which there is a large overlap region, as shown in figure 1.4a, in such collisions the number of participant nucleons, N_{part} , (also referred to as number of wounded nucleons, N_{wound}) is large. The energy density, ε , reached in the collision increases with the number of participant nucleons, and so the greater N_{part} the greater the energy density of the system. Collisions with a small overlap region are known as *peripheral* collisions, as shown in figure 1.4b, where N_{part} is small and consequently the energy density reached is a lot lower. Central collisions are described as having high *multiplicity* (i.e. the number of charged particles produced in a collision), whereas peripheral collisions have a lower multiplicity. Instead of studying separately collisions at every value of N_{part} , often, the data is divided into a number of *multiplicity classes* each of which covering a range of N_{part} .

1.5.2 Transverse and Longitudinal Momentum

In heavy ion physics a coordinate system needs to be established. In NA57 the coordinate system used is as follows: x defines the beam direction, z is perpendicular

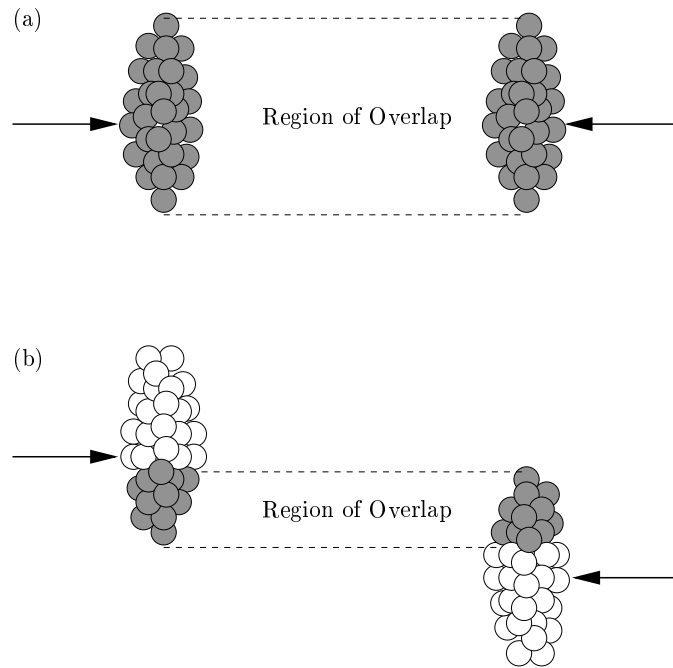


Figure 1.4: Pictorial representation of (a) a central and (b) a peripheral collision. Central collisions have a large number of participant nucleons (shaded) and high multiplicity whereas peripheral collisions have a small number of participant nucleons and low multiplicity.

to x and is in the direction of the magnetic field and y completes the right-handed orthogonal system. A momentum vector, \vec{p} , can be broken up into its components along each coordinate axis: p_x, p_y, p_z . These components can be used to define two further quantities: *transverse momentum*, p_T and *longitudinal momentum*, p_L

$$p_T = \sqrt{p_y^2 + p_z^2} \quad (1.4)$$

$$p_L = p_x \quad (1.5)$$

p_T is particularly useful as it is *invariant* under longitudinal boosts: i.e. the magnitude and shape of the distribution is the same in whatever reference system the measurement is made.

A further quantity, useful in heavy ion physics is *transverse mass*, m_T , this quantity is defined:-

$$m_T = \sqrt{p_T^2 + m^2} \quad (1.6)$$

where m is the particle mass, it follows that m_T is also invariant under longitudinal boosts.

1.5.3 Rapidity

Rapidity, y , is a dimensionless quantity defined:-

$$y = \frac{1}{2} \ln \left(\frac{E + p_L}{E - p_L} \right) \quad (1.7)$$

where E is the total energy and p_L is the longitudinal momentum. Rapidity is a useful quantity as its shape is unaffected by a longitudinal Lorentz boost: i.e. the shape of the rapidity distribution is the same in whatever frame of reference, just shifted. For example, to go from the centre of mass, cm , frame where the y distribution is centred on zero, to the frame measured in the laboratory, lab (used in fixed target experiments) is simply achieved by a shift in rapidity, described by (1.8).

$$y_{lab} = y_{cm} + y_0 \quad (1.8)$$

where y_0 is a constant.

The rapidity of a particle is a measure of where in the collision it has come from. A rapidity of zero (in the *cm* system) implies the particle has come from the centre of the collision. A positive or negative value of y implies the particle has come from the forward or backward region of the collision.

1.6 Strangeness Enhancement

It is not possible to observe a QGP directly, so in order to assess whether or not it has occurred a signature must be sought. One such signature is that of *strangeness enhancement* [15, 19, 20, 21, 22].

The family of strange particles are those which contain one or more strange quark or antiquark. These include the baryons Λ (qq_s), Ξ (qss), Ω (sss) (and their corresponding antiparticles); mesons ϕ ($s\bar{s}$), K^+ ($q\bar{s}$), K^- ($\bar{q}s$) and resonances K^* , Σ^* , Λ^* where s represents a strange quark, q the lighter up and down quarks. If a QGP has been formed the number of these strange hadrons found after hadronisation is expected to increase.

There are two reasons why the number of strange hadrons should increase if a QGP has occurred [15]. Firstly in the presence of a QGP, *chiral symmetry restoration* will occur (section 1.2.4) and the masses of the quarks will drop to their ‘bare’ masses, in the case of the strange quark this is 150 MeV. Now the temperature of the plasma is ~ 200 MeV and with the many gluons, quarks and antiquarks in a deconfined state it becomes energetically possible for many $s\bar{s}$ pairs to be produced via thermal gluon fusion ($gg \rightarrow s\bar{s}$) and the lighter quark-antiquark annihilation ($q\bar{q} \rightarrow s\bar{s}$): Feynman diagrams for these processes are shown in figure 1.5. It turns out that gluon fusion is the dominant process [22] accounting for $\sim 85\%$ of $s\bar{s}$ production as it is expected to reach equilibrium in a time similar to that of the expected plasma

lifetime.

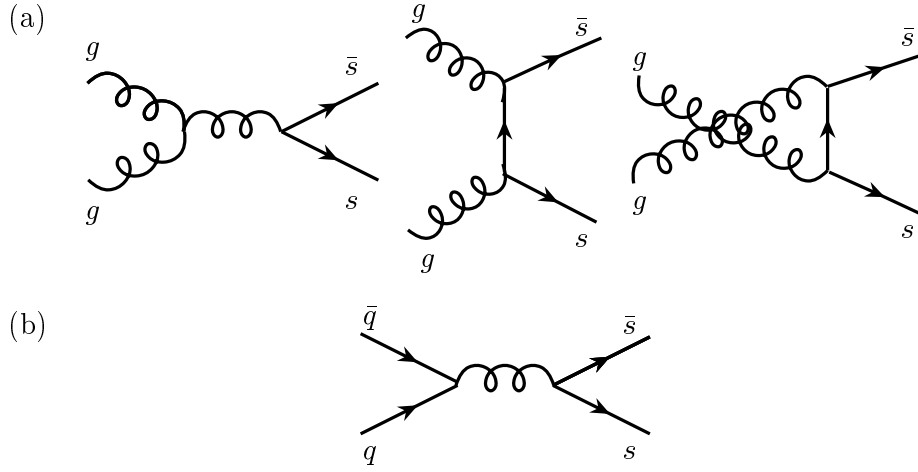


Figure 1.5: Methods of producing strange quark-antiquark pairs, (a) via thermal gluon fusion and (b) via lighter quark-antiquark annihilation.

Secondly, in the plasma there is a suppression of lighter (u and d) quark and antiquark production due to a large number of these quarks already present in the plasma as a result of the initial colliding nuclei: this is known as *Pauli Blocking* [23]. Pauli Blocking means that the ratio of $\frac{s\bar{s}}{q\bar{q}}$ production is going to increase in the presence of a plasma. It should be noted that this second reason is only true for collisions in which the colliding nuclei remain in the collision zone when hadronisation occurs.

In the ensuing hadronisation process the strange quarks and antiquarks produced in the QGP go on to form strange hadrons, a schematic diagram of which is shown in figure 1.6. It follows that the production of strange hadrons produced by a recombination of quarks from a QGP, compared to production if a QGP had not occurred, should increase with strange quark content. If ε_f is the factor by which singly strange particle production is increased if a QGP has occurred (as a result of the two reasons described above) and n is the number of strange quarks in the hadron, then the production of a given species is predicted to be enhanced by a factor of $\sim (\varepsilon_f)^n$ where at SPS energies, $\varepsilon_f \sim 2.5$ [15].

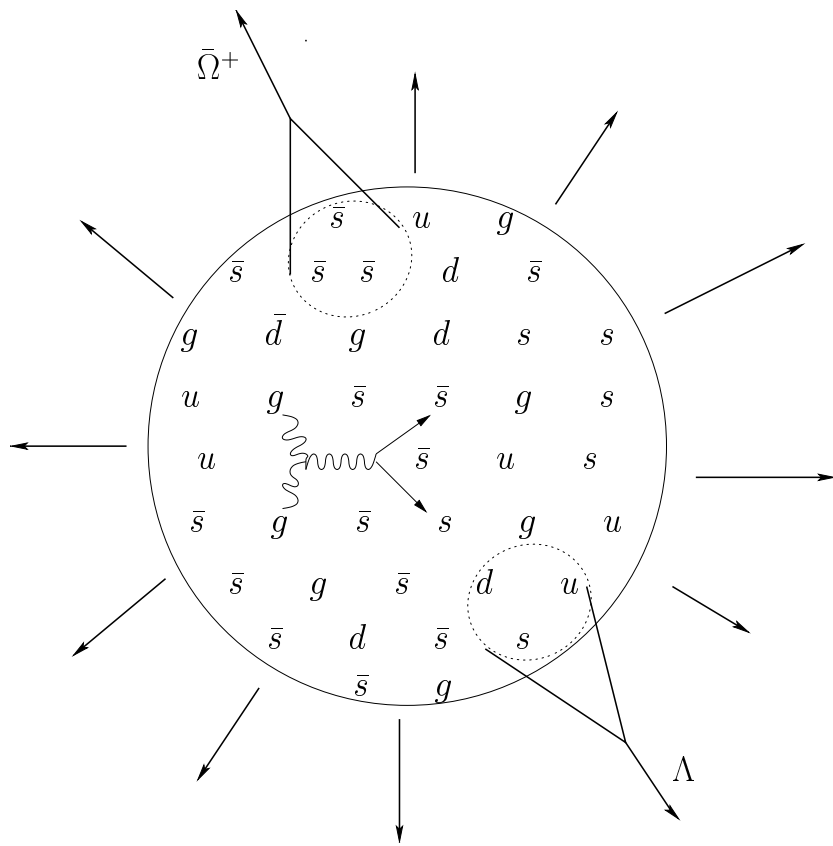


Figure 1.6: Production of strange particles and antiparticles as a signature of a QGP; gluon fusion, the predominant source of strange quark-antiquark pairs is also shown (based on an original in [4]).

Although strangeness enhancement is indicative of a QGP, strange particles and antiparticles can also be produced in a hadron gas, such as the reaction:

$$\pi^0 + p \rightarrow K^+ + \Lambda \quad (1.9)$$

However, such reactions have higher production thresholds, for example ~ 530 MeV in (1.9) (the production threshold to produce a $\bar{\Lambda}$ is even greater, as an equivalent reaction to (1.9): $\pi^0 + \bar{p} \rightarrow K^- + \bar{\Lambda}$, would first need to create a \bar{p}). To produce the multi-strange hadrons in a hadron gas requires a number of reactions; for example to produce the triply strange Ω^- particle the reactions (1.10) and (1.11) need to occur in addition to (1.9).

$$\pi^0 + \Lambda \rightarrow K^+ + \Xi^- \quad (1.10)$$

$$\pi^+ + \Xi^- \rightarrow K^+ + \Omega^- \quad (1.11)$$

In addition to the high production thresholds these numerous reactions require, in order to produce a multi-strange hadron, they are also expected to take a long time to reach equilibrium due to their small cross-sections. Furthermore, although singly strange particles produced in a hadron gas are likely to survive when they interact with surrounding nucleons and pions; multi-strange particles are not as they are more likely to interact and form singly strange particles once more.

Because of all of the reasons outlined above (namely: high production thresholds, production times and interactions with surrounding nuclei and pions) the enhancement hierarchy of singly and multi-strange particles predicted for the case of the QGP would not occur in the hadron gas scenario.

Two experiments which have studied strangeness enhancement as part of the lead programme at the CERN SPS (described further in section 1.8) are the NA49 [24] and WA97 [25] experiments (WA97 was the predecessor experiment to NA57). NA49 looks at the strange particles K^\pm , K_S^0 , ϕ , Λ , $\bar{\Lambda}$ and Ξ^\pm over a large acceptance at a number of energies between $40 A$ GeV/c and $158 A$ GeV/c. WA97 looks at K_S^0 , Λ , $\bar{\Lambda}$, Ξ^\pm and Ω^\pm signals at $158 A$ GeV/c over a smaller acceptance but with a high rate

data capability. Both experiments compare the production of strange particles in Pb–Pb collisions to p–Pb (and p–Be in the case of WA97 [26]) collisions at the same energy. Enhancements of the strange particles in the Pb–Pb system as a function of number of participants, measured by WA97 [27, 28, 29], relative to the p–Be system (p–Pb system in the case of the K_S^0 meson) are shown in figure 1.7. A clear enhancement of all strange particles can be seen, with the predicted hierarchy of multi-strange over singly strange particle production observed.

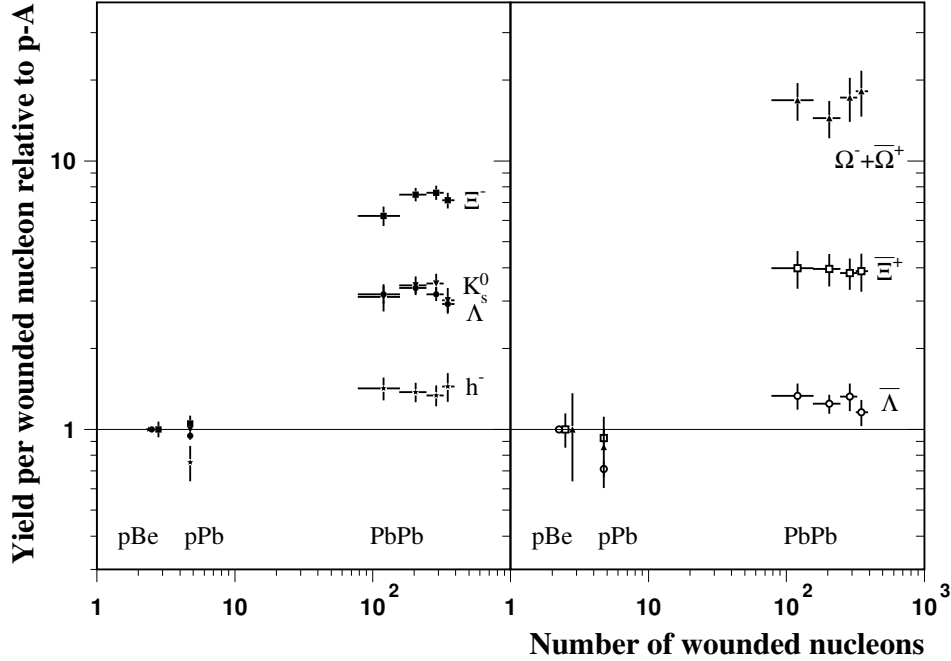


Figure 1.7: Yield per participant of strange and multistrange particles in Pb–Pb collisions at 158 A GeV/c, normalised to p–Be (p–Pb in the case of K_S^0) collisions (horizontal line) as a function of number of participant nucleons for particles (left) and antiparticles (right). The Ω data has been combined due to low statistics and the Pb–Pb data has been divided into four multiplicity classes. A clear enhancement of all strange particles can be seen, with the predicted hierarchy of multi-strange over singly strange particle production observed. (WA97 Collaboration).

The NA57 experiment looks to extend the work of WA97 (discussed further in chapter 2) and data from which is the subject of this thesis.

1.7 Other Signatures of a QGP

Besides the signature of strangeness enhancement, which probably provides the best single evidence for the formation of a QGP, there are a number of other signatures which also denote the onset of a QGP. A brief overview of the other main signals are given here.

1.7.1 J/ψ Suppression

The J/ψ particle is the second lightest member (3097 MeV), the lightest member being the η_c , of a family of mesons which are made up of a charm quark-antiquark ($c\bar{c}$) pair. Excited (heavier) members of the $c\bar{c}$ family include the ψ' and χ_c [2, 6]. The charm quark is very heavy, (about ten times greater than the strange quark) and so the J/ψ particle can only be produced in the very early stages of the collision when high energy collisions occur between partons in the colliding nuclei. Theory predicts that the J/ψ yield should be suppressed if a QGP is formed in the collisions [14, 30].

In a QGP the potential of (1.1) is replaced by [7, 30]:

$$V_{QGP} \approx -\frac{\alpha_s}{r} e^{-r/\lambda_D} \quad (1.12)$$

where the second term of (1.1) disappears as confinement no longer exists. The terms in the exponential are due to colour screening, where r is the radius of the particle (in this case the J/ψ) and λ_D is the Debye screening length ($\propto \frac{1}{T}$). Now if $\lambda_D \gg r$ the $c\bar{c}$ pair can ‘see’ one another and can form a bound J/ψ particle. However, if $\lambda_D \ll r$ colour screening prevents the $c\bar{c}$ pair ‘seeing’ one another and thus the charm quark and antiquark become disassociated with each other and will form open charm particles such as the D ($c\bar{u}$, $c\bar{d}$) and \bar{D} ($\bar{c}u$, $\bar{c}d$). As a result the yield of J/ψ should be suppressed if a QGP has been formed. Suppression also occurs in the excited states ψ' and χ_c . The same theory can be applied to the heavier Υ particle (bottom quark-antiquark pair), however the radius of the Υ system is

smaller than the J/ψ and so a smaller λ_D is required in order for a suppression due to the plasma to occur [14].

The NA50 experiment [31] at CERN studies J/ψ suppression by looking at the decay channel $J/\psi \rightarrow \mu^+\mu^-$ in p- A and Pb-Pb collisions. This is a good channel to study as the resultant pair of muons will not be affected by the strong interactions present during hadronisation and although unstable, will survive long enough to reach the detectors giving an undistorted image of earlier phases. Recent results [7, 32] are shown in figure 1.8 where the relative yield is plotted against the number of participant nucleons. As the number of participant nucleons increases the ratio of measured to expected yield decreases. The yield of J/ψ particles produced in Pb-Pb collisions is normalised to the yield produced in p- A collisions (where a QGP is not expected to occur) because J/ψ suppression will occur in other ways not attributable to the plasma, for example nuclear absorption ($J/\psi + n \rightarrow D^0 + \bar{D}^0 + X$). The horizontal line in figure 1.8 is normalised to account for known suppression, coming from nuclear absorption. Data below this line marks suppression attributable to the formation of a QGP. The distinct suppression observed in Pb-Pb collisions is strong evidence to support the formation of a QGP.

1.7.2 Dilepton Pairs

The study of pairs of electrons (e^+e^-) and the heavier muons ($\mu^+\mu^-$) provides a useful tool to study the QGP [33]. One advantage of this probe is that leptons only interact weakly and are therefore unaffected by the strong interaction. Thus pairs of leptons produced in the earliest stages of the heavy ion collision are likely to survive until reaching the experiment detector.

Hadrons with invariant masses less than ~ 1 GeV which decay into an e^+e^- pair are of interest. In this region the light vector mesons ($J^P = 1^-$): $\rho(776 \text{ MeV})$, $\omega(783 \text{ MeV})$ and $\phi(1019 \text{ MeV})$ dominate [34]. Of particular interest is the ρ which

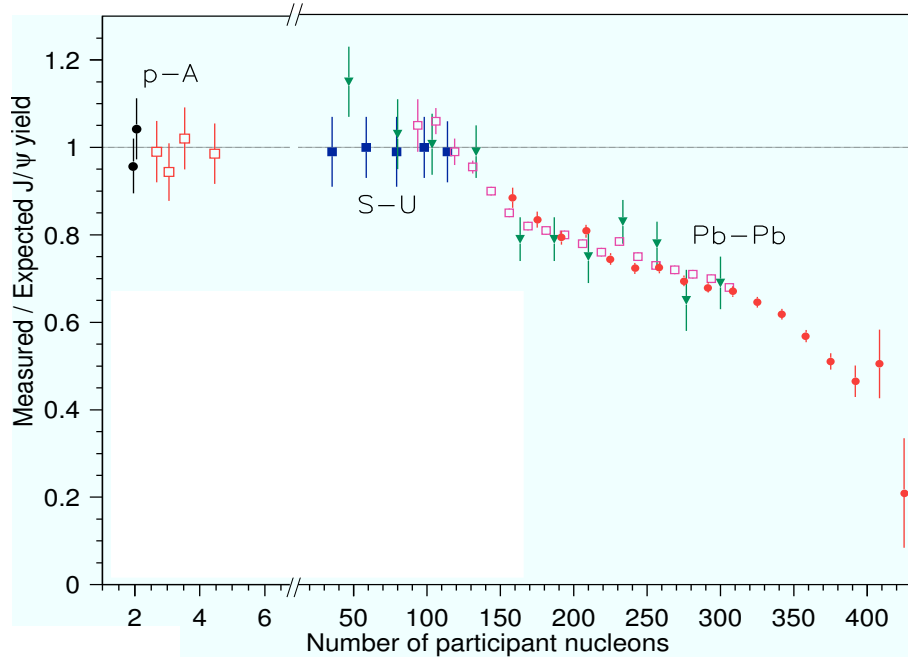


Figure 1.8: Yield of J/ψ particles in S-U and Pb-Pb collisions at 158 A GeV/c, normalised to p-A collisions (horizontal line) as a function of number of participants. A clear suppression of J/ψ production can be seen in Pb-Pb collisions. (NA50 Collaboration).

has a shorter lifetime than the lifetime of the QGP and consequently should decay whilst the QGP still exists. In the regime of the QGP, chiral symmetry restoration occurs (section 1.2.4) and the quark masses drop to their bare masses. As such, if a ρ is formed inside the QGP it is expected to have a lighter mass than if it is formed outside of a QGP [35]. Because of its short lifetime, most ρ mesons produced in the QGP will also decay inside the QGP and will therefore retain its reduced mass. By studying the dilepton pairs of the ρ (and other vector mesons) that result (for example the decay: $\rho \rightarrow e^+e^-$), the masses of the parent particles can be calculated. ρ s (and other vector mesons) of lighter mass should be reconstructed if a QGP has been formed compared with if a QGP has not been formed (i.e. the ρ s originated from normal hadronic sources).

The NA45/CERES experiment [36] at the CERN SPS measures the yield of low mass e^+e^- pairs in a Pb–Au system and compares it to the yield of low mass e^+e^- pairs in the reference p–Be and p–Au systems. In the reference systems the measured e^+e^- yields follow the expected sum of the many hadronic decays. In the Pb–Au system there is an enhancement of $2.6 \pm 0.5(\text{stat.}) \pm 0.6(\text{syst.})$ [37] in the e^+e^- pair yield within the mass range $0.25 < M_{e^+e^-} < 0.7$ GeV, as shown in figure 1.9. The NA45/CERES data shown in figure 1.9 (including the observed enhancement) is in good agreement with predictions made by theoretical transport models which include in-medium modifications, such as the dropping vector meson mass scenario [38, 39]. Thus, the decrease of vector meson masses due to the presence of a QGP provides a quantitative explanation of the observed enhancement in the e^+e^- pair yield observed by the NA45/CERES collaboration.

1.7.3 Direct Photons

Photons are produced mainly in charged particle scattering. The production of direct photons was predicted as a good signature for the study of a QGP [40, 41, 42] as (like dileptons, section 1.7.2) photons can only interact electromagnetically and

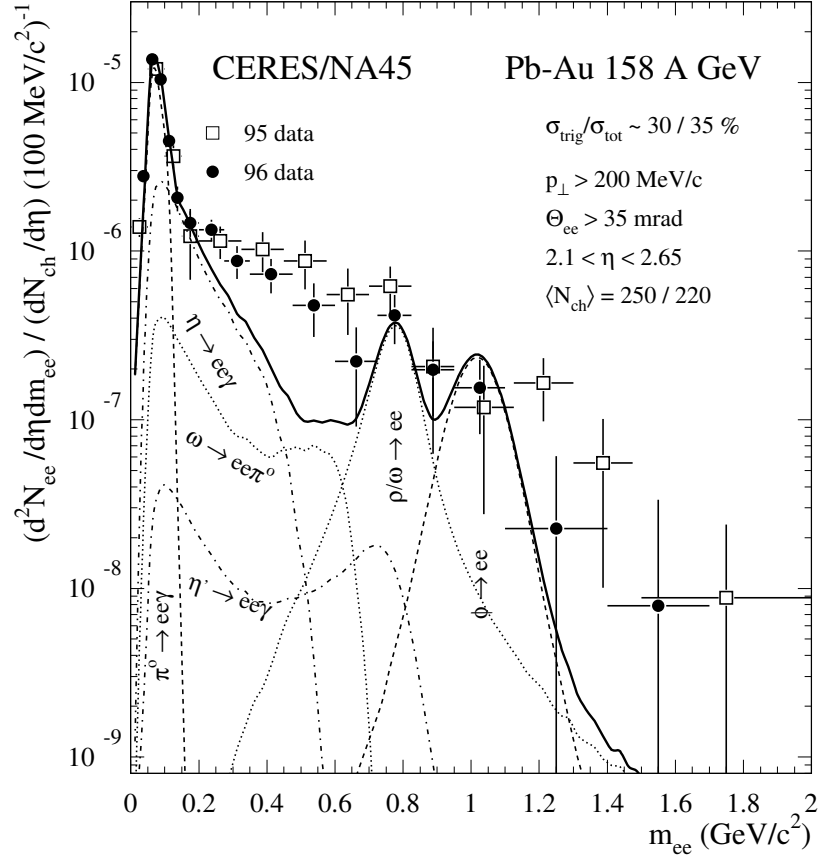


Figure 1.9: Mass spectra of e^+e^- pairs in Pb–Au collisions at 158 A GeV/c. The data (points) are compared to the sum of the expected contributions from hadron decays (solid line). A clear enhancement of the e^+e^- yield can be seen in the mass range $0.25 < M_{e^+e^-} < 0.7$ GeV. (NA45/CERES Collaboration).

so any photons produced in the QGP phase are likely to survive until detected.

The dominant source of photon production in a QGP was originally thought to be $gq \rightarrow \gamma q$ (with a small contribution from $q\bar{q} \rightarrow \gamma g$), and that of a thermal hadron gas $\pi\rho \rightarrow \gamma\rho$ [14, 40]. The result of which was that photon production rates in a QGP and hadron gas were thought to be similar: i.e. photon production was dependent on temperature, but not necessarily a signature of a QGP [40].

However, it was found that two other photon production sources existed in the QGP: bremsstrahlung $qq \rightarrow \gamma qq$ (or $qg \rightarrow \gamma qg$) and $q\bar{q}$ annihilation followed by quark or gluon rescattering which dominates at large transverse momentum (p_T) [40]. Therefore in a QGP an enhancement in direct photons is expected, particularly at large p_T .

The WA98 experiment [40, 43] at the CERN SPS has made a measurement of the direct photon production in Pb–Pb collisions at 158 A GeV/c. The results [44] of which can be seen in figure 1.10. In central collisions a clear enhancement of the number of photons measured, $(N_\gamma)_{Meas}$, over the calculated background, $(N_\gamma)_{Bkgd}$, expected from hadronic decays can be seen, with an enhancement as great as $\sim 20\%$ for $p_T > 1.5$ GeV/c.

1.7.4 High p_T Suppression and Jet Quenching

High transverse momentum, p_T , suppression is a more recently proposed signature of a QGP [45, 46, 47] which until the last few years has not been searched for experimentally. With the onset of experiments with a higher collision energy (such as RHIC at BNL [48]) this has become a signature of much interest.

In the early stages of a heavy ion collision partons (quarks and antiquarks) from the initial colliding nuclei can scatter off one another with such force that they come off from the collision with high momentum in a direction different to that

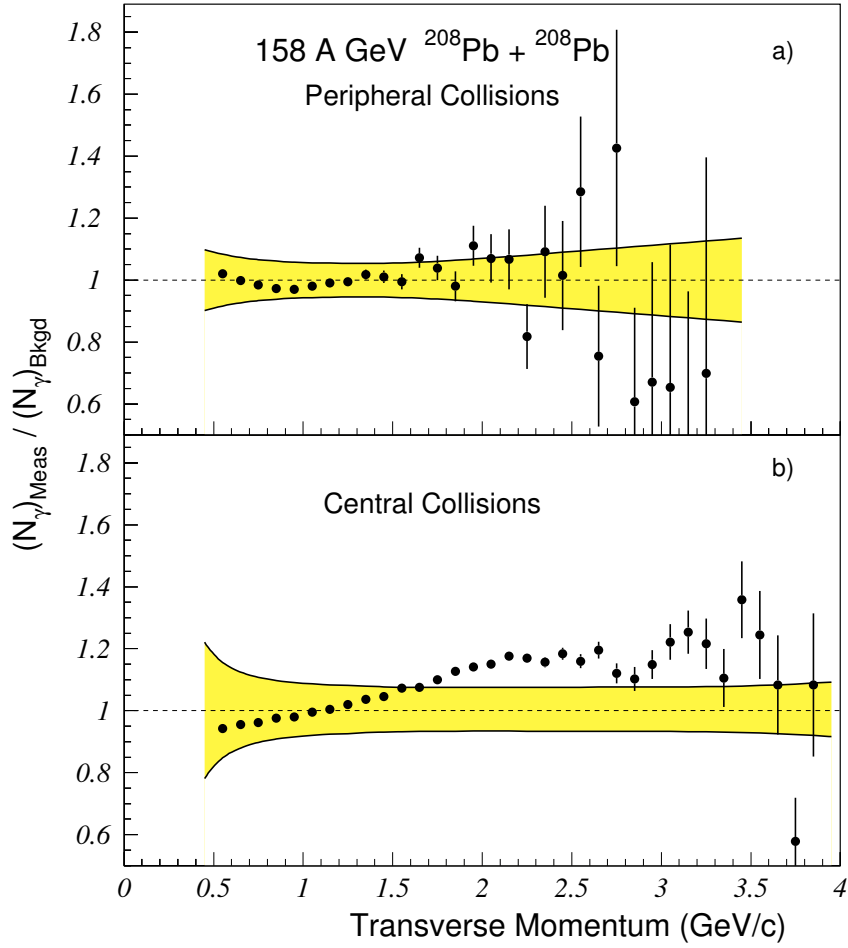


Figure 1.10: The $(N_\gamma)_{Meas}/(N_\gamma)_{Bkgd}$ ratio as a function of transverse momentum for (a) peripheral and (b) central Pb–Pb collisions at 158 A GeV/c. Errors on the data points are statistical, the p_T dependent systematic errors are shown by the shaded areas. A clear enhancement in photons can be seen at high p_T in the most central collisions. (WA98 Collaboration).

of the initial beam direction (hard scattering). Each scattered parton gives rise to a *jet* of hadrons: a highly collimated beam of hadrons coming off along the direction of the scattered parton. It turns out that in nucleus-nucleus collisions the number of particles produced at high p_T is suppressed in the most central heavy ion collisions [45]. This is thought to be due to the presence of a QGP in that the scattered partons lose momentum via bremsstrahlung as they pass through the QGP. This leads to reduced jet energies (*jet quenching*) and reduced p_T of the final particles produced [13, 34, 47].

An alternative explanation for high p_T suppression is gluon saturation [13, 45]. A saturation of gluons is predicted to reduce the number of hard scattering processes which can happen and thus reduce the number of particles with high p_T . However, this explanation can be eliminated by studying nucleus-nucleon collisions; in such collisions gluon saturation should occur, but there will not be the presence of a QGP.

High p_T suppression has been studied by all four experiments at RHIC (described in the next section); in Au–Au and d–Au collisions (an overview of which is given in [13]). Strong evidence for suppression in the most central Au–Au collisions has been seen whereas in d–Au collisions no suppression is observed, thus suggesting the high p_T suppression observed in Au–Au collisions is as a result of the QGP. This is shown clearly by the results of the STAR experiment [49], shown in figure 1.11.

These results were obtained by selecting on jets of high p_T hadrons and looking for the associated jet at $\Delta\phi = \pi$ radians (180°). In figure 1.11a p–p and d–Au collisions were considered, the latter studied both central and minimum bias (peripheral and central) collisions, which indicate in all cases back-to-back pairs of jets (a peak associated with selected particles at $\Delta\phi = 0$ radians and a recoil jet at $\Delta\phi = \pi$ radians). In figure 1.11b the central Au–Au collisions were considered: here, the characteristic selected particle peak can be seen, but an absence of any recoil peak is a suggestion that a QGP has been formed using central Au–Au collisions.

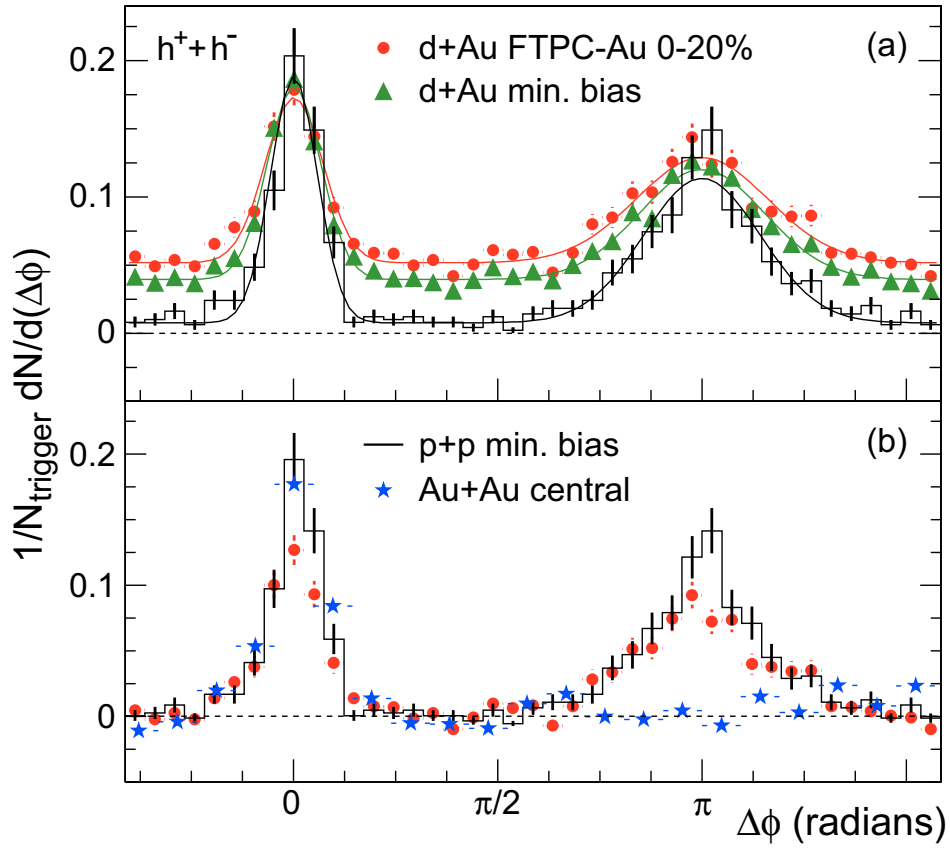


Figure 1.11: Angular correlations between pairs of high transverse momentum charged particles, referenced to a selected (trigger) particle, for (a) p–p (solid line) and d–Au central (dots) and minimum bias (triangles) collisions at $\sqrt{s_{NN}} = 200$ GeV and (b) central Au–Au (stars) collisions at $\sqrt{s_{NN}} = 200$ GeV. A clear suppression in the recoil jet for central Au–Au can be seen, whereas no suppression is observed in the p–p or d–Au systems. (STAR Collaboration).

In addition to observations of high p_T suppression in collisions at the highest RHIC energies, preliminary results indicating such an effect have also been reported by the PHENIX [50] and STAR [51] experiments at a lower RHIC energy. In addition, a search for such an effect has been made by the WA98 [52] and NA57 [53] experiments at the top CERN SPS energy.

1.8 An Overview of High Energy Heavy Ion Physics Experiments

There are three main facilities where heavy ion physics can be studied. The Super Proton Synchrotron (SPS) at CERN (the European Centre for Nuclear Physics, in Geneva, Switzerland), the Relativistic Heavy Ion Collider (RHIC) at BNL (the Brookhaven National Laboratory, in New York, United States) and the forthcoming Large Hadron Collider (LHC) at CERN [4]. In addition, one further facility is proposed: the Superconducting Synchrotrons (SIS100/300) at GSI (the Gesellschaft für Schwerionenforschung Laboratory, north of Darmstadt, Germany). A brief overview of each is given below.

The heavy ion programme at the CERN SPS [54] began in 1986 when oxygen nuclei, and then sulphur nuclei were accelerated to beam energies of 200 GeV per nucleon. Since 1994 a lead beam of energies up to 158 GeV per nucleon has been available at the SPS, extending the heavy ion programme to heavier nuclei. Seven large experiments participated in the lead beam programme: NA44, NA45/CERES, NA49, NA50, NA52/NEWMASS, WA97/NA57 and WA98; where WA and NA stand for the ‘west area’ and ‘north area’ at CERN respectively. Many of these experiments have been mentioned in sections 1.6 and 1.7 along with which signatures of the QGP they look for and the results they have reported (further details and references of all these experiments can be found at [54]).

The experiments at the CERN SPS are all fixed target experiments. One other facility which studied heavy ion collisions in fixed target experiments was at the Alternating Gradient Synchrotron (AGS) at BNL [4, 55]. The programme began in 1986 when silicon nuclei were accelerated to beam energies of 14.6 GeV per nucleon. Between 1992 and 1998, a gold beam with energies up to 11 GeV per nucleon extended the programme to heavier nuclei.

As the data taking era at the SPS draws to a close, attention has turned to RHIC which began data taking in 2000 with gold-gold collisions [56]. The beam energy of RHIC is similar to that of the SPS, but because it is a colliding beam experiment, compared with the fixed target setup at the SPS, the centre of mass (cm) energy is $2E$ rather than $\sqrt{2mE}$, where E is the beam energy (described further in appendix A), giving a total cm collision energy of approximately ten times greater than at CERN. This means the energy density is larger and the system should spend more time in the QGP phase. RHIC has four dedicated heavy ion detectors: BRAHMS [57], PHENIX [58], PHOBOS [59] and STAR [60]. STAR and PHENIX are large multipurpose experiments, BRAHMS and PHOBOS are smaller specialised experiments, together they are able to measure all aspects of the QGP.

The next stage in the heavy ion programme is the LHC due online in summer 2007 where ALICE (A Large Ion Colliding Experiment) will be the only dedicated heavy ion experiment [61]. ALICE, like all the experiments at RHIC, is a colliding beam experiment, and will study lead-lead collisions at centre of mass energies approximately thirty times greater than that of RHIC. ALICE is a multipurpose heavy ion experiment capable of observing all major signatures of the QGP.

A comparison of some of the main features of a QGP across the three main heavy ion facilities is given in table 1.1. A similar table, with references can be found at [62]. From this table it can be seen that with each successive generation of facility a QGP of increased energy density, temperature and time in the QGP phase can be achieved. As such, with each generation more can be learnt about the

nature and properties of the QGP with greater statistics.

Table 1.1: Comparison of some of the main characteristics of heavy ion collisions at the SPS, RHIC and LHC facilities.

Characteristic	SPS	RHIC	LHC
Maximum centre of mass energy, GeV	17.3	200	5500
Available range of rapidity units	6	11	17
Rapidity density (dN/dy) at $y = 0$	400	700 – 1500	3000 – 8000
Transition time of ions, fm/c	1	0.1	0.005
Formation time of QGP, fm/c	1	~ 0.2	0.1
Time in QGP phase, fm/c	≤ 2	2 – 4	≥ 10
Energy density of QGP, GeV/fm ³	3	60	1000
Ratio of temperature to critical temperature	1.1	1.9	3.0 – 4.2

Finally, and further in the future, for the heavy ion programme is the Compressed Baryonic Matter (CBM) experiment at SIS100/300 currently proposed for commission in 2014 [63, 64]. The proposed CBM experiment is a second generation fixed target experiment which utilises detector components developed for the LHC experiments. The experiment will study gold–gold (and uranium–uranium) collisions at large baryon densities with collision energies between 2 and 45 A GeV/c and will observe a number of the signatures of the QGP discussed in this chapter.

Of particular interest to the Birmingham Particle Physics Heavy Ion Group are the ALICE [65] and NA57 experiments; the latter of which is the subject of the remainder of this thesis.

Chapter 2

The NA57 Experiment

2.1 The WA97 Experiment

The NA57 experiment studies the production of strange and multistrange particles and antiparticles at the CERN SPS. Prior to NA57 was the WA97 experiment [25, 27]; this was one of three previous ion experiments that studied strange and multistrange particles at the OMEGA spectrometer at CERN. The predecessor experiments to WA97 being WA85 (S–W collisions at 200 A GeV/c) [66, 67] and WA94 (S–S collisions at 200 A GeV/c) [68, 69]. The WA97 experiment studied production of Λ_s , Ξ_s and Ω_s in Pb–Pb, p–Pb and p–Be collisions at 158 A GeV/c and completed data taking in 1996. WA97 has shown that there is an enhanced production of strange and multistrange particles in Pb–Pb interactions with respect to p– A reactions at the same energy [70]. In particular it has shown that the strangeness enhancement is progressively stronger for particles of higher strangeness content: production of Ω_s is enhanced more than that of Ξ_s , whose production in turn is more enhanced than that of Λ_s , as shown in figure 1.7. This enhancement has been predicted as a signature of a phase transition from normal hadronic matter to a deconfined QGP [20].

2.2 Motivation for the NA57 Experiment

NA57 [1, 71] aims to extend the study initiated by WA97, specifically to investigate the onset of the strangeness enhancement effect observed in central collisions at WA97 at $158 A \text{ GeV}/c$. NA57 addresses this aim by studying the strangeness enhancement effect in nucleus-nucleus collisions at two different beam energies (40 and $158 A \text{ GeV}/c$) and over an increased centrality (number of participants) range (extended down to about 50 wounded nucleons, compared to about 100 in WA97). These additional attributes of NA57 allow investigation into the minimum energy required to produce a QGP as well as the study of whether a QGP can be produced in less central (peripheral) collisions. Like the WA97 experiment, NA57 looks at Pb–Pb and p–Be interactions. The NA57 experiment was installed and commissioned in 1997 and began data taking in 1998.

2.3 The CERN SPS

NA57, like WA97 (and indeed all the other fixed target heavy ion CERN experiments) made use of the Super Proton Synchrotron (SPS) [72]. The SPS has a 9 km circumference and is one of a number of accelerators in CERN's interconnected accelerator network, as shown in figure 2.1. It was first commissioned in June 1976 when it supplied its first beam of protons at $300 \text{ GeV}/c$. The protons and lead ions used by NA57 originated from sources in LINAC 2 and LINAC 3 respectively [73], they were then accelerated through the LINAC in question to $50 \text{ MeV}/c$ for the proton beam and $4.2 A \text{ MeV}/c$ for the lead beam. On leaving the LINAC the particle beam entered the Proton Synchrotron Booster (PSB) and then the Proton Synchrotron (PS) where they were accelerated further before entering the SPS. The SPS can deliver proton beams of up to $450 \text{ GeV}/c$ and lead beams of up to $158 A \text{ GeV}/c$ ($400 \text{ GeV}/c$ per proton) [74].

CERN Accelerators (not to scale)

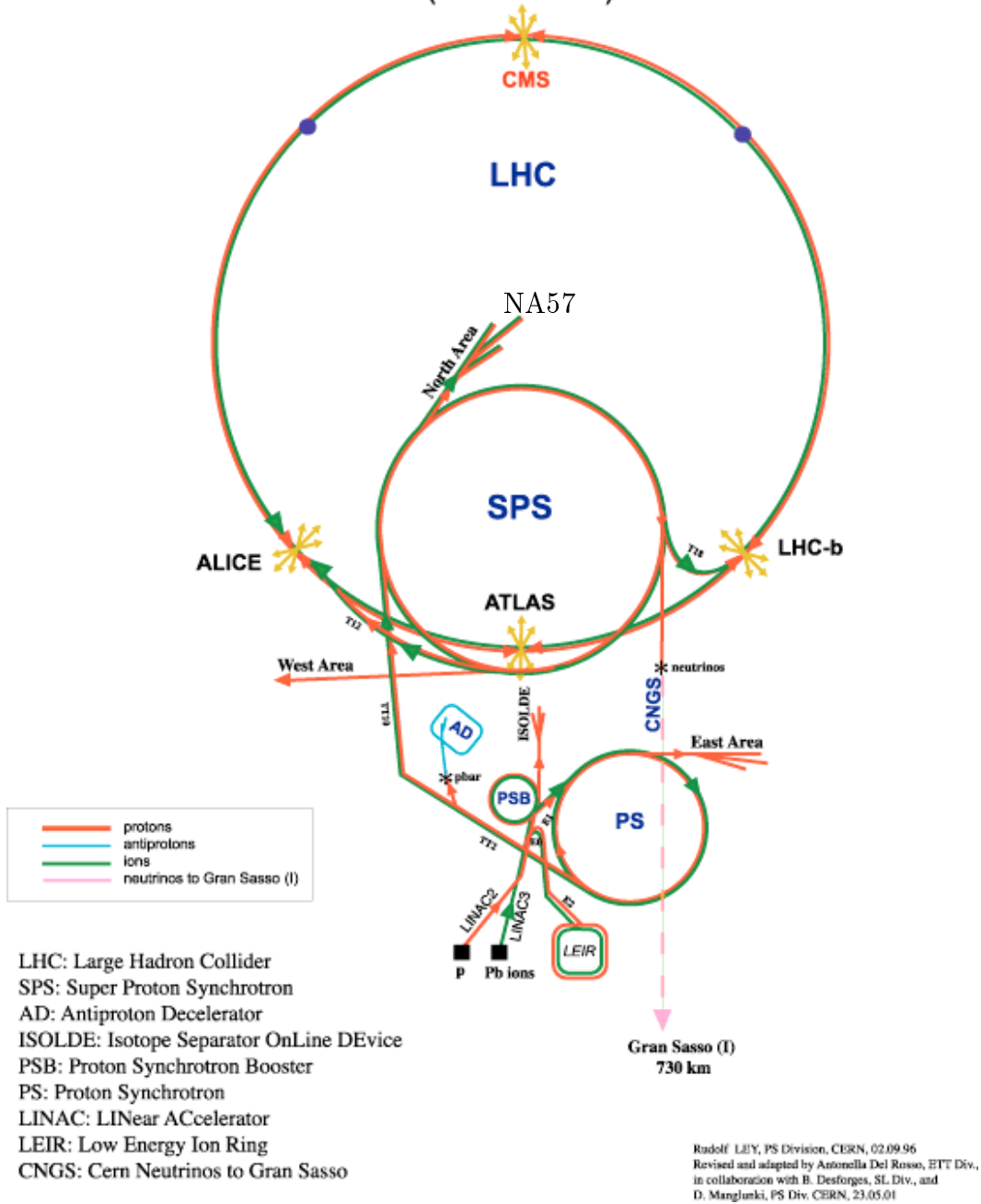


Figure 2.1: The 9 km circumference CERN SPS. The SPS is one of a number of accelerators in CERN's interconnected accelerator network.

Besides the source of beams for fixed target heavy ion experiments, the SPS has also been used as a proton-antiproton collider, where (in 1983) the W and Z particles (carriers of the weak interaction) were discovered [75]. The SPS was also used as the injector for the 27 km circumference Large Electron Positron (LEP) collider and will be the injector for its replacement, the LHC (for which a new extraction channel is currently being installed). The SPS is also to be the source for a neutrino experiment taking place 730 km away at the Gran Sasso Laboratory, Italy [74, 76].

2.4 The NA57 Experiment

The NA57 setup is shown in figure 2.2. As this thesis concentrates on the reference 40 GeV/c p-Be data, the variation of the experiment shown is for this data set. The experimental setup can be divided into four parts: beam, target, detector and trigger; each of which are described in the following four subsections. Whilst the p-Be and Pb-Pb setups are largely the same, a brief overview of how the setup differs for the case of Pb-Pb is described in the following section.

All of the apparatus downstream of (and including) the S4 counter is positioned inside the GOLIATH magnet which has a 1.4 T maximum field and was first used in the late 1970s by the CERN WA11 experiment [77].

2.4.1 Beam

The proton beams used were provided by the CERN SPS. The SPS accelerates protons to 450 GeV/c (as described in section 2.3). To obtain a proton beam of 40 GeV/c a set of beryllium targets (different to the beryllium target used in the p-Be interactions) were inserted at the point where the beam was extracted from the SPS. The emerging ‘secondary’ beam was passed through dipole magnets in order to select off particles with momenta of 40 GeV/c. Although the secondary beam

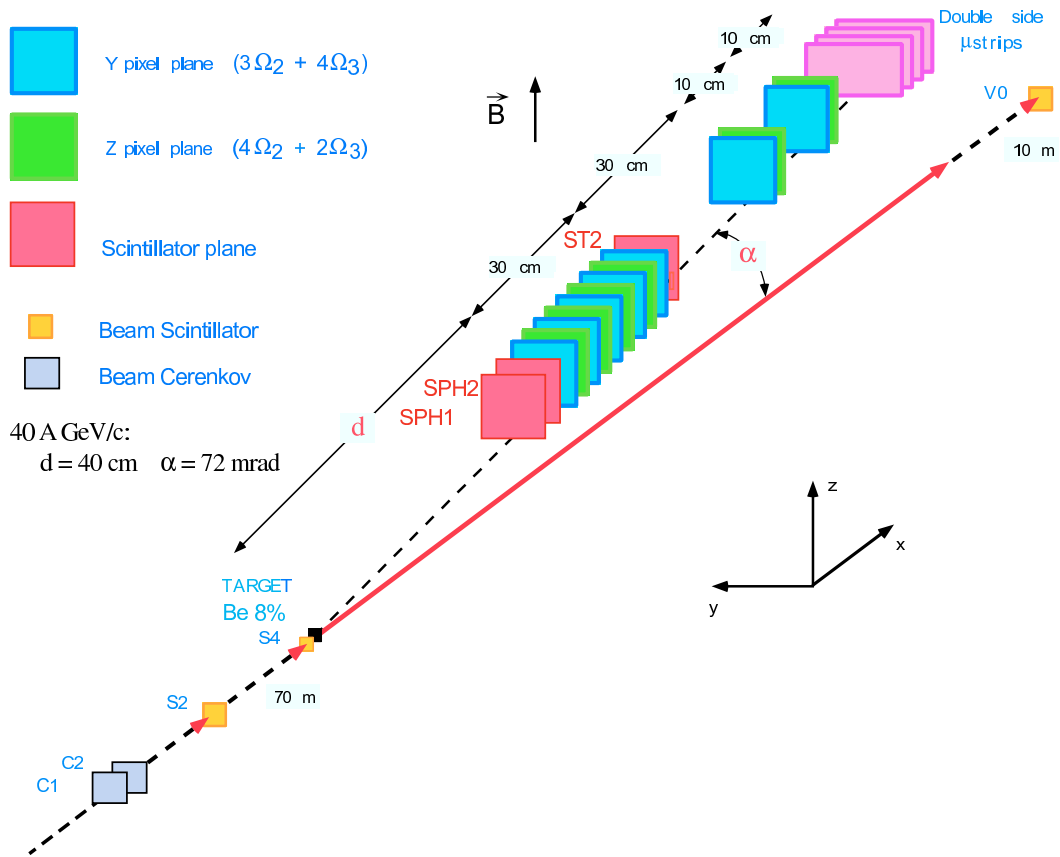


Figure 2.2: The NA57 experiment for p-Be collisions at 40 GeV/c.

was of the correct momentum it contained a mixture of pions and protons. One of the main functions of the p–Be trigger was to select events produced as a result of proton interactions and to veto events produced as a result of pion interactions (see section 2.4.4).

2.4.2 Target

The beryllium target used was 3.26 cm thick and had an interaction length of 8%. Its centre was positioned at $x = -60$ cm in the GOLIATH reference system, which is approximately 40 cm upstream of the telescope.

2.4.3 Telescope

The detector used in the NA57 experiment was a telescope of silicon pixel detector planes [71, 78]. The technique of silicon pixel detectors was pioneered successfully by WA97 in collaboration with CERN Microelectronics Research and Development Group, RD19. This type of detector was chosen because of its high rate capability to collect large statistics and its high resolution allowing it to handle the large density of tracks produced in central Pb–Pb collisions. The NA57 telescope was made up of two types of silicon pixel plane: Omega2 [79] and Omega3 [80]. The Omega2 plane was used for the seven plane telescope of WA97; the Omega3 plane was developed subsequently. It had improved readout electronics (for example a reduced dead time) compared to that of Omega2, and was designed not only to satisfy the requirements of WA97, but also with the possibility of being used as a vertex detector by the LHC in the future.

The basic building block of both types of planes is the *ladder*. The ladder consists of a matrix of reversed biased rectangular silicon detector diodes (*pixels*). In Omega2 planes each pixel has a size of $75 \times 500 \mu\text{m}^2$, in Omega3 planes the pixels have a size

of $50 \times 500 \mu\text{m}^2$. Placed behind the ladder are six front-end *readout chips*, which cover the same area as the ladder. Contained within each readout chip is a matrix of *readout cells*. In Omega2 planes there are 16×64 readout cells, of which 1,006 are sensitive cells [78], per readout chip. In Omega3 there are 16×128 readout cells, of which 2,032 are sensitive cells [78], per readout chip. The readout cells are of the same size as the pixels and are such that each pixel has a readout cell placed directly behind it. Each readout cell is connected to its corresponding pixel via a Sn–Pb solder bump of diameter $38 \mu\text{m}$, as shown in figure 2.3.

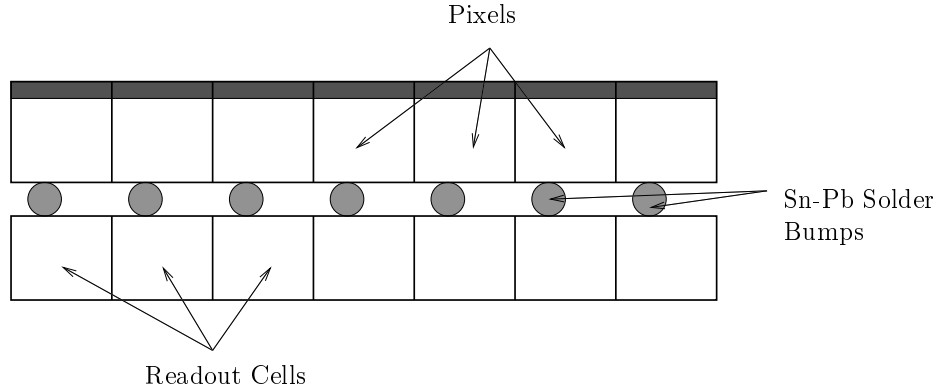


Figure 2.3: A number of silicon pixels connected to their corresponding readout cells via Sn–Pb solder bumps. The readout cells contain electronics which can store whether a charged particle has traversed the pixel or not. A large number of readout cells form part of a matrix which forms a readout chip.

Each individual readout cell contains an amplifier, followed by a comparator with an adjustable threshold and delay and some coincidence and memory components. If a charged particle is detected a bit will be stored. The total number of sensitive channels in each Omega2 ladder is 6,036, in Omega3 the number of channels is approximately doubled (12,192).

A number of ladders, spaced by a few mm are glued onto a $380 \mu\text{m}$ thick ceramic substrate: six ladders in the case of Omega2 (shown in figure 2.4), four in the case of Omega3 form half a plane. To form a whole plane two half planes are mounted

face-to-face and staggered by a few mm so as to cover the ‘dead’ areas. The sensitive area of each pixel plane is $5 \times 5 \text{ cm}^2$ and contains 72,432 channels in the case of Omega2, 97,536 channels in the case of Omega3.

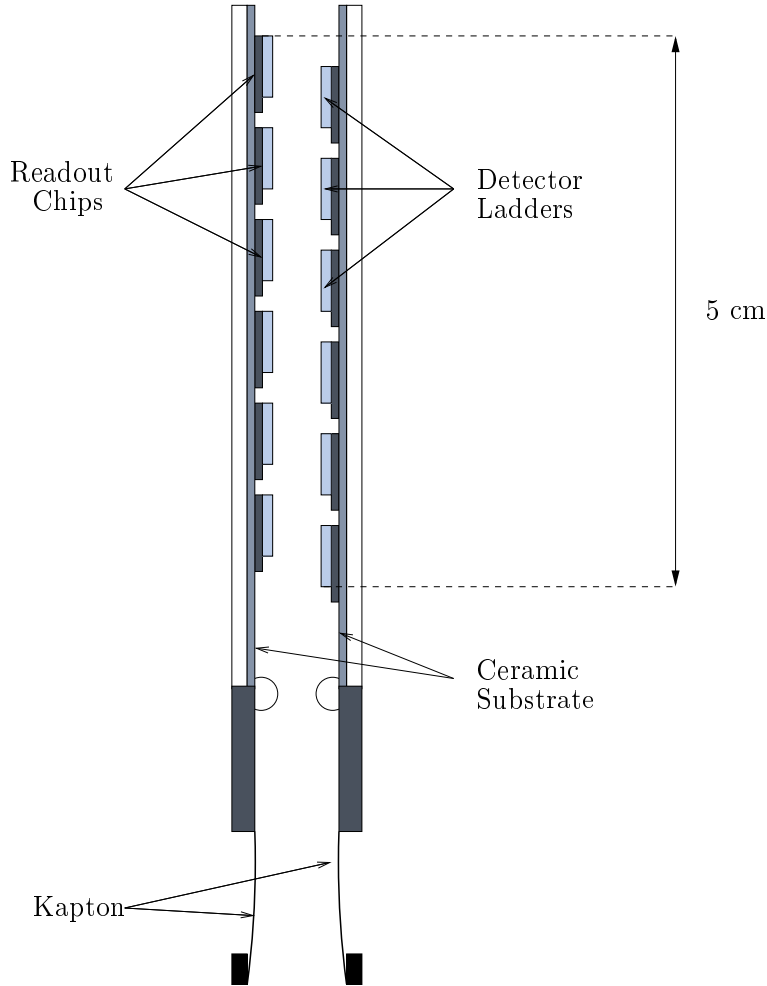


Figure 2.4: One Omega2 silicon pixel plane made up of two half planes. A half plane consists of six detector ladders (four in the case of Omega3) and their associated readout chips, mounted upon a thick ceramic substance. A scale is shown to illustrate the size of the sensitive area of the detector, the remainder of the figure is not to scale for improved clarity.

In all the NA57 telescope consisted of thirteen silicon pixel detector planes and has a total of about 1.1×10^6 channels. Seven of the planes were of Omega2 type, the remaining six of Omega3 type. The thirteen planes were not all inserted in the same orientation: instead some planes were rotated by 90° so as to achieve good

resolution in both the y and z directions.

As seen in figure 2.2, the majority of the thirteen planes (exact numbers depend on the data set) were put within the ‘compact’ part of the telescope, which is 30 cm in length. This allows accurate tracking of the curvature of charged tracks. The few remaining planes were placed towards the back of the telescope, allowing improved momentum resolution for the high momentum tracks (which will bend very little as they pass through the telescope).

The whole telescope was placed above the beam line, inclined and aligned with the lower edge of the detectors laying on a line pointing back to the target. The telescope accepted particles produced at mid-rapidity and medium transverse momentum. So as to cover about one unit of rapidity about central rapidity the inclination angle, α and the distance, d of the target from the first plane were changed with each beam momentum. In the case of p-Be at 40 GeV/c ($y_{lab} \simeq 2.2$) α is 72 mrad, d is 40 cm.

2.4.4 Trigger

The trigger system [81, 82] of the p-Be setup served two purposes: to ensure a proton beam reaches the beryllium target and that at least two tracks pass through the telescope. Each of these two aspects are considered in turn.

Two gaseous Čerenkov threshold counters, $C1$ and $C2$, [2, 6] were placed some way upstream of the target, their purpose is to veto the pion contamination from the proton beam (discussed in section 2.4.1). As the beam of particles passes through the gas inside the counters, Čerenkov radiation is given off which emits light at a characteristic angle, θ [83]:

$$\cos \theta = \frac{1}{\beta n} \quad (2.1)$$

where n is the refractive index and $\beta > 1/n$. For a given gas pressure and hence

refractive index Čerenkov radiation may or may not occur for a given particle species, depending on whether the particle is above or below the effective Čerenkov threshold velocity, β_t :

$$\beta_t = \frac{1}{n \cos \theta_c} \quad (2.2)$$

where $\theta_c = \frac{1}{2} \theta_{max}$ and θ_{max} occurs when $\beta = 1$. β_t has been chosen in NA57 such that pions give light and protons do not. If a signal is seen it is a pion and not a proton in the beam and the event can be vetoed. Two Čerenkov counters are used to confirm the signal and to increase the overall efficiency of the system.

Further downstream from the Čerenkov counters were placed two scintillators $S2$ and $S4$ which were used to ensure the proton passes through the target. $S2$ was placed outside GOLIATH; $S4$ was the same size as the target and was placed just before the target inside GOLIATH. As the particles traverses the scintillators, ionisation of atoms within the scintillator occurs leaving a line of free electrons and holes [2]. These move around until captured by an activator centre causing it to be transferred into an excited state. On returning to the ground state the activator centre emits a photon. The light given off by the scintillator is then directed into a photomultiplier tube (where it is recorded) via a light guide. On entering the photomultiplier tube the light lands on an alkali coated photocathode where electrons are liberated via the photoelectric effect. The electrons then travel to a chain of secondary electrodes (dynodes) at successively larger potentials where the electron signal is amplified. The output then enters a discriminator, and if the signal is above a certain threshold, a proton will be assumed to have traversed the scintillator.

Around the telescope were placed three scintillators: $SPH1$, $SPH2$ and $ST2$, (which work in the same way to $S2$ and $S4$) whose cross sections were the same size as the telescope ($5 \times 5 \text{ cm}^2$); The SPH scintillators were placed upstream of the telescope, $ST2$ downstream of the compact part of the telescope. Their purpose was to select those events where at least two tracks pass through the telescope; this

enabled strange hyperons to be reconstructed from their charged decay tracks. The hyperons NA57 studies decay into a baryon and meson (for example $\Lambda \rightarrow p\pi^-$). The *SPH* scintillators detected two track events; these were found by considering the voltage of the produced pulse. The voltage produced increases with the number of tracks traversing the scintillator. A pulse-height spectrum would show a peak at low voltage (corresponding to a single track event), a smaller secondary peak at a higher voltage (corresponding to a two track event). A further (smaller still) tertiary peak would be present at even higher voltages (corresponding to a three track event), and so on. However as these peaks each have a *Landau*-type distribution (sharp peak, asymmetric shape: long tail towards positive values) it is possible for a single track event or ‘noise’ to have a voltage in the region of a two track event. For this reason two *SPH* scintillators: *SPH1* and *SPH2* were used as the likelihood of a single track event or noise causing a voltage within the two track region in both scintillators simultaneously is much reduced. *ST2* only looks for one track because the baryon carries the majority of the original hyperon’s momentum and therefore will bend less in the magnet than the meson. Thus it is far more likely to pass through the entire telescope and into *ST2*.

For an event to be accepted the following trigger condition had to be met:

$$Accepted\ Event = \overline{C1} \cdot \overline{C2} \cdot S2 \cdot S4 \cdot SPH1 \cdot SPH2 \cdot ST2 \cdot \overline{BUSY} \quad (2.3)$$

where an extra trigger condition ‘ \overline{BUSY} ’ has been added, which hitherto has not been discussed. *BUSY* reflects the time which the data acquisition (DAQ) system takes to read out, compress and send an event to the event-builder. If \overline{BUSY} is present, the experiment is doing neither of these things and an event can be accepted.

A further scintillator *V0* was placed (but not used, as the trigger was sufficient without it) downstream of the target; if used, a hit recorded implied the beam had passed through the target and not interacted. This event would be rejected.

2.5 The NA57 Experiment for Pb–Pb Interactions

In addition to collecting p–Be data at 40 GeV/c, the main aim of the NA57 experiment was to collect data for the case of a lead beam interacting with a lead target at 40 A GeV/c and 158 A GeV/c. The Pb–Pb experimental set up is shown in figure 2.5. A brief overview of how the setup described in the last section for p–Be interactions differs for the case of Pb–Pb interactions is given here.

2.5.1 Beam

The CERN SPS provided lead beams at 40 A GeV/c and 158 A GeV/c. These are the minimum and maximum momentum available respectively for a beam of lead nuclei at the SPS.

2.5.2 Target

The lead target used was about 0.4 mm thick and had an interaction length of 1%. As for the Be target, its centre was positioned at $x = -60$ cm in the GOLIATH reference system at 40 A GeV/c. At 158 A GeV/c the centre of the target was moved to $x = -80$ cm in the GOLIATH reference system.

2.5.3 Telescope

For lead beams at 40 A GeV/c the inclination angle, α and the distance, d from the target to the first plane of the telescope was the same as in the case of p–Be at 40 GeV/c (section 2.4.3). For 158 A GeV/c ($y_{lab} \simeq 2.9$) α is decreased to 40 mrad and d is increased to 60 cm. The difference in α and d for the two different incoming

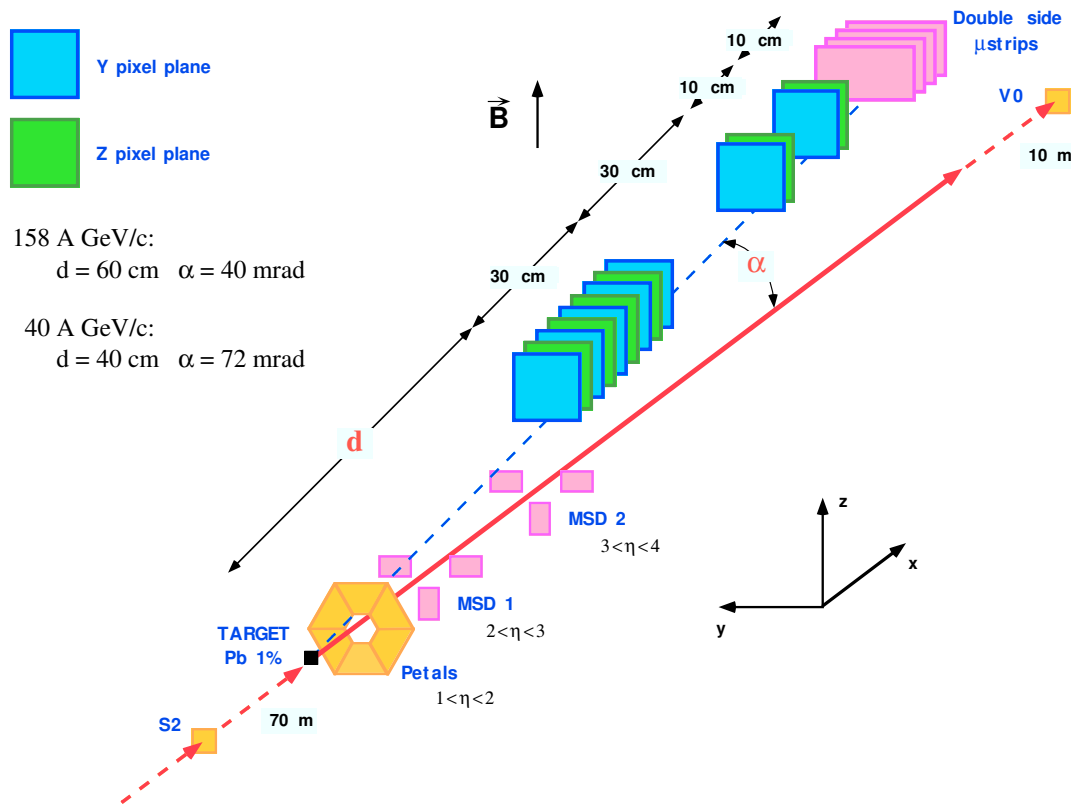


Figure 2.5: The NA57 experiment for Pb–Pb collisions at both 40 A GeV/c and 158 A GeV/c.

Pb momenta is necessary to ensure the telescope is able to accept particles with a rapidity that covers one unit of rapidity about central rapidity.

2.5.4 Trigger

The trigger for the Pb–Pb run [81] differed to that of p–Be. A single quartz Čerenkov, $S2$ replaced $C1$, $C2$, $S2$ $S4$ (used in the p–Be setup, section 2.4.4) upstream of the target; its function ensured a lead ion was incident on the lead target. This was achieved by virtue of the fact that the number of photons produced is proportional to Z^2 [6], where $Z = 82$ for lead and hence it is easy to separate lead ions from contamination with a much lower Z . Scintillators $SPH1$, $SPH2$, $ST2$ used in the p–Be trigger and $V0$ were not used in Pb–Pb runs. A further trigger was implemented: a hexagonal array of six scintillator “petals” [82] placed 10 cm downstream of the target and arranged around the beam axis were used to select out central events. In any given event a large number of tracks were expected to be produced and therefore a large number would be expected on each of the petals; for the event to be accepted ten or more tracks must be detected on four out of five of the petals (PETALS). The sixth petal was one of the two petals that traversed the $x - y$ plane of the beam and was excluded because it was saturated by δ -electrons. δ -electrons [6] are electrons from the surrounding air molecules that are removed by a charged particle beam, they have essentially zero transverse momentum and gain horizontal momentum because of the presence of a magnetic field. δ -electrons, therefore, were swept onto the sixth petal of the scintillator by the magnetic field of the experiment. Which of the two petals that traversed the $x - y$ plane of the beam were affected by δ -electrons depended upon the polarity of the magnetic field. As for the p–Be trigger, the \overline{BUSY} condition was also implemented.

For an event to be accepted the following trigger condition had to be met:

$$Accepted\ Event = S2 \cdot PETALS \cdot \overline{BUSY} \quad (2.4)$$

2.5.5 Multiplicity Detectors

For a detailed offline investigation of the collision centrality in the event, two stations of silicon multiplicity strip detectors (MSD) were placed downstream of the petals [71]. The relationship between the sampled multiplicity and the number of participant nucleons is obtained by fitting the multiplicity distribution to a curve obtained from a Glauber model calculation (see for example, [84, 85] and references within).

2.6 The Data Sets

A summary of the data collected by the NA57 experiment over its four year running period is shown in table 2.1.

Table 2.1: Summary of data taken by the NA57 experiment

System	Beam momentum	Sample size	Run
Pb–Pb	158 A GeV/c	230 M events	November 1998
p–Be	40 GeV/c	60 M events	July 1999
Pb–Pb	40 A GeV/c	290 M events	November 1999
Pb–Pb	158 A GeV/c	230 M events	October 2000
p–Be	40 GeV/c	110 M events	September 2001

The reference data set used for 158 A GeV/c is the p–Be data obtained by WA97.

One final run looking at Indium-Indium collisions at 170 A GeV/c was proposed for Autumn 2003 [86], but was rejected in February 2003 by the CERN Research Board. The purpose of the proposed In–In run was to study the A dependence of the enhancements.

It is the 1999 p-Be reference data set which is the subject of the remainder of this thesis.

Chapter 3

Λ and $\bar{\Lambda}$ Reconstruction in p–Be Collisions

3.1 Introduction

As mentioned in the previous chapter, NA57 looks for the strangeness enhancement effect, by studying the production of the strange baryons: Ω s, Ξ s and Λ s and their antiparticles. These particles are not observed directly and must be reconstructed from their decay particles. The decay channels studied by NA57 are:-

$$\begin{aligned}\Lambda &\rightarrow p \pi^- & (\bar{\Lambda} &\rightarrow \bar{p} \pi^+) \\ \Xi^- &\rightarrow \Lambda \pi^- & (\bar{\Xi}^+ &\rightarrow \bar{\Lambda} \pi^+) \\ \Omega^- &\rightarrow \Lambda K^- & (\bar{\Omega}^+ &\rightarrow \bar{\Lambda} K^+)\end{aligned}$$

So to reconstruct a Λ , two oppositely charged tracks must intersect in space; to reconstruct a Ξ^- or Ω^- a Λ must intersect in space with a third charged track . The author has been involved with the Λ and $\bar{\Lambda}$ reconstruction, which is the subject of the remainder of this chapter.

3.2 Data Acquisition

Before proceeding with details on data reconstruction, it is worthwhile mentioning the strategy of data collection. Data was not collected in one continuous running period, instead it was collected in many smaller discrete units called ‘runs’. Collecting data in runs (compared with continuously) has a number of advantages, for example it allows easy identification of where in the data collection period a particular event of interest originated. Furthermore, data collection takes place over a number of weeks, by working in runs the apparatus can periodically be checked between runs. In addition, should anything happen during a run(s), for example loss of beam or magnetic field, then the affected run(s) can easily be discarded.

In the 1999 p–Be data set discussed in this thesis, ‘good’ runs have run numbers between 7005 – 7309. However, runs 7005 – 7099 were found to be unstable and so were discarded. All analysis is performed on data from runs 7100 – 7309. For runs 7100–7188 the polarity of the magnetic field was positive (B^+), for runs 7211–7309 the polarity of the magnetic field was negative (B^-). The change in magnetic field was implemented to reduce systematic effects due to the alignment of the detectors.

3.3 Sailor and Cowboy Decays

When a particle such as the Λ decays in a magnetic field the two oppositely charged tracks which result will decay in one of two topologies: known as ‘sailor’ or ‘cowboy’. Two tracks which bend away from one another are known as a sailor topology, two tracks which bend towards one another are known as a cowboy topology: these two topologies are shown in figure 3.1. Candidates with a cowboy topology are favoured by NA57 for two reasons: firstly, candidates with this topology can be produced much less readily from combinatorial background (discussed later in this chapter) than candidates with a sailor topology, therefore, the combinatorial background is

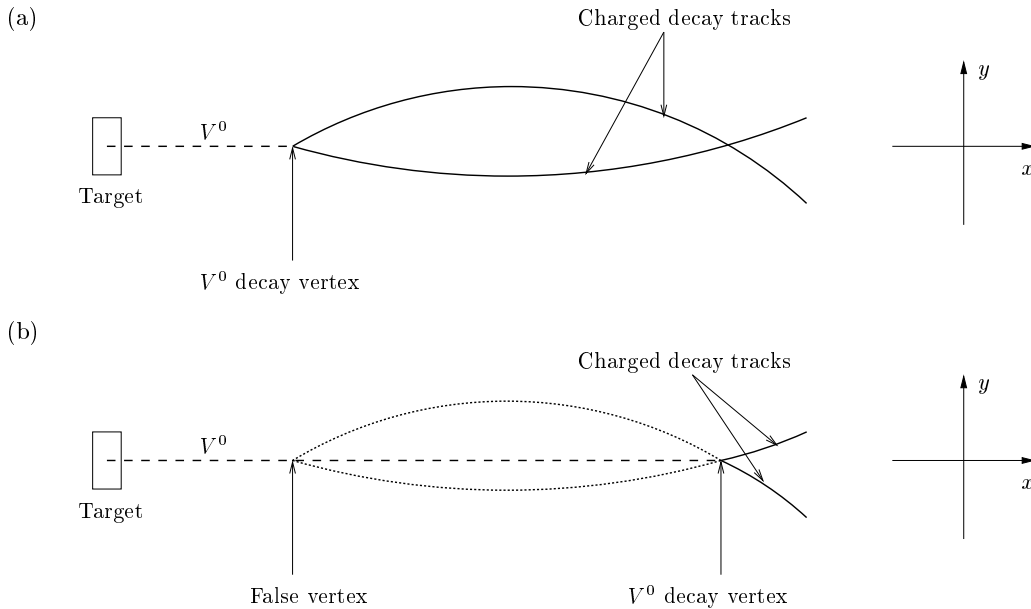


Figure 3.1: A neutral particle, known as a V^0 , decays into two oppositely charged tracks in either (a) a cowboy topology or (b) a sailor topology. NA57 favours the cowboy topology.

suppressed by choosing candidates with a cowboy topology. Secondly, the decay tracks of candidates with a cowboy topology stay nearer to each other for longer and are more likely, therefore, to pass through more planes of the telescope than candidates with a sailor topology. Only candidates with a cowboy topology, therefore, are selected in this analysis.

3.4 Reconstruction of a V^0 Candidate

A V^0 is the name given to a neutral particle which decays into two charged tracks as seen in figure 3.1, such as a Λ , $\bar{\Lambda}$ (shown in section 3.1) or K_S^0 ($K_S^0 \rightarrow \pi^- \pi^+$). The first stage of reconstruction begins by identifying possible V^0 candidates from the raw data; this is done by a program called ORHION. ORHION finds charged tracks in the raw data from hits recorded in the telescope, which are then traced back towards the target. V^0 candidates are then found by examining the charged tracks.

Each positive track is compared to each negative track and, to be accepted as a possible V^0 candidate, the distance of closest approach of the two tracks must be less than a maximum limit, in this case 0.1 cm. A check is made to ensure the track numbers differ for all V^0 candidates, i.e. a given track is used no more than once. The V^0 candidates are written to a data storage tape (DST). Loose selection criteria can be made on this data using a program called ANALYZE. One such selection made at this stage is one which simulates the trigger requirement, described more fully in section 2.4.4, that two charged tracks must pass through the two *SPH* scintillators upstream of the telescope and one through the *ST2* scintillator downstream of the compact part of the telescope. The output from ANALYZE is an ntuple which can be used in PAW [87] to tighten and determine the final selection criteria.

3.5 The Primary Vertex

In the reconstruction stage it is necessary to trace charged tracks and the V^0 back to within the target to the place where the proton beam and the beryllium target interacted for the candidate being studied. This interaction point is known as the *primary vertex*, whose x , y and z coordinates are defined by $xtarg$, $ytarg$ and $ztarg$ respectively. As the beryllium target has a finite length in x (section 2.4.2) it is not sufficient to assume that $xtarg$ always occurs at the same point, i.e. the centre of the target. Instead $xtarg$ needs to be explicitly defined for each V^0 candidate. To do this $xtarg$ is calculated by finding the position in x with which the V^0 intersects with the beam. The beam is assumed as a horizontal line increasing in x . The y and z coordinates of the centre of the beam, y_0 and z_0 , are defined from the survey (SV) database whose values were obtained from an optical survey of the beam line.

$xtarg$ can be determined in either the $x-y$ or $x-z$ planes, as shown in figure 3.2. The values calculated in the $x-z$ plane are better defined than $x-y$ since the V^0 dips more in the $x-z$ plane giving a clearer definition of the vertex: this can be seen

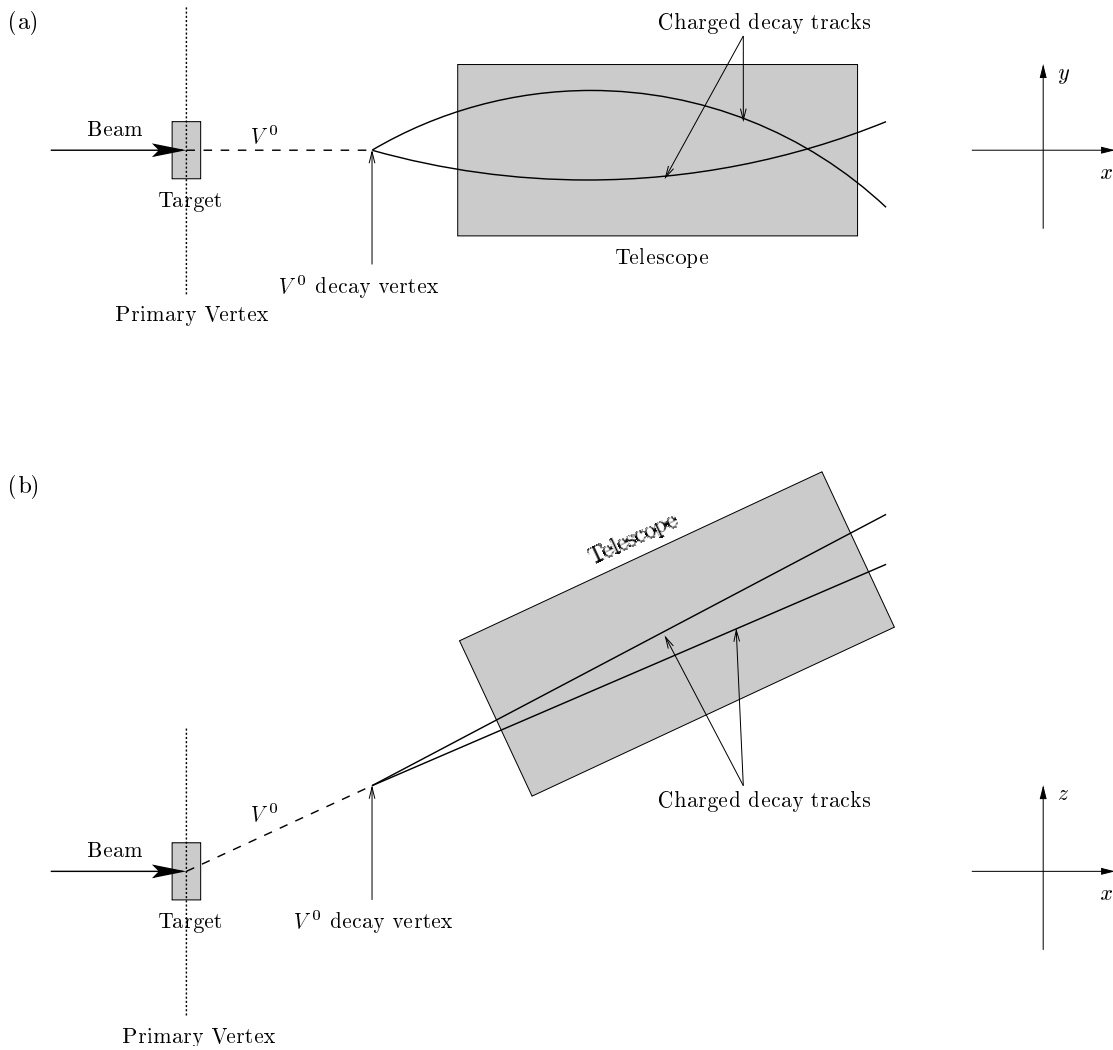


Figure 3.2: The primary vertex as determined in the (a) $x - y$ plane and (b) $x - z$ plane. It is clear that the primary vertex is best defined in the $x - z$ plane as the V^0 and beam are at a finite angle to one another. In the $x - y$ plane the beam and V^0 are almost parallel to one another and thus it is hard to determine exactly where the primary vertex is.

clearly in figure 3.2. It is in this plane in which the values of $xtarg$ are obtained. In this plane $ztarg$ is equal to z_0 (by definition), $ytarg$ is the position in y of the V^0 at $xtarg$ and as the beam has a finite width $ytarg$ does not necessarily equal y_0 . A full description of the calculation of $xtarg$ (which is implemented in the ANALYZE code) is given in appendix B, the results are shown in figure 3.3. The peak centred at -60 cm comes from interactions in the target, the subsidiary peak centred at -85 cm comes from interactions in the $S4$ scintillator. These latter candidates are removed by a selection of $xtarg > -75$ cm, shown in figure 3.3, which is the minima of $xtarg$ between the two peaks. The distribution can be seen to extend beyond the

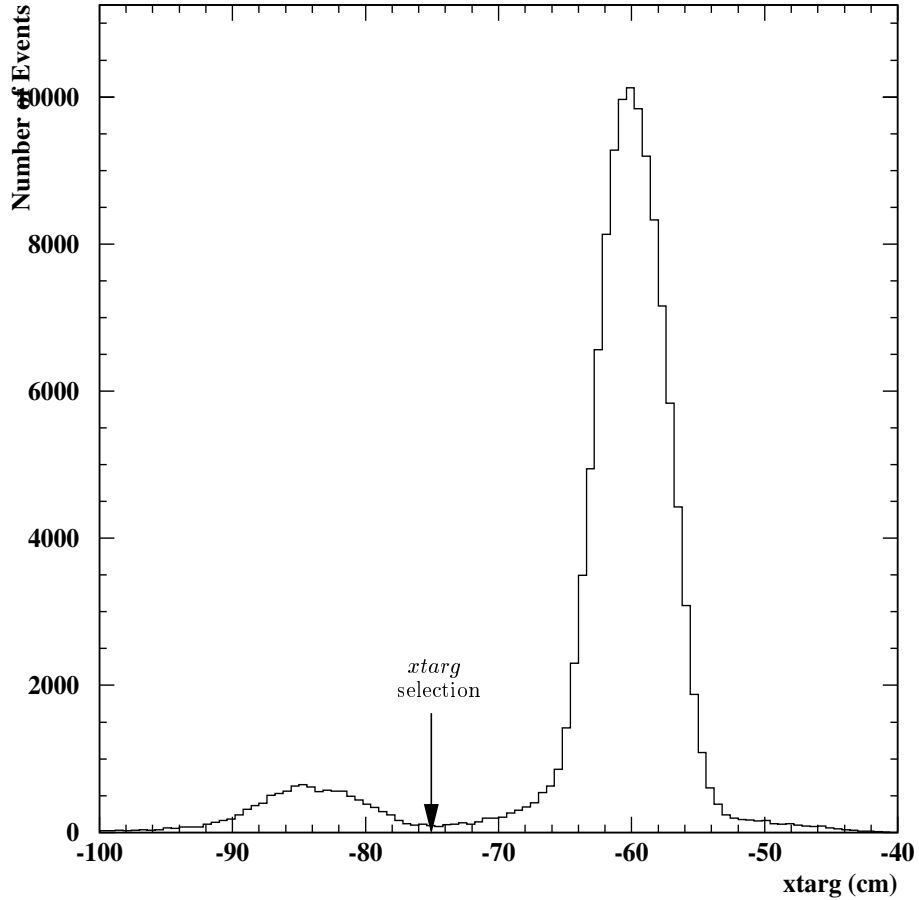


Figure 3.3: $xtarg$ calculated in the $x - z$ plane. The peak is the centre of the Be target, the subsidiary peak is due to the $S4$ scintillator counter: these latter candidates are removed by a selection of $xtarg > -75$ cm.

~ 3 cm width of the target: this is expected and due to the tracking resolution which will always reconstruct primary vertices outside of the target region. The tracking resolution in the $x - z$ plane, although better than that in the $x - y$ plane, is limited by the very small angle (72 mrad, given in section 2.4.3) between the beam and the telescope. These candidates outside of the target region are not removed as cutting away these candidates will remove real data and bias the sample.

3.6 Verifying the Database using a “Direct V^0 ” Analysis

The definition of $xtarg$, the x coordinate of the primary vertex, relies on the database values of either y_0 or z_0 (y and z coordinates of the centre of the beam). As the primary vertex was calculated in the $x - z$ plane the value of z_0 (which by definition is equal to $ztarg$) directly affects the value of $xtarg$ (section 3.5). The database used was the survey (SV) database whose value of z_0 (and hence $ztarg$) is -17.85 cm, which gives a $xtarg$ value of -60.0 cm. In order to verify these values a “direct V^0 ” analysis was implemented.

Figure 3.4 shows two possible scenarios when a proton beam and beryllium target interact, figure 3.4a shows the interaction producing a real V^0 (which then decays into two oppositely charged tracks). Figure 3.4b shows the interaction producing two “direct” oppositely charged tracks (i.e. no V^0). This type of interaction does not produce a real V^0 , just two charged tracks, and is known as a “direct V^0 ” candidate. By tracing the two oppositely charged tracks in a direct V^0 candidate back to their common vertex (interaction vertex of p-Be) will give values of $xtarg$, y_0 and z_0 , which are not reliant upon the SV database.

To obtain direct V^0 candidates two background (which are described in greater detail in section 4.2.2) tapes (one each for field up and down) were processed by

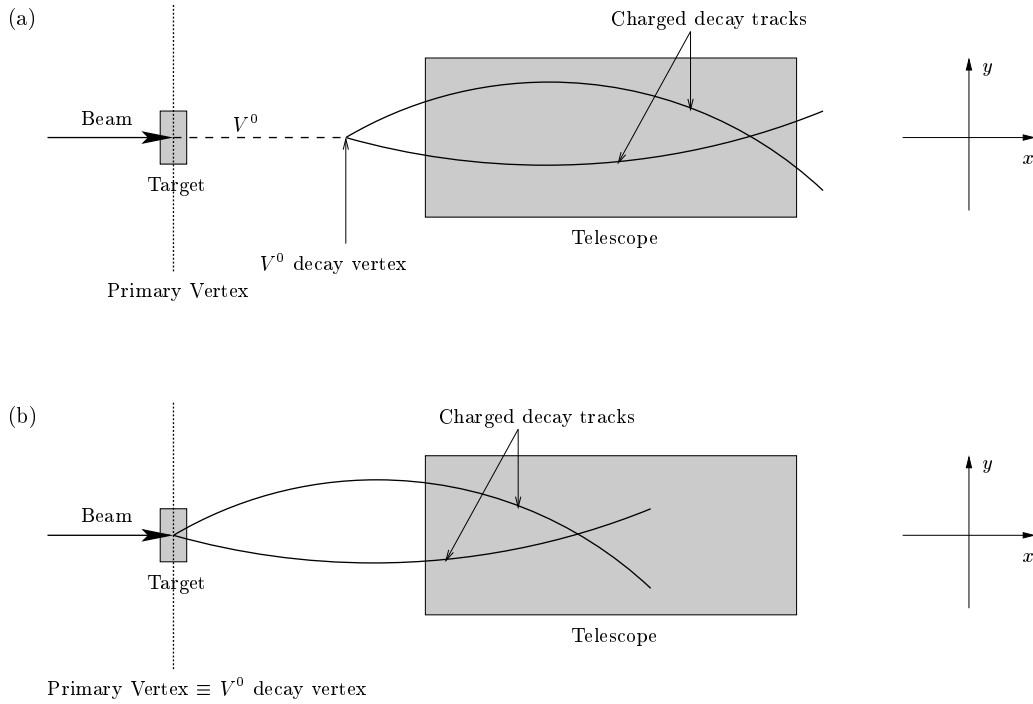


Figure 3.4: Two oppositely charged tracks detected by the telescope, produced from (a) the decay of a real V^0 : $p + Be \rightarrow V^0(\Lambda, K_S^0)$ and (b) the decay of an interaction of the p-beam with the Be target, known as a “direct V^0 ”: $p + Be \rightarrow h^+h^-$.

ORHION (section 3.4) and the output passed through ANALYZE; in both stages the selections were loosened to allow as many V^0 candidates as possible. Mass selections on Λ , $\bar{\Lambda}$ and K_S^0 of (PDG value) ± 30 MeV [6] were made, to ensure any mass signal on the background data was removed.

Figure 3.5 shows y_0 and z_0 calculated for direct V^0 candidates, a Gaussian fit has been made to each. As y_0 is the bend direction, separate values of y_0 have

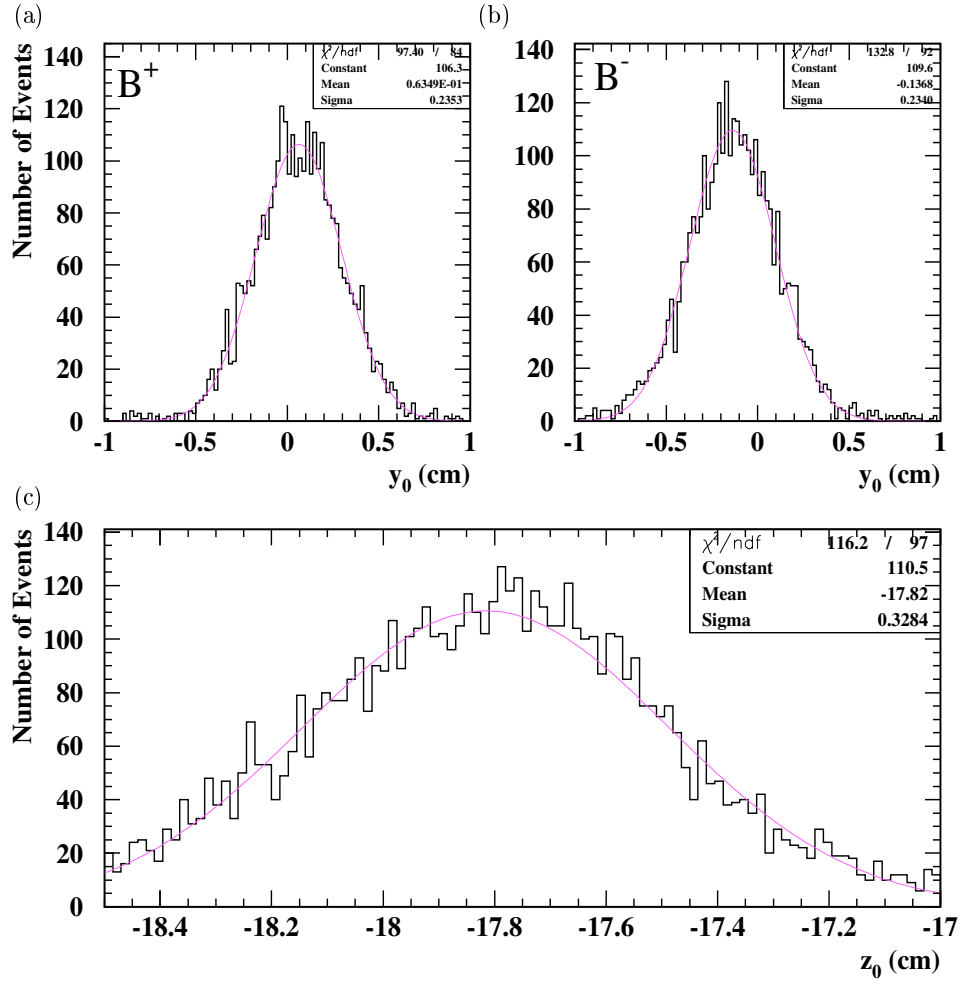


Figure 3.5: y_0 and z_0 defined by the direct V^0 method: a Gaussian fit has been made to each plot. y_0 is field dependent and therefore its value has been calculated in both the (a) B^+ and (b) B^- polarities. (c) z_0 is field independent and therefore only one value has been calculated for both field polarities.

been obtained for both field directions. The value of z_0 is not field dependent and

therefore the z_0 plot is for both polarities. All of the fits made in figure 3.5 fit the data well, indicated by the fact that the chi-squared per degree of freedom values, χ^2/ndf , are all ~ 1 . The mean value of z_0 is consistent with the SV database value of $z_0 = -17.85$ cm. Figure 3.6 shows $xtarg$ obtained from the direct V^0 analysis and

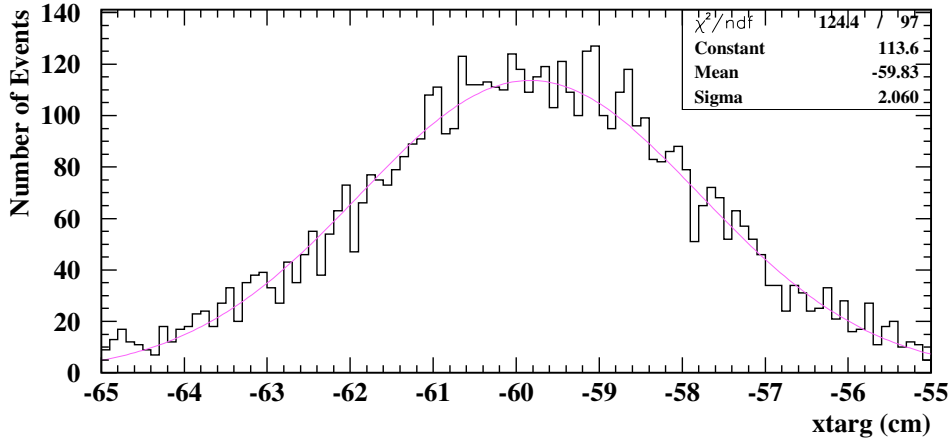


Figure 3.6: $xtarg$ defined by the direct V^0 method, a Gaussian fit has been made to the plot.

confirms that $xtarg$ is centred on the SV database value of $x = -60$ cm. A summary of all the values obtained from the direct V^0 analysis and used in the remainder of this thesis are given in table 3.1.

Table 3.1: Summary of the centred positions of $xtarg$, y_0 and z_0 , verified by the direct V^0 analysis

Coordinate	Value (cm)	
$xtarg$	-60.0	
y_0	0.06 (B^+)	-0.14 (B^-)
z_0 (= $ztarg$)	-17.85	

3.7 Separating V^0 Candidates into Λ , $\bar{\Lambda}$ and K_S^0 Candidates

The V^0 candidates identified in section 3.4 can be further subdivided into possible Λ , $\bar{\Lambda}$ and K_S^0 candidates, whose detectable decay modes are:

$$\Lambda \rightarrow p \pi^- \quad (3.1)$$

$$\bar{\Lambda} \rightarrow \bar{p} \pi^+ \quad (3.2)$$

$$K_S^0 \rightarrow \pi^- \pi^+ \quad (3.3)$$

This can be done by applying the following two selection criteria.

3.7.1 The Armenteros-Podolanski Plot

Λ , $\bar{\Lambda}$ and K_S^0 particles can be selected from the V^0 candidates by the use of an Armenteros-Podolanski plot [88] which plots q_T against α . q_T is defined as the transverse momentum component of either of the V^0 decay particles relative to the direction of the V^0 (as by conservation of momentum both are the same) and α is defined as

$$\alpha = \frac{q_L^+ - q_L^-}{q_L^+ + q_L^-} \quad (3.4)$$

where q_L^+ and q_L^- are the longitudinal momentum components of the positive and negative decay tracks respectively relative to the direction of the V^0 . α measures the momentum asymmetry in the decay.

Figure 3.7 shows an Armenteros-Podolanski plot for the 1999 p-Be data set, from which three distinct half ellipses (bands) can be seen. The largest ellipse, that of the K_S^0 band, is centred about $\alpha = 0.0$ as its decay particles are two pions which have the same mass and hence will carry similar momenta. The centres of the Λ and $\bar{\Lambda}$ bands are shifted to $\alpha = 0.7$ and $\alpha = -0.7$ respectively due to the asymmetry

between the masses of the decay particles. The proton, therefore, carries most of the momentum of the Λ in the decay $\Lambda \rightarrow p\pi^-$, and the antiproton carries most of the momentum in the decay $\bar{\Lambda} \rightarrow \bar{p}\pi^+$. A fuller description of the many features of an Armenteros-Podolanski plot can be found in appendix C.

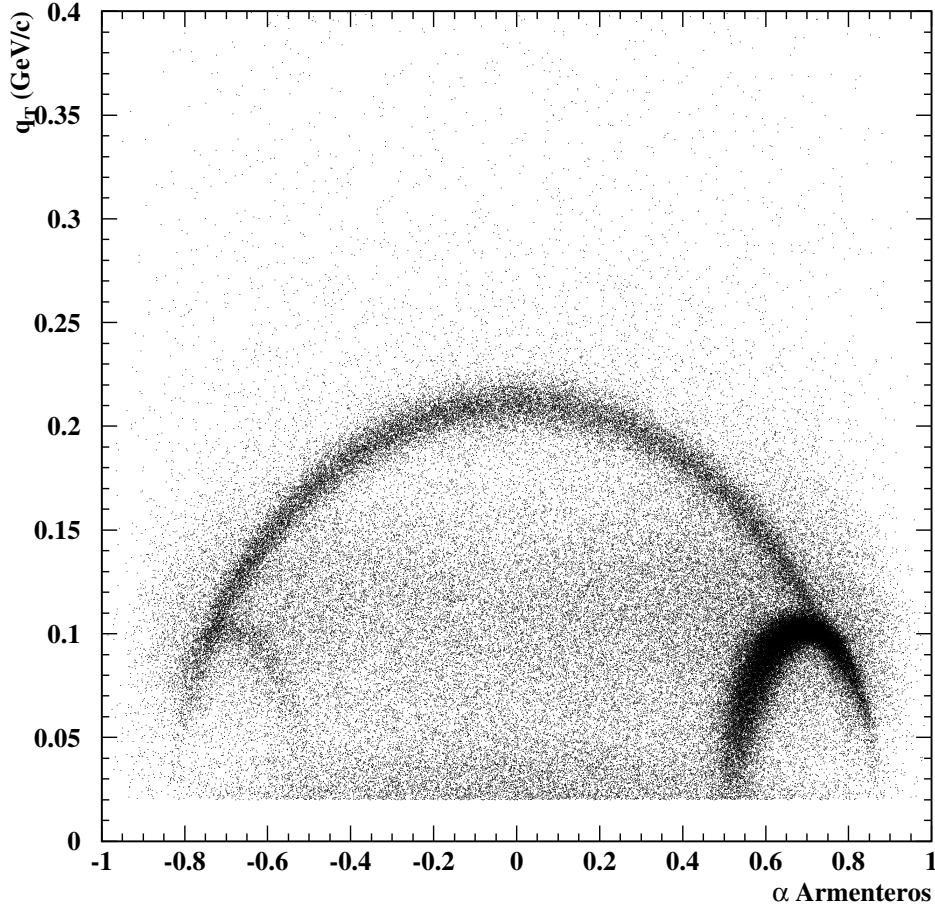


Figure 3.7: The Armenteros-Podolanski Plot for the 1999 p-Be data. Three distinct $\frac{1}{2}$ ellipses (bands) can be seen. Each band corresponds to a different particle species. The left hand band corresponds to $\bar{\Lambda}$ s, the right hand band to Λ s and the larger central band to K_S^0 s.

The three particles Λ , $\bar{\Lambda}$ and K_S^0 can thus be separated out by making appropriate alpha selections. Of interest here are the Λ and $\bar{\Lambda}$ selections which were chosen to be $\alpha > 0.45$ for Λ s and $\alpha < -0.45$ for $\bar{\Lambda}$ s. It is clear from figure C.2 that these selections will accept all potential Λ and $\bar{\Lambda}$ candidates.

A selection on q_T was also made of $0.02 \text{ GeV}/c < q_T < 0.4 \text{ GeV}/c$. The lower

limit q_T selection was made to remove any background γ conversion events (in a γ conversion event an e^-e^+ pair is resultant which has little or no q_T). The upper limit removed the few candidates with a q_T much greater than the theoretical predictions given in appendix C.

3.7.2 The K_S^0 Mass Selection

In the regions defined by the Armenteros alpha selections containing the Λ and $\bar{\Lambda}$ candidates, unwanted K_S^0 candidates remain. These are removed by an appropriate K_S^0 ‘mass’, $m(K_S^0)$, selection, as shown for the $\bar{\Lambda}$ candidates in figure 3.8. Before considering this figure in detail it is worth noting that the ‘mass’ of a V^0 , m_v , in this thesis (unless otherwise stated) refers to the *invariant* (or *effective*) mass obtained from the properties of the two resultant charged decay particles:

$$m_v^2 = m_1^2 + m_2^2 + 2(E_1E_2 - \vec{p}_1 \cdot \vec{p}_2) \quad (3.5)$$

where $m_{1,2}$, $E_{1,2}$ and $\vec{p}_{1,2}$ are the PDG mass [6], energy and momentum respectively of decay particles 1 and 2 in the laboratory frame. (3.5) comes about as a result of the famous relativistic equation $E^2 = \vec{p}^2 + m^2$.

Figure 3.8a shows the distribution of $\bar{p}\pi^+$ mass versus $\pi^-\pi^+$ mass. A distinct horizontal band of $\bar{\Lambda}$ candidates and a vertical band of K_S^0 candidates can be seen. A selection of $m(K_S^0) < 0.49$ GeV or $m(K_S^0) > 0.52$ GeV was made. This was chosen so as to remove the dense vertical band of K_S^0 candidates: a looser selection would remove too many $\bar{\Lambda}$ candidates, a tighter selection would leave a lot of unwanted K_S^0 candidates. Figure 3.8b shows the $\bar{\Lambda}$ mass plot (unshaded) with all selections, scaled to and superimposed on the mass peak (shaded) of the $\bar{\Lambda}$ signal with all selections except $m(K_S^0)$. The shaded regions which can be seen represents the effectiveness of the selection and allows one to see that more background than signal has been removed, especially at the high mass edge of the signal. Figure 3.8c confirms this by

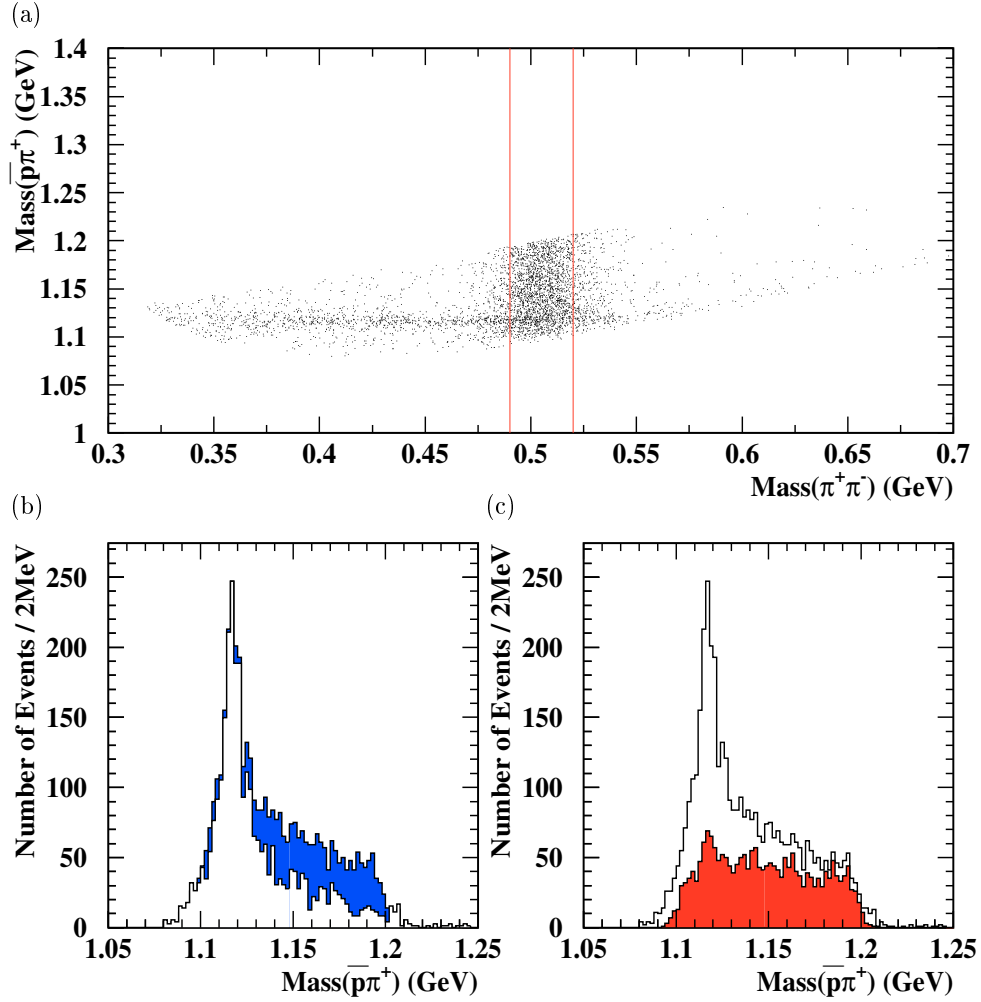


Figure 3.8: (a) $\bar{p}\pi^+$ versus $\pi^+\pi^-$ mass, with all selections except the K_S^0 mass selection, (b) antilambda mass with all selections, scaled to, and superimposed on the mass signal without the K_S^0 selection, the shaded area is what is removed. (c) What has been removed with the K_S^0 selection (shaded) superimposed on the mass signal without the K_S^0 selection.

showing what has been removed with the $m(K_S^0)$ selection (shaded) superimposed on the signal containing all selections (unshaded).

3.8 Further Selection Criteria

Once the V^0 candidates have been identified as possible Λ , $\bar{\Lambda}$ and K_S^0 candidates, additional selection criteria can be applied based on their particular decay parameters in order to remove further unwanted background candidates. The selections applied to the Λ candidates should be symmetrical to those of the $\bar{\Lambda}$ as the decay modes are the same, except charge conjugated [2]. However, as the Λ candidates are far more plentiful in comparison to the $\bar{\Lambda}$ sometimes a compromise is necessary on the tightness of the Λ selection so as not to remove many possible $\bar{\Lambda}$ candidates. For this reason the figures shown in this section are for the $\bar{\Lambda}$ as the ratio of background to signal is more critical for these candidates.

3.8.1 The x Decay Vertex

The x decay vertex of a V^0 (xvc) is defined as the point along the x -axis at which the V^0 decays into two charged tracks, as shown in figure 3.9. A plot of $\bar{p}\pi^+$ mass

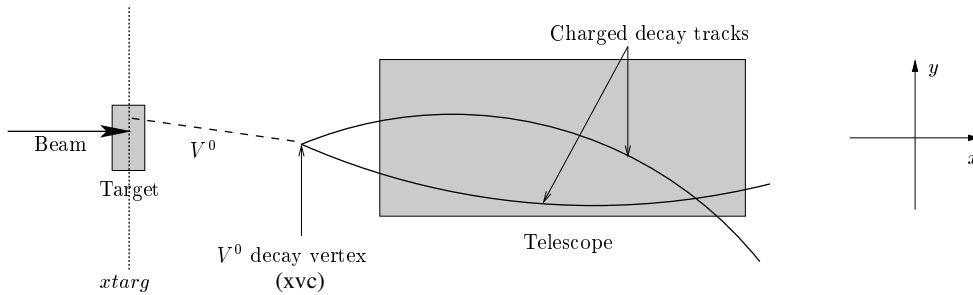


Figure 3.9: The definition of xvc : the point along the x -axis (in the GOLIATH reference system) at which the V^0 decays into two charged tracks.

versus xvc is shown in figure 3.10a. A selection of $-43 \text{ cm} < xvc < -27 \text{ cm}$ was

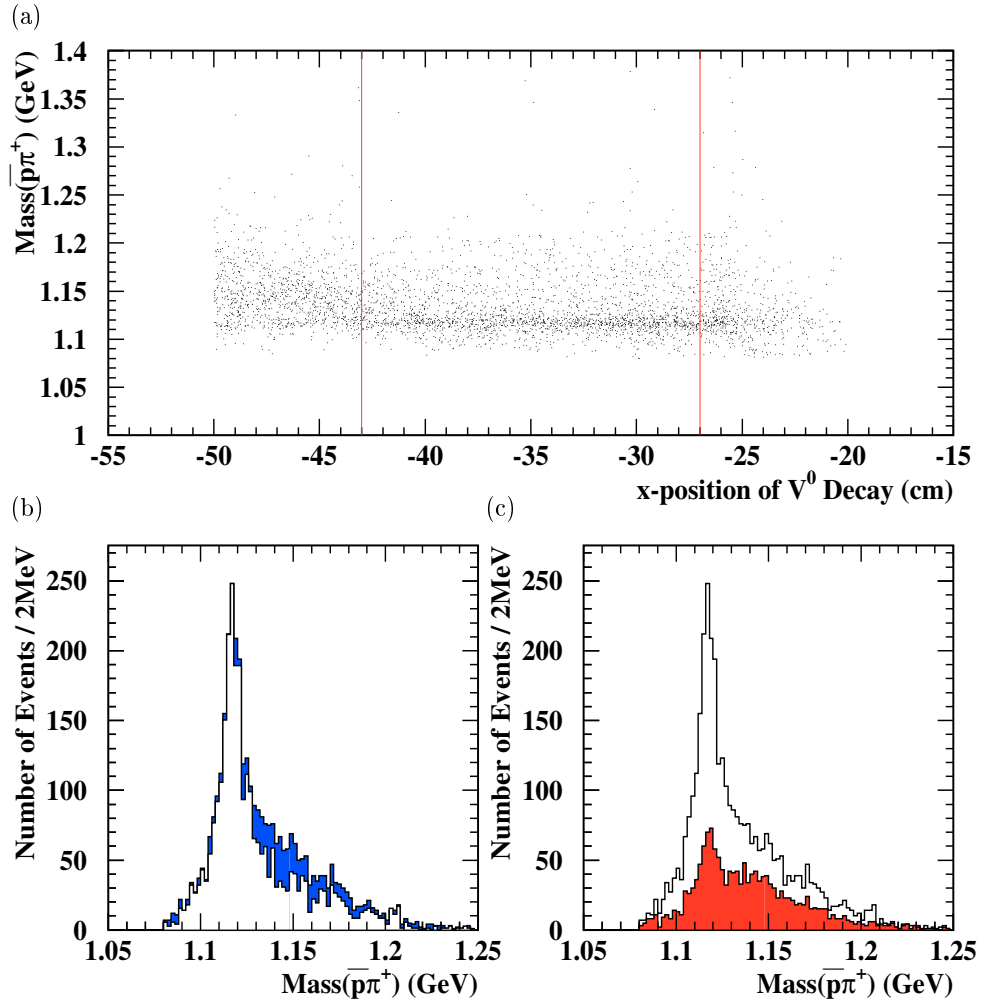


Figure 3.10: (a) $\bar{p}\pi^+$ mass versus x position of V^0 decay, with all selections except the xvc selection, (b) antilambda mass with all selections, scaled to, and superimposed on the mass signal without the xvc selection, the shaded area is what is removed. (c) What has been removed with the xvc selection (shaded) superimposed on the mass signal without the xvc selection.

made. The selection near the target ($xvc > -43$ cm) was made as the mass band is indistinct. This is because there is a high density of tracks near the target as at this point they have not been swept out by the magnetic field, therefore in this region there is a high probability of combinatorial background. A further selection was made near the telescope ($xvc < -27$ cm) removing interactions between the *SPH1* and *SPH2* scintillators. Figure 3.10b shows the $\bar{\Lambda}$ mass plot (unshaded) with all selections, scaled to and superimposed on the mass peak (shaded) of the $\bar{\Lambda}$ signal with all selections except xvc . The shaded regions which can be seen represents the effectiveness of the selection and allows one to see that more background than signal has been removed, especially at the high mass edge of the signal. Figure 3.10c confirms this by showing what has been removed with the xvc selection (shaded) superimposed on the signal containing all selections (unshaded).

3.8.2 The B_y Parameter of the V^0

The B_y parameter of the V^0 (byv) is defined as the distance in y in a vertical ($y-z$) plane, with x value fixed to $xtarg$, between the nominal centre of the beam profile, y_0 , and the intersection of the plane with the line of flight of the V^0 , i.e. the line drawn back from the V^0 vertex along the momentum vector. The definition of byv can be seen clearly in figure 3.11. The distribution is expected to be centred about

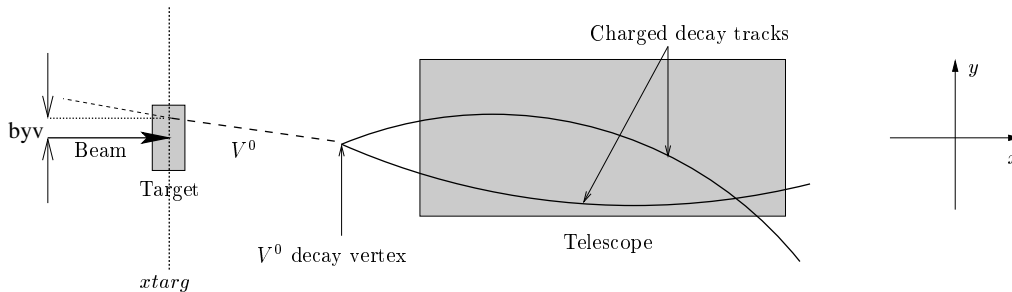


Figure 3.11: The definition of byv : the distance in y in a vertical ($y-z$) plane, with x value fixed to $xtarg$, between the nominal centre of the beam profile, y_0 , and the intersection of the plane with the line of flight of the V^0 .

$byv = 0$ since the most likely place a V^0 will originate is from the centre of the beam. However, as the beam has a finite width, it is possible for $|byv| > 0$. Figure 3.12a shows the distribution of $\bar{p}\pi^+$ mass versus byv . A fairly tight symmetrical selection of $-0.6 \text{ cm} < byv < 0.6 \text{ cm}$ was made. Figure 3.12b shows the $\bar{\Lambda}$ mass plot (unshaded)

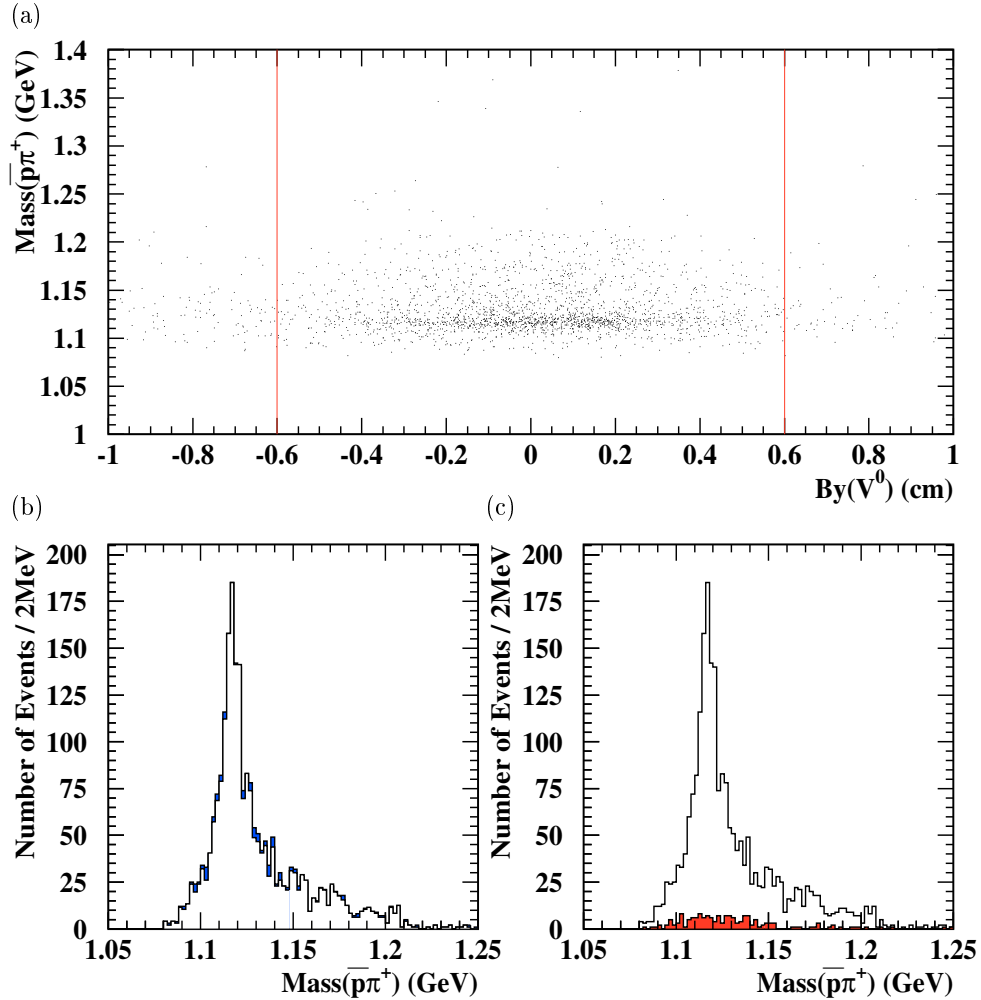


Figure 3.12: (a) $\bar{p}\pi^+$ mass versus the B_y parameter of the V^0 , with all selections except the byv selection, (b) antilambda mass with all selections, scaled to, and superimposed on the mass signal without the byv selection, the shaded area is what is removed. (c) What has been removed with the byv selection (shaded) superimposed on the mass signal without the byv selection.

with all selections, scaled to and superimposed on the mass peak (shaded) of the $\bar{\Lambda}$ signal with all selections except byv . The shaded regions which can be seen represents the effectiveness of the selection. Figure 3.12c shows what has been

removed with the byv selection (shaded) superimposed on the signal containing all selections (unshaded). Results from these latter two plots, show a slight removal of background either side of the mass peak, at the expense of minimal signal. Although a harsher selection would be desirable, it would remove more of an already limited supply of $\bar{\Lambda}$ s. In addition, by application of the same tighter selection to the Λ data would result in a much higher loss of Λ signal over combinatorial background.

3.8.3 The B_y Parameter of the Charged Tracks

Similarly to byv the B_y parameter of the charged tracks is the distance in y in a vertical ($y-z$) plane, with x fixed to $xtarg$, between the nominal centre of the beam profile, y_0 , and the intersection of the plane with the curvature of flight of each of the charged tracks. This definition can be seen clearly in figure 3.13. Because the p and \bar{p} carry most of the V^0 s momentum they are expected to bend less in the magnetic field than the π^+ and π^- and so $B_y(p) < B_y(\pi)$. In reality selections on these parameters made little difference in removing the background and so no selection on these parameters was made. The $B_y(p)$ and $B_y(\pi)$ distributions are seen in figure 3.14.

3.8.4 The V^0 Internal Decay Angle

The V^0 internal decay angle (ϕ) is not defined in the coordinate system x, y, z used thus far, but in a coordinate system of the V^0 ; x', y', z' . x' is defined as the direction of the V^0 , y' is perpendicular to x' and is in the bending ($x-y$) plane. z' is perpendicular to both x' and y' and forms an orthogonal right-handed system. In this coordinate system the decay particles come off back-to-back in the $y'-z'$ plane so as to conserve momentum. The angle at which either particle makes, when projected onto the $y'-z'$ plane, with the y' axis is the ϕ angle, as shown in figure 3.15.

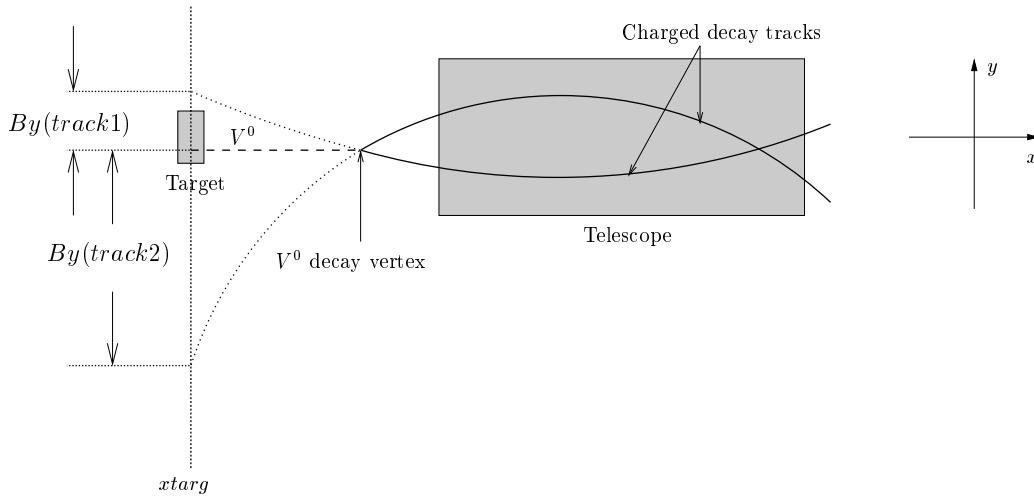


Figure 3.13: The definition of the B_y parameters of the charged tracks: the distance in y in a vertical ($y-z$) plane, with x value fixed to x_{targ} , between the nominal centre of the beam profile, y_0 , and the intersection of the plane with the curvature of flight of each of the charged tracks.

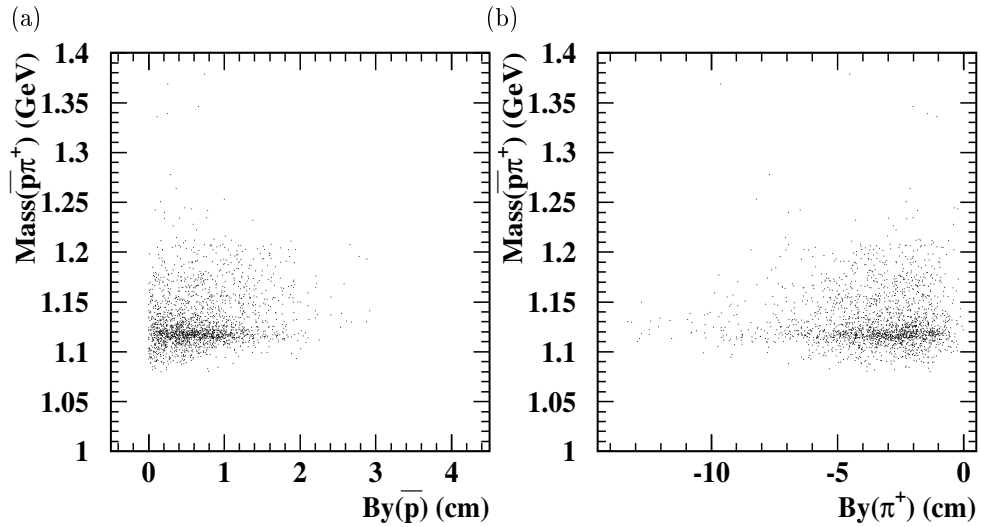


Figure 3.14: $\bar{p}\pi^+$ mass versus the B_y parameter of each of the charged decay tracks, with all other selections applied.

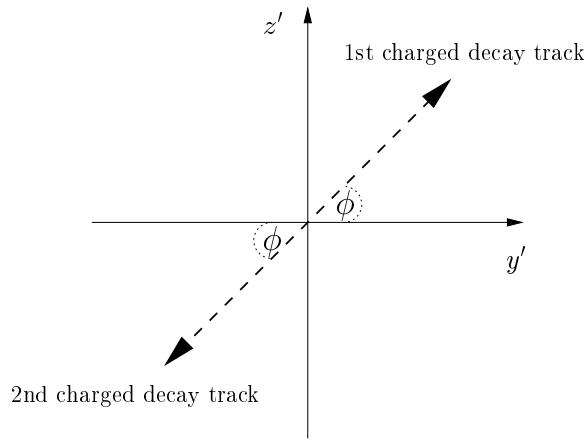


Figure 3.15: The two charged decay tracks come off back-to-back. The angle at which either particle, when projected onto the $y' - z'$ plane, makes with the y' axis is the ϕ angle

Figure 3.16 shows what happens in the $x' - z'$ plane in each of the two extreme cases: when ϕ is 0° the two charged decay tracks both come off completely in the $x' - y'$ plane (i.e. no component in the z' direction) as shown in figure 3.16a. Conversely, when ϕ is 90° the decay tracks come off completely in the $x' - z'$ plane (i.e. no component in the y' direction) at a finite angle to one another as shown in figure 3.16b. Now, the decay tracks of real V^0 s will be emitted at all angles of ϕ , whereas random tracks resultant from combinatorial background that form ‘fake’ V^0 s are most likely to be emitted with a small ϕ angle in order to be detected by the telescope. Thus, by making a selection to remove candidates with a small ϕ will be effective in the removal of unwanted combinatorial background.

Figure 3.17a shows the distribution of $\bar{p}\pi^+$ mass versus the ϕ angle, from which an appropriate selection of $-0.1 \text{ rad} < \phi < 0.1 \text{ rad}$ was made. Figure 3.17b shows the $\bar{\Lambda}$ mass plot (unshaded) with all selections, scaled to and superimposed on the mass peak (shaded) of the $\bar{\Lambda}$ signal with all selections except ϕ . Figure 3.17c shows what has been removed with the ϕ selection (shaded) superimposed on the signal containing all selections (unshaded). These latter two plots show that although signal is lost, a fairly constant amount of combinatorial background across the entire

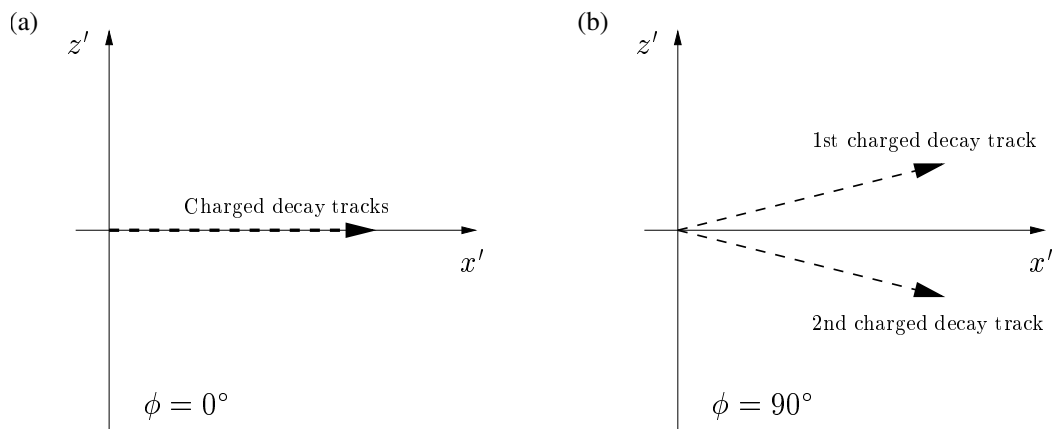


Figure 3.16: The decay geometry in the $x' - z'$ plane with the ϕ angle at two extremes: (a) $\phi = 0^\circ$ and (b) $\phi = 90^\circ$. In (a) the two charged tracks are superimposed as they are both in the $x' - y'$ plane, in (b) the two charged tracks come off in different directions as they are both in the $x' - z'$ plane.

mass range has also been removed, making the selection effective.

3.9 Summary of Λ and $\bar{\Lambda}$ Selection Criteria

Given here is a summary of the selection criteria V^0 candidates have to fulfil in order to be classified as a Λ or $\bar{\Lambda}$ candidate. Where the values between Λ and $\bar{\Lambda}$ candidates differ the $\bar{\Lambda}$ values are shown in brackets.

- The run number of the V^0 must be greater or equal to 7100
- The V^0 decay must have cowboy topology
- The closest approach of the decay tracks must be less than 0.1 cm
- Both decay tracks must pass through $SPH1$ and $SPH2$
- One decay track must pass through $ST2$
- $xtarg$ must be greater than -75 cm

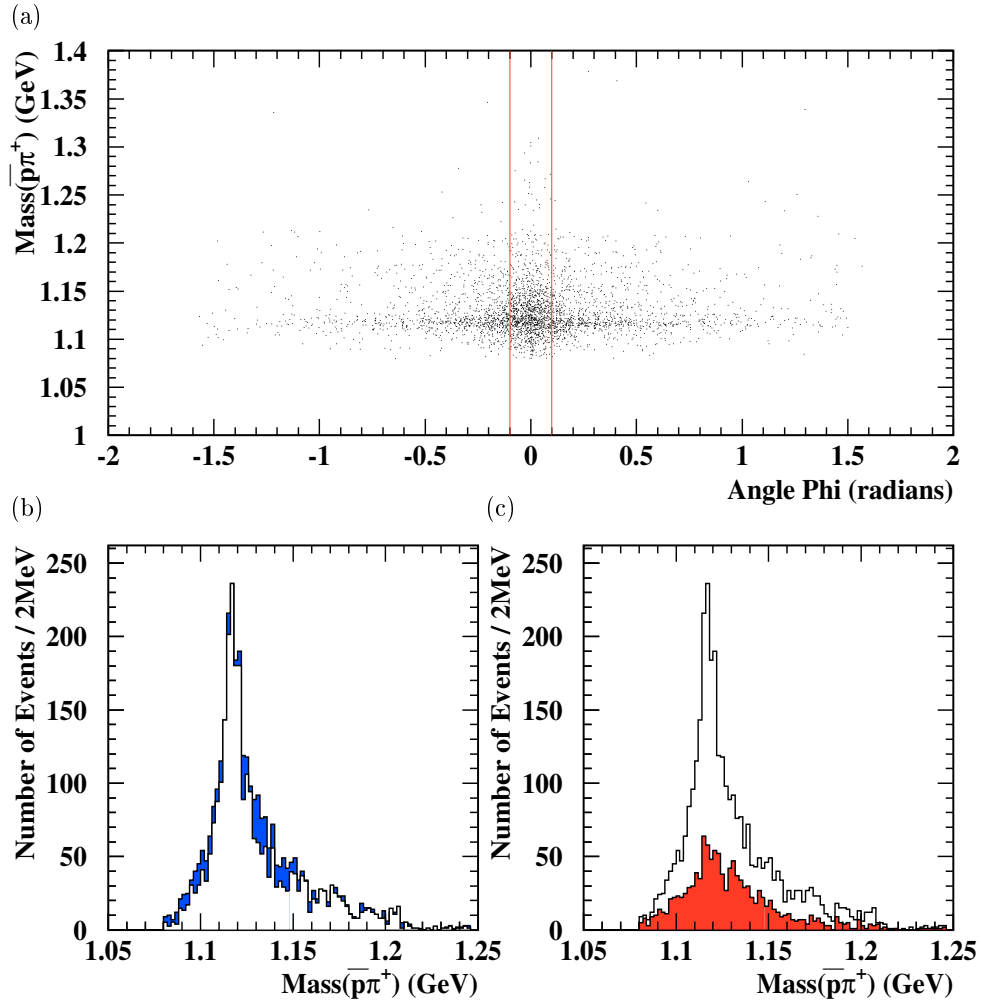


Figure 3.17: (a) $\bar{p}\pi^+$ mass versus the phi angle, with all selections except the ϕ selection, (b) antilambda mass with all selections, scaled to, and superimposed on the mass signal without the ϕ selection, the shaded area is what is removed. (c) What has been removed with the ϕ selection (shaded) superimposed on the mass signal without the ϕ selection.

- Armenteros alpha must be greater than 0.45 (less than -0.45)
- q_T must be greater than 0.02 GeV/c and less than 0.4 GeV/c
- The K_S^0 mass must be less than 0.49 GeV or greater than 0.52 GeV
- The x -decay vertex must be greater than -43 cm and less than -27 cm
- The byv parameter must be greater than -0.6 cm and less than 0.6 cm
- The V^0 internal decay angle must be less than -0.1 rad or greater than 0.1 rad

Figure 3.18 shows the mass signals for the Λ and $\bar{\Lambda}$ with all of the selection criteria, summarised above, implemented. In all, 15,689 Λ and 2,117 $\bar{\Lambda}$ candidates have been identified. The background beneath the $\bar{\Lambda}$ signal could perhaps have been reduced further by tightening some of the selections outlined above; however in doing so further signal would have been lost, outweighing the advantage of tightening these selections up.

3.10 Gold-Plated Λ and $\bar{\Lambda}$ Samples

Once all the selection criteria outlined in the previous section have been decided upon, one further selection is applied: a Λ (or $\bar{\Lambda}$) mass selection. This selection is applied to remove candidates with very low or very high Λ (or $\bar{\Lambda}$) effective mass values compared to that of the mean. The mass selection was determined by fitting a Gaussian distribution to the Λ signal of figure 3.18a. The accepted region of the signal was those candidates within $\pm 3\sigma$ of the mean. This equates to a final selection criterion of:

- The Λ mass must be greater than 1.103 GeV and less than 1.131 GeV

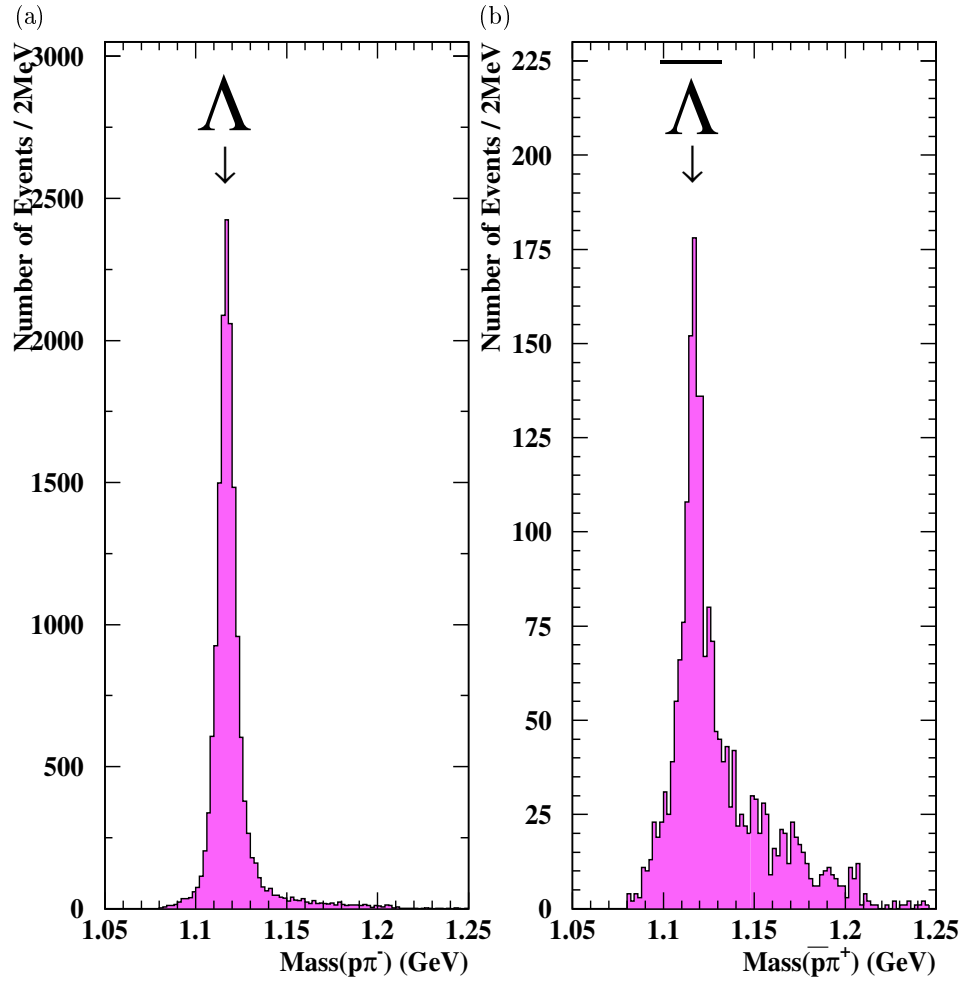


Figure 3.18: (a) Λ and (b) $\bar{\Lambda}$ mass signals with selection criteria applied.

The same mass selection was applied to the $\bar{\Lambda}$ candidates.

When the mass selection has been made (in addition to those selections in the previous section) the samples are said to be ‘gold-plated’. Figure 3.19 shows the gold-plated signals, the number of gold-plated candidates are given in table 3.2. It is these selected gold-plated candidates which are used in the following chapter.

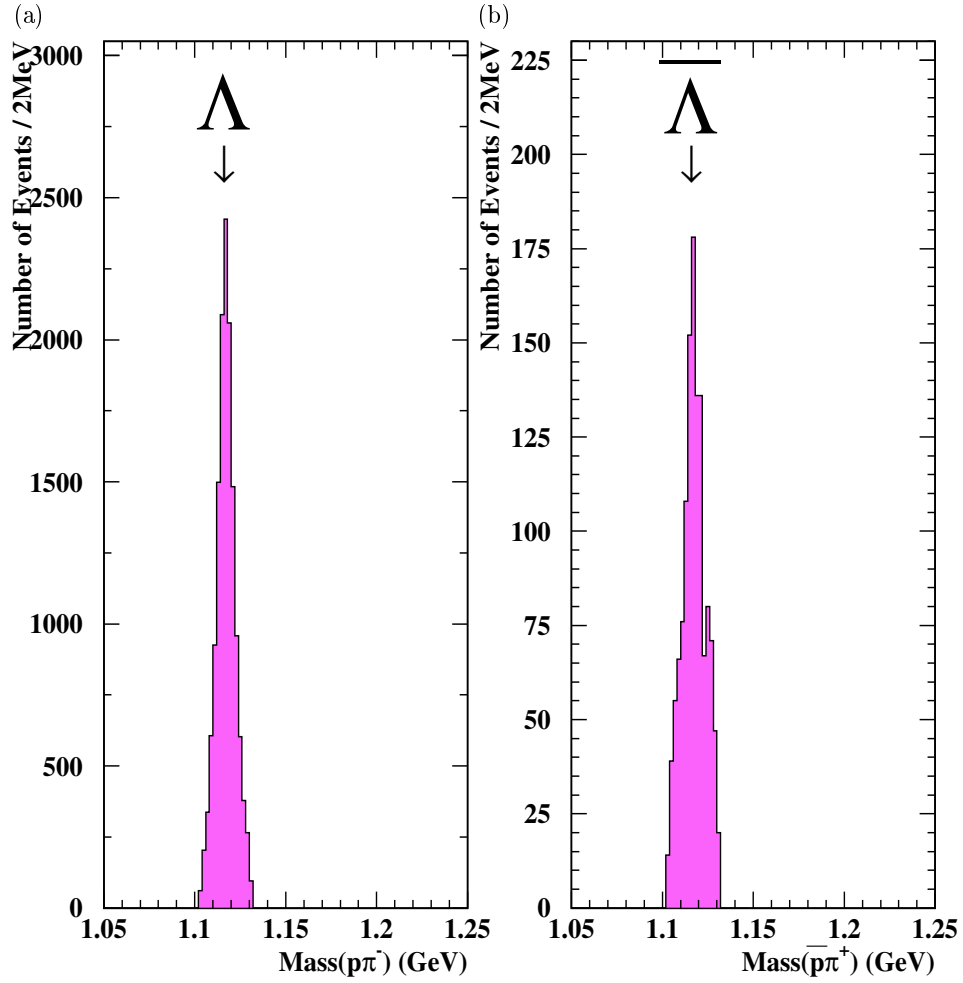


Figure 3.19: Gold-Plated (a) Λ and (b) $\bar{\Lambda}$ mass signals.

Table 3.2: Summary of the number of gold-plated Λ and $\bar{\Lambda}$ candidates found.

Candidate	Number found
Λ	13,991
$\bar{\Lambda}$	1,245

3.11 Estimation of the Combinatorial Background Beneath the $\bar{\Lambda}$ Signal

The selection criteria outlined in the previous sections have created a very ‘clean’ Λ signal and a much improved $\bar{\Lambda}$ signal. However, as can be seen from the tails in figure 3.18b, a non-negligible amount of combinatorial background still exists beneath the $\bar{\Lambda}$ signal. Two different methods have been employed to estimate the extent and shape of this remaining combinatorial background. The first method is a simpler method which makes use of a number of assumptions about the clean Λ and $\bar{\Lambda}$ signals, the second method is more sophisticated and makes use of a fitting program. The two methods are described in detail in the following two subsections.

3.11.1 Comparing the Clean Λ and $\bar{\Lambda}$ Signals

The first method to estimate the combinatorial background beneath the $\bar{\Lambda}$ signal makes use of the ‘clean’ Λ signal, with the near-accurate assumption that the combinatorial background beneath this signal, as seen in figure 3.18a is negligible.

By looking at the shape of the $\bar{\Lambda}$ signal in the regions which were removed by the mass selection (section 3.10), an estimation of the peak of the background beneath the $\bar{\Lambda}$ signal was made, this is shown as dimension “a” in figure 3.20a. Subtracting this value from the $\bar{\Lambda}$ mass peak gave the number of ‘real’ $\bar{\Lambda}$ candidates in the $\bar{\Lambda}$ mass peak, dimension “b” in figure 3.20a (the remainder being combinatorial background).

The number of candidates in the Λ peak was scaled down to the number of real $\bar{\Lambda}$ candidates in the $\bar{\Lambda}$ peak. The scaled Λ signal was then subtracted from that of the $\bar{\Lambda}$ signal: the remaining signal is the combinatorial background beneath the $\bar{\Lambda}$ signal. A polynomial fit has been made to the combinatorial background signal, which had the form:

$$N = (-3.33 + 11.3m - 14.3m^2 + 8.01m^3 - 1.69m^4) \times 10^6 \quad (3.6)$$

where N is the number of background candidates and m is the mass of the $\bar{\Lambda}$ within the range $1.085 \text{ GeV} < m < 1.225 \text{ GeV}$

The estimation of the combinatorial background peak beneath the $\bar{\Lambda}$ signal was varied until a value was chosen which allowed a satisfactory polynomial fit to be made. Figure 3.20b shows the $\bar{\Lambda}$ signal with the combinatorial background superimposed (shaded region). The polynomial fit described by (3.6) is also shown. It can be seen that both the background and fit seem reasonable. The number of combinatorial background candidates within the $\pm 3\sigma$ of the mean (section 3.10) region were counted (437 candidates) and compared to the number of gold-plated $\bar{\Lambda}$ s in table 3.2. From which the background under the $\bar{\Lambda}$ signal within the mass selection region was determined to be 35%, that within the signal tails was determined to be 88%.

3.11.2 Fitting a Combinatorial Background to the $\bar{\Lambda}$ Signal

The second method to estimate the combinatorial background beneath the $\bar{\Lambda}$ signal makes use of the CENTKK program [89] which is a chi-squared, χ^2 , minimisation program based on MINUIT [90] which produces a fit normalised to the same area as the $\bar{\Lambda}$ signal.

The overall function, $f(m)$, that is fitted consists of two parts: a function to describe the $\bar{\Lambda}$ signal, $S(m)$, and one to describe the combinatorial background,

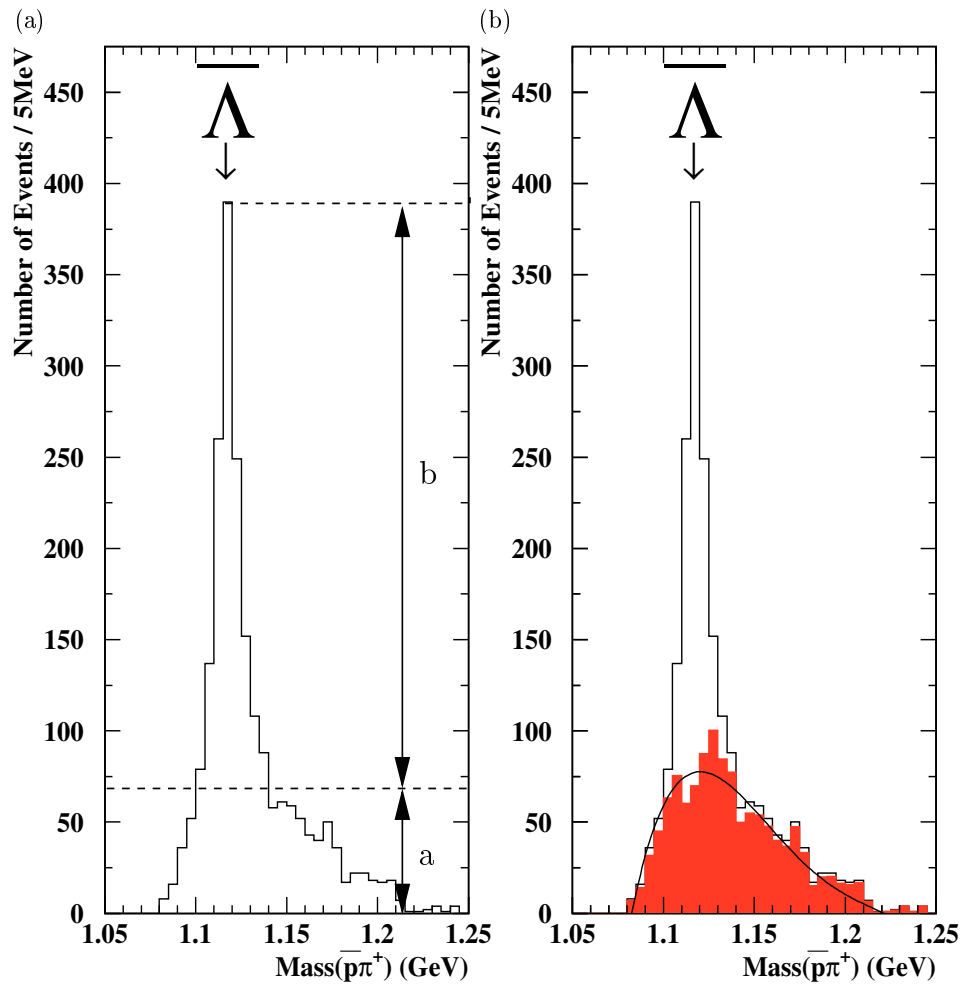


Figure 3.20: $\bar{\Lambda}$ mass signal with (a) important dimensions required for this method of background subtraction included and (b) estimated combinatorial background signal superimposed on top. To this latter signal a 4th degree polynomial fit has been made.

$B(m)$, beneath the $\bar{\Lambda}$ signal:

$$f(m) = R \times S(m) + (1 - R) \times B(m) \quad (3.7)$$

where R is the fraction of the total $\bar{\Lambda}$ signal which are ‘real’ $\bar{\Lambda}$ s.

$S(m)$ was chosen to be a Gaussian function of the form:

$$S(m) = A e^{-\left[\frac{(m-\mu)^2}{2\sigma^2}\right]} \quad (3.8)$$

where μ is the mean mass of the Gaussian, σ characterises the width of the signal and A is a normalisation constant.

$B(m)$ was chosen to have the form:

$$B(m) = (m - m_{th})^{(b_1+b_2m)} \times e^{(b_3m+b_4m^2)} \quad (3.9)$$

where m_{th} is the threshold mass and b_1 , b_2 , b_3 and b_4 are constants. This function is known as a ‘‘Granet’’ function and has been used in the past to describe combinatorial background, for example in the CERN WA102 experiment [91]. This function describes the combinatorial background well, with a rapid rise near m_{th} and a gentler fall off towards higher masses.

The CENTKK program is divided into three parts. Firstly the $\bar{\Lambda}$ signal is read into the program, along with initial estimates of the parameters R , μ , σ , b_1 , b_2 , b_3 and b_4 (all defined above). The second stage evaluates the χ^2 using these parameters. MINUIT then varies these starting parameters until ‘best fit’ values are obtained in which χ^2 is minimised. The third part of the program displays the fit using the ‘best fit’ values of R , μ , σ , b_1 , b_2 , b_3 and b_4 . These parameters are summarised in table 3.3 and the fit to the $\bar{\Lambda}$ signal is shown in figure 3.21. The function can be seen to fit the data well, both from figure 3.21 and statistically as the fit has a chi-squared per degree of freedom (χ^2/ndf) of 2.03.

The number of combinatorial background candidates beneath $B(m)$, within the $\pm 3\sigma$ of the mean (described in section 3.10) region, were counted (424 candidates)

Table 3.3: Parameters obtained from the CENTKK program which are used in the fit to describe the $\bar{\Lambda}$ signal. μ and σ are in GeV, the remaining parameters are constants and have no units.

Parameter	Value
R	0.430 ± 0.015
μ	1.117 ± 0.001
σ	$0.006 \pm 0.71 \times 10^{-8}$
b_1	600 (fixed)
b_2	$1.590 \pm 0.70 \times 10^{-8}$
b_3	$32.60 \pm 0.26 \times 10^{-7}$
b_4	$-32.75 \pm 0.49 \times 10^{-7}$

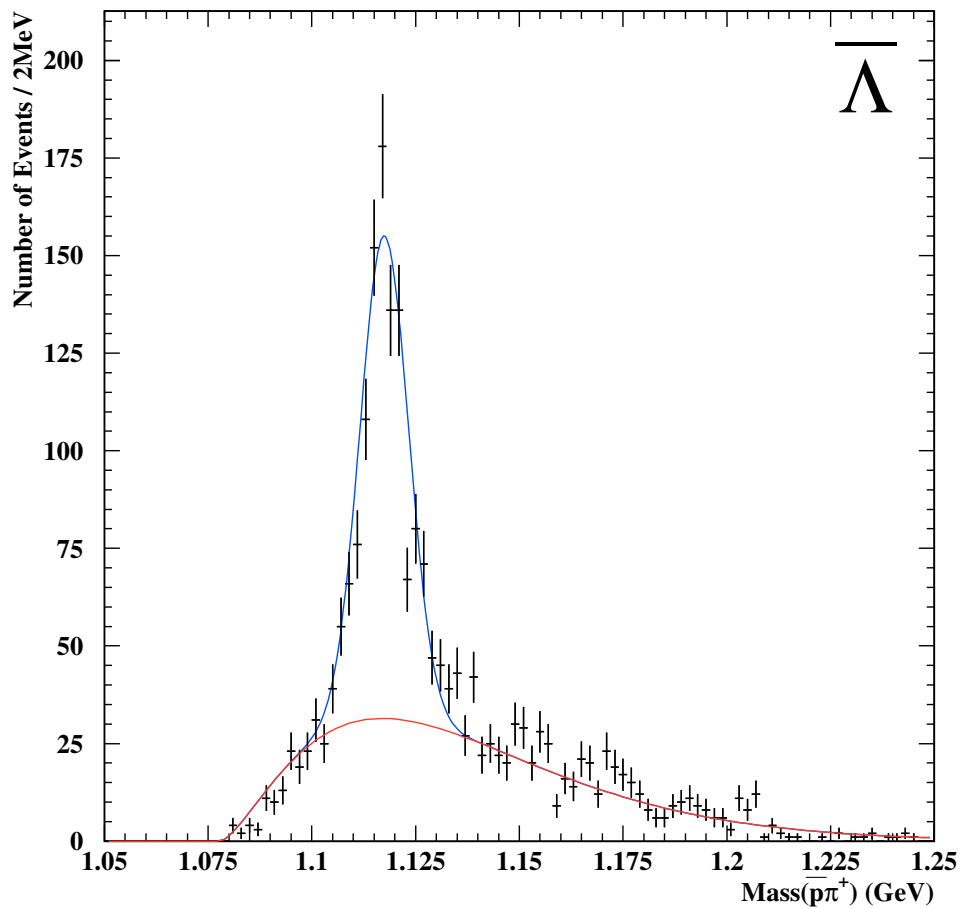


Figure 3.21: $\bar{\Lambda}$ mass signal with the Gaussian and Granet functions, scaled to the same area, superimposed on top

and compared to the number of gold-plated $\bar{\Lambda}$ s in table 3.2. From this the background under the $\bar{\Lambda}$ signal within the mass selection region was determined to be 34%.

The results from both methods provided consistent results for the fraction of the gold-plated $\bar{\Lambda}$ signal which was combinatorial background. As the latter method was more sophisticated and gave an estimate of the goodness of fit (χ^2/ndf) it is this result which will be used in the following chapter.

Chapter 4

Analysis of the Selected Λ and $\bar{\Lambda}$ Data

4.1 Introduction

In the previous chapter Λ and $\bar{\Lambda}$ candidates were selected from the reconstructed V^0 candidates obtained from the experimental data set. The number of ‘gold-plated’ candidates found for each particle type is shown in table 3.2, however for these (and other particle species) to be meaningfully compared, other factors need to be taken into account and corrected for [92]. These factors include geometric acceptance, detector efficiency, reconstruction efficiency, selection criteria and the fact that not all decay modes are detected by the experiment.

Geometric acceptance takes into account the fact that the telescope only accepts decay tracks over a small angle and so will not have detected all particles produced. The efficiency of the detector and reconstruction programs need to be taken into account as, although both are efficient, they are not 100% efficient. The choice of selection criteria needs to be accounted for, as although the selection criteria for V^0 s gets rid of most of the background, they also reduce some of the signal. This

effect needs to be corrected for in order to determine the actual number of particles produced in the sample. Finally the experiment is only able to detect charged decay tracks and so decay modes such as $\Lambda \rightarrow \pi^0 n$ cannot be detected by the experiment.

The correction to account for the above factors is made by assigning a ‘weight’ to each candidate. The weighted sample of candidates can then be used to calculate a ‘yield per interaction’ (referred to in the rest of this thesis simply as ‘yield’). Yields from all particle species in p–Be (as well as Pb–Pb) interactions can be compared for a given energy. Yields per wounded nucleon (number of nucleons involved in the collision, section 1.5.1) of strange and multistrange particles in Pb–Pb collisions are expected to be greater than in p–Be collisions if a transition to a QGP phase has occurred.

4.2 The Weighting Chain

The ‘weighting chain’ is a succession of stages required to assign a particular V^0 candidate with a ‘weight’. Each stage is described in some detail in this section.

4.2.1 Monte-Carlo Simulation

For each real V^0 candidate to be weighted a GEANT [93] simulation is performed to produce 5,000 ‘good’ (i.e. having decay tracks tracing through the telescope) Monte-Carlo particles of the required type, which then decay into two (or more) specified particles before reaching the planes of the telescope. The 5,000 particles generated are each of the same rapidity (y_{lab}) and transverse momentum (p_T) as the V^0 candidate being weighted and have primary vertices distributed in x across the entire target width. The generated V^0 s are decayed according to their lifetime across the range with a flat $\cos \theta^*$ distribution and a flat ϕ distribution (where θ^* is defined in appendix C and ϕ is the azimuthal angle). The decay products of each

V^0 are recorded as ‘hits’ in the pixel planes of the telescope, whose efficiencies have previously been measured and are taken into account in the simulation. Of course not every generated Monte-Carlo particle decays through the telescope, so GEANT continues generating (and decaying) particles until the number of good Monte-Carlo particles, N_{good} , (in this case 5,000) have been produced. The number of generated particles, N_{gen} , required to reach N_{good} is typically several tens of thousands. N_{good} is set at 5,000 so as to produce a weight with a reasonably small error.

The simulation has been set up to include the scintillators $SPH1$, $SPH2$, $ST2$ (placed in front and behind the compact part of the telescope) and $S4$ (upstream of the target), as shown in figure 2.2. $SPH1$, $SPH2$, $ST2$ are modelled as scintillator material $5 \times 5 \text{ cm}^2$ and of 1 cm thickness. Hadronic (as well as weak and electromagnetic) interactions are allowed to take place within the scintillator material. $S4$ is modelled as a $8 \times 8 \text{ mm}^2$ square of 1 cm thickness centred upon the beam. The simulation also takes into account absorption of neutral particles which might give V^0 s within the thick beryllium target. The proton beam has been given a realistic width in y and z characterised by $\sigma_y = 0.25 \text{ cm}$ and $\sigma_z = 0.50 \text{ cm}$. The beam profile was obtained from the CERN beam physicists, and is verified in section 4.3.

4.2.2 Background Mixing

The hits in the telescope from the decay particles of the 5,000 generated Monte-Carlo particles are then implanted into raw background data which come from events close to the run number in which the real particle was found. This is done using a program called MIXRAWMC. The background data originates from the real data set. As a by-product of the production, every n th event selected by the two track trigger (where n is typically 100) is stored as background data, irrespective of whether it contains a V^0 candidate or not.

4.2.3 Track Reconstruction

The output from background mixing is now in the same format as for the real data, and so, like the real data is passed through the ORHION track fitting program (described in section 3.4). The ORHION program reconstructs tracks from hits in the silicon pixel planes, including some of the decay tracks from Monte-Carlo generation.

4.2.4 V^0 Reconstruction

The ORHION output is then passed through the V^0 reconstruction program ANALYZE. The ANALYZE program finds V^0 candidates from the track pairs reconstructed by ORHION. The version of ANALYZE used is the same as that used for the real data and includes all the selection criteria, for the particle type being sought, used for the real data. If one of the Monte-Carlo particles is included in the output, it has passed successfully through the weighting chain.

4.2.5 Weight Calculation

The final stage of the weighting chain is the weight calculation. This is performed by the WGTCAL program which compares the output of the Monte-Carlo simulation with the output of ANALYZE. The weight is proportional to the number of events generated by GEANT (in order to get 5,000 ‘good’ candidates), N_{gen} , divided by the number which were found by ANALYZE, N_{found} . To obtain the true weight this fraction must be multiplied by a constant which is determined by the azimuthal angle coverage used for the generation of Monte-Carlo particles and accounts for the fact that the detector does not detect over 360° . The full equation is given in (4.1).

$$Weight = \frac{N_{gen}}{N_{found}} \times \frac{360}{(\phi_{max} - \phi_{min})} \quad (4.1)$$

Where 360 is the full 360° solid angle and ϕ_{max} and ϕ_{min} are the minimum and maximum angle (in degrees) over which the Monte-Carlo simulation generates events.

Once a gold-plated candidate has been assigned a weight, that candidate has successfully been corrected for reconstruction efficiency, geometrical acceptance, detector efficiency and choice of selection criteria.

4.3 The Weighted Λ and $\bar{\Lambda}$ Samples from the 1999 p–Be Data Set

A representative sample of gold-plated Λ candidates were weighted. The full statistics of the reconstructed gold-plated $\bar{\Lambda}$ hyperons were individually weighted. Enough of the much more abundant reconstructed gold-plated Λ sample were weighted to reach a statistical error better than the systematic error. Table 4.1 shows details of the samples used for weighting for the Λ and $\bar{\Lambda}$ candidates.

Table 4.1: Summary of the number of Λ and $\bar{\Lambda}$ candidates selected for weighting.

Candidate	Number of weighted candidates (% of full sample)	
Λ	4,662	(33%)
$\bar{\Lambda}$	1,245	(100%)

After weighting, a number of these candidates had to be discarded before further analysis was performed. This was because they were from runs in which details required to calculate the beam flux for that run were not satisfactory. The beam flux is of importance as it is required for the calculation of yields, as described in detail in section 4.6. Removing data from these runs did not affect the percentages quoted in table 4.1 because unweighted candidates from these runs were also removed.

Now, for the weighting procedure to be relied upon it is essential that the data obtained via the weighting chain simulation replicates the real data well. In order to assess this various distributions used in the selection criteria of the real data were compared. A sample of the simulated Λ data for both field polarities (black crosses) superimposed on the real gold-plated Λ data set (shaded region) for a few of these distributions are shown in figure 4.1. The areas of the simulated data have been scaled to those of the real data. There is generally a good correlation between the two, illustrating the Monte-Carlo simulation reproduces the real data well.

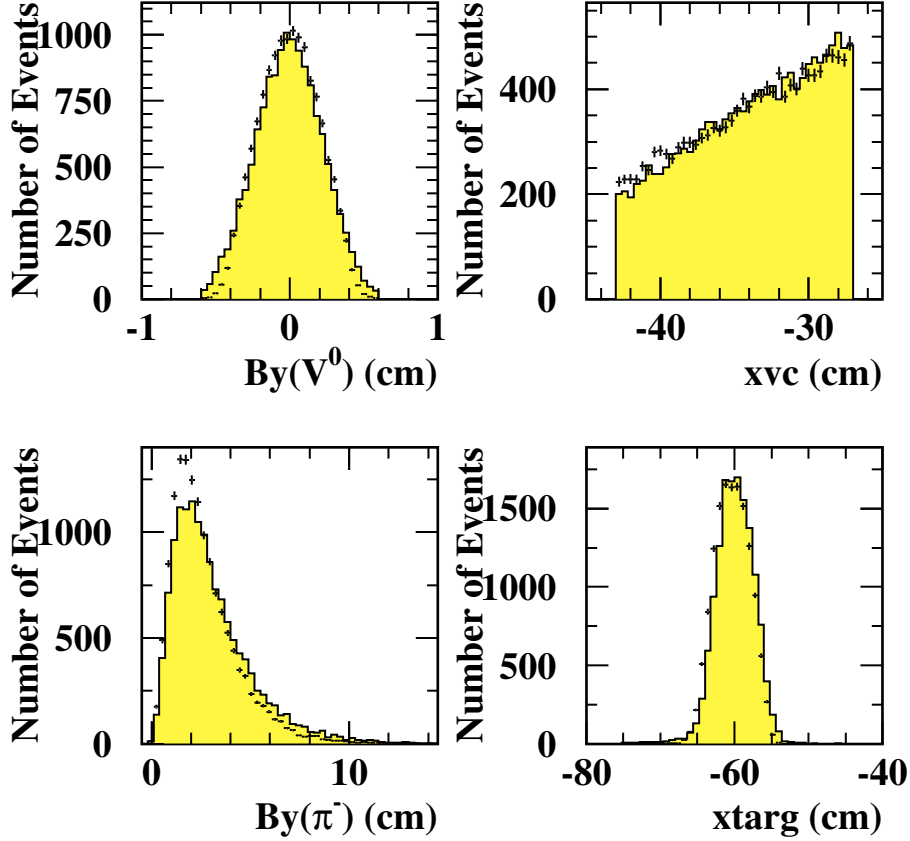


Figure 4.1: Comparison of simulated (crosses) to real (shaded region) Λ data on various distributions used in the selection criteria of the real data. The areas of the simulated data has been scaled to those of the real data.

An interesting example of requiring the Monte-Carlo simulation to reproduce the real data well is given for the beam spread of the proton beam. A sample of the

Λ candidates selected were weighted twice, firstly using a beam profile in GEANT which represents a line beam (in which $\sigma_y = \sigma_z = 0$ cm) and secondly using the beam profile obtained by the CERN beam physicists (given in subsection 4.2.1). Although most distributions shown in figure 4.1 are indifferent to this change, one distribution where the effect can be seen clearly is that of the B_y parameter of the V^0 . In figure 4.2a, the line beam profile is used, from which one can see the Monte-Carlo simulation is some way short of describing the real data. Using the correct beam profile, shown in figure 4.2b one can see that the Monte-Carlo simulation reproduces the real data well. As well as illustrating the importance of the Monte-

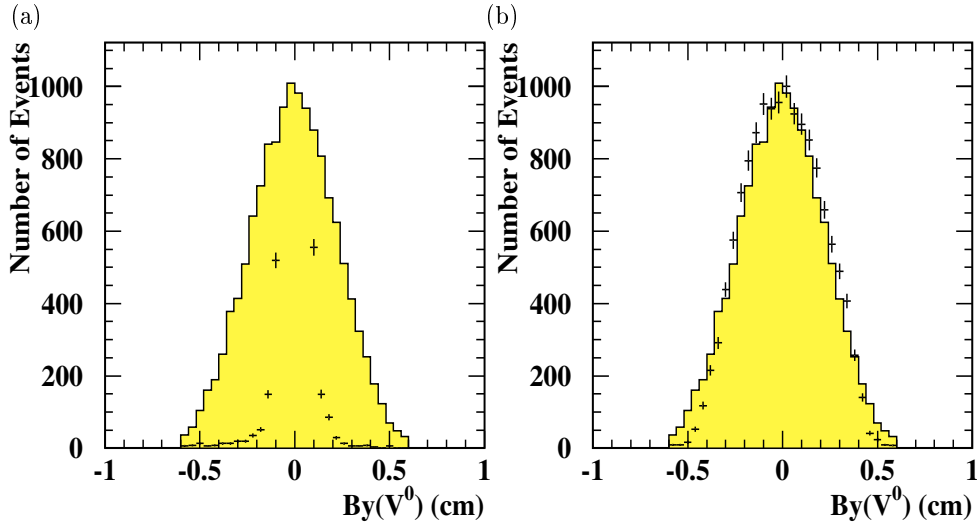


Figure 4.2: Comparison of simulated (crosses) to real (shaded region) data for a sample of the selected Λ candidates on the distribution of the B_y parameter of the V^0 using (a) a line beam and (b) the beam profile obtained by the CERN beam physicists. The areas of the simulated data has been scaled to those of the real data.

Carlo simulation reproducing the real data well, this example also verifies the beam profile obtained by the CERN beam physicists.

4.4 The Region of Good Acceptance

The weighted candidates can be projected onto a plot of p_T versus rapidity, where p_T and rapidity (explained in more detail in section 1.5) are the transverse momentum and rapidity, y , measured in the laboratory system, respectively, of the V^0 . This plot is shown in figure 4.3 for the weighted Λ and figure 4.4 for the weighted $\bar{\Lambda}$

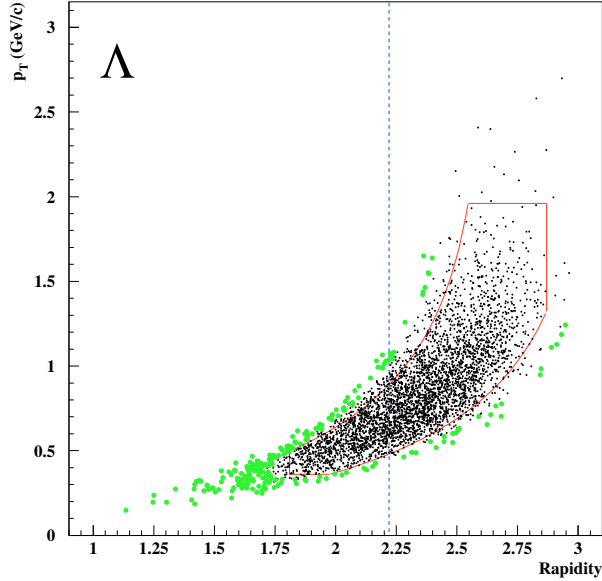


Figure 4.3: p_T versus rapidity for the weighted Λ candidates, with ‘low’ weights shown by black dots and ‘high’ weights by the larger lighter dots. The acceptance window is superimposed on top.

candidates. The distribution of points on these plots forms a characteristic shape which reflects the position and size of the telescope. The weights towards the edges of this shape are generally much higher than those within it because these candidates are at the limits of the detector acceptance.

To eliminate such candidates, which may give bad physics results the weighted data were subdivided into two groups: weights less than ten times the minimum weight (low weights) and weights greater than ten times the minimum weight (high weights). The former are shown in figures 4.3 and 4.4 as small dark dots, the latter as larger lighter dots. The high weight candidates were then removed by inserting

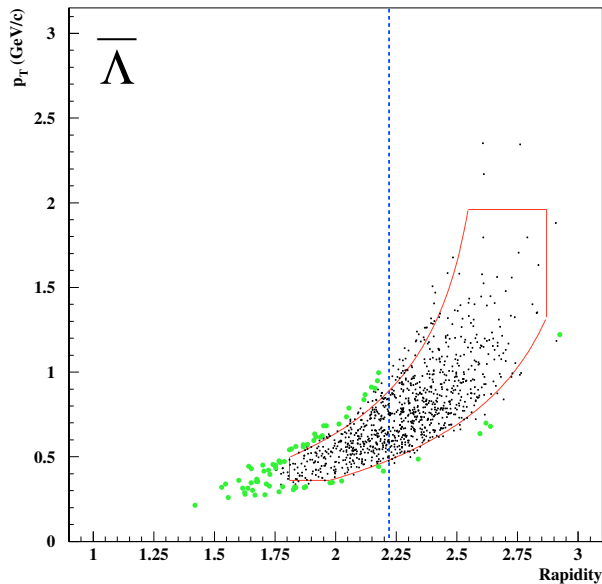


Figure 4.4: p_T versus rapidity for the weighted $\bar{\Lambda}$ candidates, with ‘low’ weights shown by black dots and ‘high’ weights by the larger lighter dots. The acceptance window is superimposed on top.

a window of good acceptance, which includes as many low weighted candidates as possible whilst excluding those with high weights.

The shape of this region of good acceptance is defined by an appropriate choice of $p_T(min)$, $p_T(max)$, $y(min)$, $y(max)$, $\theta(min)$, $\theta(max)$; where $\theta(min)$ and $\theta(max)$ are related to the angle of inclination of the telescope. The first four of these parameters define the top right and bottom left edges of the region. A value of $p_T(min)$ not equal to zero reflects the fact that the telescope is inclined above the beam line (described in section 2.4.3), $p_T(max)$ is chosen to overcome the problems of low statistics at high p_T . The lower curved region is defined by (4.2) and is characterised by $\theta(min)$

$$p_T = \frac{m \theta(min) \sinh(y)}{\sqrt{(1 - \theta(min)^2 \sinh^2(y))}} \quad (4.2)$$

where m is the mass of the V^0 . The derivation of (4.2) can be found in appendix D. The upper curved region is defined by replacing $\theta(min)$ with $\theta(max)$ in (4.2). The lower and upper curves represent the bottom and top edges of the telescope respectively. The resultant enclosed area is known as the *acceptance window* and can be seen in figures 4.3 and 4.4. It is the weights within this window which will be used

for the rest of the analysis. As the Λ and $\bar{\Lambda}$ candidates studied have the same decay channels (except charged conjugated) the windows used in both cases are the same, the parameters of which are given in table 4.2.

Table 4.2: Parameters of the acceptance window used for the weighted Λ and $\bar{\Lambda}$ candidates. p_T is quoted in GeV/c, rapidity is dimensionless and θ is in radians

$p_T(min)$	$p_T(max)$	$y(min)$	$y(max)$	$\theta(min)$	$\theta(max)$
0.36	1.96	1.81	2.87	0.087	0.137

The vertical line in figures 4.3 and 4.4 represents the central rapidity in the centre of mass system (y_{cm}). Data with $y > y_{cm}$ represents particles originating from forward of the collision zone, data with $y < y_{cm}$ represents particles originating from backwards of the collision zone.

4.5 Transverse Mass Spectra

A double-differential (y, m_T) distribution (where y is the rapidity and m_T is the transverse mass, defined in (1.6)), for each particle species, can be fitted to the weighted data samples confined within the acceptance window using the parameterisation [4, 94]

$$\frac{d^2N}{dm_T dy} = m_T f(y) e^{-m_T/T} \quad (4.3)$$

where $f(y)$ is the rapidity distribution for $|y - y_{cm}| < 0.5$ and is assumed to be flat. This is seen to be a good approximation in the case of the Λ particle, whose distribution is shown in figure 4.5 (for the $\bar{\Lambda}$ particle this is not such a good approximation and introduces a source of systematic error, which is discussed in further detail in chapter 6). Assuming $f(y) = A$, where A is a constant, (4.3) simplifies to

$$\frac{dN}{dm_T} = m_T A e^{-m_T/T} \quad (4.4)$$

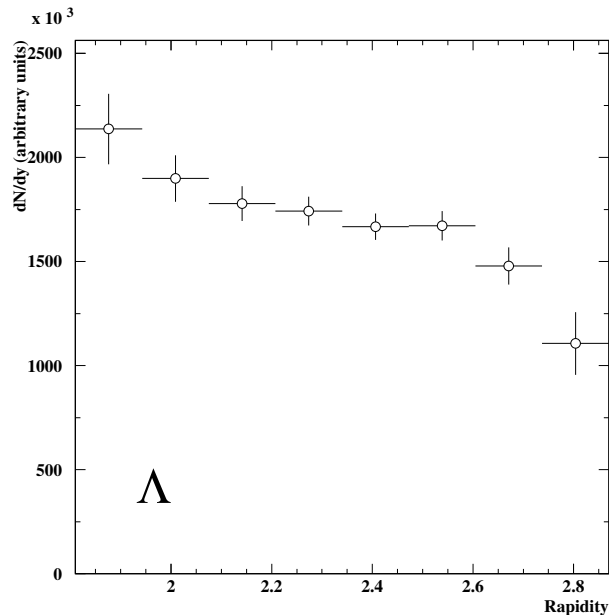


Figure 4.5: The rapidity distribution for the Λ particle. It can be seen that this distribution is approximately flat.

where T is the *inverse slope* parameter and has been obtained from a *maximum likelihood fit* of (4.4) to the data. A detailed discussion of the maximum likelihood method is given in appendix E. The results from which, for the weighted Λ and $\bar{\Lambda}$ candidates (within the acceptance window), can be seen in figures 4.6 and 4.7 where $\ln\left(\frac{1}{m_T} \frac{dN}{dm_T}\right)$ is plotted against m_T . The fit to the data shown is that obtained from the maximum likelihood fit and is seen to fit the data well. The inverse slopes are summarised in table 4.3. It can be seen that the $\bar{\Lambda}$ inverse slope is significantly lower than that of the Λ : this is expected in p–Be interactions, where a QGP is not expected to form, and is discussed further in section 7.3.

The physical significance of T is related to the local temperature and transverse flow of the evolving hadronic matter. To disentangle these two components is unavoidably model dependent. The model used by NA57 is called the *Blast-Wave* model and has been successfully employed in the analysis of Pb–Pb collisions. In these collisions, where a QGP is expected to occur, the model is particularly useful as the local temperature is defined as the thermal freezeout (discussed in section 1.4)

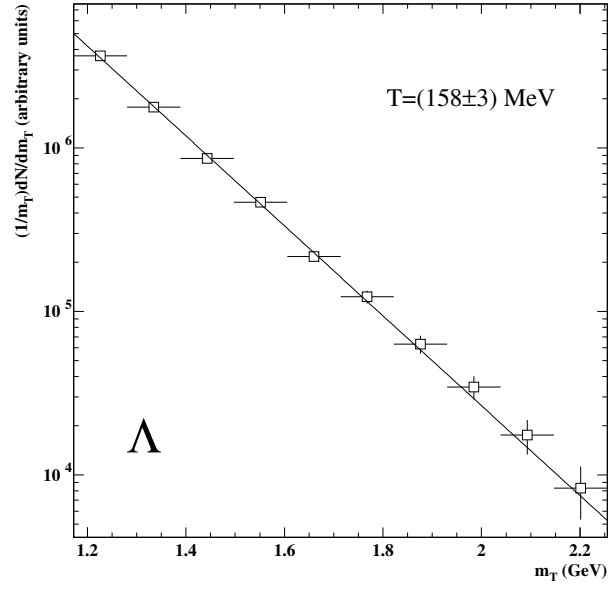


Figure 4.6: $\ln\left(\frac{1}{m_T} \frac{dN}{dm_T}\right)$ versus m_T for the Λ particle. The fitted line was obtained using a maximum likelihood fit.

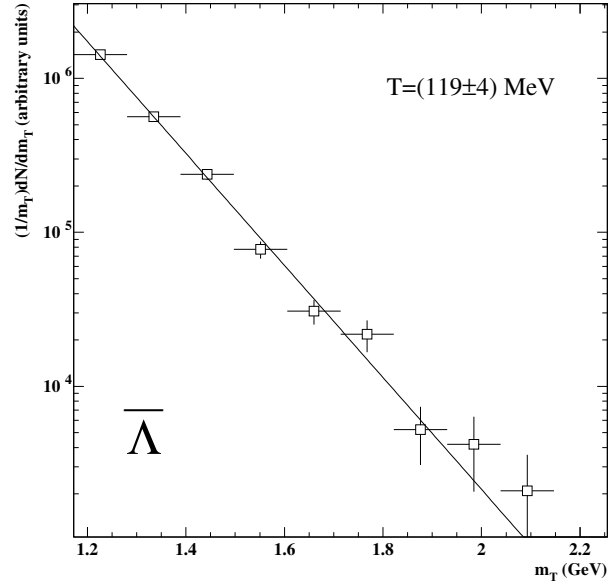


Figure 4.7: $\ln\left(\frac{1}{m_T} \frac{dN}{dm_T}\right)$ versus m_T for the $\bar{\Lambda}$ particle. The fitted line was obtained using a maximum likelihood fit.

Table 4.3: Inverse slopes obtained using a maximum likelihood fit for the weighted Λ and $\bar{\Lambda}$ candidates within the acceptance window.

Particle	Inverse Slope, T (MeV)
Λ	158 ± 3
$\bar{\Lambda}$	119 ± 4

of the fireball. A discussion of the model and results from which can be found in references [95, 96] and references within.

4.6 Particle Yields

A “yield” for both the weighted Λ and $\bar{\Lambda}$ candidates within the acceptance window has been calculated. A yield is defined as the number of particles of a given species that were produced per interaction. The yield for a given particle species from a p–Be interaction is calculated using (4.5), where the numerator is equivalent to the total number of particles produced, the denominator is the number of proton interactions.

$$Yield = \frac{\sum_{all\ runs} \left[\left(\sum_{run} Weight \right) \times \left(R_{tw} \right) \right]}{0.08 \sum_{all\ runs} [(Beam\ flux) \times (Fraction\ of\ protons)]} \quad (4.5)$$

For a given run of the data set all the weights of the weighted particle species are summed and then multiplied by a factor, R_{tw} . R_{tw} is the total number of real data candidates in that run, divided by the number of candidates which were weighted: this factor accounts for those candidates selected, but not weighted. If all candidates were weighted (as in the case of the $\bar{\Lambda}$), $R_{tw} = 1$. This process was repeated for all runs in the data set, the totals from each run were summed to form the numerator of (4.5).

The denominator of (4.5) consists of the sum over all runs of the product of beam flux and proton fraction. The beam flux is the number of particles within the beam which lead to an interaction and can be recorded (i.e. when the detector is not assigned as ‘busy’). The electronic logic for which is:

$$Flux = S2 \cdot S4 \cdot \overline{dt} \quad (4.6)$$

where to be accepted as an interaction, a ‘hit’ must be recorded in both scintillators $S2$ and $S4$ and the electronics must not be busy (\overline{dt}), all of which are described further in section 2.4.4. The flux takes into account all particle interactions from the beam. NA57 is only interested in those interactions which are from protons and so the flux must be multiplied by the proton fraction. This fraction was obtained in two ways: firstly a record of the proton fraction was kept by the CERN beam physicists at the CERN SPS during the running of the experiment. Secondly an offline investigation of several ‘special’ runs with only the beam trigger in place was carried out. For each special run the fraction of protons ($\overline{C1} \cdot \overline{C2}$, where $C1$ and $C2$ are signals from the two gaseous Čerenkov threshold counters placed upstream of the target, shown in figure 2.2) compared to other signals were calculated. The average proton fraction over these special runs was taken. Both measurements determined the proton fraction as 21%, the remaining 79% of the beam were either kaons and pions (70%) or counts due to background noise (9%), see section 2.4.1. The final component of the denominator of (4.5) is the 0.08, which takes account of the 8% interaction length of the Be target.

The yield per interaction calculated from (4.5) gives the yield in the window of good acceptance. By using the parameterisation of (4.3) used to obtain the inverse slope parameter, again assuming a flat rapidity, the yield measured in the selected acceptance window can be extrapolated into a common phase space window covering the full p_T range and one unit of rapidity about mid-rapidity.

$$Yield_{ext} = \int_m^\infty dm_T \int_{y_{cm}-0.5}^{y_{cm}+0.5} \frac{d^2N}{dm_T dy} dy \quad (4.7)$$

Thus, this procedure extrapolates the data into a common acceptance region that includes those areas about mid-rapidity not covered by experimental acceptance.

Finally the extrapolated yield must be divided by the branching ratio which takes into account the decay modes which are not detected by the experiment. In the case of the Λ and $\bar{\Lambda}$ particles the branching ratio is 0.639 ± 0.005 [6] (The remaining fraction are modes unseen by NA57: the decay $\Lambda \rightarrow \pi^0 n$ accounts for the large majority of the remainder, 0.358 ± 0.005).

The final extrapolated yields for the Λ and $\bar{\Lambda}$ particles are given in table 4.4. The magnitude of the Λ extrapolated yield is nearly an order of magnitude greater than that of the $\bar{\Lambda}$. The Λ extrapolated yield is expected to be greater than that of the $\bar{\Lambda}$ as the Λ particle can be produced via both associated production (for example: $p + p \rightarrow p + K^+ + \Lambda$) and pair production (for example: $p + p \rightarrow p + p + \Lambda + \bar{\Lambda}$), whereas the $\bar{\Lambda}$ can only be produced via pair production.

Table 4.4: Λ and $\bar{\Lambda}$ extrapolated yields at mid-rapidity ($|y - y_{cm}| < 0.5$) at 40 GeV/c.

Particle	Yield (Particles/interaction)
Λ	0.0290 ± 0.0008
$\bar{\Lambda}$	0.00348 ± 0.00019

To compare yields meaningfully for a given particle species in different colliding systems (e.g. p-Be and Pb-Pb) at a given energy, it is necessary to calculate the yield *per wounded nucleon* (number of nucleons involved in the collision, section 1.5.1). For p-Be collisions the number of wounded nucleons is estimated as 2.5 [97], and so the yields per wounded nucleon is obtained by dividing the values in table 4.4 by 2.5. The value of 2.5 was obtained from a Monte-Carlo simulation of a proton colliding with a Beryllium nucleus. The number of nucleons that were wounded in the Beryllium nucleus, as the proton (1 wounded nucleon) traversed it, was obtained. By averaging over all possible impact parameters it was found that

on average 1.5 Beryllium nucleons were wounded. Therefore in a p–Be collision 2.5 nucleons, on average, are wounded.

4.7 Stability of Results

In order to verify the stability of the inverse slopes and yields calculated for the weighted Λ and $\bar{\Lambda}$ samples, two stability checks were performed. The first check studied the results in different time periods, the second check used different acceptance windows. The time period check was implemented to ensure the results remained consistent over the entire running period and for the two magnetic field polarities. The check was performed by dividing the entire running period up into a number of smaller consecutive running periods (6 in the case of the Λ s and 3 in the case of the $\bar{\Lambda}$ s), each containing approximately equal numbers of weighted candidates. Furthermore, the smaller running periods were chosen such that the polarity of the magnetic field did not change during any running period (i.e. the change of polarity occurred between these small running periods). The inverse slopes and yields were calculated separately in each running period.

Details of the running periods used in the time period check are given in tables 4.5 and 4.6, where the field polarity changed between periods two and three for the Λ and between one and two for the $\bar{\Lambda}$. The results are shown in figures 4.8 for the Λ and figure 4.9 for the $\bar{\Lambda}$. No systematic shifts were observed in either the inverse slope or yield across the running period.

The acceptance window check was used to ensure that the choice of acceptance window had not biased the results. This check was performed by selecting one window which was larger and one window which was smaller than the selected window (table 4.2). The inverse slopes and yields for each window were calculated separately. No systematic shifts were observed in either the inverse slope or yield by using different sized acceptance windows. A fuller description of this check is

Table 4.5: The six time periods of the Λ data, each containing a similar number of weighted candidates, used to determine stability of the inverse slope and yield.

Period Number	Runs Included	Weighted Candidates
1	7100 – 7146	611
2	7147 – 7185	667
3	7211 – 7230	650
4	7234 – 7254	692
5	7255 – 7282	658
6	7283 – 7309	655

Table 4.6: The three time periods of the $\bar{\Lambda}$ data, each containing a similar number of weighted candidates, used to determine stability of the inverse slope and yield.

Period Number	Runs Included	Weighted Candidates
1	7100 – 7185	343
2	7211 – 7253	348
3	7254 – 7309	361

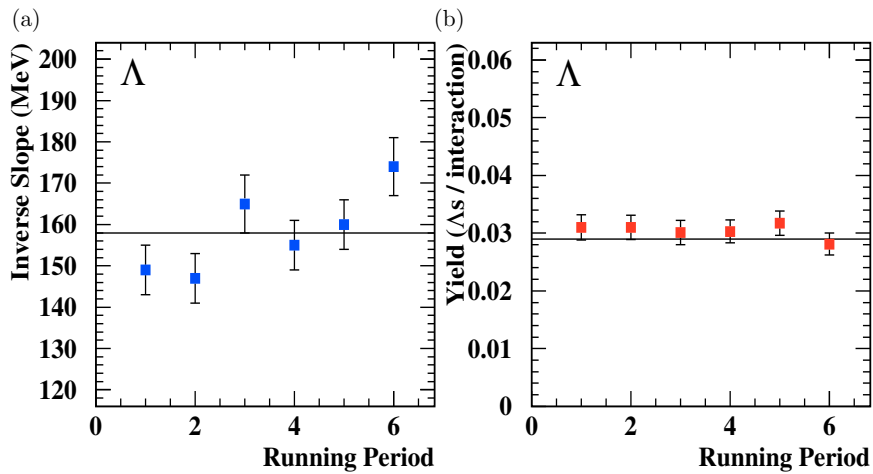


Figure 4.8: (a) Inverse slopes and (b) extrapolated yields for the Λ , calculated separately in six different consecutive time periods. The horizontal line indicates the values of the full sample.

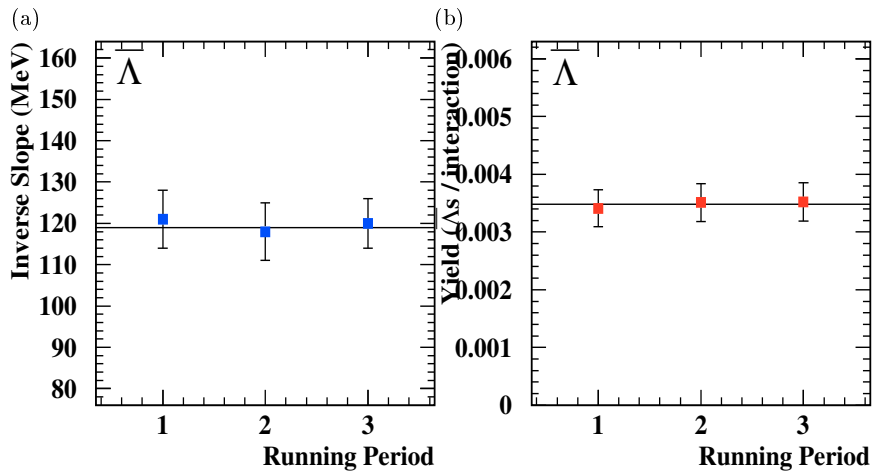


Figure 4.9: (a) Inverse slopes and (b) extrapolated yields for the $\bar{\Lambda}$, calculated separately in three different consecutive time periods. The horizontal line indicates the values of the full sample.

described in section 5.9 for the K_S^0 particle.

As no systematic shifts were observed in either the inverse slope or yield in both stability checks, the inverse slopes and yields presented in tables 4.3 and 4.4 appear to be stable and thus the results reliable.

4.8 Combinatorial Background Corrections for the $\bar{\Lambda}$ Inverse Slope and Yield

As discussed in section 3.11 the combinatorial background beneath the $\bar{\Lambda}$ signal (even after final selection criteria) is non-negligible and therefore needs to be accounted for in the inverse slope and yield calculations. The correction for each will be considered in turn in the following two subsections.

4.8.1 $\bar{\Lambda}$ Inverse Slope

The method employed (and described fully) in section 3.11.2 to estimate the combinatorial background beneath the cleaned $\bar{\Lambda}$ mass signal was repeated in order to correct for the combinatorial background included in the inverse slope calculation. The real $\bar{\Lambda}$ data (without any $\bar{\Lambda}$ mass selections) was divided up into seven smaller sub-data sets; each set containing $\bar{\Lambda}$ particles within a different part of the m_T spectra. The first six of these sub-data sets corresponded to the six m_T regions covered by the first six bins in the m_T spectra of figure 4.7. The seventh data set corresponded to the range of m_T covered by the final three bins in the m_T spectra of figure 4.7: the latter were grouped together due to low statistics. For each of the seven sub-data sets the total number of entries within the gold-plated mass range ($1.103 \text{ GeV} < mass(\bar{\Lambda}) < 1.131 \text{ GeV}$) was obtained (using PAW). A fit was then made, using the CENTKK program [89], to the $\bar{\Lambda}$ mass signal for each of the seven sub-data sets. The mean mass and width of the Gaussian for each fit were fixed at the values obtained for the full sample. Further, the two parameters used in the polynomial part of the background function were fixed, so as to reduce the number of free parameters. For each fit the number of entries beneath the background function, within the gold-plated mass range, were summed. Within the gold-plated mass region of each sub-data set the number of entries beneath the background function and the total number of entries were known: thus the percentage of background entries within the gold-plated mass region could be calculated for each sub-data set.

The fraction of combinatorial background (CB_f) within each of the seven sub-data sets was then used to correct the inverse slope. The value of $\ln\left(\frac{1}{m_T} \frac{dN}{dm_T}\right)$ in arbitrary units for each of the nine m_T bins can be obtained from figure 4.7. For each bin this number was multiplied by $(1 - CB_f)$ of that bin. Bins seven to nine each had the same fraction of background, as discussed already. The background corrected values of $\ln\left(\frac{1}{m_T} \frac{dN}{dm_T}\right)$ were then replotted against m_T and a line of best fit inserted. Although the corrected inverse slope was obtained using a line of best fit

instead of the maximum likelihood method of section 4.5, this was seen as a good approximation as the difference for the uncorrected $\bar{\Lambda}$ between using a line of best fit and the maximum likelihood fit was only 1 MeV. Figure 4.10 shows line of best fits fitted to the background uncorrected data (top) and the background corrected data (bottom): the fits are seen to fit the data well. The background corrected $\bar{\Lambda}$ inverse slope is summarised in table 4.7. A small decrease in inverse slope is observed, this is expected due to the background distribution, shown in figure 3.21, falling off more slowly towards high mass compared with the real signal.

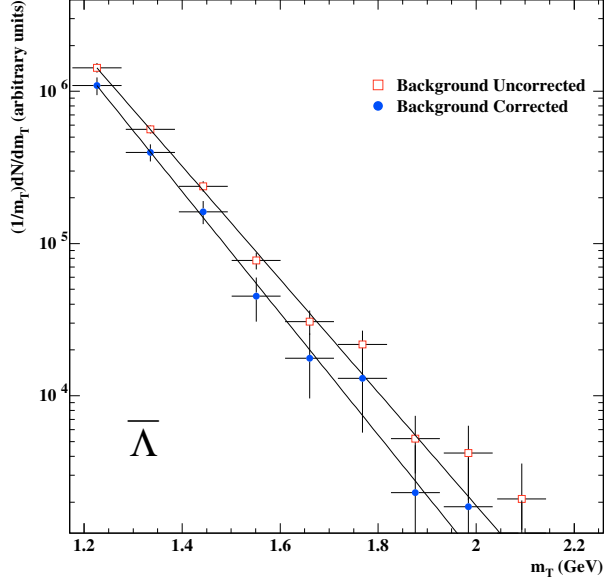


Figure 4.10: $\ln\left(\frac{1}{m_T} \frac{dN}{dm_T}\right)$ versus m_T for the $\bar{\Lambda}$ particle. The open data points are the background uncorrected data, the solid data points are the background corrected data. The fitted lines were obtained using lines of best fit, both lines fit the data well.

Table 4.7: Combinatorial background uncorrected and corrected $\bar{\Lambda}$ inverse slopes at 40 GeV/c.

Background Status	Inverse Slope, T (MeV)
Uncorrected	119 ± 4
Corrected	109 ± 7

4.8.2 $\bar{\Lambda}$ Yield

The $\bar{\Lambda}$ yield was corrected in the same way as for the inverse slope by using the CENTKK program, described in section 3.11.2. The correction to the yield was obtained by using (4.8)

$$yield_{corrected} = (1 - CBT_f) yield_{uncorrected} \quad (4.8)$$

where CBT_f is the fraction of combinatorial background to total signal within the gold-plated mass range of the whole unweighted data sample. CBT_f was evaluated in section 3.11.2, where it was expressed as a percentage. The combinatorial background uncorrected and corrected yields are shown in table 4.8

Table 4.8: Combinatorial background uncorrected and corrected $\bar{\Lambda}$ extrapolated yields at mid-rapidity ($|y - y_{cm}| < 0.5$) at 40 GeV/c.

Background Status	Yield ($\bar{\Lambda}$ s/interaction)
Uncorrected	0.00348 ± 0.00019
Corrected	0.00230 ± 0.00020

4.9 Errors

All errors quoted in this chapter are statistical in nature, the primary source of which is in the sum of the weights. In figures 4.6 and 4.7 the vertical error bars are simply

$$Err_j = \sqrt{\sum_i Wgt_i^2} \quad (4.9)$$

where Err_j is the error on the j th bin and Wgt_i is the weight of the i th candidate within bin j . The horizontal error bars represent the bin width. The errors on the yields were calculated by multiplying the fractional error on the total sum of the

weights by the extrapolated yield, where the error on the total sum of the weights were calculated using (4.9), but over all bins.

The errors on the background corrected $\bar{\Lambda}$ results, σ_A , increase to take into account the fit of the CENTKK program to the $\bar{\Lambda}$ signal. Thus the vertical error bars on the background corrected m_T spectra plots (shown in figures 4.6 and 4.7) were calculated

$$\sigma A = A \sqrt{\left(\frac{\sigma B}{B}\right)^2 + \left(\frac{\sigma S}{S}\right)^2 + \left(\frac{\sigma T}{T}\right)^2} \quad (4.10)$$

B is the uncorrected sum of the weights, A is the corrected sum of the weights, $B(1 - CB_f)$, S is the number of entries in the signal within the gold-plated mass selections, T is the total (signal and background) number of entries within the gold-plated mass selections where σS and σT are calculated by \sqrt{S} and \sqrt{T} respectively. The calculation was performed separately for each of the nine m_T bins. The error on the corrected inverse slope came from the fit performed by MINUIT. The error on the corrected yield was calculated using (4.10), where this time A represented the corrected yield, B the uncorrected yield and S and T retained the same definitions.

In addition to the statistical errors, systematic errors must also be considered; these are discussed in detail in chapter 6.

Chapter 5

Reconstruction and Correction of K_S^0 Candidates in p–Be Collisions

5.1 Introduction

In addition to the strange baryons studied via their decay channels, shown in section 3.1, NA57 also studies the K^0 short (K_S^0) strange meson via the decay channel

$$K_S^0 \rightarrow \pi^- \pi^+ \quad (5.1)$$

Study of the K_S^0 is of particular interest as it is the first in depth study made for the K_S^0 particle using the 1999 p–Be data set. In addition, an extrapolated yield has not been previously calculated for K_S^0 mesons in p–Be data by NA57 (or its predecessor, WA97 [28]) at either 40 GeV/c or 158 GeV/c energies (the Pb–Pb results published for K_S^0 by NA57 show extrapolated yields and not strangeness enhancement [98]).

The analysis procedure for the K_S^0 is similar to that for the Λ and $\bar{\Lambda}$ data, described in chapters 3 and 4. However, the K_S^0 particle and its decay channel of (5.1) has a number of differences compared to the Λ and $\bar{\Lambda}$ particles and their decay channels of (3.1) and (3.2). For example, the K_S^0 does not have an associated

antiparticle, it is a particle with a much lighter mass and it decays into two particles of the same mass. As such, the K_S^0 analysis differs in places compared to that of the Λ and $\bar{\Lambda}$. Details of, as well as differences in, the K_S^0 analysis are given in this chapter.

5.2 K_S^0 Selection Criteria

The selection criteria implemented to obtain the K_S^0 candidates are described in the following five subsections. The first four of which were used in the Λ and $\bar{\Lambda}$ selection and are described more fully in sections 3.7.1 and 3.8. As the statistics for K_S^0 mesons are higher than the $\bar{\Lambda}$ baryons, harsher selection criteria can be made on some of these parameters compared to the case of the Λ and $\bar{\Lambda}$ candidates. The fifth subsection describes the z separation parameter which for the case of K_S^0 selection is more appropriate than the internal decay angle (ϕ), as described in section 3.8.4, used for the Λ and $\bar{\Lambda}$ selection.

In addition to these selections a number of further criteria were implemented, which remain the same as for the Λ and $\bar{\Lambda}$ analysis. The K_S^0 candidate must have two decay tracks with a cowboy topology (section 3.3) whose closest approach is less than 0.1 cm (section 3.4). Both decay tracks must pass through the *SPH1* and *SPH2* scintillation counters upstream of the telescope and one track must pass through the *ST2* downstream of the compact part of the telescope, as described in section 2.4.4. The x position of the target, $xtarg$, in the GOLIATH reference system must be greater than -75 cm (section 3.5). The run number of the K_S^0 candidate must be greater than 7100 (section 3.2).

5.2.1 The Armenteros-Podolanski Plot

As discussed in section 3.7.1 and appendix C the large half ellipses of figures 3.7 and C.2 centred on $\alpha = 0$ contain K_S^0 candidates. A symmetrical selection about $\alpha = 0$ was made, accepting candidates with $|\alpha| < 0.45$. Although it is clear from figure 3.7 that the band of K_S^0 candidates extends beyond this selection, the number of K_S^0 candidates within the accepted region is plentiful, and as such, the need to widen this selection is unnecessary. Further, in widening the selection one extends into the regions containing Λ or $\bar{\Lambda}$ (in addition to K_S^0) candidates which instigates the need for Λ and $\bar{\Lambda}$ mass selections in order to remove these unwanted particle species.

As for the Λ and $\bar{\Lambda}$ selection, the requirement that $0.02 \text{ GeV}/c < q_T < 0.4 \text{ GeV}/c$ was implemented. The lower limit was to ensure any background γ conversion events were removed, the upper limit removed the few background candidates with a q_T much greater than the theoretical predictions given in appendix C.

5.2.2 The x Decay Vertex

Figure 5.1a shows the distribution of $\pi^-\pi^+$ mass versus their x decay vertex (xvc). A selection of $-40 \text{ cm} < xvc < -27 \text{ cm}$ was made. As for the Λ and $\bar{\Lambda}$ candidates the selection of $xvc < -27 \text{ cm}$ was made to remove interactions with the *SPH1* and *SPH2* scintillation counters. A tighter selection (compared to the Λ and $\bar{\Lambda}$) near the target of $xvc > -40 \text{ cm}$ was made to remove the combinatorial background, clearly visible in figure 5.1a, in the region near to the target. In this region ($xvc < -40 \text{ cm}$) there is a high probability of combinatorial background due to the high density of tracks near the target not swept out by the magnetic field. Figure 5.1b shows the K_S^0 mass plot (unshaded) with all selections, scaled to and superimposed on the mass peak (shaded) of the K_S^0 signal with all selections except xvc . The shaded regions which can be seen represents the effectiveness of the selection and allows one to see that more background than signal has been removed at the low mass edge of the

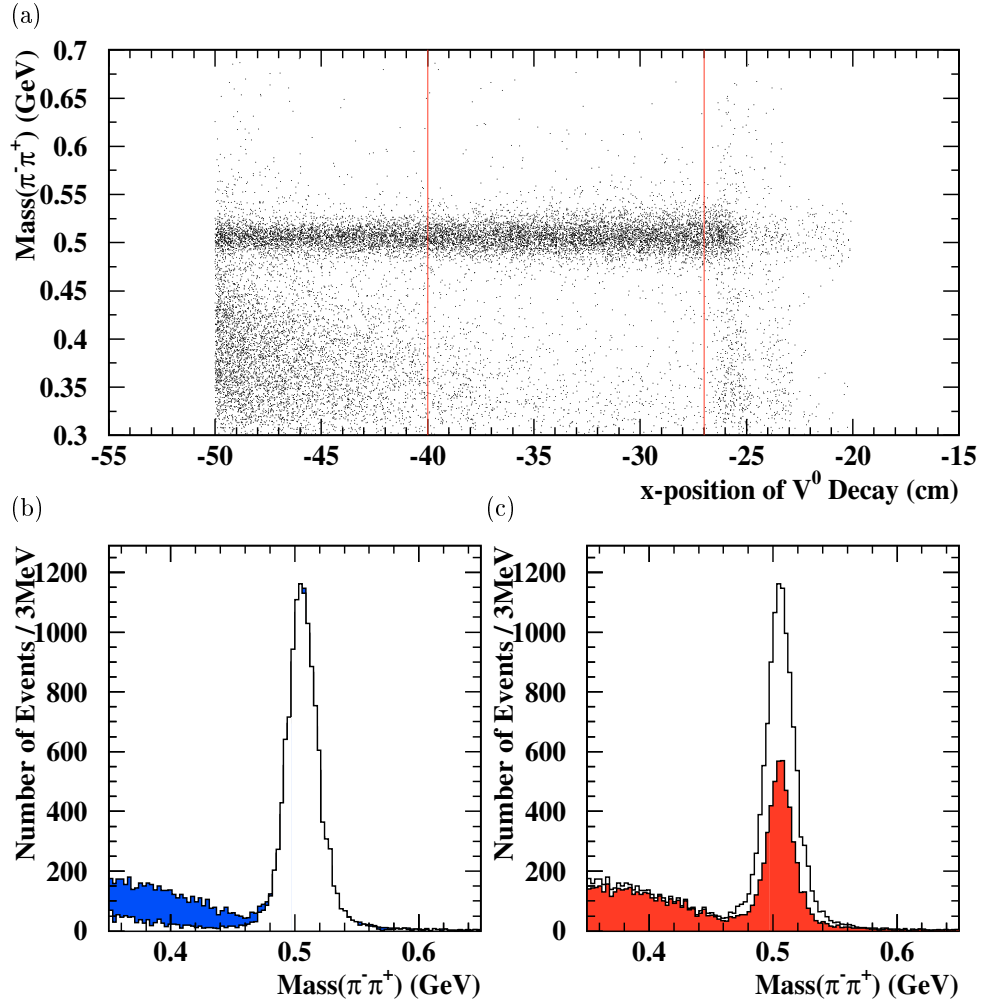


Figure 5.1: (a) $\pi^- \pi^+$ mass versus x -position of V^0 decay, with all selections except the xvc selection, (b) K_S^0 mass with all selections, scaled to, and superimposed on the mass signal without the xvc selection, the shaded area is what is removed. (c) What has been removed with the xvc selection (shaded) superimposed on the mass signal without the xvc selection.

signal. Figure 5.1c confirms this by showing what has been removed with the xvc selection (shaded) superimposed on the signal containing all selections (unshaded). It can be seen that although a lot of signal has been removed, a large amount of unwanted background candidates, especially towards the low mass edge of the signal have also been removed, making the selection successful.

5.2.3 The B_y Parameter of the V^0

Figure 5.2a shows the distribution of $\pi^-\pi^+$ mass versus their B_y parameter of the V^0 (byv). A selection of $-0.5 \text{ cm} < byv < 0.5 \text{ cm}$ was made: this selection is considerably tighter than for the Λ and $\bar{\Lambda}$. Figure 5.2b shows the K_S^0 mass plot (unshaded) with all selections, scaled to and superimposed on the mass peak (shaded) of the K_S^0 signal with all selections except byv . The shaded regions which can be seen represents the effectiveness of the selection. Figure 5.2c shows what has been removed with the byv selection (shaded) superimposed on the signal containing all selections (unshaded). Results from these latter two plots, show that although the byv selection is not as effective as the xvc selection (section 5.2.2), it does remove a fairly constant amount of unwanted background between 0.35 GeV and 0.54 GeV, with the loss of negligible signal from the peak. As can be seen from figure 5.2a, a more harsh selection of byv would have removed a lot of signal, and a limited amount of additional background.

5.2.4 The B_y Parameter of the Charged Tracks

Selecting on the B_y parameter of the charged tracks, had little effect and so, like for the case of the Λ and $\bar{\Lambda}$, no selection was made on this parameter.

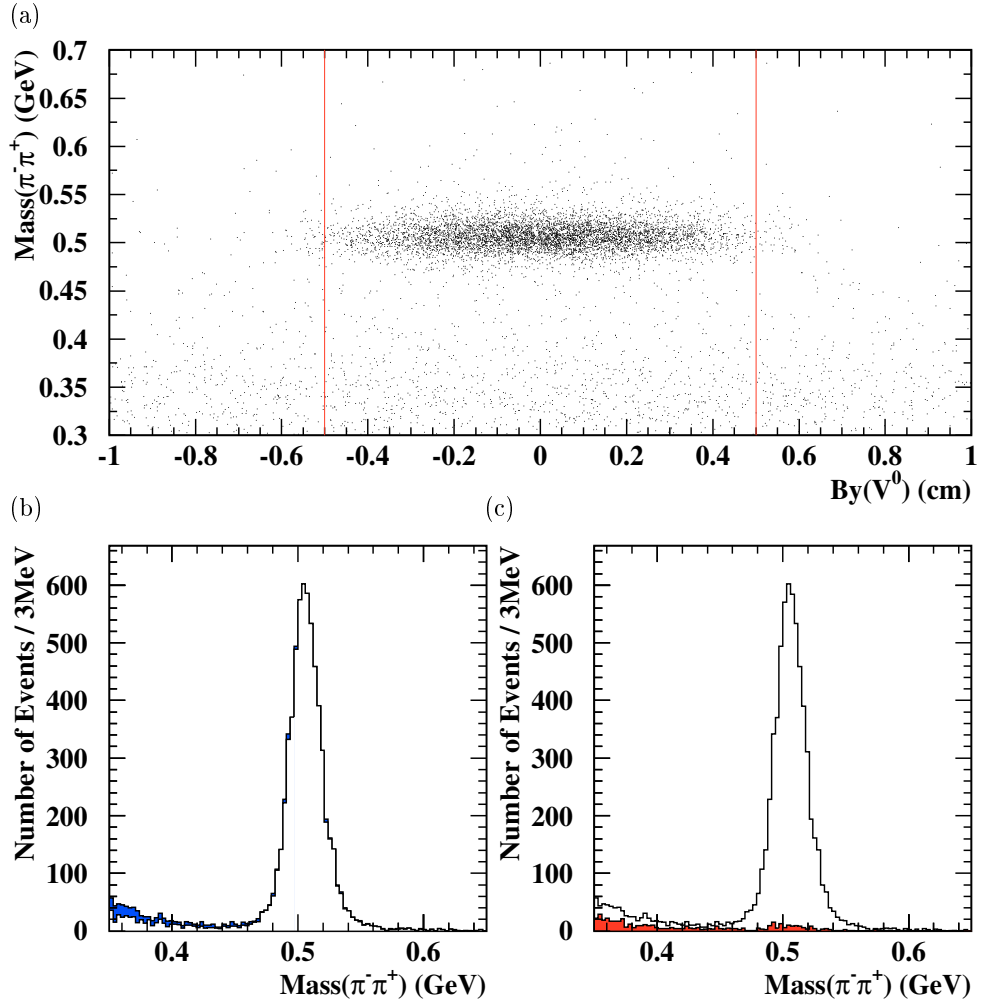


Figure 5.2: (a) $\pi^- \pi^+$ mass versus the B_y parameter of the V^0 , with all selections except the byv selection, (b) K_S^0 mass with all selections, scaled to, and superimposed on the mass signal without the byv selection, the shaded area is what is removed. (c) What has been removed with the byv selection (shaded) superimposed on the mass signal without the byv selection.

5.2.5 The z Separation Parameter

A plot of $\pi^-\pi^+$ mass versus the V^0 internal decay angle, ϕ , is shown in figure 5.3. From which it is clear that it is difficult to make a meaningful ϕ selection for the

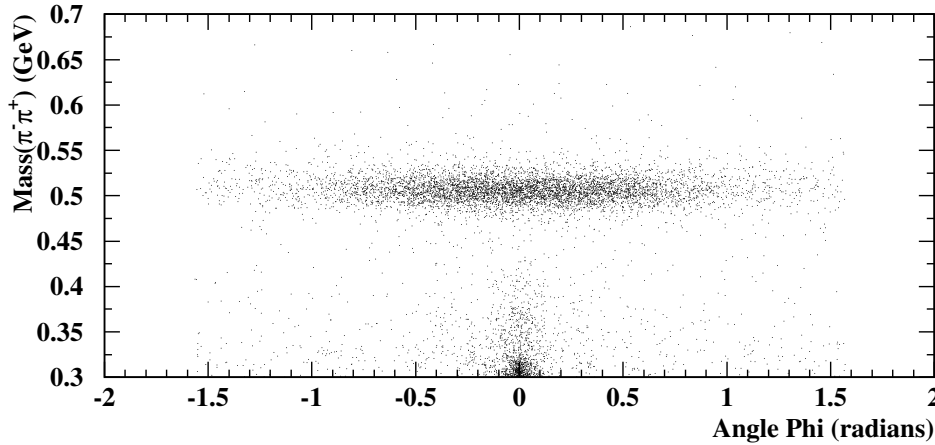


Figure 5.3: $\pi^-\pi^+$ mass versus the internal decay angle, ϕ , with all selections applied. It is clear that selecting on the ϕ parameter is not appropriate for the case of K_S^0 .

K_S^0 , as there is no distinct smearing of the horizontal $\pi^-\pi^+$ band at $|\phi| \sim 0$, unlike in the case of the $\bar{\Lambda}$ in figure 3.17a. Although a separate distinct region of low mass candidates near $|\phi| \sim 0$ can be seen, a large ϕ selection would be required to remove this and would remove a lot of ‘good’ signal. Furthermore, these candidates would be removed when the mass selection was made on the signal (section 5.3) and so a ϕ selection in the case of the K_S^0 mesons is inappropriate. Therefore, in order to remove candidates formed from random tracks resulting from combinatorial background (as was done using the ϕ selection) a z separation ($zsep$) selection was implemented.

In the $x - z$ plane the two charged tracks will come off from the V^0 as straight lines (figure 3.2). The angles, θ_1 and θ_2 that charged tracks 1 and 2 make with respect to the x axis can be calculated using the momentum components in the x and z directions for each track. The difference between θ_1 and θ_2 is equal to $\Delta\theta$. In figure 5.4a the sailor and cowboy topologies are shown in the $x - y$ plane. In

figure 5.4b the same decay is shown in the $x - z$ plane, except in this case the two charged tracks are expressed in terms of one track, at an angle $\Delta\theta$ to the x axis.

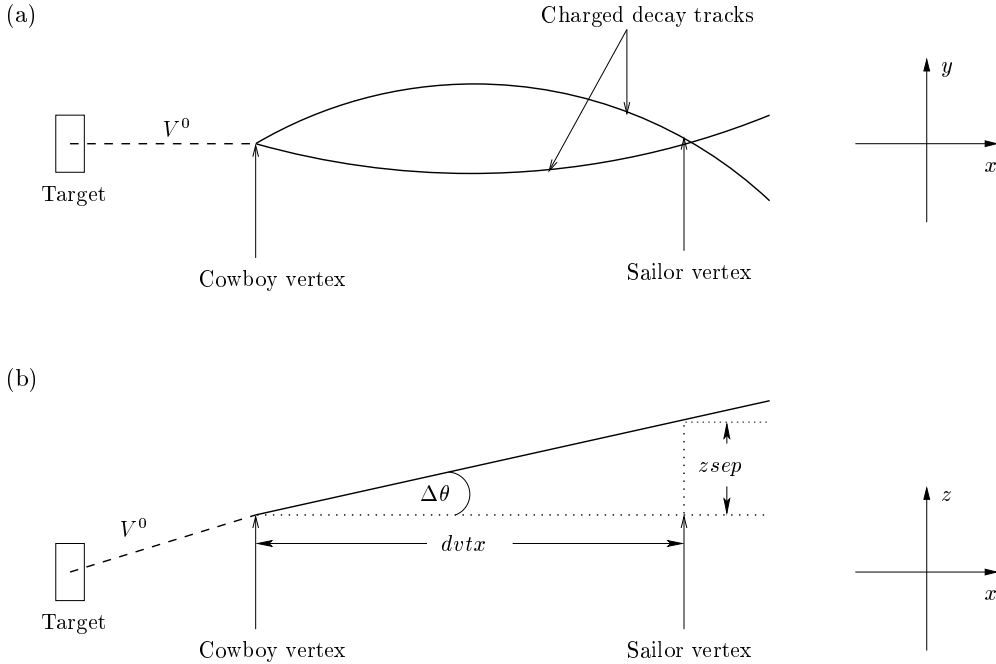


Figure 5.4: The definition of the $zsep$ parameter of the charged decay tracks. A characteristic V^0 decay in (a) the $x - y$ plane can be viewed in the (b) $x - z$ plane where the two decay tracks of (a) are expressed as one, separated by an angle, $\Delta\theta$, from which $zsep$ can be defined.

It is clear from the trigonometry of figure 5.4b, that

$$zsep = (dvtx) \tan \Delta\theta \quad (5.2)$$

where $\tan\Delta\theta \sim \Delta\theta$ as $\Delta\theta$ is small and the distance ($dvtx$) between the cowboy and sailor vertices is known from the data recorded. When $\Delta\theta$ is 0° the two charged decay tracks will come off in the same direction. Charged tracks from ‘real’ V^0 decays are expected to exhibit some separation in the $x - z$ plane due to the Q-value [5] of the decay (difference between the rest mass of the V^0 and the sum of the rest masses of the two decay particles). However ‘fake’ V^0 candidates are expected to have tracks with little or no separation in the $x - z$ plane in order for them to be detected by the telescope. Of course, it is possible for two charged tracks, resultant

from the decay of a real V^0 , to come off in the same direction (i.e. completely in the $x - y$ plane), although the probability of this happening is small. Therefore, by removing candidates with a small $|zsep|$ removes candidates which are most likely to be fake V^0 candidates made up of combinatorial background tracks.

Figure 5.5a shows the distribution of $\pi^- \pi^+$ mass versus their $zsep$ parameter. A selection of $|zsep| > 0.2$ cm was made. Figure 5.5b shows the K_S^0 mass plot (un-

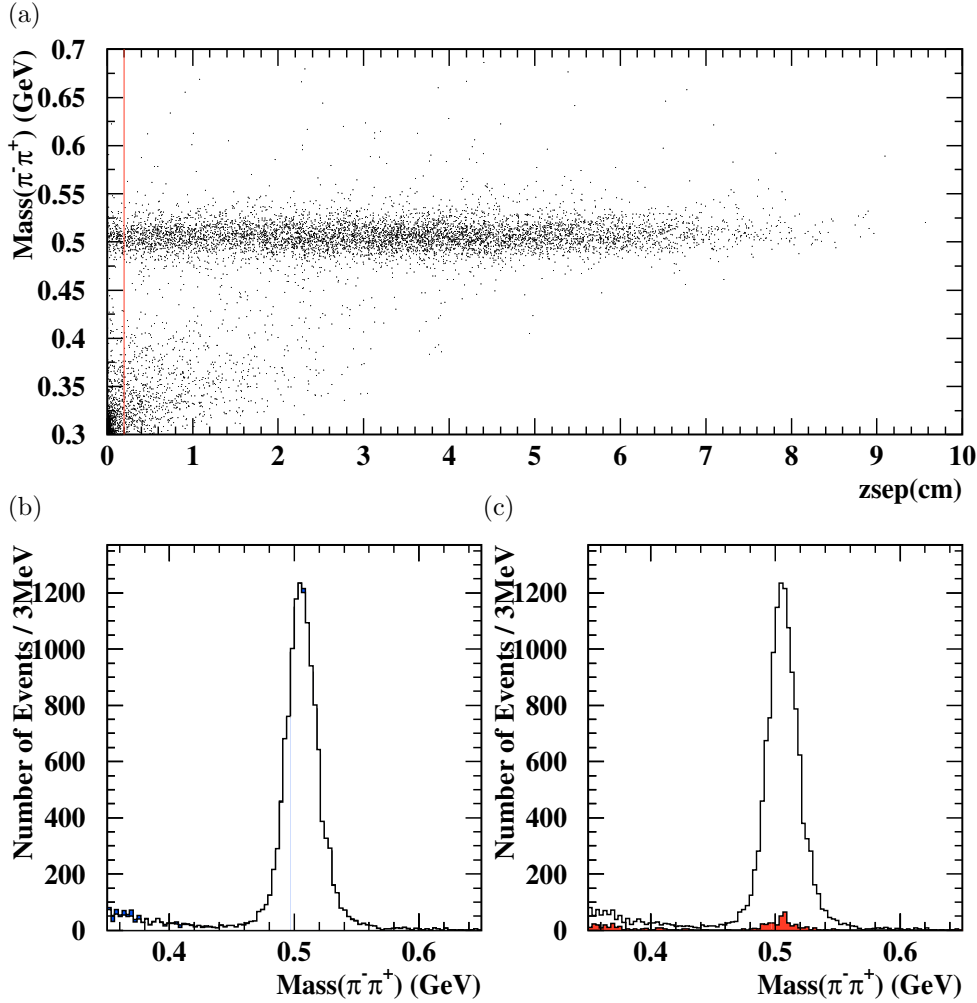


Figure 5.5: (a) $\pi^- \pi^+$ mass versus the $zsep$ parameter of the V^0 , with all selections except the $zsep$ selection, (b) K_S^0 mass with all selections, scaled to, and superimposed on the mass signal without the $zsep$ selection, the shaded area is what is removed. (c) What has been removed with the $zsep$ selection (shaded) superimposed on the mass signal without the $zsep$ selection.

shaded) with all selections, scaled to and superimposed on the mass peak (shaded) of the K_S^0 signal with all selections except $zsep$. The shaded regions which can be seen represents the effectiveness of the selection. Figure 5.5c shows what has been removed with the $zsep$ selection (shaded) superimposed on the signal containing all selections (unshaded). Less than 3% of candidates from within the mass signal (described in section 5.3) were removed by this selection. However, by making this selection the removal of candidates where the decay tracks come off at the same angle, most likely to be combinatorial background, was ensured.

5.3 Summary of K_S^0 Selection Criteria

Given here is a summary of the selection criteria V^0 candidates have to fulfil in order to be classified as a K_S^0 candidate.

- The run number of the V^0 must be greater or equal to 7100
- The V^0 decay must have cowboy topology
- The closest approach of the decay tracks must be less than 0.1 cm
- Both decay tracks must pass through $SPH1$ and $SPH2$
- One decay track must pass through $ST2$
- $xtarg$ must be greater than -75 cm
- Armenteros alpha must be greater than -0.45 and less than 0.45
- q_T must be greater than 0.02 GeV/c and less than 0.4 GeV/c
- The x -decay vertex must be greater than -40 cm and less than -27 cm
- The byv parameter must be greater than -0.5 cm and less than 0.5 cm

- The $|zsep|$ parameter must be greater than 0.2 cm

Figure 5.6a shows the mass signals for the K_S^0 with all of the selection criteria summarised above implemented. In all, 7,039 K_S^0 candidates have been identified.

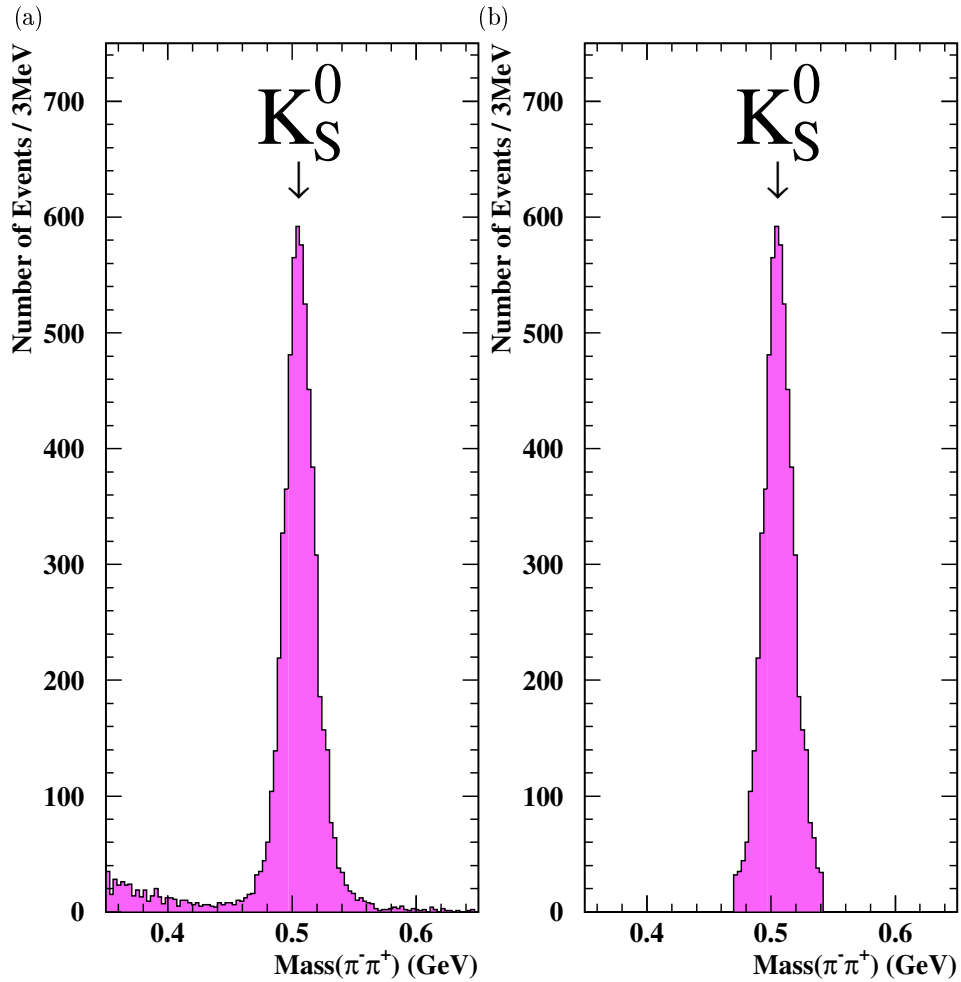


Figure 5.6: K_S^0 mass signals with all selection criteria implemented (a) except the K_S^0 mass selection and (b) including the K_S^0 mass selection, i.e. gold-plated.

To these K_S^0 candidates a final selection was applied so as to remove candidates with a very low or very high mass value compared to that of the mean. The mass selection was determined by fitting a Gaussian distribution to the K_S^0 signal of figure 5.6a (in the same way as for the Λ and $\bar{\Lambda}$, described in section 3.10). The

accepted candidates were those whose effective mass was within $\pm 3\sigma$ of the mean. This equates to a final selection criterion of:

- The K_S^0 mass must be greater than 0.470 GeV and less than 0.542 GeV

where these remaining candidates are defined as ‘gold-plated’ K_S^0 candidates.

Figure 5.6b shows the gold-plated signal, the number of gold-plated candidates are given in table 5.1. It is these selected gold-plated candidates which are used in the remainder of this chapter.

Table 5.1: Summary of the number of gold-plated K_S^0 candidates found.

Candidate	Number found
K_S^0	5,903

5.4 Combinatorial Background Beneath the K_S^0 Mass Signal

The CENTKK program, described fully in section 3.11, was employed to estimate the combinatorial background beneath the K_S^0 signal within the accepted mass region of figure 5.6b. As the background was clearly significantly less than for the $\bar{\Lambda}$ and the shape different, the background function, $B(m)$, of (3.9) was replaced with a simple first order exponential function. The precise form of $B(m)$ was determined to be:

$$B(m) = e^{(1.8-10.3 m)} \quad (5.3)$$

where the constants were obtained from the CENTKK fit. The fit, like for the $\bar{\Lambda}$ fit, assumed that the signal function, $S(M)$, took the form of a Gaussian distribution.

Figure 5.7 shows the results of the CENTKK fit to the K_S^0 data of figure 5.6a, where the fit is seen to fit the data well. A χ^2 per degree of freedom of 2.14 confirms the goodness of fit.

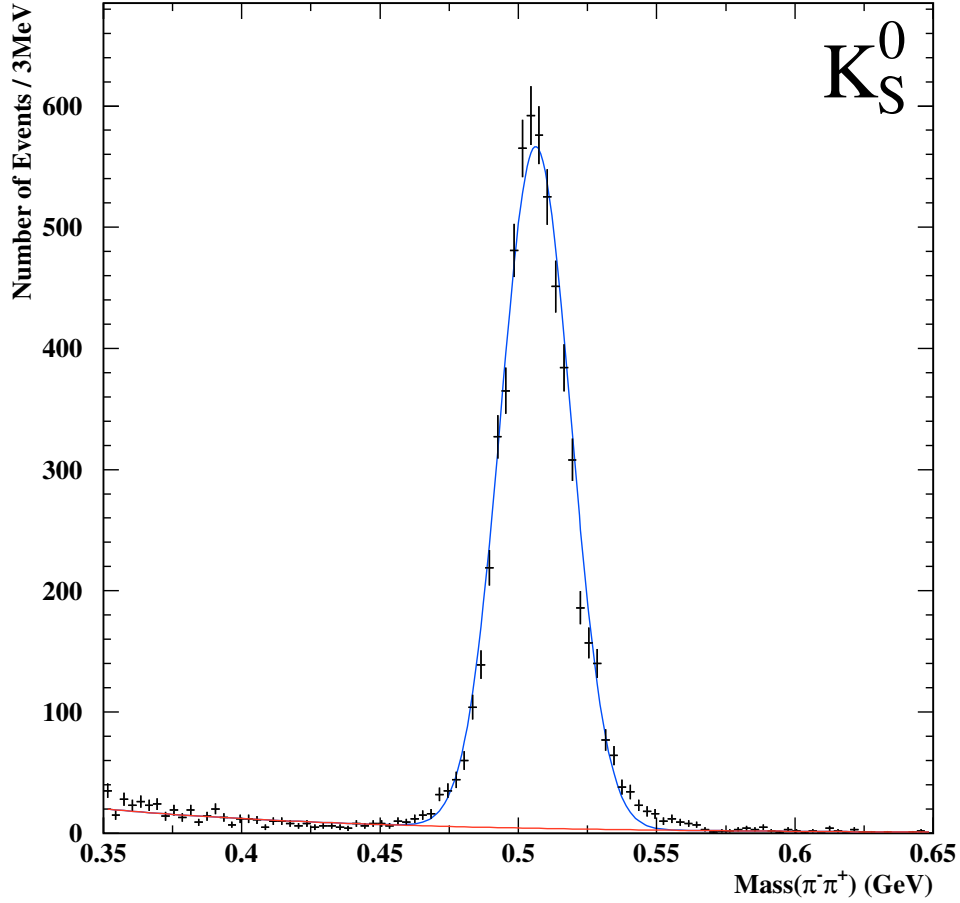


Figure 5.7: K_S^0 mass signal with the Gaussian and exponential functions, scaled to the same area, superimposed on top.

The number of combinatorial background candidates beneath $B(m)$, within the $\pm 3\sigma$ of the mean (given in section 5.3) region, were counted (102 candidates) and compared to the number of gold-plated K_S^0 mesons in table 5.1. From which the total amount of combinatorial background beneath the K_S^0 mass signal, within the accepted mass range, was estimated at 1.7% and therefore can safely be neglected.

5.5 The Weighted K_S^0 Sample

Each of the 5,903 gold-plated K_S^0 candidates, identified in sections 5.2 and 5.3, has been corrected for detector and reconstruction efficiency, geometric acceptance and selection criteria using the weighting procedure described in section 4.2. Again, as in section 4.3, once weighting was complete, a number of candidates were then discarded because they were from runs in which details on the beam flux (required for the yield calculation, described in section 4.6) were not satisfactory.

The quality of the simulation was examined by comparing a number of distributions used in the real data selection with that of the simulated data. It is important that the distributions produced by the simulated data reproduces those of the real data well as the selection criteria used in the real data are also used in the simulation. If the results of the real data are not reproduced well in the simulation, then the results of the weighting procedure cannot be relied upon. Figure 5.8 shows a few of the distributions for the K_S^0 : a sample of the simulated data (black crosses), when scaled by area to that of the real data (shaded region), is seen to replicate the real data well and thus the simulation can be relied upon.

5.6 The Region of Good Acceptance

A plot of transverse momentum, p_T , versus rapidity, y , for the weighted K_S^0 candidates can be produced, onto which is inserted an acceptance window: this is seen in figure 5.9. Like for the Λ and $\bar{\Lambda}$ plots of figures 4.3 and 4.4 the small dark dots represent weights less than ten times the minimum weight (low weights), the lighter larger dots represent the weights which are greater than ten times the minimum weight (high weights). The acceptance window was fitted to include as many low weights as possible, whilst removing the high weights. Further details defining the acceptance window are given in section 4.4, the parameters which define the acceptance window

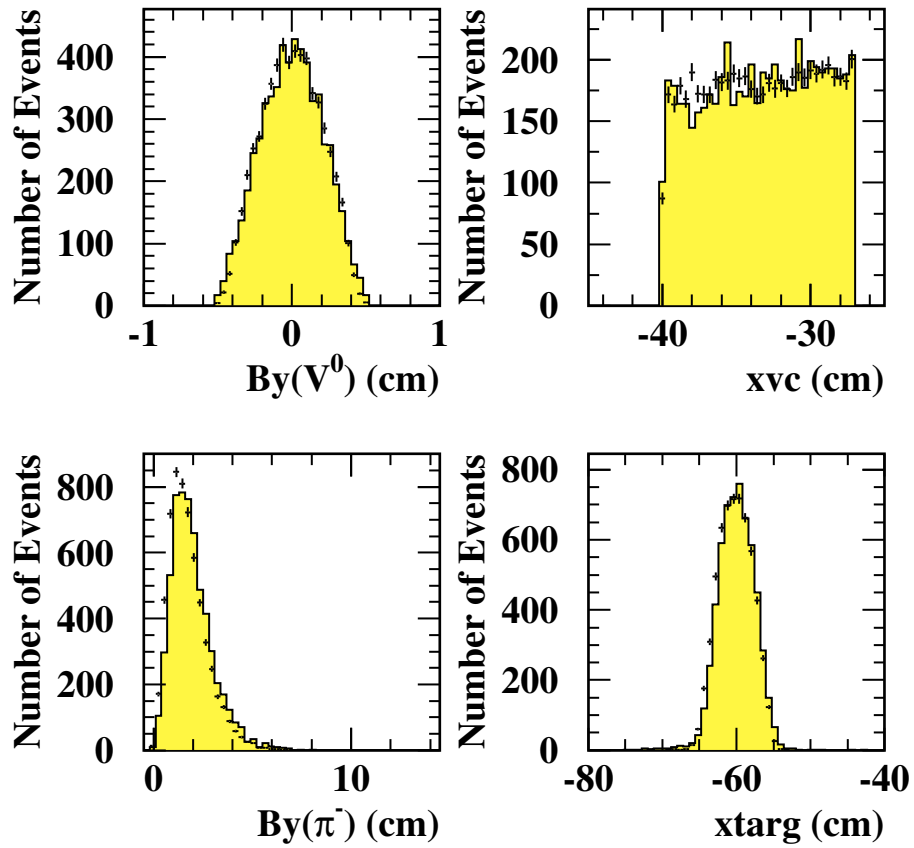


Figure 5.8: The simulated K^0 data (crosses) and real data (shaded region) compared, the areas of the simulated data has been scaled to those of the real data.

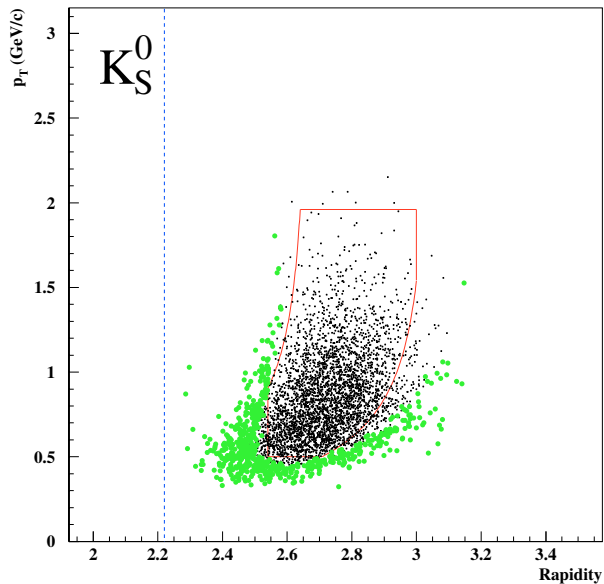


Figure 5.9: p_T versus rapidity for the weighted K_S^0 candidates, with ‘low’ weights shown by black dots and ‘high’ weights by the larger lighter dots. The acceptance window is superimposed on top.

fitted to the weighted K_S^0 candidates are given in table 5.2.

Table 5.2: Parameters of the acceptance window used for the weighted K_S^0 candidates. p_T is quoted in GeV/c, rapidity is dimensionless and θ is in radians

$p_T(min)$	$p_T(max)$	$y(min)$	$y(max)$	$\theta(min)$	$\theta(max)$
0.50	1.96	2.54	3.00	0.095	0.139

There are two interesting differences between figure 5.9 and figures 4.3 and 4.4. Firstly, all K_S^0 candidates have a rapidity greater than that of central rapidity, y_{cm} , ($y > y_{cm}$), i.e. all particles originate forward of the collision zone, whereas the rapidity of the Λ and $\bar{\Lambda}$ candidates are evenly distributed about y_{cm} . Secondly, the shape of the acceptance window differs between the case of the K_S^0 and that of the Λ and $\bar{\Lambda}$.

The K_S^0 candidates all being forward of the collision zone is due to the acceptance of the experiment. The decay particles are of the same species (except charge

conjugated) and so they both (on average) carry approximately equal momentum. As a result the two pions will each bend significantly and as such it is unlikely that the decay tracks will fulfil the trigger requirements of the experiment (i.e. both tracks must pass through the *SPH* scintillators upstream of the telescope and one track must pass through the *ST2* scintillator downstream of the compact part of the telescope, as described in section 2.4.4) if the K_S^0 candidate originated from behind the collision zone ($y < y_{cm}$). In the case of the Λ , where the much heavier baryon takes the majority of the momentum compared with the lighter pion, the baryon will bend only a small amount and therefore will almost certainly pass through the telescope. This greatly increases the probability that both pion and proton can be reconstructed for $y < y_{cm}$ in the case of a Λ decay, and also that the trigger conditions be satisfied.

The difference in shape between the acceptance windows of the K_S^0 and the Λ (or $\bar{\Lambda}$) can be understood from (4.2), where for a given θ , the value of p_T depends only on y and m . The range of y is much smaller for K_S^0 and values are all greater than y_{cm} . As p_T increases more rapidly as y gets larger it follows that the lower and upper curvature of the window will rise sharply over the small change in rapidity. The shape will further be altered as $m(K_S^0)$ is less than half that of $m(\Lambda)$.

5.7 K_S^0 Transverse Mass Spectra

The differential distribution parameterisation of (4.4) which assumes a flat rapidity distribution and was used on the Λ and $\bar{\Lambda}$ weighted data cannot be used for the weighted K_S^0 data.

The rapidity distribution of the K_S^0 particle is shown in figure 5.10, from which it can be seen that the distribution increases towards central rapidity. It cannot be described as flat. For this reason the double differential parameterisation of (4.3)

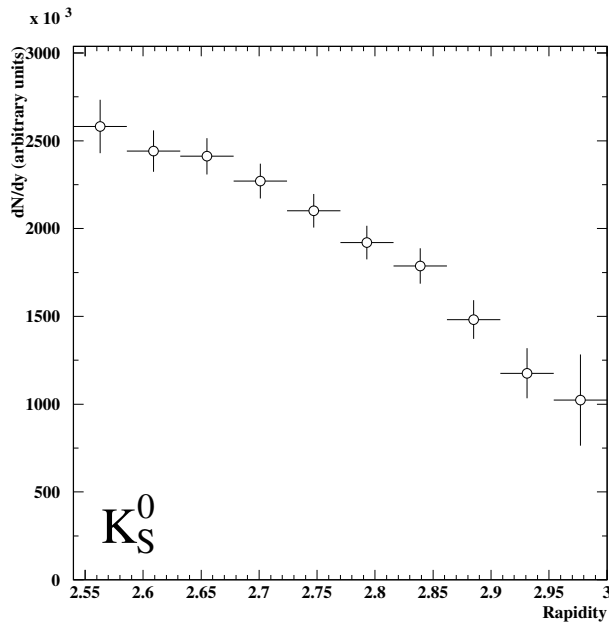


Figure 5.10: The rapidity distribution for the K_S^0 particle. It can be seen that this distribution is increasing towards central rapidity.

was used for the K_S^0 analysis where $f(y)$ takes the form of a straight line

$$\frac{d^2N}{dm_T dy} = A (1 + ky) m_T e^{-m_T/T} \quad (5.4)$$

where A is the normalisation constant and k is defined as b/c where b and c are the gradient and intercept of the straight line respectively. These latter two parameters were obtained from a fit to the rapidity distribution of figure 5.10 and their values are summarised in table 5.3. As the rapidity interval over which the weighted K_S^0

Table 5.3: Fit parameters of gradient, b , and intercept, c , which define the straight line fitted to the K_S^0 rapidity distribution.

Parameter	Value
b	$(-3.6 \pm 0.3) \times 10^6$
c	$(12.02 \pm 0.96) \times 10^6$

candidates lie is small (< 0.5 units), compared with the rapidity range expected

from collisions of 40 GeV/c momenta (~ 4.4 units), a straight line fit is a valid fit to the data.

Using the maximum likelihood fit of (5.4) to the weighted K_S^0 data, inside of the acceptance window of table 5.2, the inverse slope parameter, T , has been obtained. The results from which can be seen in figure 5.11 where $\ln\left(\frac{1}{m_T} \frac{dN}{dm_T}\right)$ is plotted against m_T . The fit to the data shown is that obtained from the maximum likelihood fit and is seen to fit the data very well. The inverse slope is summarised in table 5.4.

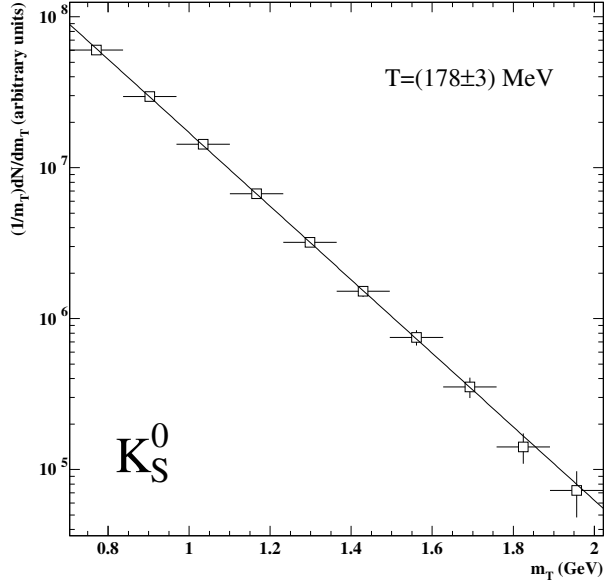


Figure 5.11: $\ln\left(\frac{1}{m_T} \frac{dN}{dm_T}\right)$ versus m_T for the K_S^0 particle. The fitted line was obtained using a maximum likelihood fit.

Table 5.4: Inverse slope obtained using a maximum likelihood fit for the weighted K_S^0 candidates within the acceptance window.

Particle	Inverse Slope, T (MeV)
K_S^0	178 ± 3

5.8 K_S^0 Yield

The yield, as described in section 4.6, for the K_S^0 (number of K_S^0 s produced per interaction) was calculated using (4.5). As the K_S^0 candidates were taken from the same runs as the Λ and $\bar{\Lambda}$, the denominator remains the same. Furthermore, as all the gold-plated K_S^0 candidates were weighted, the ratio, $R_{tw} = 1$.

An extrapolated yield was then obtained by using a similar expression to (4.7):

$$Yield_{ext} = \int_m^\infty dm_T \int_{y(min)}^{y(max)} \frac{d^2N}{dm_T dy} dy \left(\frac{1}{y(max) - y(min)} \right) \quad (5.5)$$

where $\frac{d^2N}{dm_T dy}$ assumes the parameterisation of (5.4) and $y(min)$ and $y(max)$ are defined in table 5.2. The limits $y(min)$ and $y(max)$ replace those in (4.7) of $(y_{cm} - 0.5)$ and $(y_{cm} + 0.5)$, used for the Λ and $\bar{\Lambda}$ data, as the K_S^0 data is not centred on y_{cm} . By using the same limits for the K_S^0 particle as for the Λ and $\bar{\Lambda}$ particles would involve extrapolation over a region in rapidity for which there was little or no K_S^0 data. By using the limits in (5.5) allows extrapolation only over the region in which there is data: the factor $\left(\frac{1}{y(max) - y(min)} \right)$ normalises the result to one unit of rapidity.

Finally, the extrapolated yield was divided by the branching ratio for the decay $K_S^0 \rightarrow \pi^- \pi^+$ which is 0.6895 ± 0.0014 [6]. This is necessary to account for the decay modes not detected by the experiment: the majority of which, 0.3105 ± 0.0014 , is due to the unseen decay mode $K_S^0 \rightarrow \pi^0 \pi^0$.

The final extrapolated yield for the K_S^0 is given in table 5.5, where the error quoted is statistical only (section 4.9).

5.9 Stability of Results

The two checks for stability of the inverse slope and extrapolated yield used for the Λ and $\bar{\Lambda}$ in section 4.7, were repeated for the K_S^0 . The first check, the time period

Table 5.5: K_S^0 extrapolated yield in the rapidity interval $2.54 < y < 3.00$ (normalised to one unit of rapidity) at 40 GeV/c

Particle	Yield (Particles/interaction)
K_S^0	0.0323 ± 0.0008

check, ensured the results were stable across the entire running period. The second check, the acceptance window check, ensured the choice of acceptance window did not bias the results.

The time period check was performed in the same way to that of the Λ . The running period was divided into the same six consecutive time periods as in table 4.5, except the number of weighted candidates within each was ~ 800 . The separately calculated inverse slopes and extrapolated yields for each were seen to be stable.

As the acceptance window check was not illustrated for the Λ or $\bar{\Lambda}$ candidates, it is the results of this check for the K_S^0 which will be shown and described further here.

Figure 5.12 shows the three different windows used. The central window (solid outline) is that whose details are given in table 5.2 and shown in figure 5.9. One larger and one smaller window (dashed outlines) are also shown. Whilst the choice of the smaller window was restricted to some extent to avoid low statistics, the choice of the larger window was restricted so as not to include too many of the ‘high’ weights (weights greater than ten times the minimum weight, section 4.4). It was impossible not to include any high weights as the window, of table 5.2, used for the analysis was chosen so as to include as many low weighted candidates as possible and no high weights. In all 37 high weights were included within this larger window, but none of which were greater than eighteen times the minimum weight. The data of figure 5.9 is not superimposed on figure 5.12 in order that the three windows can be seen clearly. The number of weighted candidates within each of the three windows

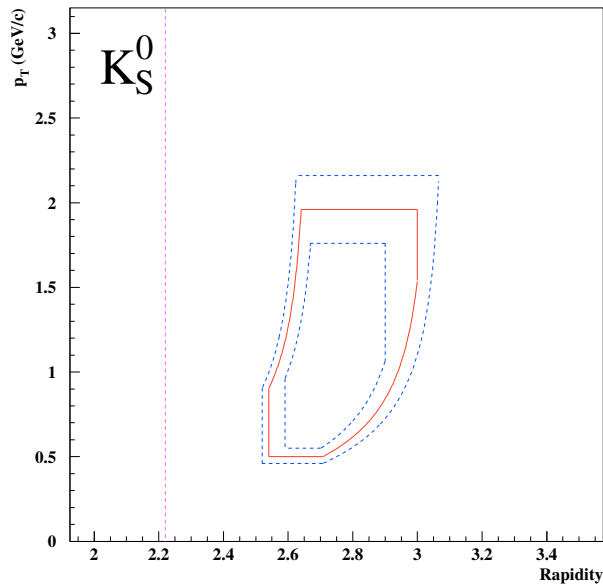


Figure 5.12: p_T versus rapidity showing the three acceptance windows. The middle window (solid outline) is that used for the K_S^0 analysis.

are given in table 5.6. The results for the three acceptance windows are shown in

Table 5.6: The number of weighted candidates within each of the three acceptance windows used on the K_S^0 data to determine stability of the inverse slope and yield.

Window Number	Window Size	Weighted Candidates Within Window
-1	Small	2,924
0	Medium (used)	3,828
+1	Large	4,129

figure 5.13, the horizontal lines represent the values obtained for the window used for the final analysis (window 0). It is clear from which that the results are extremely stable across the three acceptance windows, and that choice of acceptance window does not bias the final results.

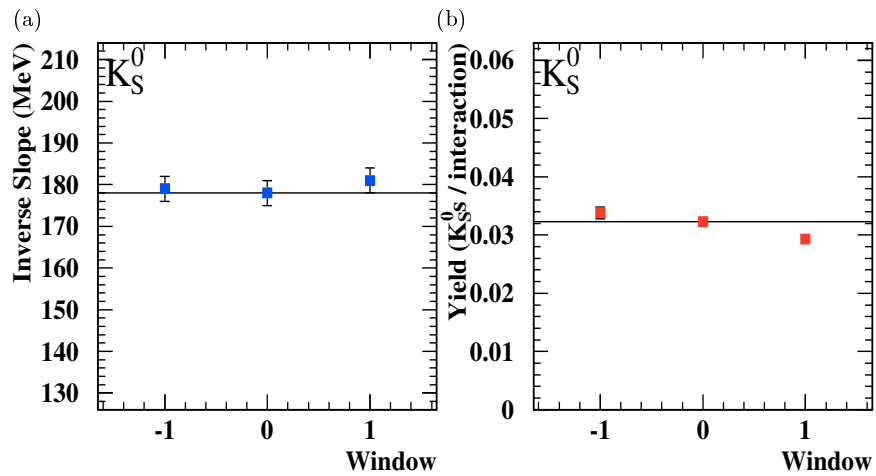


Figure 5.13: (a) Inverse slopes and (b) extrapolated yields for the K_S^0 , calculated separately using the three different acceptance windows. The horizontal line indicates the values of the final analysis (using window 0).

Chapter 6

Study of Systematics

6.1 Introduction

In chapters 3, 4 and 5 the analysis and results for the Λ , $\bar{\Lambda}$ and K_S^0 particle species from the 1999 p–Be data have been presented. The important results of inverse slopes and extrapolated yields, obtained from which, are so far only quoted with a statistical error. Of course, final physics results also require an estimation of a systematic error. In this chapter three major sources of systematic error are discussed: the total number of p–Be interactions, the assumed rapidity distributions and comparison of results between the two p–Be data sets taken by NA57. The first of these three is only applicable to the extrapolated yields, whereas the latter two apply to both the inverse slopes and extrapolated yields.

6.2 The Number of p–Be Interactions

In section 4.6 an overview was given describing how the number of p–Be interactions was calculated: one of the components of this calculation was the fraction of protons

in the beam. The proton fraction was determined in two ways: firstly a record was kept by the CERN beam physicists and secondly an offline investigation was carried out. A description of the latter is given here. There exists a small difference between the fraction of protons obtained using each method which provides the source of one of the largest systematic errors on the extrapolated yield.

During the 1999 p–Be data collection, four ‘special’ runs (taken at intervals across the entire running period) were made with only the beam trigger in place: these run numbers were 7143, 7171, 7252 and 7291. Now, the beam does not supply a continuous flux of particles, instead the particles arrive in small groups called ‘bursts’. Each run consists of ~ 100 bursts. For each burst the fraction of protons ($\overline{C1} \cdot \overline{C2}$) compared to other signals (pions, kaons and background noise) was calculated. Figure 6.1a shows, for run number 7143, the fraction of each burst which were not protons versus burst number¹. Figure 6.1b shows a projection of figure 6.1a, from which the mean fraction of run number 7143 which were not protons (\overline{p}_{mean}) was obtained. The fraction of protons from the run is simply $1 - \overline{p}_{mean}$. The fraction of protons obtained from each of the four special runs are summarised in table 6.1. The

Table 6.1: Proton fraction obtained from each of four special runs taken during 1999 data collection where only the beam trigger was implemented.

Run	Proton Fraction
7143	0.191 ± 0.010
7171	0.191 ± 0.009
7252	0.192 ± 0.008
7291	0.193 ± 0.009

overall proton fraction was obtained by taking the weighted average of the results

¹This, and all other results in this section are courtesy of Dr. Roman Lietava of the University of Birmingham.

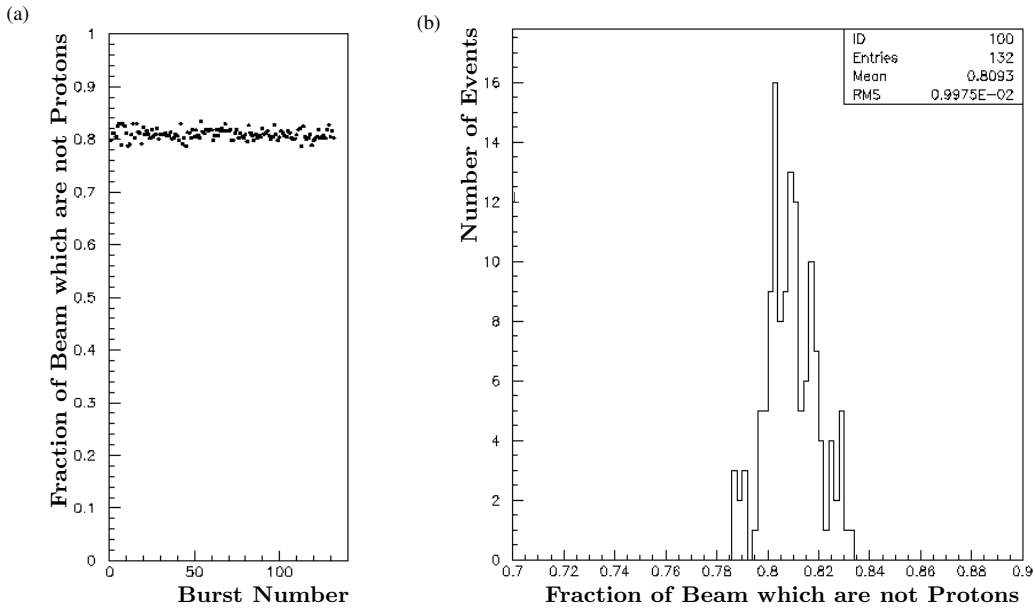


Figure 6.1: (a) Fraction of the beam which are not protons versus burst number for run number 7143, the projection of which is shown in (b).

from the four runs. This weighted average and its error are given by (6.1) and (6.2).

$$a = \frac{\sum (a_i / \sigma_i^2)}{\sum (1 / \sigma_i^2)} \quad (6.1)$$

$$1 / \sigma^2 = \sum (1 / \sigma_i^2) \quad (6.2)$$

where a_i is the fraction of protons in the i th run and σ_i is its associated error.

From which the offline investigation gave a proton fraction of 0.192 ± 0.005 . This compares to 0.21 recorded by the CERN beam physicists which was the fraction used for the final analysis. The 9% difference between these two figures provides the systematic error on the beam fraction.

6.3 Rapidity Distributions

As seen in chapters 4 and 5, one of the important factors in the parameterisation from which the inverse slope and extrapolated yield are obtained is the function, $f(y)$, which describes the rapidity distribution of a particular particle species. For the Λ and $\bar{\Lambda}$ particles a flat rapidity distribution (in common with all NA57 analysis), $f(y) = A$, was assumed. For the K_S^0 particle it was clear that the distribution was non-flat and so a straight line function to describe the rapidity distribution, $f(y) = A(1 + ky)$ was made. By considering a realistic alternative function to describe the rapidity distribution for each of the three particle species, an estimation of the systematic errors on the rapidity distributions can be made.

For the Λ particle the best alternative description of the rapidity distribution (shown in figure 4.5) was a straight line fit. The parameterisation of (5.4) was used both to extract the inverse slope, T , and obtain the extrapolated yield by using (4.7). The fit parameters of gradient, b , and intercept, c , are given in table 6.2 and the

Table 6.2: Fit parameters of gradient, b , and intercept, c , which define the straight line fitted to the Λ rapidity distribution.

Parameter	Value
b	$(-0.7 \pm 0.1) \times 10^6$
c	$(3.3 \pm 0.3) \times 10^6$

inverse slope and extrapolated yield in table 6.3

Figure 6.2 shows the rapidity distribution of the $\bar{\Lambda}$ particle. The flat description used for the full analysis is shown and is seen to fit the data reasonably well. It is clear a straight line function cannot be fitted to this distribution and so, instead, a Gaussian (*gauss*) distribution was fitted of the form

$$f(y) = e^{-\left[\frac{(y-\mu)^2}{2\sigma^2}\right]} \quad (6.3)$$

Table 6.3: Inverse slopes and extrapolated yields assuming different descriptions of the Λ rapidity distribution.

Description	Inverse Slope (MeV)	Extrapolated Yield (Λ s per interaction)
<i>flat</i>	158 ± 3	0.0290 ± 0.0008
<i>line</i>	170 ± 3	0.0288 ± 0.0008

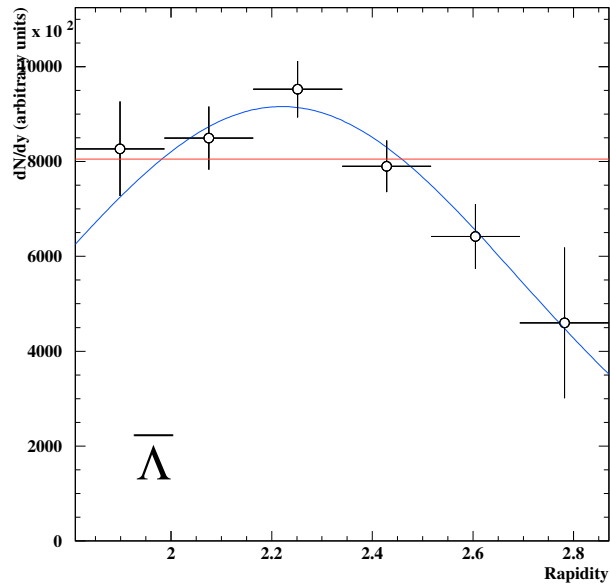


Figure 6.2: The rapidity distribution for the $\bar{\Lambda}$ particle, onto which is fitted a flat and a Gaussian description of the data.

where μ is the mean, fixed at central rapidity, and σ characterises the width which was set as a free parameter: determined as 0.470 ± 0.069 . This distribution is superimposed on figure 6.2. (6.3) was used in the parameterisation of (4.3) both to extract the inverse slope and the extrapolated yield by using (4.7). The results of which are given in table 6.4

Table 6.4: Combinatorial background uncorrected inverse slopes and extrapolated yields assuming different descriptions of the $\bar{\Lambda}$ rapidity distribution.

Description	Inverse Slope (MeV)	Extrapolated Yield ($\bar{\Lambda}$ s per interaction)
<i>flat</i>	119 ± 4	0.00348 ± 0.00019
<i>gauss</i>	125 ± 5	0.00319 ± 0.00018

For the K_S^0 particle (whose distribution is shown in figure 5.10) a Gaussian distribution was also fitted of the form (6.3), where again μ was fixed at central rapidity and σ was allowed to vary and was determined as 0.643 ± 0.038 . The inverse slope was obtained, again using (4.3). This parameterisation was then used in (5.4) to obtain the extrapolated yield. The results are seen in table 6.5

Table 6.5: Inverse slopes and extrapolated yields assuming different descriptions of the K_S^0 rapidity distribution.

Description	Inverse Slope (MeV)	Extrapolated Yield (K_S^0 s per interaction)
<i>line</i>	178 ± 3	0.0323 ± 0.0008
<i>gauss</i>	175 ± 3	0.0340 ± 0.0009

In each of the tables 6.3, 6.4 and 6.5 the differences between the two functions used to describe the rapidity distributions provides the source of systematic errors

on the inverse slopes and extrapolated yields from the rapidity distribution. A summary of these results is given in table 6.6

Table 6.6: Systematic effects on inverse slopes and extrapolated yields assuming different descriptions of rapidity distributions. Results are expressed as a percentage.

Particle Species	Inverse Slope	Extrapolated Yield
Λ	8%	1%
$\bar{\Lambda}$	5%	8%
K_S^0	2%	5%

6.4 Results from the 2001 p–Be Data

As can be seen from table 2.1 additional p–Be data at 40 GeV/c were taken by NA57 in 2001. The analysis of the Λ , $\bar{\Lambda}$ and K_S^0 particle species from these data has been performed by other members of the NA57 collaboration², who have also performed the systematic checks presented in section 6.5.7. The inverse slopes and extrapolated yields from these data are given in table 6.7. The $\bar{\Lambda}$ yield is corrected for combinatorial background, but the combinatorial background corrected $\bar{\Lambda}$ inverse slope is unavailable at present. All of the results in table 6.7 were calculated assuming a flat rapidity distribution.

The values from table 6.7 can be compared to the values obtained for the 1999 data set, where the values from tables 4.3, 4.4, 4.7 and 4.8 for the Λ and $\bar{\Lambda}$ are summarised in table 6.8. The K_S^0 results in this table assume a flat rapidity (so as the 1999 and 2001 results can meaningfully be compared) and thus differ from

²Dr. Ivan Králik and Mr. Marek Bombara, both of the Institute of Experimental Physics, Slovak Academy of Science, Košice, Slovakia.

Table 6.7: Inverse slopes and extrapolated yields at mid-rapidity ($|y - y_{cm}| < 0.5$) for the Λ , $\bar{\Lambda}$ and K_S^0 particle species obtained from the 2001 p-Be data

Particle Species	Inverse Slope (MeV)	Extrapolated Yield (Particles/Interaction)
Λ	140 ± 4	0.0401 ± 0.0011
$\bar{\Lambda}$	unavailable at present	0.00270 ± 0.00020
K_S^0	154 ± 2	0.0466 ± 0.0034

the results presented in tables 5.4 and 5.5. The results of the $\bar{\Lambda}$ are corrected for combinatorial background.

Table 6.8: Inverse slopes and extrapolated yields at mid-rapidity ($|y - y_{cm}| < 0.5$) for the Λ , $\bar{\Lambda}$ and K_S^0 particle species obtained from the 1999 p-Be data

Particle Species	Inverse Slope (MeV)	Extrapolated Yield (Particles/Interaction)
Λ	158 ± 3	0.0290 ± 0.0008
$\bar{\Lambda}$	109 ± 7	0.00230 ± 0.00020
K_S^0	168 ± 3	0.0394 ± 0.0010

The inverse slopes can be seen to be systematically lower in 2001 compared with 1999, and the extrapolated yields systematically higher in 2001 compared with 1999. These differences are non-negligible and cannot be ignored. A detailed investigation has been made by the author and colleagues to try to understand the source of this discrepancy. Two of the more important of these investigations are described in the following two sections: section 6.5 consider the different software used for the two analyses, section 6.6 considers properties of the beam. Although neither of these investigations provides a satisfactory explanation for the discrepancies observed, they are instructive in estimating systematic errors. The investigation to account

for the discrepancy between the two data sets is still going on.

As the Λ data was the most plentiful of the three particle species studied and had a rapidity distribution centred about mid-rapidity, the investigations described in the following two sections have only been concerned with this particle species.

6.5 The Data Analysis Programs and Selection Criteria

Although each of the various analysis programs used for the 1999 and 2001 data analyses were fundamentally the same, they were developed independently so as to fulfil the particular requirements of the user and the specific details of the experimental setup for the data taking year in question. For the same motives, the selection criteria used to obtain gold-plated candidates were chosen independently for both analyses.

It was, therefore, necessary to ensure that the observed inconsistencies between the two data sets were not due to any unaccountable differences in analysis programs or selection criteria: to this end, the 1999 data was analysed with programs used for the 2001 data. Whilst the 2001 programs and selection criteria were changed as little as possible, certain things specific to the 1999 data set had to be changed for the results to be meaningful.

In the first five subsections of this section, each program used on the 2001 data is considered in turn where it is applied to the 1999 data. In the case of the ANALYZE reconstruction program, the selection criteria of the 2001 data are also implemented. The sixth subsection is a culmination of the first five subsections, where all of the 2001 analysis programs are used together on the 1999 data. The seventh subsection, for completeness, uses the 1999 analysis programs on the 2001 data.

Of course, to re-weight the entire 4,662 Λ candidates weighted for the full analysis (section 4.3) would have been both unrealistic and too CPU time intensive. Instead a much smaller sample of candidates was used for these investigations. For some investigations every 50th gold-plated Λ candidate was used (242 candidates in all), for others, every candidate from a specific run (or runs) was more appropriate. Despite the much lower statistics, the results from these investigations were valid as they were always compared to the results obtained using all of the 1999 analysis programs and selection criteria on the same 242 candidates or reconstructed candidates from the same run(s).

6.5.1 Monte-Carlo Simulation

Every 50th gold-plated Λ candidate (242 in all) were weighted using the 2001 GEANT program. The remainder of the weighting chain was performed using the 1999 programs used for the full analysis of chapter 4. After all the essential changes specific to the 1999 data set, one difference which remained was the 2001 program required 10,000 ‘good’ (i.e. having decay tracks tracing through the telescope) Monte-Carlo particles, instead of the 5,000 required by the 1999 program. Figure 6.3 shows a plot of weight obtained using the 2001 GEANT versus the weight obtained using the 1999 GEANT, for all of the Λ particles that were within one order of magnitude of the minimum weight. The line at 45° , inserted to guide the eye, enables one to see that the weights are the same regardless of which version of the GEANT program was used. Slight differences in the individual weights can be accounted for due to the different ‘seeds’ used to generate the ‘good’ Λ candidates. The inverse slopes and extrapolated yields, with the same 242 candidates, using both GEANT programs are given in table 6.9 (where the acceptance window used was that defined by table 4.2). It is clear from which that the results from using either GEANT program are consistent.

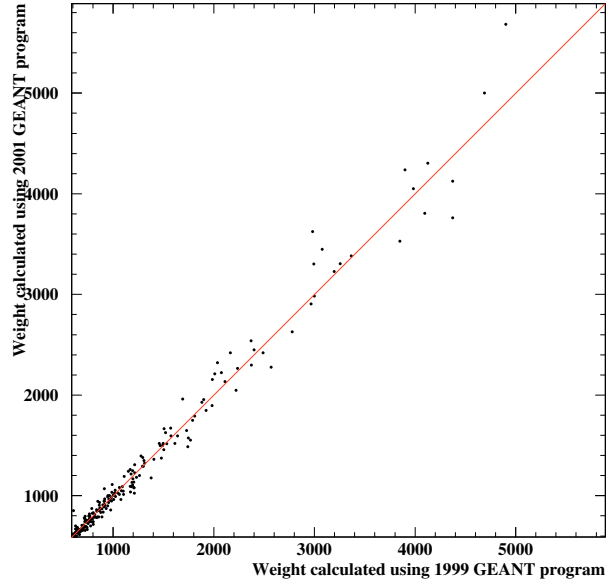


Figure 6.3: Comparison of the Λ weights calculated using the 1999 GEANT program and the weights calculated using the 2001 GEANT program, the rest of the weighting chain is that of the 1999 analysis.

Table 6.9: Inverse slopes and extrapolated yields for the 242 Λ which were weighted using the 1999 weighting chain and either the 1999 or 2001 GEANT program.

GEANT Program	Inverse Slope (MeV)	Extrapolated Yield (Particles/Interaction)
1999	172 ± 12	0.0263 ± 0.0031
2001	172 ± 11	0.0270 ± 0.0032

6.5.2 Background Mixing

Every 50th gold-plated Λ candidate (242 in all) were weighted using the 2001 MIXRAWMC program. The remainder of the weighting chain was performed using the 1999 programs used for the full analysis of chapter 4. Besides changing the run number and background tapes, no further modification to the 2001 MIXRAWMC program was needed for it to run on the 1999 data. The inverse slopes and extrapolated yields, with the same 242 candidates, using both MIXRAWMC programs are given in table 6.10 (where the acceptance window used was that defined by table 4.2). It is clear from which that the results from using either MIXRAWMC program are consistent.

Table 6.10: Inverse slopes and extrapolated yields for the 242 Λ which were weighted using the 1999 weighting chain and either the 1999 or 2001 MIXRAWMC program.

MIXRAWMC Program	Inverse Slope (MeV)	Extrapolated Yield (Particles/Interaction)
1999	172 ± 12	0.0263 ± 0.0031
2001	170 ± 12	0.0267 ± 0.0031

6.5.3 Track reconstruction

The track reconstruction stage of the weighting chain is perhaps the hardest stage to compare. Although the ORHION programs are essentially the same, they make use of a database which inputs into ORHION details specific to the particular data collection period: in particular, information on the efficiencies of the pixel planes, which will have changed over the four year running period of NA57.

However, the programs were compared in the following two ways. Firstly, every 1000th gold-plated Λ candidate (12 in all) was weighted using the 2001 ORHION

program (and 1999 ORHION database). The remainder of the weighting chain used the 1999 programs of the full analysis of chapter 4. The number of tracks found in the telescope by ORHION (tracks successfully reconstructed from the decay tracks of the 5,000 ‘good’ GEANT generated Λ candidates and the background tracks implanted by MIXRAWMC) and the weight assigned to each of these 12 candidates were compared to the values calculated for the same 12 candidates using the 1999 weighting chain: the results are shown in table 6.11. It is clear that the

Table 6.11: Number of tracks found in the telescope and weights calculated for each of 12 Λ candidates, which were weighted using the 1999 weighting chain and either the 1999 or 2001 ORHION program (and 1999 database in both cases).

Λ Candidate	Tracks in Telescope		Weight	
	1999 ORHION Program	2001 ORHION Program	1999 ORHION Program	2001 ORHION Program
1,000	8,199	8,204	$4,902 \pm 419$	$4,902 \pm 419$
2,000	10,738	10,738	674 ± 36	682 ± 36
3,000	9,557	9,549	955 ± 57	952 ± 57
4,000	9,526	9,519	911 ± 53	908 ± 53
5,000	9,763	9,762	$1,294 \pm 77$	$1,289 \pm 77$
6,000	9,162	9,173	$3,197 \pm 287$	$3,197 \pm 287$
7,000	9,962	9,954	714 ± 37	721 ± 37
8,000	8,867	8,864	$13,550 \pm 1,004$	$13,550 \pm 1,004$
9,000	10,279	10,295	688 ± 35	695 ± 35
10,000	9,248	9,266	$1,210 \pm 76$	$1,225 \pm 78$
11,000	8,294	8,296	$17,700 \pm 2,195$	$18,260 \pm 2,300$
12,000	8,526	8,539	$9,786 \pm 1,145$	$9,922 \pm 1,169$

number of tracks found in the telescope and the weights for each candidate are consistent regardless of which ORHION program was used. Secondly, the same 242

Λ candidates used in sections 6.5.1 and 6.5.2, were weighted using the 2001 ORHION program and the 2001 database. The remainder of the chain being that used for the full 1999 analysis. The results compared to using the complete 1999 weighting chain can be seen in table 6.12 (where the acceptance window used was that defined by table 4.2). Although it would clearly be wrong to use the 2001 database in

Table 6.12: Inverse slopes and extrapolated yields for the 242 Λ which were weighted using the 1999 weighting chain and either the 1999 or 2001 ORHION program and database.

ORHION Program	Inverse Slope (MeV)	Extrapolated Yield (Particles/Interaction)
1999	172 ± 12	0.0263 ± 0.0031
2001	170 ± 12	0.0281 ± 0.0031

ORHION for the full 1999 analysis, it is clear from table 6.12 that the results using either ORHION program (and database) are consistent.

6.5.4 V^0 Reconstruction and Selection Criteria

The V^0 reconstruction program, ANALYZE, which included within it the selection criteria applied to obtain gold-plated Λ candidates was perhaps the most likely of all the the analysis programs to cause the observed discrepancy. In addition to the differences in individual programs, which were modified significantly and independently for the 1999 and 2001 analysis, the selection criteria, which although applied to largely the same parameters, were generally harsher in 2001 than those of 1999 due to the greater statistics of the raw data.

The 2001 ANALYZE program was verified by applying it to the 1999 data as was done for the previous stages of the weighting chain, as described in sections 6.5.1, 6.5.2 and 6.5.3. In addition, the ANALYZE program had also to be

applied to the real data, as the same ANALYZE program used for the weighting chain must, for consistency, also be used for selection of the real gold-plated data. For this reason it was not appropriate to use the sample of 242 Λ candidates used in the previous three subsections. Using the 2001 selection criteria and ANALYZE program would produce a different sample of gold-plated Λ candidates, which would not necessarily include all of the 242 candidates selected using the 1999 selection criteria and ANALYZE program, and therefore the comparison of inverse slopes and extrapolated yields would be unjustified. Instead, each of the two versions of ANALYZE were applied separately to the 1999 real data, from which two gold-plated Λ signals were obtained (the one obtained using the 1999 ANALYZE program is that given in figure 3.19a). Of interest within each signal were Λ s which originated from one of five randomly selected runs across the complete running period: 7136, 7172, 7242, 7266 and 7304.

The two samples were then weighted in turn: the sample obtained using the 1999 ANALYZE was weighted using the 1999 weighting chain, the sample obtained using the 2001 ANALYZE was weighted using the 2001 ANALYZE and the rest of the 1999 weighting chain. The number of candidates found in the five chosen runs of real data, N_{real} , along with the inverse slopes and extrapolated yields from the weighting chains for each of the two samples are shown in table 6.13 (where the acceptance window used was that defined by table 4.2). It is clear that the inverse slopes and extrapolated yields obtained using either ANALYZE program and selection criteria are consistent. Furthermore, despite the obvious differences in selection criteria, seen by the vast difference in N_{real} between the two samples, the agreement of the inverse slopes and extrapolated yields from table 6.13 shows how well the weighting chain procedure accounts for choice of selection criteria.

Table 6.13: Number of real Λ candidates found from within five randomly selected runs when using either the 1999 or 2001 ANALYZE program (including selection criteria). The inverse slopes and extrapolated yields of these candidates when weighted using the 1999 weighting chain and either the 1999 or 2001 ANALYZE program (including selection criteria) are also shown.

ANALYZE Program	N_{real}	Inverse Slope (MeV)	Extrapolated Yield (Particles/Interaction)
1999	684	161 ± 7	0.0251 ± 0.0017
2001	268	153 ± 10	0.0265 ± 0.0029

6.5.5 Weight Calculation

The WGTCAL programs, used to calculate the final weights, were the same for both the 1999 and 2001 analysis, and as such provide consistent results.

6.5.6 The 2001 Analysis Programs using the 1999 Data

In the previous five sections it has been shown that the observed inconsistencies between the results of the Λ in the 1999 and 2001 data, given in tables 6.8 and 6.7, cannot be accounted for by any one of the analysis programs alone. Indeed results from the 1999 data set were consistent in each stage regardless of which version of the analysis program was used. However, for completeness, a further analysis program check was performed. This check used all of the 2001 analysis programs and selection criteria on the 1999 data for both the extraction of real data (ORHION and ANALYZE) and for the subsequent weighting procedure. This check also enabled a systematic error on the analysis programs and selection criteria to be evaluated.

Nine randomly selected raw data files, obtained from the 1999 data collection, corresponding to run numbers 7136, 7147, 7172, 7186, 7222, 7242, 7266, 7294, 7304, were passed through the 2001 ORHION and ANALYZE programs. The former was

a stage not performed for the check of section 6.5.3, the latter included the 2001 selection criteria. The number of gold-plated Λ candidates found within these nine runs, N_{real} , were then weighted in turn using the complete 2001 weighting chain.

An inverse slope and extrapolated yield was then calculated (where the acceptance window used was that defined by table 4.2). These results, along with N_{real} , can be seen in table 6.14, where they are compared to the results obtained from the same nine runs using all of the 1999 analysis programs and selection criteria. As was expected from the results of the previous subsections, the inverse slope and

Table 6.14: Inverse slopes and extrapolated yields for the N_{real} Λ candidates identified from the real data (using the 2001 analysis programs) of nine randomly selected runs from the 1999 data. These candidates were then weighted using the 2001 weighting chain. The results are compared to analysis using all of the 1999 analysis programs.

Analysis Programs	N_{real}	Inverse Slope (MeV)	Extrapolated Yield (Particles/Interaction)
1999	1,361	163 ± 5	0.0267 ± 0.0013
2001	461	163 ± 8	0.0247 ± 0.0021

extrapolated yields using either the 1999 or 2001 analysis programs show consistency. Although the former are in complete agreement, a 3% systematic error was estimated on the inverse slope. The 7% difference between the latter provides the systematic error on the extrapolated yield.

6.5.7 The 1999 Analysis Programs using the 2001 Data

One final software check was performed, similar in nature to that of section 6.5.6. This check was performed using the 1999 selection criteria, GEANT and ANALYZE programs on the 2001 data, the remainder of the weighting chain was that used for the 2001 analysis. The differences in MIXRAWMC and WGTAL between 1999

and 2001 have already been shown in sections 6.5.2 and 6.5.5 not to be critical. Furthermore, ORHION, as explained in section 6.5.3, is specific to the data year in question and besides has also been seen in table 6.12 not to be critical.

This exercise was performed in a similar way to that of the previous section: namely, replacing the 2001 GEANT and ANALYZE programs in the real analysis and weighting chain with the 1999 programs. These analysis programs were used on data from run number 16436. Results of N_{real} , inverse slope and extrapolated yield as compared to the results using the entire 2001 analysis programs are given in table 6.15 [99].

Table 6.15: Inverse slopes and extrapolated yields for the N_{real} Λ candidates identified from the real data (using the 1999 ANALYZE program) of one randomly selected run from the 2001 data. These candidates were then weighted using the weighting chain which used the 1999 GEANT and ANALYZE programs. The results are compared to analysis using all of the 2001 analysis programs.

Analysis Programs	N_{real}	Inverse Slope (MeV)	Extrapolated Yield (Particles/Interaction)
1999	110	133 ± 17	0.0480 ± 0.0070
2001	55	150 ± 26	0.0430 ± 0.0080

As for table 6.14, the results of inverse slope and extrapolated yield using either the 1999 or 2001 analysis programs show consistency. Because of the lower statistics used for this check the systematic errors assigned in section 6.5.6 will be used in the calculation of the overall systematic error in section 6.7.

6.5.8 Summary of Checks on the Analysis Programs

In summary, studies have been carried out to ensure that the observed inconsistencies between the results from the two data sets were not due to any unaccountable

differences in analysis programs or selection criteria. The 2001 analysis programs have been tested extensively on the 1999 data, as have the 1999 analysis programs on the 2001 data. The results from all investigations show that for a given data sample consistent results are achieved regardless of which version of the analysis program(s) are used. Although these investigations cannot explain the observed inconsistency, they do allow a systematic error due to the software to be assigned to the inverse slopes and extrapolated yields of 3% and 7% respectively.

6.6 Properties of the Proton Beam

6.6.1 Beam Spread

The experimental set up for the 2001 p-Be running period was very similar to that of 1999, described in section 2.4. Perhaps the most important difference between the two set ups was that of the beam profile, and as such provided a source of systematic error. In 1999 the beam profile was elliptical in shape with widths in y and z characterised by $\sigma_y = 0.25$ cm and $\sigma_z = 0.5$ cm respectively. As the procedure for the reconstruction of V^0 candidates is heavily reliant on the position in z with which the candidate intersects with the beam, described in section 3.5, it is more important for the width of the beam to be narrower in z than in y . For this reason the elliptical shape of the beam was changed, such that for 2001 it was characterised by $\sigma_y = 0.3$ cm and $\sigma_z = 0.2$ cm respectively. Of course it was not possible to change the physical beam used for the data collection, but of interest here is how changing σ_z in GEANT would affect the inverse slope and extrapolated yield, and thus an idea of dependence of the weighting chain on the shape of the beam could be realised.

All analysis programs used were those used in the full 1999 analysis (of chapters 3 to 5). The 165 real gold-plated Λ candidates obtained from randomly chosen run 7172 were weighted three times: the only difference between each re-weighting was

σ_z in GEANT. The σ_z used were the measured 0.5 cm, the much larger 1.0 cm and the smaller 0.2 cm measured for the 2001 data collection. Results for inverse slopes and extrapolated yields as a function of σ_z are given in table 6.16

Table 6.16: Inverse slopes and extrapolated yields for the 165 Λ candidates of run 7172 which were weighted using the 1999 weighting chain, where a variety of beam profiles in GEANT were implemented.

σ_z (cm)	Inverse Slope (MeV)	Extrapolated Yield (Particles/Interaction)
0.2	163 ± 14	0.0233 ± 0.0033
0.5	159 ± 13	0.0245 ± 0.0035
1.0	162 ± 14	0.0238 ± 0.0034

The results are seen to vary very little as σ_z changes significantly, thus showing that the profile of the beam in the weighting chain is unimportant. However, the 3% difference in inverse slope and the 5% difference in extrapolated yield which exists between the results when σ_z is changed from the 1999 value to that of 2001 provides the systematic error due to the beam profile on these two parameters.

6.6.2 Beam Position

Like for the beam spread, the position of the beam was fixed throughout the real data collection and as such this position cannot be changed offline. Indeed the position of the beam in the important z direction, z_0 , was measured, and verified using the direct V^0 analysis, described in section 3.6, as -17.85 cm. However, what is of interest here is how sensitive the values of the inverse slope and extrapolated yields are to z_0 .

As in the previous section, the randomly chosen run 7172 was used. Three

positions of z_0 were chosen: the measured position of -17.85 cm and a 5 mm shift either side of this position, -17.35 cm and -18.35 cm. These values were used in turn in the V^0 reconstruction stage (the $xtarg$ selection criteria used to remove interactions with the $S4$ scintillator, shown in section 3.5, was adjusted each time to prevent either signal loss, or interactions with $S4$ being included in the results: this was necessary as a small shift in z_0 resulted in a large shift of $xtarg$). For each position of z_0 , the number of reconstructed Λ candidates, N_{real} , were then weighted. The only difference to the weighting chain used for the full 1999 analysis was z_0 in GEANT and ANALYZE, the $xtarg$ selection criteria in ANALYZE and a line beam was used in GEANT, $\sigma_y = \sigma_z = 0$ cm. The latter, although unrealistic, was used to allow the dependence of z_0 to be seen clearly. The values of N_{real} , inverse slope and extrapolated yield are given as a function of z_0 in table 6.17.

Table 6.17: Inverse slopes and extrapolated yields for the Λ candidates of run 7172 which were reconstructed successfully, N_{real} , as the position of the beam in z , z_0 , was varied.

z_0 (cm)	Shift (cm)	N_{real}	Inverse Slope (MeV)	Extrapolated Yield (Particles/Interaction)
-17.35	$+0.5$	167	163 ± 14	0.0199 ± 0.0028
-17.85	0.0	165	158 ± 13	0.0236 ± 0.0034
-18.35	-0.5	165	154 ± 13	0.0298 ± 0.0044

The results show a strong dependence of z_0 on inverse slope and extrapolated yield: moving z_0 up or down by 5 mm causes a change in slope and extrapolated yield of ~ 4 MeV and ~ 0.0050 As per interaction respectively. However, in order to account for the observed discrepancy z_0 would need moving by at least 1 cm (which would equate to a shift of ~ 10 cm in $xtarg$), this is clearly unrealistic considering the beam position is known and has been verified. As such it is not possible to consider a shift in z_0 greater than ± 0.5 mm. Using the linear nature of the results from table 6.17, a shift of $z_0 = \pm 0.05$ cm gives rise to a negligible systematic error

on the inverse slope and a small 2% systematic error on the extrapolated yield.

6.7 Estimation of Overall Systematic Errors

The individual systematic errors identified and estimated in this chapter were used to obtain an overall systematic error. This was done using (6.4):

$$Systematic = \sqrt{\sum_i^N S_i^2} \quad (6.4)$$

where *Systematic* is the overall systematic error and S_i are the various individual systematic errors ($S_1 \cdots S_N$) identified in this chapter. The individual and overall systematic errors on each of the three particle species are given in tables 6.18 and 6.19, where the former is for inverse slope and the latter for extrapolated yield. Although the software (which includes the analysis programs and selection criteria) and beam systematic errors were only estimated using the Λ data, the same analysis programs and beam were used for all three particle species and so the systematic error is assumed the same for all three cases.

The results from table 6.8 are given again in table 6.20 where the first error quoted is statistical and the second is systematic.

6.8 Conclusions

The main sources of systematic errors on the Λ , $\bar{\Lambda}$ and K_S^0 particle species from the 1999 p-Be data have been investigated in this chapter. From these, an overall systematic error has been estimated for the three particle species, whose results are shown in table 6.20. The systematic errors are fairly small on the inverse slope, but larger on the extrapolated yield, due largely to the systematic error on the fraction of the protons obtained from the beam. The reason for the inconsistency

Table 6.18: Summary of individual and overall systematic errors obtained for each of the three particle species studied on the inverse slope.

Source of Systematic	Λ (%)	$\bar{\Lambda}$ (%)	K_S^0 (%)
Rapidity Distribution	8	5	2
Software	3	3	3
Beam Spread	3	3	3
Beam Position	0	0	0
Overall	9	7	5

Table 6.19: Summary of individual and overall systematic errors obtained for each of the three particle species studied on the extrapolated yield.

Source of Systematic	Λ (%)	$\bar{\Lambda}$ (%)	K_S^0 (%)
Proton Fraction	9	9	9
Rapidity Distribution	1	8	5
Software	7	7	7
Beam Spread	5	5	5
Beam Position	2	2	2
Overall	13	15	14

Table 6.20: Results of inverse slopes and extrapolated yields for the Λ , $\bar{\Lambda}$ and K_S^0 particle species obtained from the 1999 p-Be data

Particle Species	Inverse Slope (MeV)	Extrapolated Yield (Particles/Interaction)
Λ	$158 \pm 3 \pm 14$	$0.0290 \pm 0.0008 \pm 0.0037$
$\bar{\Lambda}$	$109 \pm 7 \pm 8$	$0.00230 \pm 0.00020 \pm 0.00035$
K_S^0	$178 \pm 3 \pm 9$	$0.0323 \pm 0.0008 \pm 0.0044$

between the results from the 1999 and 2001 p–Be data has not yet been clarified, however it has been shown that it is not due to either the analysis software or the properties of the beam. One possible explanation for the observed inconsistency may be an error in the inclination of the silicon telescope which has a number of allowed set positions. Whilst its configuration for the 2001 data set has recently been re-checked and confirmed, a similar re-check for the configuration used for the 1999 p–Be data collection is no longer possible since the telescope has subsequently been reused (and thus each time reconfigured) for the 1999 Pb–Pb, 2000 and 2001 data collections. The investigation into the inconsistency is still going on. Irrespective of how the inconsistency is resolved it will be seen in the following chapter that a definite enhancement in all three of these particle species is observable when moving from p–Be to Pb–Pb collisions at $40 A \text{ GeV}/c$.

Chapter 7

Physics Interpretation of Results, Outlook and Conclusions

7.1 Introduction

In the previous four chapters of this thesis, the singly strange Λ , $\bar{\Lambda}$ and K_S^0 candidates have been reconstructed from the 1999 40 GeV/c p–Be data. These candidates were chosen based on a number of geometrical and kinematical selections, which allowed the extraction of signal with minimal background. The selected candidates were then corrected for detector and reconstruction efficiency, geometric acceptance, selection criteria and decay modes not detected by the experiment. This was achieved by assigning a weight to each gold-plated candidate, which was calculated by means of a Monte-Carlo procedure based on GEANT. From which, two important quantities: extrapolated yield (particles produced per interaction) and inverse slope (apparent temperature), along with an estimation of the statistical and systematic errors, for all three particle species have been obtained (as summarised in table 6.20). In this chapter the physical significance of these two results are addressed. The results are then compared to results from NA57 at the top SPS energy and to the results from

other experiments. A brief overview of the future heavy ion programme is presented before an overall conclusion given.

7.2 Strangeness Enhancement at 40 A GeV/c

As described in numerous places already in this thesis, the purpose of calculating an extrapolated yield in p–Be interactions for each particle species is to provide a reference for the extrapolated yield(s) calculated in Pb–Pb interactions at the same beam momenta, in this case 40 A GeV/c. From which, one can assess if an enhancement in strange particle production, for a given particle species, has occurred in Pb–Pb collisions with respect to p–Be collisions.

The Pb–Pb data, collected towards the end of 1999 as shown in table 2.1, was analysed using a similar procedure to that of the p–Be data. One major difference which existed however was that the data were divided into five centrality classes (labelled 0 – IV). These centrality classes contained data from the most peripheral collisions (class 0), where the average number of wounded nucleons, $\langle N_{wound} \rangle$, was 57 ± 5 to the most central collisions (class IV), where $\langle N_{wound} \rangle$ was 346 ± 1 [100]. An extrapolated yield was calculated for each centrality class.

Figure 7.1 shows a plot of extrapolated yield as a function of $\langle N_{wound} \rangle$ for both p–Be and Pb–Pb collisions [101, 102] for the three particle species studied in this thesis. The numerical values from this figure are given in appendix F. The yields are shown separately for particles which contain at least one valence quark in common with the colliding nuclei (left) and for those with no valence quark in common with the colliding nucleons (right). A steady increase of the particle yields as a function of participants is observed.

Of course, it is not unreasonable to assume that as the system size (i.e. $\langle N_{wound} \rangle$) increases the production of strange particles will also increase. What is of interest is

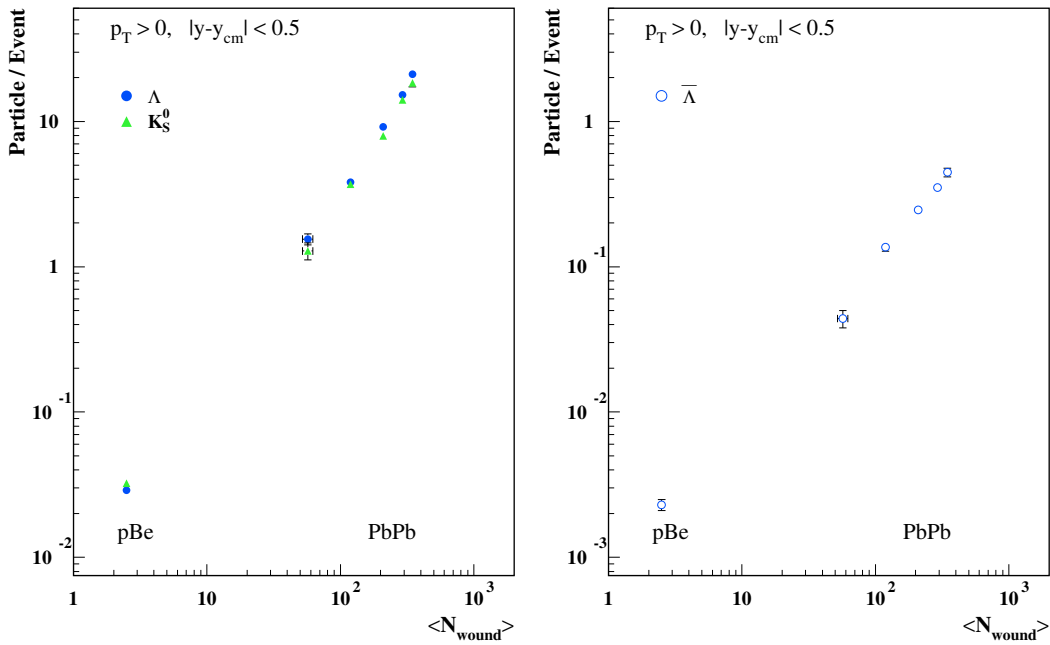


Figure 7.1: Particle yields from p–Be and Pb–Pb interactions at 40 A GeV/c as a function of the number of wounded nucleons using the results in this thesis. The vertical lines represents the statistical errors.

any enhancement of strange particles over and above this increase with $\langle N_{wound} \rangle$. In order to assess this one must define a quantity called strangeness enhancement, E :

$$E = \left(\frac{Y}{\langle N_{wound} \rangle} \right)_{Pb-Pb} / \left(\frac{Y}{\langle N_{wound} \rangle} \right)_{p-Be} \quad (7.1)$$

where Y is the extrapolated yield. The numerator of (7.1) calculates the yield per wounded nucleon in Pb–Pb collisions, the denominator does the same for p–Be collisions. This equation allows one to see immediately by what factor the production of strange particles increases (if at all) when going from the p–Be system (where a QGP is not expected to occur) to the Pb–Pb system (where a QGP is expected to form). As a yield has been calculated for each of the five Pb–Pb centrality classes it follows that a strangeness enhancement can also be calculated for each of these classes.

Figure 7.2 shows the enhancement of each of the three particle species studied

in this thesis: Λ , $\bar{\Lambda}$ and K_S^0 in the five Pb–Pb centrality classes at 40 A GeV/ c relative to the 1999 p–Be data. Also shown in this figure are the multistrange Ξ

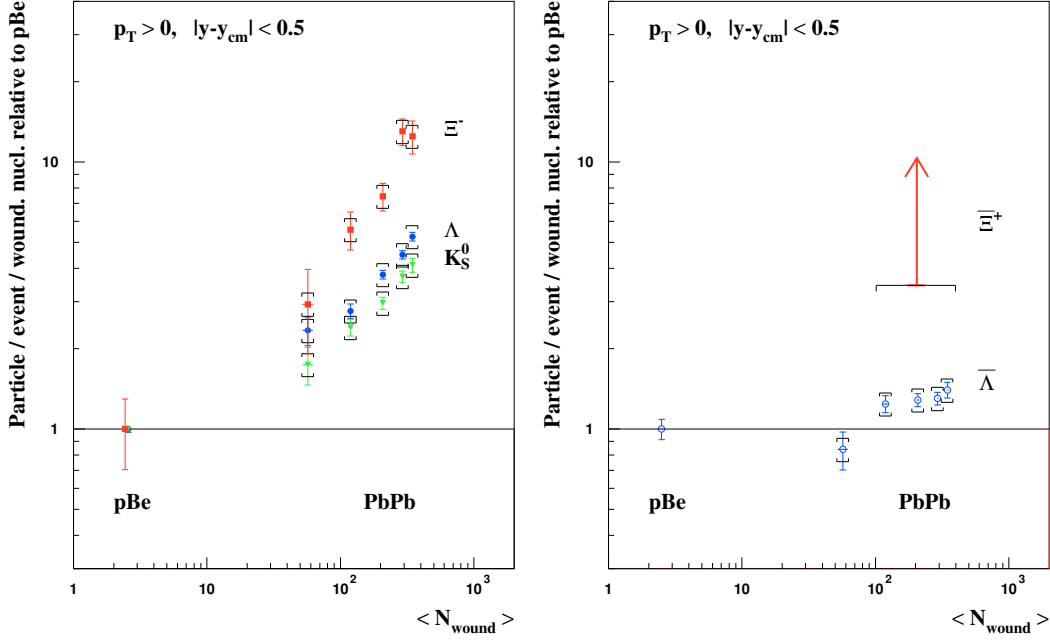


Figure 7.2: Particle yields per wounded nucleon in Pb–Pb, relative to p–Be, interactions at 40 A GeV/ c as a function of the number of wounded nucleons using the results in this thesis. The vertical lines represents the statistical errors, the \square symbols represents the systematic errors.

particles, whose values are published in [101]. Due to low statistics in the 1999 p–Be data, the Ξ^- Pb–Pb data are shown with respect to the 2001 p–Be data. Due to the low cross section and limited statistics, even in the 2001 p–Be data, only an estimation on the upper limit of the Ξ^+ yield in p–Be collisions could be made. From which a lower limit was placed on the Ξ^+ enhancement, with 95% confidence: this is shown by the arrow in figure 7.2. The horizontal line represents the predicted centrality dependence if the extrapolated yields were to increase proportionally to $\langle N_{wound} \rangle$ from p–Be to the most central Pb–Pb collisions. As for the yields, the enhancements are shown separately for particles which contain at least one valence quark in common with the colliding nuclei (left) and for those with no valence quark in common with the colliding nucleons (right).

From figure 7.2 it can be seen that there is a significant enhancement of strangeness production when going from p–Be to Pb–Pb in all particle species except for the $\bar{\Lambda}$, here an enhancement is observed in the four most central classes but not in the most peripheral class. The greater enhancement of particles over antiparticles of the same species is expected due to the valence quarks from the colliding nuclei which remain in the collision zone when hadronisation occurs.

For the Λ , $\bar{\Lambda}$ and K_S^0 particles the enhancement increases with centrality (although the centrality dependence is less strong for the $\bar{\Lambda}$). This is true also for the Ξ^- , although a small saturation in enhancement may exist for the two most central classes. Furthermore, an increased strangeness enhancement with strangeness content of the particle, predicted as a signature of a QGP, is also observed, namely: $E(\Lambda) \approx E(K_S^0) < E(\Xi^-)$ and $E(\bar{\Lambda}) < E(\bar{\Xi}^+)$.

It should be noted that normalising the Pb–Pb points to the 2001 p–Be reference points of table 6.7 for the Λ , $\bar{\Lambda}$ and K_S^0 particles would slightly reduce the magnitudes of the enhancements, for example the enhancements for the Λ would range from a factor of 1.7 to 3.8 (depending on centrality) compared to 2.3 to 5.3 using the 1999 p–Be point. However definite enhancements would still exist and the features of figure 7.2 discussed in this section and their physical interpretation remains the same.

7.3 Inverse Slopes at 40 A GeV/c

The inverse slopes, T , obtained from the m_T spectra, provide another source of physical interest, particularly when the 1999 40 GeV/c p–Be results are compared to the Pb–Pb results at the same energy. These results are shown in table 7.1, where the Pb–Pb values are for the most central 53% of the inelastic cross-section (corresponding to centrality classes 0 – IV) for Pb–Pb collisions and are published elsewhere [103, 104].

Table 7.1: Inverse Slopes for p–Be and the most central 53% of Pb–Pb collisions at 40 A GeV/c. Statistical (first) and systematic (second) errors are also quoted.

Particle Species	Inverse Slope (MeV)	
	p–Be	Pb–Pb
Λ	$158 \pm 3 \pm 14$	$261 \pm 4 \pm 26$
$\bar{\Lambda}$	$109 \pm 7 \pm 8$	$263 \pm 6 \pm 26$
K_S^0	$178 \pm 3 \pm 9$	$214 \pm 3 \pm 21$

From table 7.1 there are three interesting things to note. Firstly, the inverse slopes in p–Be collisions are all considerably lower than in Pb–Pb collisions. Secondly, there is $\sim 30\%$ difference between the inverse slopes of the Λ and $\bar{\Lambda}$ particle species for p–Be collisions, compared to less than 1% difference between these two particles in Pb–Pb collisions. Thirdly, the inverse slope increases by greater than 100 MeV when going from p–Be to Pb–Pb collisions for both Λ and $\bar{\Lambda}$ particles, whereas the increase for K_S^0 is much smaller at ~ 30 MeV. These three factors can be explained [4] and provide further evidence to suggest formation of a QGP at 40 A GeV/c.

As briefly outlined in section 4.5 the inverse slope, also known as the *apparent temperature*, is comprised of two parts: the local temperature, T_l , and transverse flow of the evolving hadronic matter. Now, the difference between the fireballs created by the p–Be and the Pb–Pb colliding systems is in the number of participant nucleons (described in section 1.5.1). With an increased number of participants a much hotter, denser fireball is created which leads to a larger and more violent explosion. This in turn enhances the transverse velocity, $\langle \beta_T \rangle$ (and hence the flow) at the time of particle production. Therefore a higher inverse slope is predicted in the extreme conditions created by colliding the heavier Pb–Pb ions together, compared with the much lighter p–Be system.

In section 1.6 it was discussed that in a hadron gas there is an asymmetry in particle production between strange particles of a given species and their associated antiparticle, for example the Λ is more readily produced than the $\bar{\Lambda}$. As a result, an asymmetry in m_T spectra, and thus inverse slopes, should also exist if the strange particles and antiparticles have been produced as a result of hadronic processes: this is observed in the p–Be collisions, where a QGP is not expected to form. In contrast, a symmetry in the m_T spectra (and hence inverse slopes) of strange particles and their associated antiparticles in Pb–Pb collisions suggests a common mechanism of strange particle and antiparticle production by a source such as a QGP fireball which treats matter and antimatter in the same way.

Finally, one can consider whether the smaller increase in slope can be accounted for when going from p–Be to Pb–Pb collisions for the K_S^0 particle, compared to the Λ and $\bar{\Lambda}$ particles. It has been predicted, in the regime of the QGP, that the inverse slope should increase with the mass of the particle, m_0 , for instance in [105] it has been derived that $T \approx T_i + m_0 \langle \beta_T^2 \rangle$. From which, due to its lighter mass, the inverse slope of the K_S^0 is expected to be lower than for the heavier Λ and $\bar{\Lambda}$ particles in Pb–Pb collisions (for the same $\langle \beta_T^2 \rangle$). Thus there will be a smaller increase for K_S^0 going from p–Be to Pb–Pb than for hyperons.

The difference in inverse slopes between the 1999 and 2001 p–Be data is of little importance here as the Pb–Pb values are much greater than either of the p–Be values for a given particle and the interpretation is not changed by using either result.

7.4 Comparison with Other Experiments

Comparing the p–Be 40 GeV/c results with other experiments is difficult since no other heavy ion experiment (with the exception of NA57’s predecessor: WA97) studies p–Be collisions. Although the NA49 experiment studies p–Pb collisions, it only does so at 158 GeV/c, so is of limited use in comparison to the p–Be data at

40 GeV/c. However, three comparisons can be made: firstly, the inverse slopes from the p–Be data can be compared with Pb–Pb results from other experiments at the same energy. Secondly, a compendium of p–p yields at a variety of energies has been made by [106] and, although no measurement at 40 GeV/c has been made, one can see how the NA57 p–Be results fit the general trend. Finally, the p–Be results at 40 GeV/c can be compared with those obtained by WA97 at 158 GeV/c. Each comparison is described in turn in this section.

Table 7.2 shows a comparison of the p–Be inverse slopes from NA57 at 40 GeV/c with the inverse slopes at the same energy using Pb–Pb collisions from NA49 [107, 108] (where the K_S^0 is assumed to be the average of the K^- and K^+) and Pb–Au collisions from NA45/CERES [109]. The results from which, along with the centrality and rapidity ranges with which they relate are presented in this table, where the NA57 results in the most central class (*IV*) [102] are also presented for completeness.

Table 7.2: Inverse slopes for NA57 p–Be and the most central Pb–Pb (NA57 and NA49) and Pb–Au (NA45/CERES) collisions at 40 *A* GeV/c. The bracketed rapidity value for NA49 applies to the K_S^0 result. Statistical (first) and Systematic (second) errors are also quoted (where available).

	Inverse Slope (MeV)			
	p–Be (NA57)	Pb–Pb (NA57)	Pb–Pb (NA49)	Pb–Au (CERES)
Centrality		0 – 5%	0 – 7.2%	0 – 4.8%
Rapidity		$ y - y_{cm} < 0.5$	$ y - y_{cm} < 0.4$ (0.1)	$ y - y_{cm} < 0.2$
Λ	$158 \pm 3 \pm 14$	$279 \pm 9 \pm 28$	$231 \pm 8 \pm 20$	273 ± 20
$\bar{\Lambda}$	$109 \pm 7 \pm 8$	$276 \pm 16 \pm 28$	$283 \pm 16 \pm 20$	–
K_S^0	$178 \pm 3 \pm 9$	$209 \pm 7 \pm 21$	$229 \pm 3 \pm 5$	–

From table 7.2 it can be seen that the Λ and $\bar{\Lambda}$ p–Be values at 40 GeV/c

are both significantly lower than the Pb–A values presented by NA57, NA49 and NA45/CERES. Although the K_S^0 values in p–Be are lower than the NA57 and NA49 Pb–Pb values, the difference is not as great, this is expected and was discussed in further detail in section 7.3. The Pb–A values from these experiments are all compatible within errors, the Λ result from NA57 and NA45/CERES are in very good agreement. A greater asymmetry in the NA49 results between the Λ and $\bar{\Lambda}$ results does exist compared to the NA57 results.

Attention now turns to strange particle yields, where a cross check on the order of magnitude of the NA57 yields, for all three particles studied in this thesis, taken over one unit of rapidity has been made to p–p yields taken over the entire rapidity spectra. The latter are a compilation of yields from p–p collisions from a variety of experiments at beam momenta between 2.8 GeV/c and 405 GeV/c which has been made by [106]. The yields are presented in figure 7.3 as a function of the Fermi variable, F [110]:

$$F = \frac{(\sqrt{s_{NN}} - 2m_p)^{3/4}}{\sqrt{s_{NN}}^{1/4}} \quad (7.2)$$

where $\sqrt{s_{NN}}$ is the centre of mass energy (described in appendix A, where it was referred to as E_{cm}) and m_p is the mass of the proton. The NA57 data at 40 GeV/c have a value of $F = 2.45 \text{ GeV}^{1/2}$.

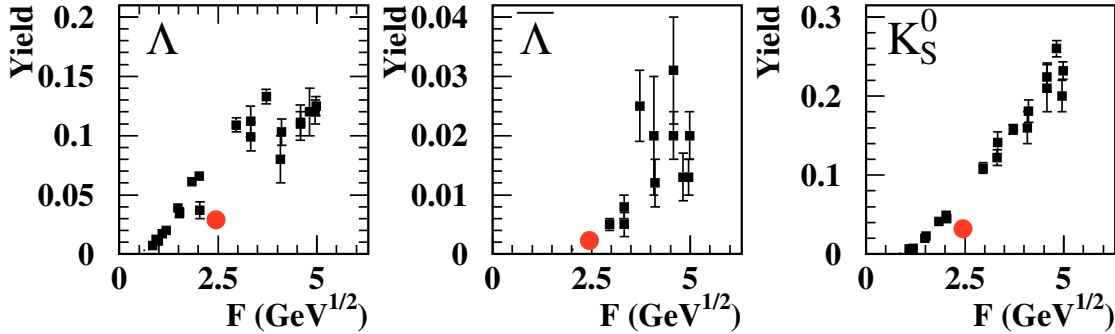


Figure 7.3: Comparison of NA57 yields over one unit of rapidity from p–Be collisions at 40 GeV/c (large dots) with yields over the entire rapidity spectra from p–p collisions (smaller squares) as a cross check on the order of magnitude of the NA57 yields. The yields of Λ , $\bar{\Lambda}$ and K_S^0 particles are presented as a function of the Fermi variable, F .

From this figure one can see that the NA57 p–Be yields at 40 GeV/c are clearly of the right order of magnitude. However, due to the differences in rapidity ranges between the data the yields of Λ and K_S^0 particles from p–Be data are lower than predicted by the trends of the p–p data. For this reason, this comparison is perhaps of limited use, however it does confirm the order of magnitude of the results and due to the lack of other published data for p–A collisions at 40 GeV/c it is worthy of discussion.

Finally, as mentioned above, the NA57 experiment and its predecessor, WA97, are the only heavy ion experiments that studied p–Be interactions. For completeness, a comparison is made here to the p–Be results obtained by WA97 (and used by NA57) at 158 GeV/c. The inverse slopes at 158 GeV/c are given later in table 7.4, a comparison of the yields are given in table 7.3 [70], where the results for the K_S^0 are excluded as no extrapolated yield was calculated in p–Be interactions at 158 GeV/c. A fuller table for all three particles studied, which includes the comparison of the Pb–Pb results is given in appendix F.

Table 7.3: Hyperon extrapolated yields for p–Be interactions at 40 GeV/c and 158 GeV/c. The errors quoted are statistical only.

Particle Species	Particles/Interaction	
	40 GeV/c	158 GeV/c
Λ	0.0290 ± 0.0008	0.0344 ± 0.0005
$\bar{\Lambda}$	0.00230 ± 0.00020	0.0111 ± 0.0002

From table 7.3 it can be seen that the yield increases for both particle species when going from 40 GeV/c to 158 GeV/c. This is expected and is due to the extra energy in the system at the higher collision energy making it easier to produce particles via hadronic processes.

7.5 Energy Dependence

The results of sections 7.2 and 7.3 are compared in the following two subsections to the results from NA57 at the top SPS energy of $158 A \text{ GeV}/c$ ($\sqrt{s_{NN}} = 17.3 \text{ GeV}$) and to the results from STAR at RHIC at both $\sqrt{s_{NN}} = 130 \text{ GeV}$ and 200 GeV . In addition, in the first of these two subsections, results are given from the AGS and other SPS and RHIC experiments.

7.5.1 Strangeness Enhancement and Particle Yields

Of course, as mentioned already, strangeness enhancement is not restricted to Pb–Pb collisions at $40 A \text{ GeV}/c$. Indeed, strangeness enhancement has been observed by a variety of experiments at different facilities over a wide energy spectra. This is illustrated well in figure 7.4 [111] which shows the ratio of the strange K^+ ($u\bar{s}$) particle to the non strange π^+ particle (K^+/π^+) as a function of the centre of mass energy, $\sqrt{s_{NN}}$, in nucleus–nucleus (A – A) and proton–proton (p–p) collisions. It can be seen that the K^+/π^+ ratio for A – A collisions follows a fast threshold rise in the AGS energy regime, the ratio then reaches a sharp maximum (or *peak*) at the low SPS energy regime, before settling to a lower plateau value for higher SPS and RHIC energies. The sharp maximum at low SPS energies is not observed in p–p collisions.

Whilst the interpretation of these results for (especially low) AGS energies is still under discussion, it is believed that the peak observed at low SPS energies for A – A collisions signals the collision energy required for the onset of the QGP phase [111, 112]. The peak is thought to occur due to the coexistence of hadronic and deconfined phases at energies around $30 A \text{ GeV}/c$ ($\sqrt{s_{NN}} = 7.6 \text{ GeV}$) [113, 114]. If this interpretation is correct, then it is clear from figure 7.4 that a QGP is expected to be formed at $40 A \text{ GeV}/c$ ($\sqrt{s_{NN}} = 8.73 \text{ GeV}$): a result which is supported in this thesis by the enhancements observed for all particle species in figure 7.2.

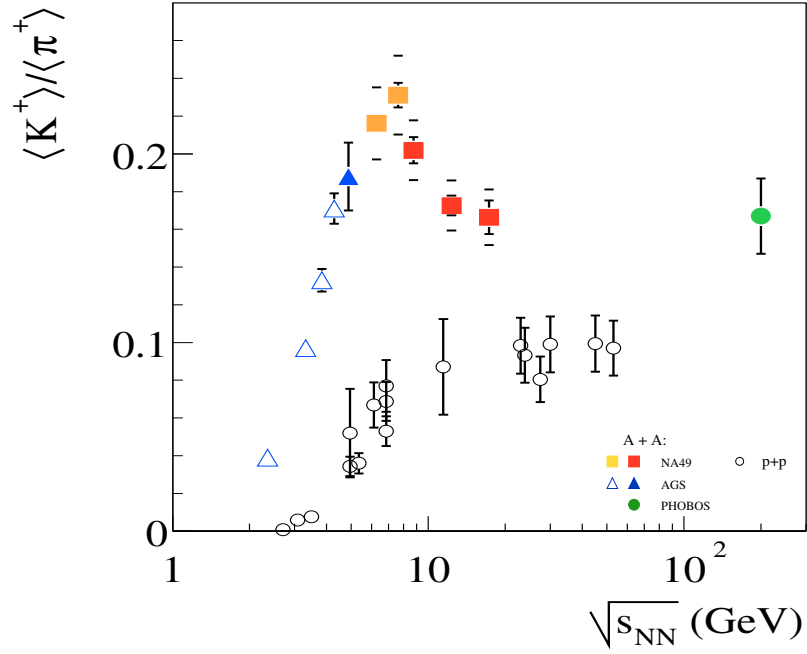


Figure 7.4: K^+/π^+ ratio as a function of the centre of mass collision energy for central Pb–Pb and Au–Au collisions (full symbols and open triangles) and inelastic p–p collisions (open circles). A distinctive maximum is seen in the low energy SPS region for A – A collisions indicating the possible onset of the QGP phase.

Attention now turns, in this section, to the results obtained at higher energy from NA57 at 158 A GeV/ c ($\sqrt{s_{NN}} = 17.3$ GeV) and from STAR at $\sqrt{s_{NN}} = 200$ GeV.

Figure 7.5 shows a similar plot to figure 7.2, whose layout is described fully in section 7.2, for beam momentum of 158 A GeV/ c . The Pb–Pb data were taken by NA57, the p–Be and p–Pb data by WA97. The particle yields per wounded nucleon in Pb–Pb [70, 115] and p–Pb collisions were both normalised, like for the 40 A GeV/ c results, to the p–Be values [70]. In the case of the K_S^0 particle the yields per wounded nucleon were normalised to the p–Pb value [28]. At this higher beam

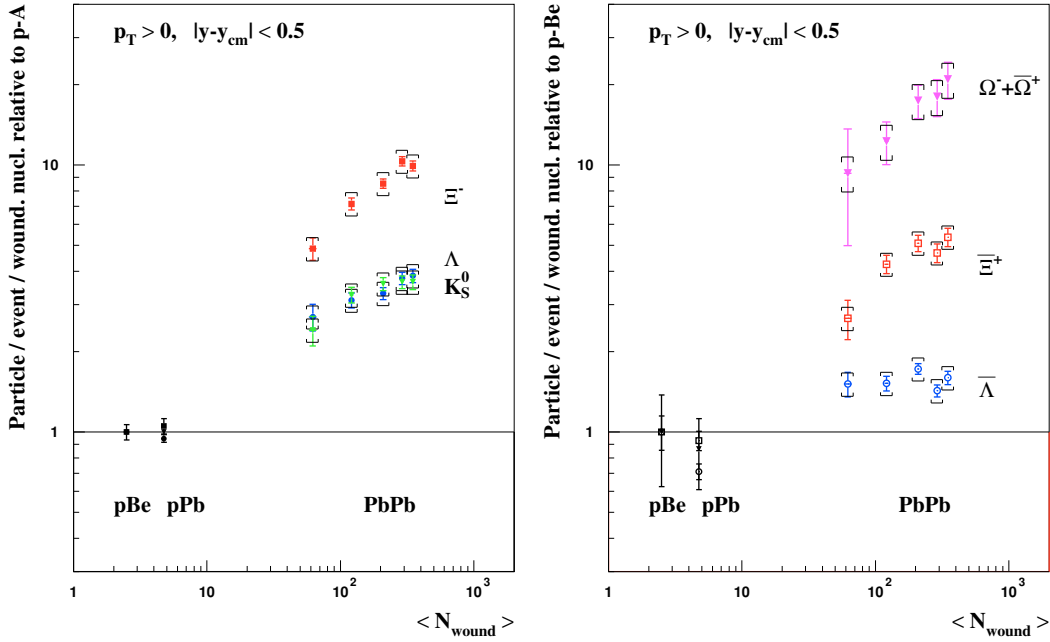


Figure 7.5: Particle yields per wounded nucleon in Pb–Pb, relative to p–Be (p–Pb in the case of K_S^0), interactions at 158 A GeV/ c as a function of number of wounded nucleons. The vertical lines represents the statistical errors, the \square symbols represents the systematic errors. (NA57 Collaboration).

momentum data was sufficient to study both the multistrange Ξ and Ω particles although, due to limited statistics, the Ω^- and $\bar{\Omega}^+$ data had to be combined.

The 158 A GeV/ c results confirm the pattern already observed by WA97 (shown in figure 1.7), i.e. the enhancement increases with strangeness content of the particle,

and extends the Pb–Pb measurements towards lower centrality.

Figure 7.6 shows another similar plot to figure 7.2 showing preliminary results for the STAR experiment at RHIC energy of $\sqrt{s_{NN}} = 200$ GeV [116]. Here the yield per participants (N_{part}) in Au–Au collisions are normalised to the yield per participants in p–p collisions.

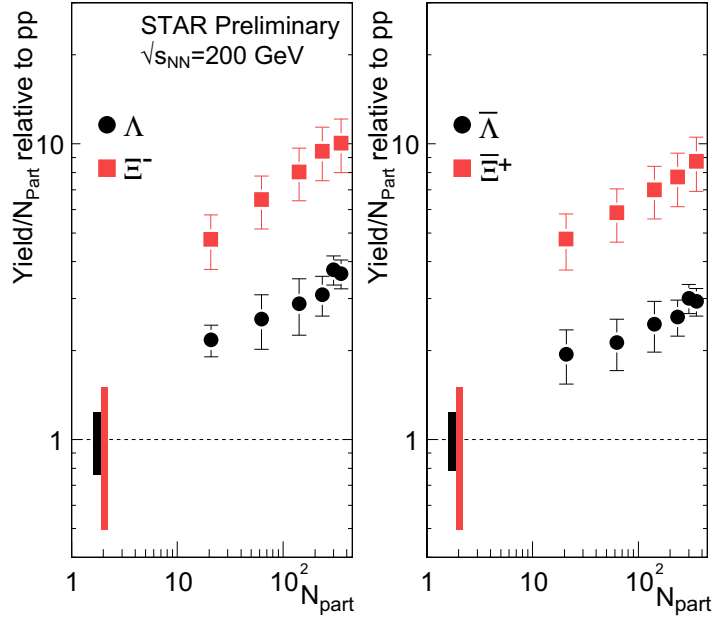


Figure 7.6: Particle yields per number of participants relative to p–p interactions at $\sqrt{s_{NN}} = 200$ GeV as a function of number of participants. The error bars represent the statistical errors, the range for the p–p results indicate the systematic uncertainty. (Preliminary results from the STAR Collaboration).

Comparing the results at $\sqrt{s_{NN}} = 17.3$ GeV and 200 GeV to those at $\sqrt{s_{NN}} = 8.73$ GeV one can see that for all particles and antiparticles the hierarchy of strangeness enhancement of $E(\Omega) > E(\Xi) > E(\Lambda)$ is observed at all energies. Furthermore, it can be seen that the increase in enhancements with $\langle N_{wound} \rangle$ is steeper at $\sqrt{s_{NN}} = 8.73$ GeV than at both $\sqrt{s_{NN}} = 17.3$ GeV and 200 GeV for the Λ and Ξ^- particles. The enhancement of the K_S^0 particle as a function of $\langle N_{wound} \rangle$ is also steeper at $\sqrt{s_{NN}} = 8.73$ GeV compared with $\sqrt{s_{NN}} = 17.3$ GeV. The enhancements

of the central most classes are greater at $\sqrt{s_{NN}} = 8.73$ GeV compared with $\sqrt{s_{NN}} = 17.3$ GeV and 200 GeV (in the case of the $\bar{\Lambda}$ the enhancements are similar in all three energy ranges, however at $\sqrt{s_{NN}} = 8.73$ GeV enhancements are seen only in the four most central classes).

These results of the strangeness enhancement hierarchy of multistrange over strange particles at all energies and the evidence for increasing enhancements with decreasing energy is predicted using the canonical suppression model [117, 118, 119]. This model is a statistical model which implements canonical strangeness conservation. Two types of system are considered in the model: the small system (such as p-p and p-A collisions) and the large system (such as A-A collisions). The small system is known as the *Canonical* regime, the large system as the *Grand Canonical* regime. In the Canonical regime all quantum numbers, for example strangeness, have to be conserved locally on an event-by-event basis, i.e. energy and volume has to be available for strangeness creation. This leads to the result that strange particle production is suppressed, known as *canonical suppression*, in small systems due to lack of phase space. Conversely in the Grand Canonical regime all quantum numbers need only be conserved within the system as a whole, but not necessarily locally. This removes the suppression and hence the strange particle production becomes constant. It is clear from the definition of strangeness enhancement given in (7.1) that if the denominator is reduced by canonical suppression then the enhancement is increased.

It turns out that the suppression factor for a given volume (assumed in the model to be proportional to N_{part} ($N_{part} = \langle N_{wound} \rangle$, as stated in section 1.5.1)) is smaller for particles of greater strangeness content [117]. Thus the model predicts the observed enhancement hierarchy of $E(\Omega) > E(\Xi) > E(\Lambda)$. This is shown in figure 7.7a for collisions at $\sqrt{s_{NN}} = 8.73$ GeV; the shape of each curve is a reflection of the transformation from the Canonical to the Grand Canonical regime in A-A collisions as N_{part} , or volume, increases. Finally, as the collision energy is increased

the suppression of the p–A interactions is reduced and hence the enhancement is also reduced [118]. The energy dependence for the Λ particle can be seen in figure 7.7b.

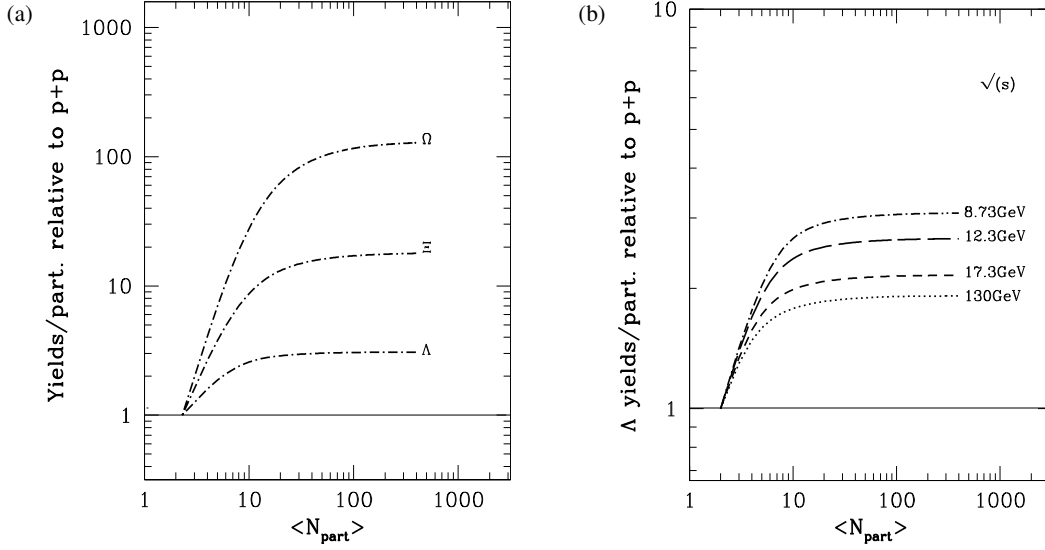


Figure 7.7: Predictions by the canonical suppression model of particle yields per participant in central Pb–Pb relative to p–p collisions illustrating (a) enhancement hierarchy and centrality dependence of enhancements in at $\sqrt{s_{NN}} = 8.73$ GeV and (b) Λ enhancements (relative to p–p collisions) at different collision energies.

By comparing the results of figures 7.2, 7.5 and 7.6 with the predictions of the model shown in figure 7.7 one can see the success of the model. For example, the model predicts accurately the enhancement hierarchy with strangeness content of the particle and also for a given particle species the increased enhancement with lower collision energy in the most central collisions. However, the model neither accurately predicts the correct amount of the enhancement or the centrality dependence which the results of figures 7.2, 7.5 and 7.6 exhibit. It is thought that the temperatures assumed by the model and the assumption that volume scales with N_{part} may be the cause of this discrepancy [120].

Finally, it is of interest to compare the extrapolated yields of the strange particles in A–A collisions as a function of energy. This is done in figure 7.8 where the yields per unit rapidity from NA57 at $\sqrt{s_{NN}} = 8.73$ GeV and 17.3 GeV are compared to

those from STAR at $\sqrt{s_{NN}} = 130$ GeV [98]. For the purposes of this comparison

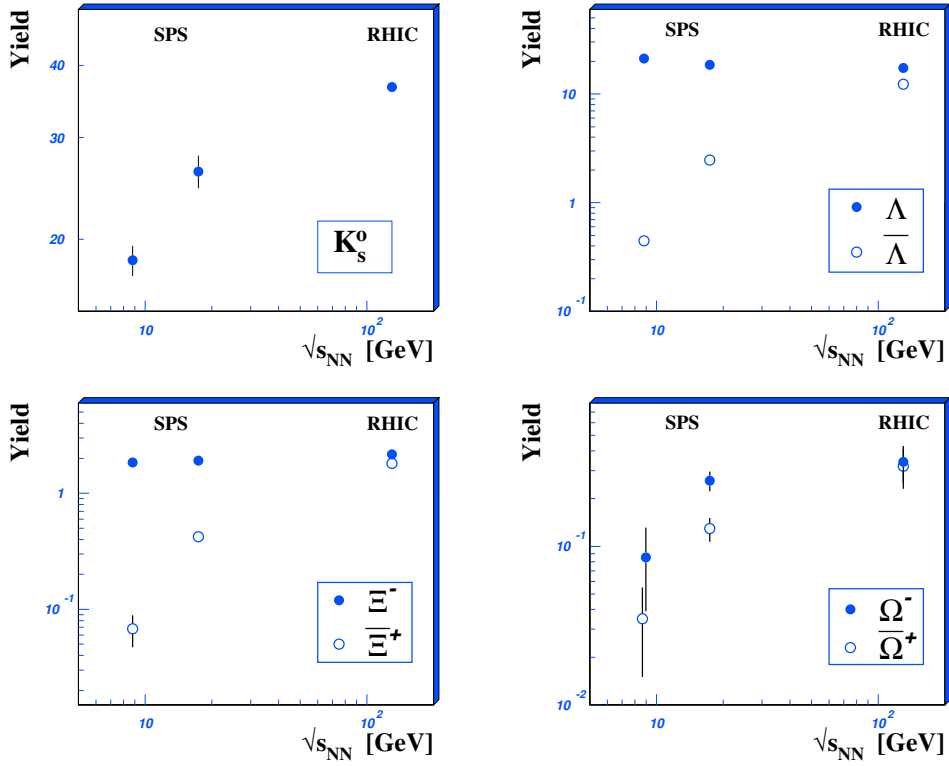


Figure 7.8: Energy dependence of extrapolated yields in A - A collisions for K_S^0 , Λ , Ξ and Ω as a function of energy.

the NA57 Pb-Pb data is restricted to the same ranges used for the STAR Au-Au data (i.e. the most central 6%, 5%, 10% and 11% for K_S^0 , Λ , Ξ and Ω respectively). The most striking feature of figure 7.8 is the different behaviour in the yields of the baryons and antibaryons as the energy increases. Whilst the Λ and Ξ^- yields do not vary much from the lowest SPS to RHIC energies, the antibaryons and K_S^0 yields are all seen to increase as the available energy increases. The increase in antibaryon and K_S^0 yields with collision energy can be understood as due to a decrease in net quark density with increasing collision energy. The approximately constant values of the Λ and Ξ^- yields over an order of magnitude increase in $\sqrt{s_{NN}}$ reflects an interesting balance between the decrease in net quark density, which causes a reduction in yields, and the increase in available energy, which causes an enlargement in yields [116].

7.5.2 Inverse Slopes

The inverse slopes at $\sqrt{s_{NN}} = 17.3$ GeV for the Λ , $\bar{\Lambda}$ and K_S^0 particle species in p–Be and the most central (53%) of Pb–Pb collisions have been obtained [95, 101] and are shown in table 7.4

Table 7.4: Inverse Slopes for p–Be and the most central 53% of Pb–Pb collisions at 158 A GeV/c. Statistical (first) and systematic errors, (second) are also quoted (where published).

Particle Species	Inverse Slope (MeV)	
	p–Be	Pb–Pb
Λ	180 ± 2	$289 \pm 7 \pm 29$
$\bar{\Lambda}$	157 ± 2	$287 \pm 6 \pm 29$
K_S^0	197 ± 4	$237 \pm 4 \pm 24$

The results show the same pattern as for $\sqrt{s_{NN}} = 8.73$ GeV, namely: the inverse slopes in p–Be are all lower than in Pb–Pb collisions, a large difference in slopes exist between Λ and $\bar{\Lambda}$ in p–Be collisions, whereas the Λ and $\bar{\Lambda}$ slopes in Pb–Pb collisions are the same. Finally, the difference between the inverse slope of the K_S^0 particle between p–Be and Pb–Pb is much smaller than for Λ and $\bar{\Lambda}$.

One difference which does exist between the values at $\sqrt{s_{NN}} = 8.73$ GeV and 17.3 GeV is that the magnitude of all values in table 7.4, for $\sqrt{s_{NN}} = 17.3$ GeV, are greater than the equivalent values for $\sqrt{s_{NN}} = 8.73$ GeV given in table 7.1: this is due to the difference in collision energy of the two systems. This result is confirmed in table 7.5 which shows the results from the most central Pb–Pb collisions at both NA57 energies [95, 102] and Au–Au collisions at STAR energy of $\sqrt{s_{NN}} = 130$ GeV [121].

Table 7.5: Inverse slopes for the most central Pb–Pb collisions at NA57 at $\sqrt{s_{NN}} = 8.73$ GeV and 17.3 GeV and Au–Au collisions at STAR at $\sqrt{s_{NN}} = 130$ GeV. The rapidity in all cases is $|y - y_{cm}| < 0.5$. Statistical (first) and Systematic (second) errors are also quoted.

	Inverse Slope (MeV)		
	Pb–Pb (NA57)	Pb–Pb (NA57)	Au–Au (STAR)
$\sqrt{s_{NN}}$	8.73 GeV	17.3 GeV	130 GeV
Centrality	0 – 5%	0 – 4.5%	0 – 5%
Λ	$279 \pm 9 \pm 28$	$305 \pm 15 \pm 31$	$307 \pm 6 \pm 28$
$\bar{\Lambda}$	$276 \pm 16 \pm 28$	$295 \pm 14 \pm 30$	$318 \pm 6 \pm 30$
K_S^0	$209 \pm 7 \pm 21$	$234 \pm 9 \pm 23$	$289 \pm 3 \pm 17$

7.6 Summary

By studying the yields per wounded nucleon and m_T spectra in both p–Be and Pb–Pb collisions at 40 A GeV/ c it is clear there is strong evidence (as described in this chapter) to suggest a QGP has been created in the laboratory in Pb–Pb collisions at the lowest SPS energy available to NA57. The results have been compared with a number of other experiments both at 40 A GeV/ c and at other energies. Comparison with other experiments at 40 A GeV/ c is difficult as p– A data is limited, however, comparison has been made with p–p data as well as with Pb–Pb data at this energy at NA45/CERES and NA49. Detailed comparisons have also been made with NA57 results at the top SPS energy and with the results from STAR at RHIC energies.

7.7 The Future for Heavy Ion Physics

NA57 has been successful in probing the QGP at both the SPS energies which it studied. However, the data taking era of NA57 has now come to a close and

the emphasis of current (RHIC) and future (LHC) experiments is to study the QGP using much higher energy beams, as outlined in section 1.8. In addition (also outlined in section 1.8), a proposal has been made to study heavy ion collisions at lower energies and high baryon densities using the CBM experiment at the GSI facility. One of the main aims of this latter proposal is to study the energy region in detail between AGS and SPS energies (2–45 A GeV/c) where the threshold collision energy for QGP formation is suggested to lie [111]. The CBM experiment will study gold–gold, uranium–uranium, proton–nucleus and proton–proton collisions and search for a number of signatures indicative of a QGP formation including strangeness enhancement. The proposed commission date for the experiment is 2014.

Of particular interest to the Birmingham Particle Physics Heavy Ion Group, is the ALICE experiment, shown in figure 7.9, which uses a dedicated detector to study heavy ion collisions at the CERN LHC. The machine will provide Pb–Pb collisions with a centre of mass energy of 5.5 TeV/c per nucleon. ALICE will be able to study the QGP at a variety of energy densities, with a maximum three orders of magnitude greater than NA57. The time in the QGP phase will also be increased by an order of magnitude and the initial colliding nuclei will not be in the collision zone by the time hadronisation occurs. ALICE is designed to study all major signatures of the QGP (i.e. unlike all previous experiments), including the signature of this thesis: strangeness enhancement.

Because of the high number of particles expected to be produced in a single LHC Pb–Pb interaction, statistics will be great enough to study K_S^0 and possibly Λ particles on an event by event basis, as shown by a Monte-Carlo simulation in figure 7.10 [15]. Also shown in this figure are the number of events which are required to see a Ξ and Ω signal, from which it is clear ALICE will be able to study these rarer doubly and triply strange particles with high statistics.

In addition to studying Pb–Pb collisions, ALICE will also study physics from proton–proton (p–p) and proton–nucleus collisions, as well as the collisions of lighter

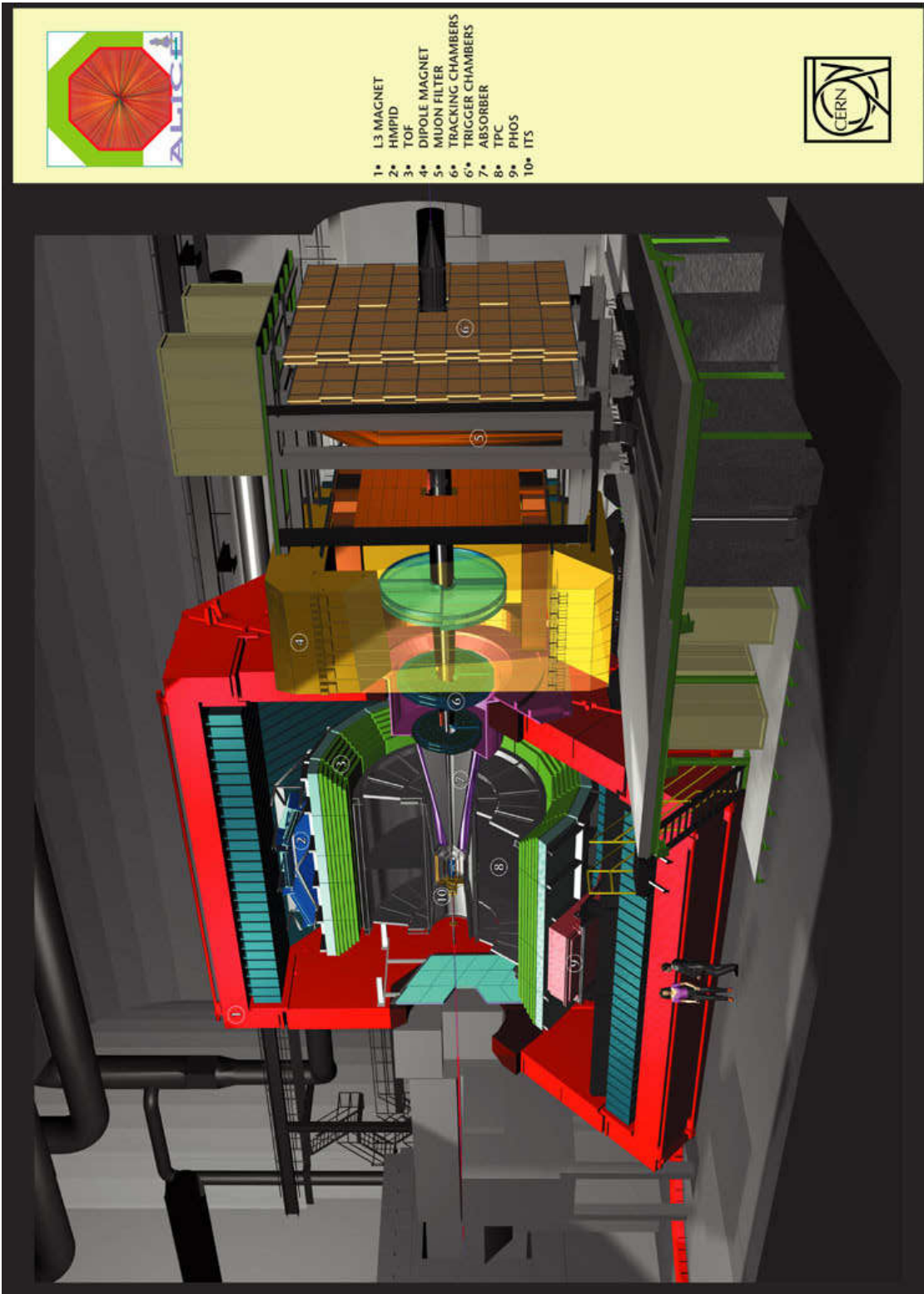


Figure 7.9: A schematic diagram showing the ALICE detector.

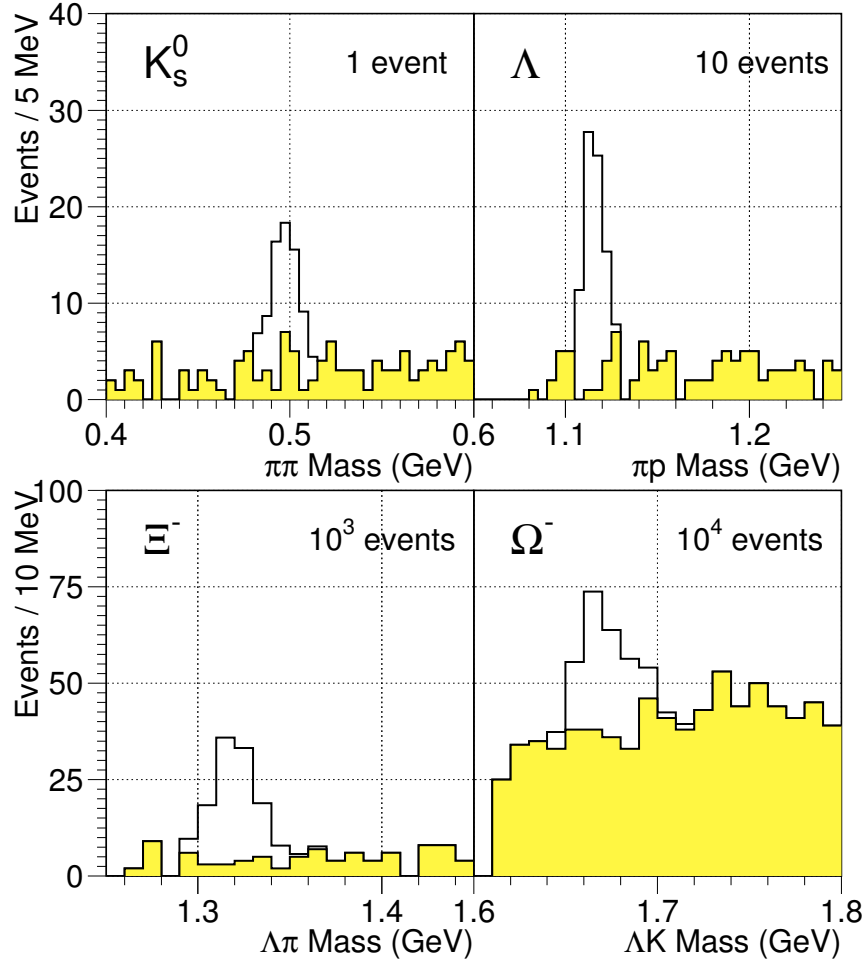


Figure 7.10: Effective mass distributions for the K_S^0 , Λ , Ξ^- and Ω^- candidates from 1, 10, 10^3 and 10^4 central Pb–Pb events, respectively, from an ALICE Monte-Carlo Simulation.

nuclei. p–p data will be the first data which will be obtained by ALICE when the LHC machine is switched on and will be used as reference data for Pb–Pb collisions. In addition, p–p physics can also be analysed in its own right by ALICE due to the excellent particle identification and tracking of the detector.

The ALICE detector is currently under construction at CERN, completion of which is expected by summer 2007 when the LHC begins operation.

7.8 Conclusion

NA57 has continued the work started by its predecessor WA97 in the search for deconfined strongly interacting matter, known as a QGP, which was thought to have existed until 10^{-5} seconds after the universe began. NA57 has confirmed the results of WA97 (but over a larger centrality range) at 158 A GeV/c, before turning its attention to a search for the QGP at the lower collision energy of 40 A GeV/c.

This thesis has been concerned with the singly strange Λ , $\bar{\Lambda}$ and K_S^0 particle production in the reference p–Be collisions at 40 GeV/c. The gold-plated particle samples underwent a GEANT Monte-Carlo simulation to correct for geometric acceptance and efficiency losses. Using the corrected samples, m_T spectra and extrapolated yields were calculated, where the results for the $\bar{\Lambda}$ were corrected for combinatorial background: which for this particle species was non-negligible.

From the corrected m_T spectra the inverse slopes (also known as the ‘apparent temperatures’) for each particle species were obtained. These were compared to the equivalent Pb–Pb results at the same energy, from which the p–Be values were all significantly lower and an asymmetry observed between the Λ and $\bar{\Lambda}$ results which was not observed in Pb–Pb collisions.

From the corrected p–Be yields, yields per wounded nucleon in each of the three particle species were calculated, these values were then used to normalise the Pb–

Pb yields per wounded nucleon. From which, enhancements could be seen for all particle species (with the exception of the $\bar{\Lambda}$ particles in the most peripheral Pb–Pb collisions). Enhancements could also be seen for the doubly strange Ξ particles, which were enhanced more than the singly strange particles, although statistics were insufficient to study the triply strange Ω particle. These results have been compared to results from NA57 at the top SPS energy and results from STAR at RHIC energies.

These results provide strong evidence to suggest deconfined strongly interacting matter has been created in the laboratory at the lowest SPS energy and provides evidence, along with other experiments, to suggest a QGP has been created. Attention in the field now turns to the ALICE experiment at the CERN LHC, due online in 2007, which will investigate all signatures of the QGP by colliding Pb ions with a centre of mass energy ~ 320 times greater than that of the top SPS centre of mass energy.

With new results currently being obtained from RHIC, the prospect of ALICE being switched on in two years time and the proposal of the CBM experiment at GSI aimed specifically at probing the threshold energy required to allow transition into the QGP phase, it is a very bright and exciting time in the field of QGP physics.

Appendix A

Energy Available for New Particle Production in Fixed Target and Colliding Beam Experiments

The energy available for new particle production when two ions interact differ depending on whether the two ions collide in a fixed target experiment or in a colliding beam experiment [2].

Consider one ion, with energy E_A and momentum \vec{p}_A interacting with a second ion, with energy E_B and momentum \vec{p}_B , all quantities are measured in the laboratory.

Now the 3-momentum, \vec{p} , of a system are the 3 components of momentum already met: p_x, p_y, p_z (section 1.5.2). This idea can be extended one step further to the 4-momentum, p , of a system where the first three components are simply the 3-momentum vector, \vec{p} , and the fourth component is iE where E is the total energy of the system and i is an imaginary number

$$p^2 = p_x^2 + p_y^2 + p_z^2 + (-iE)^2 \tag{A.1}$$

which can be rewritten as

$$p^2 = \vec{p}^2 - E^2 \quad (\text{A.2})$$

The centre of mass (*cm*) system is defined as the system in which $\vec{p} = 0$ and so (A.2) can be written as

$$p^2 = -E_{cm}^2 \quad (\text{A.3})$$

Combining (A.2) and (A.3) one can write the total *cm* energy for the two ion system described above:

$$E_{cm}^2 = -p^2 = E^2 - \vec{p}^2 = (E_A + E_B)^2 - (\vec{p}_A + \vec{p}_B)^2 \quad (\text{A.4})$$

and when multiplied out (A.4) becomes

$$E_{cm}^2 = E_A^2 + E_B^2 + 2E_A E_B - (\vec{p}_A^2 + \vec{p}_B^2 + 2\vec{p}_A \cdot \vec{p}_B) \quad (\text{A.5})$$

Using the well known relationship between E , \vec{p} and rest mass, m , of a particle

$$E^2 = \vec{p}^2 + m^2 \quad (\text{A.6})$$

(A.5) can be simplified to

$$E_{cm}^2 = m_A^2 + m_B^2 + 2E_A E_B - 2\vec{p}_A \cdot \vec{p}_B \quad (\text{A.7})$$

Now consider the two cases in turn:

1. In the *fixed target* case ion B is at rest in the lab system and therefore, $\vec{p}_B = 0$ and from (A.6) $E_B^2 = m_B^2$ and so (A.7) becomes

$$E_{cm}^2 = m_A^2 + m_B^2 + 2E_A m_B \quad (\text{A.8})$$

In this type of heavy ion collision $E_A \gg m_A, m_B$ and so E_{cm} for this type of collision is

$$E_{cm} \simeq \sqrt{2E_A m_B} \quad (\text{A.9})$$

2. In the case of the colliding beam experiments both beams have equal energy, $E_A = E_B$, and travel in opposite directions and so, $\vec{p}_A = -\vec{p}_B$ and so (A.7) becomes

$$E_{cm}^2 = m_A^2 + m_B^2 + 2E_A^2 + 2|p_A|^2 \quad (\text{A.10})$$

In this type of heavy ion collision $E_A \gg m_A, m_B$ which means (via (A.6)) $E_A \sim p_A$ and so (A.10) becomes

$$E_{cm} \simeq 2E_A \quad (\text{A.11})$$

Thus it can be seen how a greater cm energy can be achieved with colliding beam over fixed target experiments. The former scale as $\propto E_A$ as seen in (A.11), the latter as $\propto \sqrt{E_A}$ as seen in (A.9).

Appendix B

The Primary Vertex

The primary vertex ($xtarg$, $ytarg$, $ztarg$) is defined as the point at which the proton beam interacts with the beryllium target for a given V^0 candidate. $xtarg$ can be calculated as the point at which the V^0 intersects with a nominal beam, modelled as a horizontal line (i.e. zero gradient) increasing in the x -direction. The y and z coordinates of the beam are defined from the survey database as y_0 and z_0 respectively.

$xtarg$ can be calculated in either the $x - y$ or $x - z$ planes. The calculation used, that of the $x - z$ plane (section 3.5) is given here.

A given V^0 will come off from the target with a gradient, m_V :

$$m_V = \frac{p_z}{p_x} \tag{B.1}$$

where p_x and p_z are the x and z components of momentum of the V^0

Using this gradient and the decay vertex (the point at which the V^0 decays into two oppositely charged tracks) of the V^0 (x_1 , z_1), the intercept of the V^0 at the point $x = 0$ (c') can be calculated from the equation of a straight line: $z = mx + c$.

$$c' = z_1 - m_V x_1 \tag{B.2}$$

Now the gradient of the V^0 , modelled as a straight line, is known from (B.1), the coordinates at $x = 0$ are known (from (B.2)) to be $(0, c')$ and the primary vertex coordinates are $(xtarg, ztarg)$ where $ztarg$ is taken from the database and $xtarg$ is to be determined.

Now, the basic equation of a gradient is:-

$$m = \frac{z_a - z_b}{x_a - x_b} \quad (\text{B.3})$$

where (x_a, z_a) and (x_b, z_b) are two points on a straight line with gradient, m . Substituting into (B.3)

$$m_V = \frac{c' - ztarg}{0 - xtarg} \quad (\text{B.4})$$

Rearranging (B.4) and substituting m_V from (B.1) allows the value of $xtarg$ to be determined:

$$xtarg = \frac{ztarg - c'}{p_z/p_x} \quad (\text{B.5})$$

To complete the definition of the primary vertex $ytarg$ and $ztarg$ are also needed. $ytarg$ is the value in y of a given V^0 at $x = xtarg$, and as the beam has a finite width $ytarg$ need not necessarily equal y_0 . $ztarg = z_0$ by definition. Thus the value of the primary vertex can be calculated for each V^0 candidate.

Appendix C

The Armenteros-Podolanski Plot

C.1 Features of the Armenteros-Podolanski Plot

The features of the Armenteros-Podolanski plot [88] can be completely understood by considering the kinematics of the decay of a neutral V^0 candidate (for example a Λ) into two charged particles ($\Lambda \rightarrow p\pi^-$). To begin, this system has to be considered in both the laboratory system (in which measurements are made) and in the centre of mass system (in which the V^0 is at rest and consequently the two charged particles must come off back-to-back so as to conserve momentum) as shown in figure C.1.

It is clear from figure C.1b that in the centre of mass system the transverse and longitudinal momenta (discussed in section 1.5.2), relative to the direction in which the V^0 was moving in the laboratory system, are defined

$$q_T^* = p^* \sin\theta^* \tag{C.1}$$

$$q_L^* = p^* \cos\theta^* \tag{C.2}$$

where all quantities in the centre of mass system are denoted by a *

To express these quantities in the laboratory system requires the use of the

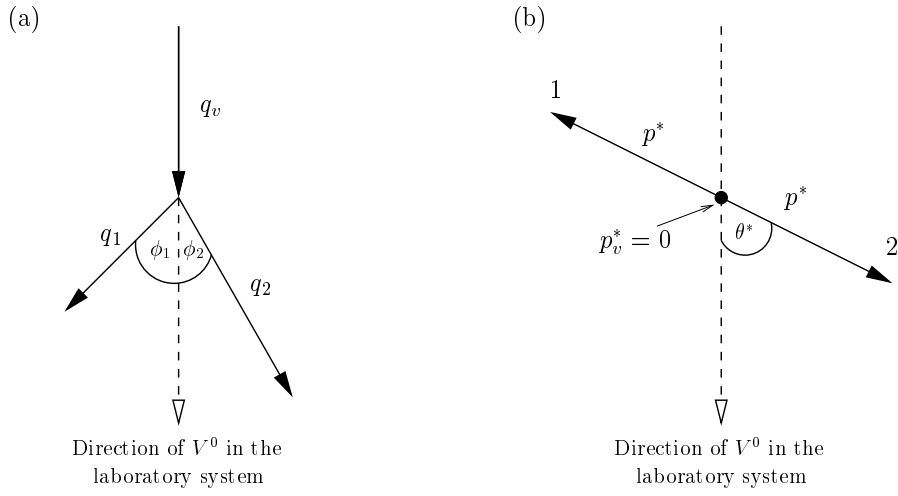


Figure C.1: The decay of a neutral V^0 into two charged tracks in (a) the laboratory system and (b) the centre of mass system. In the latter system the two decay particles must come off back-to-back so as to conserve momentum

Lorentz transformations

$$\begin{pmatrix} E \\ q_L \end{pmatrix} = \begin{pmatrix} \gamma & \gamma\beta \\ \gamma\beta & \gamma \end{pmatrix} \begin{pmatrix} E^* \\ q_L^* \end{pmatrix} \quad (\text{C.3})$$

where $\beta = v/c$: v is the velocity of the particle and c is the speed of light. γ is defined as $\gamma = 1/\sqrt{1-\beta^2}$.

When (C.3) is expanded it will give a definition of q_L in terms of q_L^*

$$q_L = \gamma\beta E^* + \gamma q_L^* \quad (\text{C.4})$$

Substituting (C.2) into (C.4) gives

$$q_L = \gamma\beta E^* + \gamma p^* \cos\theta^* \quad (\text{C.5})$$

As discussed in section 1.5.2 transverse momentum is Lorentz invariant and so

$$q_T = q_T^* = p^* \sin\theta^* \quad (\text{C.6})$$

Now *Armenteros alpha*, α , is defined

$$\alpha = \frac{q_L^+ - q_L^-}{q_L^+ + q_L^-} \quad (\text{C.7})$$

Using (C.5) and given that $\cos(\theta + \pi) = -\cos(\theta)$, (C.7) becomes

$$\alpha = \frac{\gamma\beta(E_1^* - E_2^*) + 2\gamma p^* \cos\theta^*}{\gamma\beta(E_1^* + E_2^*)} \quad (\text{C.8})$$

assuming particle 1 is the positively charged particle and particle 2 is the negatively charged one.

Now energy, E^* , is conserved and so in the centre of mass system,

$$E^* = E_1^* + E_2^* \quad (\text{C.9})$$

where using the relativistic equation $E^2 = p^2 + m^2$, E^* , E_1^* and E_2^* are given by

$$E^* = m_v, \quad E_1^* = \sqrt{p^{*2} + m_1^2}, \quad E_2^{*2} = \sqrt{p^{*2} + m_2^2} \quad (\text{C.10})$$

where in the centre of mass system the momentum of the V^0 , p_v^* , is zero.

By substituting (C.10) into (C.9)

$$E_1^* + E_2^* = m_v \quad (\text{C.11})$$

(C.11) can be used in (C.8), along with the approximation that relativistically $v \approx c$ and so $\beta \approx 1$. The γ s cancel and so (C.8) becomes

$$\alpha = \frac{(E_1^* - E_2^*)}{m_v} + \frac{2p^* \cos\theta^*}{m_v} \quad (\text{C.12})$$

From (C.12) the variables $\bar{\alpha}$ and a can be defined

$$\bar{\alpha} = \frac{(E_1^* - E_2^*)}{m_v} \quad (\text{C.13})$$

$$a = \frac{2p^*}{m_v} \quad (\text{C.14})$$

and so (C.12) can be re-written as

$$\alpha = \bar{\alpha} + a \cos\theta^* \quad (\text{C.15})$$

Making use of the trigonometrical relationship

$$\cos^2\theta + \sin^2\theta = 1 \quad (\text{C.16})$$

$\cos\theta$ and $\sin\theta$ can be substituted from (C.6) and (C.15) to give

$$\left(\frac{\alpha - \bar{\alpha}}{a}\right)^2 + \left(\frac{q_T}{p^*}\right)^2 = 1 \quad (\text{C.17})$$

which is simply the equation of an ellipse, whose parameters are shown in figure C.2

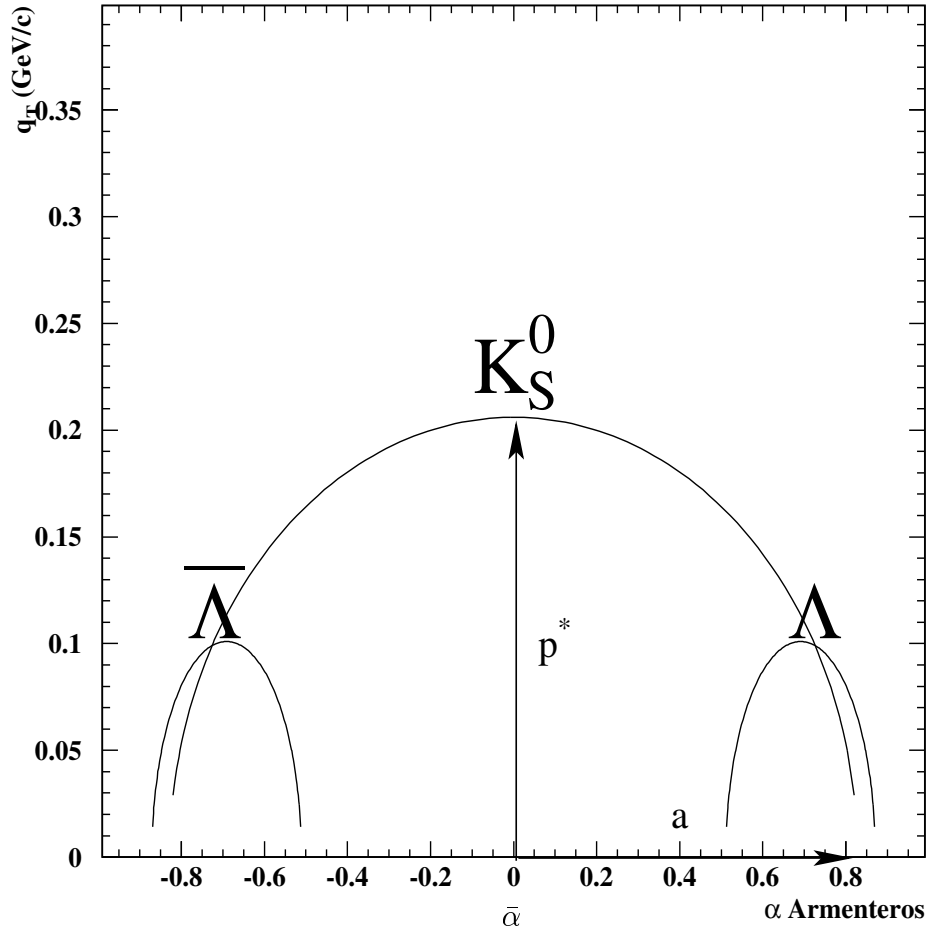


Figure C.2: The Armenteros-Podolanski plot showing the K_S^0 , $\bar{\Lambda}$ and Λ half ellipses. Also marked are the parameters p^* , a and $\bar{\alpha}$ for the K_S^0 .

C.2 Expressing p^* in Terms of Mass

By expressing p^* in terms of the masses of the particles involved in the decay would allow a numerical calculation of all features of the Armenteros-Podolanski plot. Below is a derivation which will allow this. The derivation relies heavily on the relativistic equation

$$E^2 = p^2 + m^2 \quad (\text{C.18})$$

Initially in the centre of mass system the V^0 particle of mass m_v is at rest ($\vec{p} = 0$) and so from (C.18)

$$E_v^* = m_v \quad (\text{C.19})$$

Finally the two decay particles of mass, m_1 and m_2 travel with momentum p_1^* and p_2^* and so

$$E_1^{*2} = p_1^{*2} + m_1^2, \quad E_2^{*2} = p_2^{*2} + m_2^2 \quad (\text{C.20})$$

Now in the centre of mass system the mass is invariant and so the mass initially equals the mass finally and thus using (C.19), (C.20) and (C.18)

$$m_v^2 = (\Sigma E)^2 - (\Sigma p)^2 = (E_1^* + E_2^*)^2 - (\vec{p}_1^* - \vec{p}_2^*)^2 \quad (\text{C.21})$$

which expanding and using (C.18) gives

$$m_v^2 = m_1^2 + m_2^2 + 2(E_1^* E_2^* - \vec{p}_1^* \cdot \vec{p}_2^*) \quad (\text{C.22})$$

Substituting for E_1^* and E_2^* by using (C.18) and rearranging gives

$$\left[\frac{(m_v^2 - m_1^2 - m_2^2) + 2\vec{p}_1^* \cdot \vec{p}_2^*}{2} \right]^2 = p_1^{*2} p_2^{*2} + m_1^2 m_2^2 + p_2^{*2} m_1^2 + p_1^{*2} m_2^2 \quad (\text{C.23})$$

Now in the centre of mass system the two decay particles come off with equal and opposite momentum so as to conserve momentum, and so $\vec{p}_1^* = p^*$ and $\vec{p}_2^* = -p^*$.

Further expansion of (C.23) and making this substitution

$$\left[\frac{(m_v^2 - m_1^2 - m_2^2)^2 + 4p^{*4} - 4p^{*2}(m_v^2 - m_1^2 - m_2^2)}{4} \right] = p^{*4} + m_1^2 m_2^2 + p^{*2} m_1^2 + p^{*2} m_2^2 \quad (\text{C.24})$$

Rearranging and collecting together terms in p^*

$$(m_v^2 - m_1^2 - m_2^2)^2 - 4m_1^2 m_2^2 = 4p^{*2} m_v^2 \quad (\text{C.25})$$

Expanding the brackets on the left hand side of (C.25) and rearranging to make p^* the subject gives

$$p^* = \frac{1}{2m_v} \sqrt{m_v^4 + m_1^4 + m_2^4 - 2m_v^2 m_1^2 - 2m_v^2 m_2^2 - 2m_1^2 m_2^2} \quad (\text{C.26})$$

Now from (C.13), (C.14), (C.26) all features of the Armenteros-Podolanski plot can be evaluated simply by knowing the mass of the V^0 and the masses of the particles it decays into.

C.3 Numerical Values of a , $\bar{\alpha}$ and p^*

Substituting the mass of the V^0 and their two decay particles [6] into (C.10), (C.13), (C.14), (C.26) allows the determination of a , $\bar{\alpha}$ and p^* , the results of which are shown in table C.1. These values are seen in the theoretical Armenteros-Podolanski plot shown in figure C.2.

Table C.1: Numerical values in the Armenteros-Podolanski plot

Decay	m_v (GeV)	m_1 (GeV)	m_2 (GeV)	$\bar{\alpha}$	p^*	a
$\Lambda \rightarrow p\pi^-$	1.1156	0.93828	0.13957	0.691	0.101	0.180
$\bar{\Lambda} \rightarrow \bar{p}\pi^+$	1.1156	0.13957	0.93828	-0.691	0.101	0.180
$K_s^0 \rightarrow \pi^+\pi^-$	0.49770	0.13957	0.13957	0	0.206	0.828

Appendix D

The Equation of the Curved Edges of the Acceptance Window

The acceptance window defined in section 4.4 forms a characteristic shape. The upper and right edges of which are two perpendicular lines defined by $p_T(max)$ and $y_{lab}(max)$, the lower and left edges by $p_T(min)$ and $y_{lab}(min)$. The curved lines which join the left edge to the upper edge and the lower edge to the right edge and represent the top and bottom of the telescope are defined by p_T which is a function of y_{lab} and θ , where θ is related to the angle of inclination of the telescope in the $x - z$ plane.

The equation which results from the following derivation allows these two curved lines to be evaluated. To begin the definition of rapidity is required:

$$y = \frac{1}{2} \ln \left(\frac{E + p_L}{E - p_L} \right) \quad (D.1)$$

By multiplying both sides of (D.1) by 2, then taking the exponential and using the identity

$$e^{\ln x} = x \quad (D.2)$$

(D.1) can be rewritten as

$$e^{2y} = \left(\frac{E + p_L}{E - p_L} \right) \quad (\text{D.3})$$

Multiplying out (D.3) and collecting terms in p_L allows p_L to become the subject

$$p_L = \left(\frac{e^{2y} - 1}{e^{2y} + 1} \right) E \quad (\text{D.4})$$

A factor of e^y is then taken outside of (D.4)

$$p_L = \frac{e^y}{e^y} \left(\frac{e^y - e^{-y}}{e^y + e^{-y}} \right) E \quad (\text{D.5})$$

Now by definition, $\sinh(y)$ and $\cosh(y)$ are

$$\sinh(y) = \frac{1}{2}(e^y - e^{-y}) \quad (\text{D.6})$$

and

$$\cosh(y) = \frac{1}{2}(e^y + e^{-y}) \quad (\text{D.7})$$

respectively. By substituting (D.6) and (D.7) into (D.5), (D.5) becomes

$$p_L = \left(\frac{\sinh(y)}{\cosh(y)} \right) E \quad (\text{D.8})$$

Now by definition

$$\tanh(y) = \frac{\sinh(y)}{\cosh(y)} \quad (\text{D.9})$$

By substituting (D.9) and squaring, (D.8) becomes

$$p_L^2 = E^2 \tanh^2(y) \quad (\text{D.10})$$

Using the definition

$$\cosh^2(y) - \sinh^2(y) = 1 \quad (\text{D.11})$$

Squaring (D.9) and using (D.11) to substitute for $\sinh(y)$, (D.9) becomes

$$\tanh^2(y) = 1 - \frac{1}{\cosh^2(y)} \quad (\text{D.12})$$

By substituting (D.12) into (D.10), p_L^2 can be expressed in terms of $\cosh^2(y)$

$$p_L^2 = E^2 - \frac{E^2}{\cosh^2(y)} \quad (\text{D.13})$$

which when rearranged becomes

$$E^2 - p_L^2 = \frac{E^2}{\cosh^2(y)} \quad (\text{D.14})$$

An expression for $E^2 - p_L^2$ can be found by using the definition of momentum (in terms of transverse and longitudinal momentum),

$$p^2 = p_T^2 + p_L^2 \quad (\text{D.15})$$

the well known relationship between energy, momentum and particle mass (mentioned in appendix A)

$$E^2 = p^2 + m^2 \quad (\text{D.16})$$

and the definition for transverse mass (section 1.5)

$$m_T^2 = p_T^2 + m^2 \quad (\text{D.17})$$

E^2 and p_L^2 can be expressed in terms of m_T^2 when (D.15) and (D.16) are substituted into (D.17)

$$E^2 = m_T^2 + p_L^2 \quad (\text{D.18})$$

Substituting (D.18) into (D.14) and making E^2 the subject:

$$E^2 = m_T^2(1 + \sinh^2(y)) \quad (\text{D.19})$$

Multiplying out and collecting E^2 and m_T^2 on the left hand side the following is obtained

$$E^2 - m_T^2 = m_T^2 \sinh^2(y) \quad (\text{D.20})$$

From which, using (D.18), (D.20) becomes

$$p_L^2 = m_T^2 \sinh^2(y) \quad (\text{D.21})$$

This becomes

$$p_L^2 = (p_T^2 + m^2) \sinh^2(y) \quad (\text{D.22})$$

when (D.17) is substituted for m_T^2 .

Now p_T and p_L by definition form a right angle to each other, the total momentum, p , forms the hypotenuse of this triangle. The angle between p_L and p is θ . Now using the simple trigonometric relationships:

$$p_L = p \cos(\theta) \quad (\text{D.23})$$

$$p_T = p \sin(\theta) \quad (\text{D.24})$$

Substituting (D.23) and (D.24) into (D.22) for p_L and p_T gives

$$p^2 \cos^2(\theta) = m^2 \sinh^2(y) + p^2 \sin^2(\theta) \sinh^2(y) \quad (\text{D.25})$$

Collecting terms in p^2 together (D.25) becomes

$$p^2 (\cos^2(\theta) - \sin^2(\theta) \sinh^2(y)) = m^2 \sinh^2(y) \quad (\text{D.26})$$

Now using (D.24), (D.26) can be expressed in terms of p_T

$$p_T = \frac{m \sin(\theta) \sinh(y)}{\sqrt{(\cos^2(\theta) - \sin^2(\theta) \sinh^2(y))}} \quad (\text{D.27})$$

Using the approximations, $\cos(\theta) \sim 1$ and $\sin(\theta) \sim \theta$ this equation becomes the same as (4.2):

$$p_T = \frac{m \theta \sinh(y)}{\sqrt{(1 - \theta^2 \sinh^2(y))}} \quad (\text{D.28})$$

Appendix E

Maximum Likelihood Method

The maximum likelihood method (MLM) is used to obtain the inverse slope, T , parameter. Given N particles each with a given transverse mass, m_T : m_{T1} , m_{T2} , $m_{T3} \dots m_{TN}$ and the probability distribution that describes m_T (assuming a flat rapidity distribution), given by (4.4), $f(m_{Ti}, T)$

$$f(m_{Ti}, T) = m_T A(T) e^{-m_T/T} \quad (\text{E.1})$$

T can be determined using the maximum likelihood method. In order to determine T , the constant $A(T)$ must first be evaluated in terms of T . This is done by integrating $f(m_T, T)$ over the entire acceptance window, and normalising the result by setting this equal to 1, as seen in (E.2)

$$\int_{\text{window}} f(m_T, T) dm_T = 1 \quad (\text{E.2})$$

Now the probability of measuring m_{T1} is $f(m_{T1}, T)$, m_{T2} is $f(m_{T2}, T)$ and m_{TN} is $f(m_{TN}, T)$, so the probability of getting the results which were obtained is:

$$\mathcal{L} = f(m_{T1}, T) f(m_{T2}, T) \dots f(m_{TN}, T) = \prod_{i=1}^N f(m_{Ti}, T) \quad (\text{E.3})$$

where \mathcal{L} is the *likelihood function*.

Now, as seen in section 4.2.5, for every one particle that is detected with a given m_T there are many more which are not detected by experiment due to detector and reconstruction inefficiencies, acceptance of the telescope, and so on. To correct for this a weight for each particle has been calculated, as explained in section 4.2. To correct for the weight [122] (E.3) becomes

$$\mathcal{L} = f(m_{T1}, T)^{W_1} f(m_{T2}, T)^{W_2} \dots f(m_{TN}, T)^{W_N} = \prod_{i=1}^N f(m_{Ti}, T)^{W_i} \quad (\text{E.4})$$

where W_i is the weight assigned to the i th particle

Next, T is selected such that \mathcal{L} is maximised

$$\frac{\partial \mathcal{L}}{\partial T} = 0 \quad (\text{E.5})$$

It is easier to maximise $\ln \mathcal{L}$ rather than \mathcal{L} (both of which are in the same place) and in doing so the product of (E.2) becomes a summation:

$$\ln \mathcal{L} = \sum_{i=1}^N \ln f(m_{Ti}, T)^{W_i} \quad (\text{E.6})$$

which becomes

$$\ln \mathcal{L} = \sum_{i=1}^N W_i \ln f(m_{Ti}, T) \quad (\text{E.7})$$

and so the maximisation condition becomes:

$$\frac{\partial \ln \mathcal{L}}{\partial T} = \sum_{i=1}^N W_i \frac{\partial}{\partial T} \ln f(m_{Ti}, T) = 0 \quad (\text{E.8})$$

The maximum likelihood method is performed using a program called MINUIT [90], which is used to find the minimum (or maximum) value of a multi-parameter function and analyse the shape of the function about the minimum (or maximum).

Appendix F

Λ , $\bar{\Lambda}$ and K_S^0 yields from NA57 at 40 A GeV/c and 158 A GeV/c

Given in tables F.1 and F.2 are the full results of yields for the three particles studied in p–Be and Pb–Pb collisions at 40 A GeV/c [101, 102] and p–Be, p–Pb and Pb–Pb collisions at 158 A GeV/c [28, 70, 115].

Table F.1: Yields at 40 A GeV/c in p–Be and in the five Pb–Pb centrality classes. Quoted errors are statistical only.

	p–Be (NA57)	Pb–Pb (NA57)				
Class		0	1	2	3	4
$\langle N_{wound} \rangle$	2.5	57 ± 5	119 ± 5	208 ± 4	292 ± 1	346 ± 1
Λ	0.0290 ± 0.0008	1.549 ± 0.133	3.824 ± 0.167	9.147 ± 0.293	15.238 ± 0.532	21.117 ± 0.775
$\bar{\Lambda}$	0.00230 ± 0.00020	0.044 ± 0.006	0.136 ± 0.008	0.246 ± 0.013	0.350 ± 0.019	0.446 ± 0.030
K_S^0	0.0323 ± 0.0008	1.284 ± 0.172	3.693 ± 0.214	7.971 ± 0.383	14.064 ± 0.679	18.384 ± 1.100

One can see that the yield in p–Be interactions increases for both Λ and $\bar{\Lambda}$ particles when going from 40 GeV/c to 158 GeV/c. A clear increase for the K_S^0 is seen between the p–Be result at 40 GeV/c and the p–Pb result at 158 GeV/c. These results are due to the extra energy in the system at the higher collision energy, making it easier to produce particles via hadronic processes. Looking at the Pb–Pb

Table F.2: Yields at 158 A GeV/c in p-Be, p-Pb and in the five Pb-Pb centrality classes. Quoted errors are statistical only.

	p-Be (WA97)	p-Pb (WA97)	Pb-Pb (NA57)				
Class			0	1	2	3	4
$\langle N_{wound} \rangle$	2.5	4.75	62 ± 4	121 ± 4	209 ± 3	290 ± 2	349 ± 1
Λ	0.0344 ± 0.0005	0.060 ± 0.002	2.30 ± 0.22	5.19 ± 0.29	9.50 ± 0.50	15.0 ± 0.80	18.5 ± 1.1
$\bar{\Lambda}$	0.0111 ± 0.0002	0.015 ± 0.001	0.417 ± 0.035	0.82 ± 0.04	1.60 ± 0.07	1.84 ± 0.10	2.47 ± 0.14
K_S^0	–	0.098 ± 0.004	3.08 ± 0.34	8.14 ± 0.48	15.5 ± 0.8	21.8 ± 1.2	26.2 ± 1.7

results at the two energies, it is clear the Λ particles do not exhibit much energy dependence. Conversely, the yields of both the K_S^0 and $\bar{\Lambda}$ particles increase in all classes when going from 40 A GeV/c to 158 A GeV/c. This can be understood as due to a decrease in net quark density with increasing collision energy.

Bibliography

- [1] NA57 Proposal, *CERN/SPSLC/96-40 SPSLC/P300*, (August 1996).
- [2] D.H. Perkins, *Introduction to High Energy Physics*, Addison-Wesley Publishing Company, Third Edition, (1987).
- [3] F. Halzen and A.D. Martin, *Quarks and Leptons: An Introductory Course in Modern Particle Physics*, John Wiley & Sons, (1984).
- [4] J. Letessier and J. Rafelski, *Hadrons and Quark-Gluon Plasma*, Cambridge University Press, (2002).
- [5] W.S.C. Williams, *Nuclear and Particle Physics*, Oxford University Press, (1997).
- [6] S. Eidelman *et al.*, (Particle Data Group), *Phys. Lett. B* **592**, (2004), 1-1109.
- [7] S. Hands, *Contemp. Phys.* **42**, (2001), 209-225.
- [8] D.J. Gross and F. Wilczek, *Phys. Rev. Lett.* **30**, (1973), 1343-1346.
- [9] H.D. Politzer, *Phys. Rev. Lett.* **30**, (1973), 1346-1349.
- [10] Thesis of D. Evans, *Strange & Multistrange Baryon & Antibaryon Production in Sulphur-Tungsten Interactions at 200 GeV/c per Nucleon*, The University of Birmingham, (1992).
- [11] K. Rajagopal, *SLAC Beam Line: A Periodical of Particle Physics* **31N2**, (2001), 9-15.

- [12] E. Shuryak, The QCD Vacuum, Chiral Phase Transition and Quark-Gluon Plasma, *hep-ph/9503427*, (March 1995).
- [13] D.J. Hofman, *Eur. Phys. J. C* **33**, (2004), s589-s593.
- [14] J.W. Harris and B. Müller, *Annu. Rev. Nucl. Part. Sci.* **46**, (1996), 71-107.
- [15] S. Margetis, K. Šafařík, O. Villalobos Baillie, *Annu. Rev. Nucl. Part. Sci.* **50**, (2000), 299-342.
- [16] F. Weber, *J. Phys. G: Nucl. Part. Phys.* **27**, (2001), 465-474.
- [17] E. Quercigh and J. Rafelski, *Phys. World* **13N10**, (2000), 37-42.
- [18] D. Teaney, Chemical Freezeout in Heavy Ion Collisions, *nucl-th/0204023*, (April 2002).
- [19] J. Rafelski, *Phys. Rep.* **88**, (1982), 331-347.
- [20] P. Koch, J. Müller and J. Rafelski, *Phys. Rep.* **142**, (1986), 167-262.
- [21] F. Wang, *J. Phys. G: Nucl. Part. Phys.* **27**, (2001), 283-292.
- [22] J. Rafelski and J. Letessier, *J. Phys. G: Nucl. Phys.* **30**, (2004), S1-S28.
- [23] T. Matsui, B. Svetitsky, L.D. McLerran, *Phys. Rev. D* **34**, (1986), 783-793.
Erratum. *Phys. Rev. D* **37**, (1988), 844.
- [24] S. Afanasiev *et al.*, (NA49 Collaboration), *Nucl. Instr. and Meth. in Phys. Res. A* **430**, (1999), 210-244.
- [25] WA97 Proposal, *CERN/SPSLC/91-29 SPSLC/P263*, (May 1991).
- [26] D. Elia *et al.* (WA97 Collaboration), *Nucl. Phys. A* **661**, (1999), 476c-480c.
- [27] E. Andersen *et al.*, (WA97 Collaboration), *Phys. Lett. B* **433**, (1998), 209-216.
- [28] E. Andersen *et al.*, (WA97 Collaboration), *Phys. Lett. B* **449**, (1999), 401-406.

- [29] F. Antinori *et al.* (WA97 Collaboration), *Nucl. Phys. A* **661**, (1999), 130c-139c.
- [30] T. Matsui and H. Satz, *Phys. Lett. B* **178**, (1986), 416-422.
- [31] NA50 Proposal, *CERN/SPSLC/91-55 SPSLC/P265*, (November 1991).
- [32] M.C. Abreu *et al.*, (NA50 Collaboration), *Phys. Lett. B* **477**, (2000), 28-36.
- [33] C. Lourenço, *Nucl. Phys. A* **698**, (2002), 13c-22c.
- [34] H.J. Specht, *Nucl. Phys. A* **698**, (2002), 341c-359c.
- [35] G.Q. Li, C.M. Ko, G.E. Brown, *Nucl. Phys. A* **606**, (1996), 568-606.
- [36] NA45/CERES Proposal, *CERN/SPSC/88-25 SPSC/P237*, (June 1988).
- [37] B. Lenkeit *et al.*, (CERES Collaboration), *Nucl. Phys. A* **661**, (1999), 23c-32c.
- [38] R. Rapp and J. Wambach, Vector Mesons in Medium and Dileptons in Heavy-Ion Collisions, *nucl-th/0001014*, (January 2000).
- [39] R. Rapp and J. Wambach, *Adv. Nucl. Phys.* **25**, (2000) 1.
- [40] M.M. Aggarwal *et al.*, (WA98 Collaboration), Direct Photon Production in 158 A GeV $^{208}\text{Pb}+^{208}\text{Pb}$ Collisions, *nucl-ex/0006007*, (June 2000).
- [41] E.L. Feinberg, *Nuovo Cimento A* **34**, (1976), 391.
- [42] E.V. Shuryak, *Phys. Lett. B* **78**, (1978), 150-153.
- [43] WA98 Proposal, *CERN/SPSLC/91-17 SPSLC/P260*, (May 1991).
- [44] M.M. Aggarwal *et al.*, (WA98 Collaboration), *Phys. Rev. Lett.* **85**, (2000), 3595-3599.
- [45] T. Ludlam, *CERN Courier: International Journal of High-Energy Physics* **43N7**, (2003), 18-20.

- [46] M. Gyulassy and M. Plümer, *Phys. Lett. B* **243**, (1990), 432-438.
- [47] X.N. Wang and M. Gyulassy, *Phys. Rev. Lett.* **68**, (1992), 1480-1483.
- [48] RHIC (Relativistic Heavy Ion Collider), *www.bnl.gov/RHIC*.
- [49] J. Adams *et al.*, (STAR Collaboration), *Phys. Rev. Lett.* **91**, (2003), 072304.
- [50] D. d'Enterria, *J. Phys. G: Nucl. Part. Phys.* **31**, (2005) S491-S512.
- [51] J.L. Klay, *J. Phys. G: Nucl. Part. Phys.* **31**, (2005) S451-S464.
- [52] M.M. Aggarwal *et al.*, (WA98 Collaboration), *Eur. Phys. J. C* **23**, (2002), 225-236.
- [53] F. Antinori *et al.*, (NA57 Collaboration), Central-to-peripheral nuclear modification factors in Pb–Pb collisions at $\sqrt{s_{NN}} = 17.3$ GeV, *nucl-ex/0507012*, (July 2005), accepted by *Phys. Lett. B*.
- [54] U. Heinz and M. Jacob, Evidence for a New State of Matter: An Assessment of the Results from the CERN Lead Beam Programme, *nucl-th/0002042*, (February 2000).
- [55] J.L. Nagle, *J. Phys. G: Nucl. Part. Phys.* **27**, (2001) 567-569.
- [56] T. Schaefer, *Phys. World* **16N6**, (2003), 31-35.
- [57] F. Videbæk *et al.*, (BRAHMS Collaboration), *Nucl. Phys. A* **566**, (1994), 299c-303c.
- [58] D.P. Morrison *et al.*, (PHENIX Collaboration), *Nucl. Phys. A* **638**, (1998), 565c-569c.
- [59] B. Wyslouch *et al.*, (PHOBOS Collaboration), *Nucl. Phys. A* **566**, (1994), 305c-309c.
- [60] J.W. Harris *et al.*, (STAR Collaboration) *Nucl. Phys. A* **566**, (1994), 277c-286c.

- [61] J. Schukraft *et al.*, (ALICE Collaboration), *Nucl. Phys. A* **566**, (1994), 311c-319c.
- [62] K.J. Eskola, High Energy Nuclear Collisions, *hep-ph/9911350*, (November 1999).
- [63] The CBM Collaboration, Letter of Intent for the Compressed Baryonic Matter Experiment at the Future Accelerator Facility in Darmstadt, *www.gsi.de/zukunftsprojekt/experimente/CBM*, (January 2004).
- [64] P. Senger, *J. Phys. G: Nucl. Part. Phys.* **28**, (2002) 1869-1875.
- [65] The Alice Experiment, *www.ep.ph.bham.ac.uk/exp/ALICE*.
- [66] WA85 Proposal, *CERN/SPSC/84-76 SPSC/P206*, (October 1984).
- [67] F. Antinori *et al.*, (WA85 Collaboration), *Phys. Lett. B* **447**, (1999), 178-182.
- [68] WA94 Proposal, *CERN/SPSLC/91-5 SPSLC/P257*, (January 1991).
- [69] D. Evans *et al.*, (WA85 and WA94 Collaborations), *J. Phys. G: Nucl. Part. Phys.* **25**, (1999) 209-216.
- [70] V. Manzari *et al.*, (NA57 Collaboration), *Nucl. Phys. A* **715**, (2003) 140c-150c.
- [71] V. Manzari *et al.*, (NA57 Collaboration), *J. Phys. G: Nucl. Part. Phys.* **25**, (1999) 473-479.
- [72] CERN Accelerators and Beam Operations Group, SPS Section, *ab-dep-op-sps.web.cern.ch/ab-dep-op-sps*.
- [73] C.E. Hill, CERN Hadron LINACS, *linac2.home.cern.ch/linac2/default.htm*, (October 2003).
- [74] K.H. Kissler, SPS and LEP Status Report, *CERN SL-98-053 DI*, (September 1998).

- [75] P. Watkins, *Story of the W and Z*, Cambridge University Press, (1986).
- [76] A. Bettini, *Nucl. Phys. B (Proc. Suppl.)* **100**, (2001), 332-337.
- [77] WA11 Proposal, *CERN/SPSC/76-3 SPSC/P58*, (January 1976).
- [78] V. Manzari *et al.*, (NA57 Collaboration), *Nucl. Phys. A* **661**, (1999) 716c-720c.
- [79] F. Antinori *et al.*, (RD19 and WA97 Collaborations), *Nucl. Instr. and Meth. in Phys. Res. A* **360**, (1995), 91-97.
- [80] E.H.M. Heijne *et al.*, (RD19 and WA97 Collaborations), *Nucl. Instr. and Meth. in Phys. Res. A* **383**, (1996), 55-63.
- [81] Thesis of M. Thompson, *Hyperon Production in Lead-Lead and Proton-Beryllium Interactions at 158 GeV/c per Nucleon*, The University of Birmingham, (October 1999).
- [82] Thesis of R.F. Clarke, *Proton-Beryllium Interactions at 40 GeV/c*, The University of Birmingham, (September 2004).
- [83] R. Fernow, *Introduction to Experimental Particle Physics*, Cambridge University Press, (1990).
- [84] N. Carrer *et al.*, (WA97 and NA57 Collaborations), *J. Phys. G: Nucl. Part. Phys.* **27**, (2001) 391-396.
- [85] C.Y. Wong, *Introduction to High Energy Heavy-Ion Collisions*, Singapore: World Scientific, (1994).
- [86] Extension to Indium of the NA57 Programme, *CERN/SPSC/2003-003 SPSC/P300/Add 1*, (January 2003).
- [87] Physics Analysis Workstation, *An Introductory Tutorial*, CERN Program Library, Long Writeup Q121, (1995).
- [88] J. Podolanski and R. Armenteros, *Phil. Mag.* **45**, (1954), 13.

- [89] O. Villalobos Baillie, *The Program CENTKK* (Internal Document), The University of Birmingham, (November 2004).
- [90] F. James, MINUIT, *Reference Manual*, CERN Program Library, Long Writeup D506, (1994).
- [91] D. Barberis *et al.*, (WA102 Collaboration), *Phys. Lett. B* **507**, (2001), 14-18.
- [92] Thesis of P. Norman, *Hyperon Production in p -Be Interactions at 158 GeV/c per Nucleon at the WA97 CERN Experiment*, The University of Birmingham, (October 1999).
- [93] GEANT, *Detector Description and Simulation Tool*, CERN Program Library, Long Writeup W5013, (1993).
- [94] H.C. Eggers and J. Rafelski, *Int. J. Mod. Phys. A* **6**, (1991), 1067.
- [95] F. Antinori *et al.*, (NA57 Collaboration), *J. Phys. G: Nucl. Part. Phys.* **30**, (2004), 823-840.
- [96] G.E. Bruno *et al.*, (NA57 Collaboration), *J. Phys. G: Nucl. Part. Phys.* **31**, (2005), S127-S133.
- [97] R.A. Fini *et al.*, (WA97 Collaboration), *Nucl. Phys. A* **681**, (2001) 141c-148c.
- [98] D. Elia *et al.*, (NA57 Collaboration), *J. Phys. G: Nucl. Part. Phys.* **30**, (2004), S1329-S1332.
- [99] I. Králik, *1999/2001 discrepancies in p -Be at 40 GeV/c Λ s*, results presented at NA57 Collaboration meeting, (8th-9th June 2004).
- [100] F. Antinori *et al.*, (NA57 Collaboration), *J. Phys. G: Nucl. Part. Phys.* **31**, (2005), 321-335.
- [101] G.E. Bruno *et al.*, (NA57 Collaboration), *J. Phys. G: Nucl. Part. Phys.* **30**, (2004), S717-S724.

- [102] A. Kravčáková, private communication.
- [103] F. Antinori *et al.*, (NA57 Collaboration), *Phys. Lett. B* **595**, (2004), 68-74.
- [104] A. Kravčáková, K_S^0 production in Pb–Pb interactions at 40 GeV, results presented at NA57 Collaboration meeting, (25th-26th September 2003).
- [105] U. Heinz, *Nucl. Phys. A* **638**, (1998) 357c-364c.
- [106] M. Gaździcki and D. Röhrich, *Z. Phys. C* **71**, (1996), 55-63.
- [107] T. Anticic *et al.* (NA49 Collaboration), *Phys. Rev. Lett.* **93**, (2004), 022302.
- [108] S.V. Afanasiev *et al.* (NA49 Collaboration), *Phys. Rev. C* **66**, (2002), 054902.
- [109] W. Schmitz *et al.* (CERES Collaboration), *J. Phys. G: Nucl. Part. Phys.* **28**, (2002), 1861-1868.
- [110] E. Fermi, *Prog. Theor. Phys.* **5**, (1950), 570.
- [111] M. Gaździcki *et al.*, (NA49 Collaboration), *J. Phys. G: Nucl. Part. Phys.* **30**, (2004), S701-S708.
- [112] C.A. Ogilvie, *J. Phys. G: Nucl. Part. Phys.* **23**, (1997), 1803-1816.
- [113] M. Gaździcki and M.I. Gorenstein, *Acta Phys. Polon. B* **30**, (1999), 2705.
- [114] M. Gaździcki, *Acta Phys. Polon. B* **35**, (2004), 187-190.
- [115] G.E. Bruno, K_S^0 production in Pb–Pb interactions at 160 GeV, results presented at NA57 Collaboration meeting, (10th-11th April 2003).
- [116] H. Caines, *J. Phys. G: Nucl. Part. Phys.* **31**, (2005), S101-S117.
- [117] A. Tounsi and K. Redlich, Strangeness Enhancement and Canonical Suppression, *hep-ph/0111159*, (November 2001).
- [118] K. Redlich and A. Tounsi, *Eur. Phys. J. C* **24**, (2002), 589-594.

- [119] A. Tounsi, A. Mischke and K. Redlich, *Nucl. Phys. A* **715**, (2003), 565c-568c.
- [120] H. Caines *et al.*, (STAR Collaboration), *J. Phys. G: Nucl. Part. Phys.* **31**, (2005), S1057-S1060.
- [121] M.A.C. Lamont *et al.*, (STAR Collaboration), *J. Phys. G: Nucl. Part. Phys.* **28**, (2002), 1721-1728.
- [122] W.T. Eadie *et al.*, *Statistical Methods in Experimental Physics*, Elsevier Science Publishers, Third Reprint, (1988).